

Equivalent frame models for in-plane and out-of-plane response of unreinforced masonry buildings

Thèse N° 9741

Présentée le 30 août 2019

à la Faculté de l'environnement naturel, architectural et construit
Laboratoire du génie parasismique et dynamique des structures
Programme doctoral en génie civil et environnement

pour l'obtention du grade de Docteur ès Sciences

par

Francesco VANIN

Acceptée sur proposition du jury

Prof. A. Berne, président du jury
Prof. K. Beyer, Prof. A. Penna, directeurs de thèse
Prof. E. Spacone, rapporteur
Prof. B. Stojadinovic, rapporteur
Dr M. Fernández Ruiz, rapporteur

2019

Acknowledgements

Firstly I would like to acknowledge the people who contributed to this work with their guidance and advice. My supervisor, Prof. Katrin Beyer, who followed this work with interest and enthusiasm, leading it to its goal and at the same time leaving the space for experimenting different directions. Her commitment, passion for research and professionalism are among the most important things I had the opportunity to learn in these years at EPFL. A great thanks goes also to my co-supervisor Prof. Andrea Penna, for the fruitful discussions we had that contributed to the development of this work.

I would also like to thank the members of my thesis jury, Prof. Alexis Berne (president), Dr. Miguel Fernández Ruiz, Prof. Enrico Spacone and Prof. Božidar Stojadinovic, for their interest in my work and the insightful comments they provided.

A grateful mention goes to the people with whom I mostly discussed some parts of this work, starting from Prof. João P. Almeida to Dr. Michele Godio and Dr. Bastian Wilding. I greatly appreciated their input, their availability, and their opinions and comments.

I would also thank the other members of the EESD laboratory, firstly Yvonne, for her help in all administrative issues, and comprehension for my many delays. Then my office mates, Danilo, with whom, other than four years at the same desk, I shared a love for mountaineering and a disgraceful passion for Inter, Angelica, who made way more enjoyable the time spent here, and Ryan. I would also thank all the other people working in EESD, Igor, Amir, Mahmoud, Enio, Aarash, and the former members who are now appreciated engineers, Alessandro, Zerba, Ioannis, Raluca, Marco, Sarah, and the wise Shenghan. I would also acknowledge some students I had the opportunity to work with, who contributed to some parts of this work and, mainly, brought a friendly and relaxed atmosphere to these offices, from Dario to Dyonisia, Maria, Tarscha, Ayoub, Paolo and Giuseppe. Lastly, a mention to the friends I met in EPFL, Raffaele, Francesco, Manuel, Myrsini, Maria, Aida, Georgia, Eleni.

Finally, I want to thank my family, for their unconditional support and presence even from far away, and for many more reasons that do not need to be mentioned here.

Lausanne, August 19, 2019

Francesco Vanin

Abstract

The seismic assessment of masonry buildings, both modern unreinforced masonry (URM) buildings and historical heritage constructions, is a complex task, characterised by a several sources of uncertainty, which regard the appropriate modelling strategy of the problem, the model parameters, and the seismic input. In order to properly account for all sources of uncertainty and provide a robust risk estimate, simple models to be run under different conditions are necessary. In this framework, equivalent frame modelling of masonry buildings is an approach which can produce reliable estimates of the seismic demands, in terms of displacement and acceleration, for buildings showing a predominant in-plane failure mode. The simplicity of the approach allows performing multiple simulations at a reasonable computational cost.

This thesis concentrates on the extension of the equivalent frame modelling approach for describing both the in-plane and the out-of-plane response of masonry buildings. Making use of the computational simplicity of equivalent frame models, it further proposes an approach for the probabilistic assessment of buildings, which aims at being potentially applicable also outside the research domain, to which probabilistic methods are mainly confined at the state of the art.

In order to collect information on the uncertainties related to the assessment of the in-plane behaviour of masonry elements, with a particular regard to stone masonry, a database of 128 shear compression tests on walls was collected and analysed. Distributions and median values of the most relevant material properties were derived, including the displacement capacities at cracking, yielding, maximum force capacity, significant damage and collapse limit states. Moreover, the uncertainty on the determination of force capacity and stiffness was discussed.

This data was then used to apply to a case study a simplified approach for the explicit introduction of uncertainty in the seismic assessment of a building. The method was compared to established approaches of similar complexity and a reference Monte Carlo simulation. From the analysis, the relative impact of all sources of uncertainty on the total model uncertainty could be evaluated, showing the major relevance of the displacement capacity in determining the seismic performance.

Secondly, a formulation of a macro-element model for the simulation of the in-plane and out-of-plane response of masonry walls is proposed. Its formulation and the validation of its use for describing the dynamic in-plane and out-of-plane response of a masonry element are shown. The extension of its use to reproduce the dynamic behaviour of entire buildings is further discussed through the comparison of numerical simulations to two shaking table tests. The proposed macro-element is able to describe the main features of the out-of-plane dynamic response of buildings, highlighting the major sources of vulnerability and simulating the effect of the quality of connections on the global response, both in terms of displacement demands and failure modes.

Sommario

La valutazione della sicurezza sismica di edifici in muratura, sia nel caso di edifici contemporanei che di beni appartenenti al patrimonio storico e culturale, è un processo complesso, caratterizzato da molteplici fonti di incertezza, che possono riguardare l'approccio stesso alla modellazione, nella scelta di una strategia adeguata, quanto i parametri dei modelli da applicare, e l'incertezza, predominante, che riguarda la determinazione dell'input sismico. Al fine di considerare adeguatamente tutte queste fonti di incertezza e produrre una stima robusta del rischio sismico, sono necessarie simulazioni semplici in grado di tenere conto di diversi scenari.

A questo riguardo, la modellazione a telaio equivalente di edifici in muratura è un approccio che può produrre delle stime sufficientemente affidabili della domanda sismica sull'edificio, in termini di domanda di spostamento e di accelerazione, per edifici regolari che mostrino un comportamento sismico dominato dalla risposta nel piano degli elementi strutturali. La semplicità dell'approccio permette di effettuare diverse simulazioni a un costo computazionale contenuto, ed è per questo motivo particolarmente adeguata ad essere applicata in un contesto, quale quello della valutazione sismica di edifici in muratura, caratterizzato da rilevanti fonti di incertezza.

Questo lavoro di tesi si concentra sull'estensione di modelli a telaio equivalente per la modellazione sia del comportamento nel piano che fuori piano di edifici in muratura. Sfruttando la semplicità computazionale di questo tipo di modellazione, propone di conseguenza un approccio probabilistico per l'analisi sismica di edifici, che mira ad essere potenzialmente applicabile anche fuori dal ristretto ambiente della ricerca accademica, dentro al quale, allo stato dell'arte, è essenzialmente confinato.

Allo scopo di raccogliere dati sulle incertezze che caratterizzano il comportamento nel piano della muratura in pietra, è stato raccolto un database di 128 prove sperimentali a taglio e compressione su murature. Sono state ricavate le distribuzioni delle proprietà meccaniche più rilevanti ai fini dell'analisi sismica di edifici in muratura, tra cui le capacità di spostamento agli stati limite di fessurazione, *yielding*, alla massima resistenza laterale, e allo stato limite di *significant damage* e di collasso. Oltre alla stima dei valori mediani rilevati sperimentalmente, viene discussa l'incertezza che caratterizza i modelli comunemente utilizzati per descrivere la rigidezza, la resistenza laterale e la capacità di spostamento di elementi in muratura di pietra.

Questi dati vengono quindi utilizzati nell'applicazione, attraverso un caso-studio, di una metodologia semplificata per l'introduzione esplicita di valutazioni probabilistiche nell'analisi di un edificio. Il metodo viene confrontato con altri approcci maggiormente radicati nella ricerca e con una più complessa analisi di tipo Monte Carlo, utilizzata come soluzione di riferimento. Dall'analisi dell'impatto delle diverse fonti di incertezza emerge quanto sia rilevante la capacità di spostamento degli elementi strutturali nel determinare la performance sismica di un edificio.

Sommario

Da ultimo, viene proposta la formulazione di un macro-elemento per l'analisi del comportamento in piano e fuori piano di pareti in muratura. Ne viene derivata la formulazione e ne viene validato l'uso nel descrivere il comportamento nel piano e fuori piano di singoli pannelli in muratura. L'estensione dell'impiego di tale elemento nella simulazione del comportamento dinamico di interi edifici viene ulteriormente discussa attraverso la simulazione numerica di alcuni test su tavola vibrante. L'approccio proposto è in grado di modellare la risposta dinamica fuori piano, evidenziando le principali vulnerabilità dell'edificio e simulando l'effetto della qualità delle connessioni nel determinare la risposta globale, tanto in termini di domanda di spostamento quanto a meccanismo di rottura.

Résumé

L'évaluation sismique des bâtiments en maçonnerie, qu'il s'agisse de bâtiments modernes en maçonnerie non armée ou de constructions du patrimoine historique, est une tâche complexe, caractérisée par plusieurs sources d'incertitude concernant la stratégie de modélisation même plus appropriée au problème, les paramètres du modèle et l'input sismique. Afin de bien prendre en compte toutes ces sources d'incertitude et de produire une estimation robuste du risque sismique, il faut procéder à des simulations simples, prenant en compte nombreux scénarios différents.

La modélisation à cadre équivalent des bâtiments en maçonnerie est une approche qui peut produire des estimations suffisamment robustes de la demande sismique, en termes de demande de déplacement et d'accélération, pour les bâtiments montrant un comportement sismique dominé par la réponse dans le plan des éléments structurels. La simplicité de l'approche permet d'effectuer différentes simulations à un coût computationnel contenu. Son application est donc particulièrement appropriée dans un contexte, comme l'évaluation sismique des bâtiments en maçonnerie, caractérisé par des relevants sources d'incertitude.

Ce travail de thèse se concentre sur l'extension de modèles à cadre équivalent pour décrire la réponse sismique soit dans le plan soit hors plan des bâtiments en maçonnerie. Profitant de la simplicité de ce type de modélisation, cette thèse propose une approche probabiliste à l'analyse sismique des bâtiments, potentiellement applicable même dehors de l'environnement de la recherche universitaire, dans lequel, à l'état de l'art, il est essentiellement confiné.

Afin de recueillir des informations sur les incertitudes liées à l'évaluation du comportement dans le plan des éléments de maçonnerie, et en particulier de la maçonnerie en pierre, une base de données de 128 tests expérimentaux de compression et cisaillement sur des murs a été collectée et analysée. Les distributions de les propriétés mécaniques plus importants pour l'analyse sismique des bâtiments en maçonnerie ont été obtenues, y compris la capacité de déplacement aux états limites de fissuration, yielding, résistance latérale maximale, et l'état limite de *significant damage* et collapse. Outre l'estimation des valeurs médianes détectées expérimentalement, on discute l'incertitude qui caractérise les modèles couramment utilisés pour décrire la rigidité, la résistance latérale et la capacité de déplacement des éléments en maçonnerie.

Ces données ont ensuite été utilisées pour l'application, à travers une étude de cas, d'une méthodologie simplifiée pour l'introduction explicite d'évaluations probabilistes dans l'analyse d'un bâtiment. La méthode est comparée à d'autres approches plus établies dans la recherche, et à une analyse plus complexe du type Monte Carlo, utilisée comme solution de référence. À partir de l'analyse, l'impact relatif de toutes les sources d'incertitude sur l'incertitude totale du modèle pourrait être évalué, montrant ainsi la relevance de la capacité de déplacement dans la détermination de la performance

Résumé

sismique d'un bâtiment.

Enfin, la formulation d'un macro-élément pour l'analyse du comportement dans le plan et hors plan de murs en maçonnerie est proposée. Sa formulation et la validation de son utilisation pour décrire la réponse dynamique dans le plan et hors du plan d'un élément de maçonnerie sont présentées. L'extension de l'utilisation de cet élément dans la simulation du comportement dynamique de bâtiments entiers est examinée plus en détail à travers la simulation numérique de deux tests sur table vibrante. L'approche proposée permet de modéliser la réponse dynamique hors plan, en soulignant les principales vulnérabilités du bâtiment et en simulant l'effet de la qualité des connexions sur la détermination de la réponse globale, soit en termes de demande de déplacement soit de mécanisme de rupture.

Contents

Acknowledgements	i
Abstract (English)	iii
Sommario (Italian)	v
Résumé (French)	vii
Introduction	1
1 Stiffness, strength and drift capacity of stone masonry walls	11
1.1 Introduction	12
1.2 Database of tests on stone masonry walls	14
1.2.1 Bilinear approximation of the force-displacement curve	16
1.2.2 Distribution of properties of test units contained within the database	17
1.2.3 Quality control of measured peak strength	20
1.3 Aleatoric variability of stiffness, strength and drift limits	21
1.4 Effect of load history on stiffness, strength and drift limits	22
1.5 Stiffness of stone masonry walls	24
1.5.1 Ratio of effective to uncracked stiffness	24
1.5.2 E-modulus as a function of the masonry typology	25
1.5.3 Determining the E-modulus from compression tests or dynamic identification tests	27
1.5.4 Determining the E-modulus from the compression strength	27
1.6 Strength of stone masonry walls	29
1.6.1 Strength equations in Eurocode 8, Part 3	29
1.6.2 Application of strength equations to database	30
1.6.3 Turnšek and Čačovič criterion and calibration of the tensile strength	32
1.6.4 Comparison of different strength models	33
1.7 Drift capacity of stone masonry walls	34
1.7.1 Sensitivity of drift capacities at different limit states	36
1.7.2 Simple drift capacity models for engineering practice	38
1.8 Summary and conclusions	46

Contents

2	Treatment of epistemic uncertainty through a Point-Estimate Method	51
2.1	Introduction	52
2.2	Treatment of epistemic uncertainty	54
2.2.1	Latin Hypercube Sampling (LHS)	55
2.2.2	Response Surface Method (RSM)	57
2.2.3	First-Order Second-Moment method (FOSM)	58
2.2.4	Point Estimate Methods (PEM)	59
2.3	Modeling uncertainties in a historical stone masonry building	64
2.3.1	Sources of uncertainty modeled through random variables	65
2.4	Comparison of methods for evaluation of the epistemic uncertainty	68
2.4.1	Simplified method for accounting for spatial variability of properties	71
2.4.2	Influence of modeling uncertainties for flexural and shear global failure modes	74
2.5	Conclusions	75
2.6	Repository	76
2.7	Acknowledgements	77
3	Three-dimensional macro-element for modelling masonry walls	79
3.1	Introduction	80
3.2	Macroelement formulation	81
3.3	Three-dimensional flexural response	87
3.4	Shear response	90
3.5	In-plane displacement capacity	96
3.6	Out-of-plane behaviour	98
3.6.1	Static Out-Of-Plane Response	98
3.6.2	Dynamic Out-Of-Plane Response	99
3.7	Conclusions	103
3.8	Repository	105
3.9	Acknowledgements	106
4	Simulation of shaking table tests including out-of-plane response	107
4.1	Introduction	107
4.2	Tools developed for 3D equivalent frame modelling in OpenSees	109
4.2.1	Macro-element formulation	109
4.2.2	Orthotropic membrane elements	109
4.2.3	Nonlinear floor connections	110
4.2.4	Wall-to-wall connections	112
4.3	Stone masonry building	112
4.3.1	Model calibration	113
4.3.2	Sensitivity analysis	115
4.3.3	Time-history response	119
4.4	Mixed reinforced concrete/unreinforced masonry structure	120
4.4.1	Model calibration	123
4.4.2	Time history response	124

4.5 Conclusions	126
Conclusions	129
A Formulation of the three dimensional macro-element: derivations	133
A.1 Co-rotational formulation of compatibility relations	133
A.2 Incremental equilibrium matrix	136
A.3 Effect of distributed loads along the element	136
A.4 Nonlinear elastic flexural model	137
A.5 Consistent mass matrix	139
Bibliography	143
Bibliography	155
Curriculum Vitae	157

Introduction

Masonry is a common construction material with which a large variety of building typologies are built, from monuments of historical and cultural value to modern unreinforced masonry buildings. The material is popular due to its low cost, simplicity of construction, and good durability and thermal insulation properties. All these characteristics make it, still today, a competitive building typology, particularly in countries exposed to low to moderate seismicity. Moreover, a major part of heritage buildings are stone or solid masonry buildings. This patrimony constitutes for many European countries not only a great cultural value to preserve, but also an relevant economical resource, since the touristic industry attracts visitors every year.

Masonry, however, proved to be in past earthquakes (D'Ayala and Paganoni, 2011) a particularly vulnerable material to seismic loading. This is due to some intrinsic properties of the material, particularly to its limited strength when subjected to traction, and, in the case of stone masonry buildings, to the often poor interlock between the stone units. On top of this, since many existing masonry buildings lack an effective system of connections between structural elements, they are one of the most exposed typologies to suffer severe damage, and in some cases even structural collapse, after seismic events.

For this reason, a reliable assessment of their seismic performance is essential for properly evaluating the risk of these buildings and, if necessary, to design adequate intervention strategies. It must be underlined that, since a relevant part of masonry buildings are heritage constructions, mostly in historical city centres, their safety and the necessity of interventions needs to deal not only with stability considerations, but also with conservation issues. Interventions, therefore, must be limited to the minimum necessary, and justified by reliable methods that do not excessively underestimate the building performance.

Fundamentally, when assessing the seismic behaviour of a building, two failure types must be considered, in-plane and out-of-plane failure modes. In plane failure involves the development of the full capacity of a wall, that can reach its maximum resistance either for flexural failure types, or for shear failure with diagonal cracking of the panel, or else, much more rarely, for sliding of the wall along a line of bed-joints (Magenes and Calvi, 1997). The seismic response of the building, in this case, depends strongly on the material characteristics, particularly when shear failure is dominant, and, on the in-plane displacement capacity of elements, i.e. by the maximum deformation that they can reach

Introduction

before losing the capacity to bear in-plane loads, and, ultimately, vertical loads. This deformation that defines the maximum displacement capacity of a masonry wall is generally expressed in terms of drift ratio, i.e. the ratio between the lateral displacement of a panel and its height.

Out-of-plane failure modes, on the contrary, can take place before the building develops its maximum capacity for in-plane loads, being related to the rotation in the out-of-plane direction of portions of the building which are not sufficiently connected to the rest of the structure. The problem of the out-of-plane response, although governed by the dynamics of rocking bodies and related to the complex interaction between the different components of a building, is often assessed through simple idealisations of a kinematic chain of rigid bodies (Lagomarsino, 2006), starting from the case of a single rocking block to describe the overturning of a façade, to more complex formulations accounting for refined modelling of the geometry of the mechanism and for the interactions between blocks. In the research field, parallel to the rigid body mechanism models, discrete element models are often used to assess the dynamics of the out-of-plane rocking motion (Casolo and Milani, 2010; AlShawa et al., 2017). However, even refined and numerically expensive analyses of the out-of-plane response rarely account for the interactions between in-plane and out-of-plane response.

The out-of-plane problem, however, is a complex phenomenon that depends also on the boundary conditions imposed by the in-plane behaviour (Tondelli et al., 2016a), which in turn, if the modelling method does not account for the possibility of developing an out-of-plane mechanism, is reliable only as long as the hypotheses on the out-of-plane response hold. An integrated methodology, therefore, simple enough to be applicable to the professional practice, combining in one numerical model the two responses, is highly desirable.

Equivalent frame modelling of masonry buildings, among the possible modelling strategies for the in-plane response of masonry buildings, has proved to be an effective tool with limited numerical cost. The methodology consists in idealising the structural behaviour of a masonry façade as the one of an equivalent frame of pier and spandrel elements, connected by confined portions of masonry that can be assumed as much more rigid and less subjected to inelastic deformations. Observations of damage patterns after seismic events, in many cases, although exceptions exist, confirm this type of behaviour for buildings with a regular layout of openings. For this building typology the method can, when defined by reliable input data, yield satisfactory evaluations of the global response in terms of displacement demands and acceleration profiles, as emerges by comparison with experimental measures and observations (Penna et al., 2016).

A critical review of blind predictions on the behaviour of masonry buildings, successively tested for example in shaking table tests, shows, however, that the research community is far from being able to simulate *a priori* the nonlinear response of a building (Mendes et al., 2017), particularly when predicting the behaviour close to collapse conditions. This consideration extends to many approaches, including refined and costly numerical simulations. Although refined methods can, in principle, be fed in the future with increasingly detailed input data and therefore provide more accurate predictions and a deeper insight into the structural response, at the state of the art, the assessment of masonry structures has to deal with a large number of uncertainties that affect largely the modelled response.

These uncertainties concern different domains. A certain degree of approximation, particularly in simplified methods, is introduced by the modelling approach itself, because the set of modelling hypotheses are not always fully met by the real structure. As mentioned, equivalent frame models, for example, often assume that the the out-of-plane response is not significantly influencing the in-plane behaviour, and that the out-of plane mass can be rigidly lumped to the in-plane walls. Other sources of uncertainty concern the discretion of elements, the stiffness and more generally the interaction between floors and walls; the modelling of the response of elements, piers and spandrels, as element with a bilinear response or through more complex models, is a further source of modelling uncertainty. More simplified approaches carry an even larger number of hypotheses that can be at least partially oversimplifying the problem, such as the two opposite cases of strong-spandrel-weak-pier models, or strong-pier-weak-spandrel models. Such uncertainty can be regarded as epistemic, as it stems from the simplifications introduced by the modelling approach and the limited insight into the structural behaviour.

A second type of uncertainty is the parameter uncertainty, related to the variability and difficult predictability of the parameters that govern the numerical model. For equivalent frame models, these are mainly the models used to define the stiffness, strength and deformation capacity of piers and spandrels. For refined models, the problem is defined by more fundamental, local, physical quantities, which are however often difficult too determine experimentally and are affected by a high level of uncertainty. Such uncertainty can only in part be regarded as epistemic, as it depends both on the limited set of experiential data available, but also on the intrinsic variability of the material response, related to its heterogeneity. If a force-based seismic assessment is applied, i.e. the performance of a building is related to its maximum shear capacity, the modelling uncertainty on forces is obviously dominant. If, however, displacement based assessment is considered, as it proved to be more reliable than the previous, the uncertainty on the displacement capacity becomes the most relevant, as presented in Figure 1, showing the impact of different sources of uncertainty on the evaluation of the seismic performance of an existing masonry building, described in more detail in chapter 3.

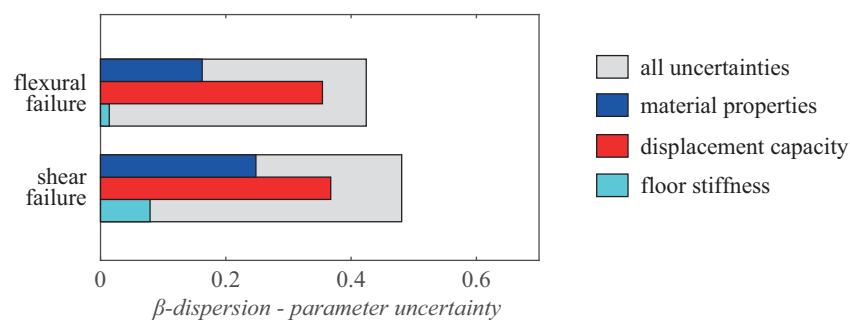


Figure 1 – Influence of modelling parameters in determining the total model uncertainty: β -dispersion of the estimated peak-ground acceleration for which the case-study building in Chapter 3 attains ultimate limit state.

A third, often considered predominant, source of uncertainty in the seismic domain regards the input side, i.e. the indeterminate input characteristics and the variability of the structural response to

Introduction

ground motions of similar intensity and different duration or frequency content. This third source of uncertainty, clearly, can be considered as aleatoric.

This whole set of uncertainty can only in part be reduced by employing increasingly refined modelling formulations. A probabilistic consideration of all uncertainties, however, could significantly improve the quality of the predictions, allowing for the evaluation of a scenario of possible failure modes rather than one, even wisely, selected performance. A probabilistic approach, however, even in simplified formulations, requires a relevant number of simulations of the building response under a set of different conditions. In this sense, simplified models, such as equivalent frames, paying a relatively small price in terms of model accuracy, can almost counter-intuitively provide with a better insight on the structural behaviour, since such models allow also the professional engineer to run multiple simulations and account explicitly for the uncertainty that characterise the domain of the seismic analysis of masonry buildings.

Given this context, this work is developed with the objectives of:

- developing an integrated in-plane and out-of plane modelling strategy, based on an equivalent frame approach, able to capture the main features of each of the two responses in a unique model of a building, preserving the limited computational requirements that characterise equivalent frame models;
- proposing a framework for the probabilistic assessment of a building, simple enough, and adequately reliable, to have the potential of being transferred from the research field to the professional practice, which still rarely applies probabilistic methods to the analysis of existing buildings
- providing such probabilistic framework with an experimental based estimate of the level of uncertainty that governs the problem of the modelling of the seismic response of a building.

Organisation of the document

The document is structured as a paper-based thesis, since most chapters consist in paper published or submitted for publication. The contributions of each author are presented at the beginning of each paper-based chapter.

- In Chapter 1, the main sources of uncertainty on the in-plane response of stone masonry wall, i.e. the stiffness, force and displacement capacity, are discussed and determined through the analysis of a database of shear and compression tests on stone masonry walls available in the literature, collected for this scope.
- The quantification of the uncertainty parameters is then used for the analysis of a case study building, in Chapter 2. The case study serves as an example with which a simplified approach for the probabilistic assessment of buildings is proposed, in a novel application to seismic

engineering, and compared to both equally demanding simplified approaches and a reference Monte Carlo simulation. The analysis is also used to evaluate which sources of uncertainty affect the most the in-plane seismic response of a building, when estimated through nonlinear static procedures.

- Chapter 3 aims at defining a framework for including in equivalent-frame models of limited computational cost, to be potentially applied in the same context of a probabilistic assessment, also the out-of-plane behaviour of masonry walls. For this scope, a macro-element formulation, developed building on existing robust approaches for the simulation of the in-plane response, is derived, and its implementation in the open-source software OpenSees (McKenna et al., 2000) is described. Adequate material models and sectional response models have been developed to capture the main features of the in-plane and out-of-plane response of unreinforced masonry walls.
- The application of such approach is presented in Chapter 4, where two buildings tested in a shaking table are modelled. The computational tools for modelling the complex nonlinear interaction between the elements composing the building—particularly the connection between floors and walls—are developed and applied. The sensitivity of the out-of-plane response of the two numerical models to the parameters that mostly affect the response is discussed, and the stronger and weaker points of the modelling approach are presented.

Equivalent-frame modelling of masonry buildings

Equivalent-frame models of masonry buildings are idealisations of the structural behaviour of a façade which is assumed to perform structurally as a frame, made, in general, of piers, spandrels and nodes. This approach requires clearly that each façade of the building has a regular layout of windows, allowing for a frame idealisation. While residential buildings, also in historical city centres comply with minimal regularity requirements, monumental buildings, churches in particular, are often not fit for this modelling approach. Moreover, the reliability of the method decreases when particular geometrical ratios are assigned to the elements, as discussed in Siano et al. (2018). The comparison of simplified micromodelling approaches and equivalent frame models of the same façade shows that for squatter elements the agreement between the two methods decreases and the applicability of an equivalent frame model becomes questionable.

Simplified equivalent frame models: limit cases

Equivalent frame models that can be solved analytically or using basic numerical approaches apply further hypotheses to the definition of the substitute structural model. The so-called weak pier-strong spandrel model (Figure 2a) assumes that spandrels are undeformable and the only elements subjected to deformations are the piers. The strong coupling applied by a rigid idealisation of the spandrels imposes a double bending moment profile on the piers and tends to model shear failure of the vertical elements. On the other hand, the opposite limit case is considering a strong pier-weak

spandrel idealisation (Figure 2b), which neglect completely the coupling role of spandrels, treated as truss elements, and model the piers as cantilever walls. In this case, flexural failure of the piers is usually imposed. These cases can be assumed as limit conditions, between which the most realistic solution can lay. A more refined model, still allowing for hand calculations, is proposed by Pfyl-Lang et al. (2011b). the approach assumes failure at the bottom storey, considering the deformation of the remaining piers as elastic, allowing however to assume any moment profile along the height of a single pier to calculate its strength and stiffness. Such methods, despite the crude simplifications, allow for the use of simple mechanical models and hand calculation of the response of the structure.

Force-displacement response of walls: analytical/mechanical models

Analytical approaches to the computation of the force-displacement response of masonry walls have been proposed by Benedetti and Steli (2008) and Petry and Beyer (2015) for flexure-dominated piers. Both methods are based in the determination of a sectional force-deformation analytical expression for the parts of the masonry panel experiencing cracking of the section. Assuming a no-tension, perfectly plastic material such expressions, in two-dimensions and disregarding the cyclic behaviour, are easily determined. A similar approach will be adopted in Chapter 3 for implementing a simple sectional law to the proposed element. Double integration along the height of the panel, treated as Timoshenko beam, yields expressions for the top displacements of a wall as a function of the applied shear. Petry and Beyer (2015) proposed also a criterion, based on experimental observations, to determine the maximum displacement capacity of the element, imposing a condition on the extension of the crushed portion of the section.

For such models the nonlinearity in the shear deformations depends only on the partialisation of the sections. Wilding and Beyer (2017) proposed a method that explicitly introduces the possibility of diagonal cracking in a panel subjected to shear, and writes the kinematics of these two blocks and the shear transfer between them. The approach has also been generalised to account for cyclic loading.

Effective height of piers

Analytical expressions derived from mechanical models can be applied to model the behaviour of a building only under limiting conditions, as discussed. A more refined approach can be obtained assigning to the spandrels both a flexibility and a realistic force-displacement model. The use of macroelements, describing phenomenologically the force-displacement response of each wall, is the most common approach. When defining complete equivalent frame models, a certain regard should be given to the definition of the model geometry, and in particular the effective pier height. For elements that do not have the same free height at both sides, several approaches have been proposed. On the basis of the observation of typical crack patterns after seismic events, Parisi and Augenti (2013a) proposed the use of different effective heights when loading in opposite directions (Figure 3). Although such method describes well the change in stiffness and expected damage to piers in different directions when subjected to different boundary conditions at their sides, it can be applied effectively only to monotonic analyses. Methods that do not consider the loading direction, and are therefore applicable

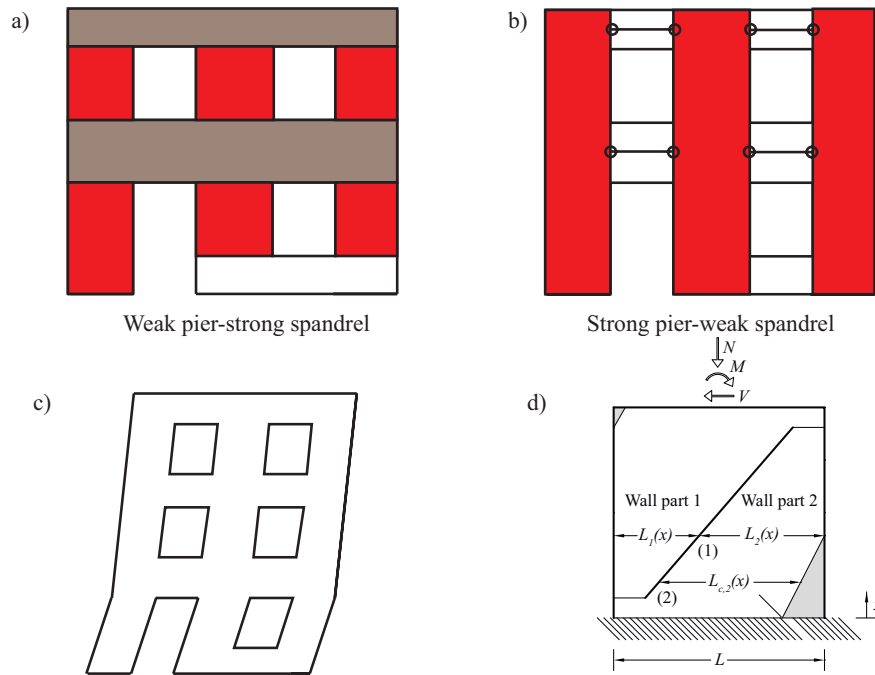


Figure 2 – Simplified structural schemes for masonry buildings: a) weak pier-strong spandrel assumption; b) strong pier-weak spandrel assumption; c) base story failure as postulated in Lestuzzi. d) Scheme of the analytical model proposed by Wilding and Beyer (2017) (adapted from Wilding and Beyer (2017))

to cyclic and dynamic analyses, apply a cone diffusion of damage for determining the effective height of piers (Lagomarsino et al., 2013).

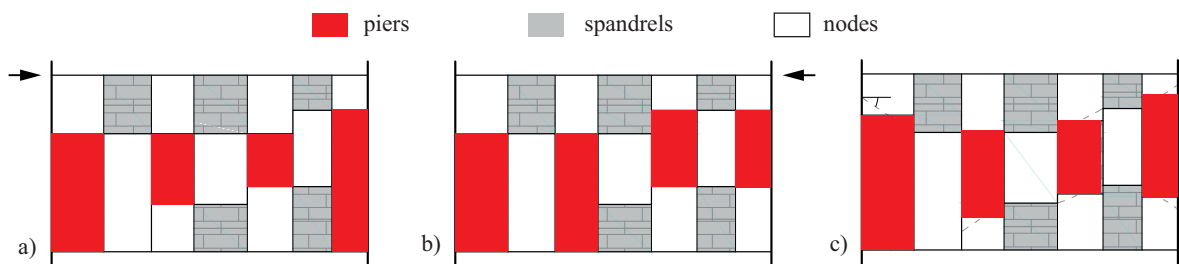


Figure 3 – Different schemes the assumption of the effective pier height in equivalent frames: a-b) approach proposed by Parisi and Augenti (2013a); c) approach implemented in Tremuri with cone diffusion limitation (Lagomarsino et al., 2013)

Macroelement formulations: Tremuri (Lagomarsino et al., 2013)

The force-displacement relation for every element needs to be described by a proper model attached to the macro-element. A simple approach, applied in the commercial version of the software Tremuri

Introduction

(Lagomarsino et al., 2013), assumes a bilinear model, defined by appropriate strength criteria depending on the actual forces applied to the element, with damage unloading. The maximum displacement capacity is a quantity imposed in terms of drifts, possibly different for shear or flexural failure modes. In a more elaborate version of the macro-element, several drops are applied to the force capacity of the element, before it loses all its lateral load bearing capacity. In the modelling approach adopted in Tremuri, elements can lose their lateral capacity for exceeding a drift limit, but never lose their axial load bearing capacity.

Macroelement by Penna et al. (2014)

A more refined approach was proposed by Penna et al. (2014), including the modelling of rocking/flexural deformations, with an uplift of the element. The model is based on the idealisation of a masonry wall into a panel deformable in shear which can rotate around two interfaces, at the two base sections, defined by a no tension material, with finite compressive strength and damage in (Figure 4a). In such way, the element captures the uplift for flexural deformations, as well as the explicit dependency of the shear response on the applied axial load. The macro-element however maintains a limited numerical complexity, further reduced by the analytical integration of the material response at the sectional level, avoiding the use of a fibre numerically integrated section model. The element proposed by Penna et al. (2014) has been validated by comparison with the dynamic response of models and buildings (Penna et al., 2016). The formulation derived in Chapter 3 builds on the same approach, proposing the application of a similar method to capture also the out-of-plane response of masonry walls.

The modelling of the section uplift is particularly important for capturing the action of spandrels in buildings with very deformable floors, such as historical buildings with single planks timber floors. In these buildings, the compressive force in spandrels is too little to model any coupling action if the spandrel, when initially failing in tension, does not elongate. As a result, modelling the spandrels of these buildings with bilinear elements may result in an underestimation of the spandrel coupling action, and therefore approach a strong pier-weak spandrel model. On the contrary, if the coupling action is accounted for, the predicted force capacity and failure mode of the building can considerably change.

Discrete element for masonry panels (Caliò et al., 2012)

A more complex macro-element formulation for masonry panels has been proposed by Caliò et al. (2012). It consists in a quadrangular element, defined by four nodes, whose deformability is governed by four flexural interfaces with distributed axial springs, similarly to end interfaces of the macro-element proposed by (Penna et al., 2014). The shear response is governed by two diagonal nonlinear springs describing the effect of diagonal cracking of the panel. Despite the increased numerical complexity, this macro-element can relax the hypotheses of regularity of the opening layout, as it does not strictly define an equivalent-frame model, but it can adapt to more complex geometries at the cost of a more refined meshing.

Force-based beam elements for the modelling of masonry walls

A more mechanically consistent approach for the modelling of masonry panels in equivalent-frame models is the use of elements based on the beam theory. If the kinematics of the panel can be approximated by the one of a beam, in this way the response of the panel can be referred to the behaviour of the material. The approximation of the kinematics of a masonry panel can be rather accurate, especially for slender panels, as long as diagonal cracking does not occur. After diagonal cracking, the match between the fibre deformations and the true deformations of a wall, as measured in experimental tests (Petry and Beyer, 2014a), is verified only in average sense. The use of displacement-based beam formulations is particularly problematic in the nonlinear phase, since equilibrium is imposed only in average sense and a large force unbalance is found between the sections of elements which should nominally be subjected to a constant axial load profile. Subdivision of every element in more than one beam can only partially solve the problem.

As an alternative, force-based beam elements can be used to enforce an exact force profile along each element, as proposed by Raka et al. (2015), Siano et al. (2018), and more recently by Peruch et al. (2019a,b). The exact enforcement of force equilibrium at the sectional level is performed through a nested cycles of iterations at every displacement update assigned to the end nodes. This iteration cycles, called state determination, can however be not easily solved when elements with zero tensile strength are subjected to traction, for problems of both uniqueness of the solution and singularity of the stiffness matrix of the element. The flexural response can be captured by fibre section models, equipped with material models accounting for limited compressive strength, crushing, stiffness loss, and, if necessary, a small tensile strength.

In such models, the shear response of the element can be captured either through a nonlinear shear spring or through a shear model aggregated to every section. The shear model consists in a generic uniaxial material law, able to describe a complex hysteretic behaviour. In both cases, the coupling between flexural and shear responses is accounted for only in terms of equilibrium of forces at the element level (Marini and Spacone, 2006). However, the dependency of the shear force capacity on the applied axial load is necessarily lost, and the use of this approach is reliable only as long as the axial load on an element remains approximately constant throughout an analysis. One approach proposed in Vanin et al. (2017a) tries to overcome the problem of not imposing an axial force-dependent criterion for the shear strength by using a fibre section accounting for two-dimensional response of each fibre. The shear problem in such way is solved at the fibre level, and then numerically integrated. If appropriate two-dimensional material models are applied to the fibres, the element can capture the response in flexure and shear, a decrease of shear stiffness related to the flexural deformations, and realistic compressive strains at the toe if adequate integration schemes are applied. In such way, also the displacement capacity of the element in flexure could be related to the material behaviour, more precisely to the fracture energy in compression.

However, as the formulations increase in accuracy, the original simplicity of the modelling approach is partially lost. In this perspective, the macro-element formulation in Chapter 3 proposes a modelling approach which tends to limit as much as possible the increase of numerical complexity, in order to

Introduction

setup a tool with the potentiality of being used in multiple nonlinear dynamic analyses with limited computational cost.

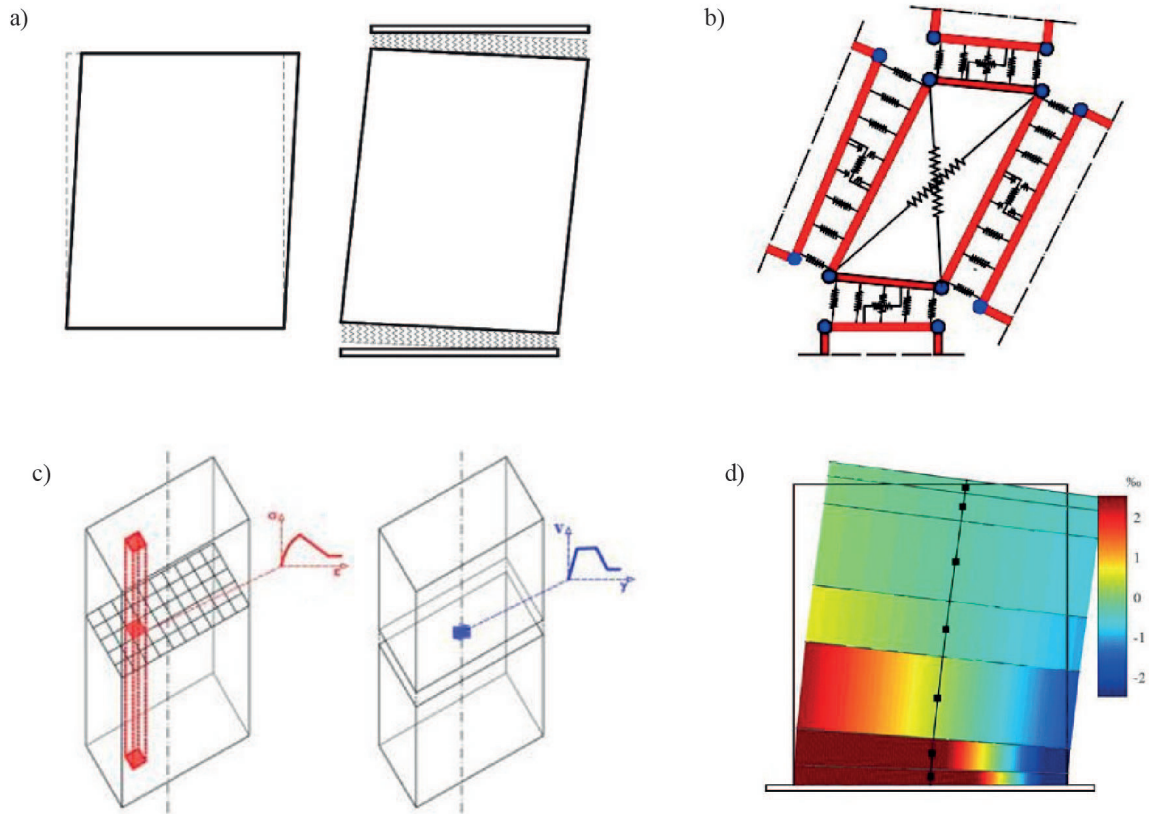


Figure 4– a) macroelement proposed by Penna et al. (2014) (adapted from the reference); b) macroelement proposed by Caliò et al. (2012) (adapted from the reference); c) force-based beam element for the modelling of masonry elements proposed by Raka et al. (2015); Siano et al. (2018) (adapted from the second reference); d) vertical strain field as modelled by a force based element: application to a flexure dominated wall.

1 Stiffness, strength and drift capacity of stone masonry walls

This chapter represents the post-print version of the article:

Vanin, F., Zaganelli, D., Penna, A. and Beyer, K. (2019). "Estimates for the stiffness, strength and drift capacity of stone masonry walls based on 123 quasi-static cyclic tests reported in the literature". *Bulletin of Earthquake Engineering*, 15, 12, 5435-5479. DOI: 10.1007/s10518-017-0188-5

The formatting and numbering of equations, tables and figures have been updated to this document. The contributions of the first author are: collection and organisation of the database, analysis of stiffness and force capacity estimates, writing the article. Contributions of the second author: data collection. Contributions of the third author: co-writing the article. Contributions of the fourth author: development of the drift models, supervision of the first author, co-writing the article.

Abstract

This paper summarises 123 existing quasi-static shear-compression tests on stone masonry walls and evaluates the results to provide the input required for the displacement-based assessment of stone masonry buildings. Based on the collected data, existing criteria for estimating lateral strength and stiffness of stone masonry walls are reviewed and improvements proposed. The drift capacity of stone masonry walls is evaluated at six different limit states that characterise the response from the onset of cracking to the collapse of the wall. To provide input data for probabilistic assessments of stone masonry buildings, not only median values but also the corresponding coefficients of variation are determined. In addition, analytical expressions that estimate the ultimate drift capacity either as a function of masonry typology and failure mode or as a function of masonry typology, shear span and axial load ratio are proposed. The paper provides also estimates of the uncertainty related to the natural variability of stone masonry by analysing repeated tests and investigates the effect of mortar injections and the effect of the loading history (monotonic *vs* cyclic) on stiffness, strength and drift capacities. The data set is made publicly available.

1.1 Introduction

Many buildings that are part of the European cultural heritage are stone masonry buildings. Furthermore, stone masonry construction is still used today in several developing countries. Due to the low tensile strength of the mortar and the often poor interlock between stones, stone masonry buildings are among the most vulnerable buildings when subjected to seismic loading (Grünthal, 1998). Buildings with stone masonry walls can fail due to in-plane loading, out-of-plane loading or a combination of the two failure modes (Figure 1.1). Out-of-plane failure modes are promoted by the large mass of stone masonry walls, the small restraint provided by timber floors and the poor interlock between the stones (D'Ayala and Speranza, 2003). They are the most frequent cause for the partial or complete collapse of existing stone masonry buildings during earthquakes and their assessment is therefore of high importance (Costa et al., 2015). If out-of-plane failures are prevented by appropriate structural details such as anchors and ties, the structure can develop a global response that is governed by the in-plane behaviour of the walls and the diaphragm stiffness (Penna, 2015). In-plane failure modes include the failure of piers and spandrels. While the failure of spandrels causes local failures and a global decrease in stiffness and strength, the failure of piers can lead to the collapse of the building (Beyer and Mangalathu, 2012). The deformation capacity of the piers is therefore essential when assessing the ultimate limit state of stone masonry buildings.

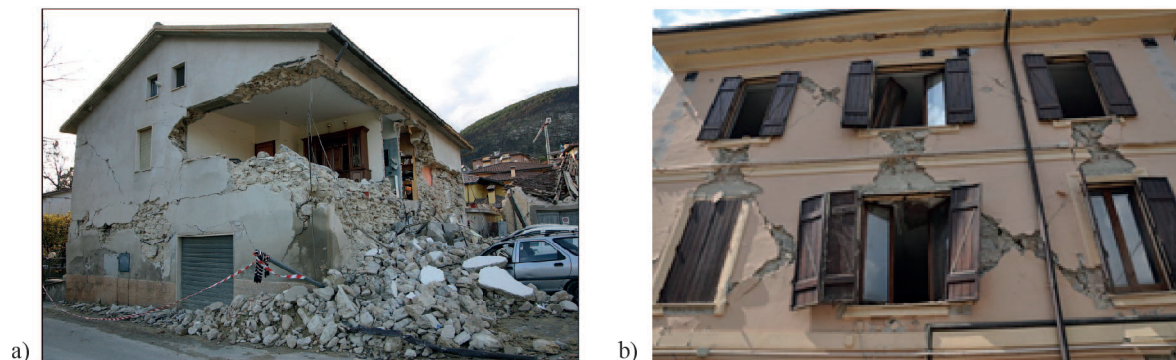


Figure 1.1 – Stone masonry buildings after the 2009 L'Aquila earthquake that failed due to an out-of-plane mechanism (a, Photo: A. Dazio) and an in-plane mechanisms (b, Photo: A. Penna).

Current codes do not distinguish between different masonry typologies when assessing the drift capacity (for a review of drift capacity models in codes, see Petry and Beyer (2014a)). Eurocode 8, Part 3 (CEN, 2005) assigns the drift capacity based on the failure mode (shear *vs* flexure) and the shear span ratio H_0/L where H_0 is the height of zero moment and L the wall length:

$$\text{Shear failure:} \quad \delta_{SD} = 0.4\% \quad (1.1)$$

$$\text{Flexural failure:} \quad \delta_{SD} = 0.8\% \frac{H_0}{L} \quad (1.2)$$

Although the current version of EC8-3 is limited to concrete and brick masonry (CEN, 2005), due to the lack of alternative values for other masonry typologies, in engineering practice these values are often also applied to stone masonry. Equation 1.1 gives the drift capacities for the limit state “Significant Damage” (SD). To obtain the drift capacity at 20% strength loss (defined as near collapse limit state, NC), the drift capacities of Equation 1.1.2 are multiplied by a factor 4/3 (CEN, 2005). Recent works investigated the correlation of these drift capacity models with tests on clay block masonry walls (Pfyl-Lang et al., 2011b; Petry and Beyer, 2014a). However, the proposed models cannot be applied directly to stone masonry since stone masonry differs from block masonry with regard to the material properties, the shape of the stones, the fabric of the masonry and the number of leaves. Kržan et al. (2014) provide on the basis of three test series minimum and maximum values of drift capacity at the SD and NC limit state but do not differentiate between different types of stone masonry.

The objective of this paper is to provide the input data for the wall limit states that is required for the probabilistic displacement-based assessment of stone masonry buildings. While the framework of probabilistic assessment procedures are established (Dolšek, 2009; Vamvatsikos and Fragiadakis, 2010), their application to stone masonry buildings is at the moment limited by the lack of information on the distribution of drift capacities. To provide this information, this paper evaluates median values and coefficients of variations of drifts for the following six element limit states:

- Drift at the onset of cracking δ_{cr}
- Drift at yield δ_y
- Drift limit “Significant damage” which is defined as $\delta_{SD} = \min(3\delta_{cr}, \delta_{max})$
- Drift at maximum force δ_{max}
- Drift at ultimate LS (20% strength drop) δ_u
- Drift at collapse (50% strength drop) δ_c

The drift at the onset of cracking is the drift for which first cracks were reported. The yield drift results from the bilinear approximation of the force-displacement response (see Section 1.2.1). The drift at maximum force δ_{max} is relevant as it marks the onset of damage concentration in few cracks (Petry and Beyer, 2014a). The definition of the drift limit state “Significant damage” is slightly modified criterion from (Tomažević, 2007). For the data set analysed here, the drift limit SD is governed in approximately half of the cases by the limit $3\delta_{cr}$ and in the other half by δ_{max} . The ultimate drift δ_u is defined as the drift at which the strength has dropped to 80% of the peak strength. This is a common definition of the ultimate deformation capacity, which is used for many different structural elements and materials. The definition of collapse, on the other hand, is more subjective. Ideally, it would be related to the loss of axial load bearing capacity. Since this state was not attained by most tests a definition related to the loss in lateral strength was chosen. It is expected that the drift at axial load bearing collapse is only marginally larger given that the strength loss is rapid and shear and axial failures strongly coupled.

To determine the probability distributions of these drift capacities and investigate on which parameters the drift capacities depend, this paper collects the results of 123 in-situ and laboratory shear-compression tests on stone masonry walls (Section 1.2) and evaluates for these the stiffness, the strength and drift capacities (Sections 1.5-1.7). The analysis of the test data showed—as it had also been observed for clay block masonry walls (Petry and Beyer, 2014a)—that monotonic tests lead to significantly larger drift capacities than cyclic tests while the load history has only little influence on stiffness and strength (Section 1.4). Since drift capacities are typically used for seismic assessments and therefore cyclic loads, monotonic tests are disregarded when calculating drift capacities (Section 1.7). All tests are quasi-static tests, i.e., the effect of strain rates on the response of stone masonry walls are beyond the scope of this study.

The effect of the variability of stone masonry properties on the seismic assessment of stone masonry buildings can be analysed by means of Monte-Carlo simulations, which assign each building model a different drift capacity for the stone masonry walls (Rota et al., 2014a). However, also the walls within a building have different drift capacities due to the natural variability of the stone masonry. To evaluate this aleatoric uncertainty, tests of identical wall configurations are analysed with regard to the variability of stiffness, strength and deformation capacity (Section 1.3). Seismic assessments often also investigate the effect of a strengthening measures on the performance of a building. The database contains few pairs of strengthened and unstrengthened walls. The strengthening measures aim at improving the integrity of the stone masonry walls by mortar injections or horizontal reinforcements through the wall thickness in order to improve the connection between leaves. The paper closes with a discussion of the obtained results. Based on these, future research needs are outlined that aim at improving the understanding of the various parameters that influence the in-plane properties of stone masonry walls.

1.2 Database of tests on stone masonry walls

The database contains 123 shear-compression tests on stone masonry walls from 16 test campaigns (Table 1.1). Collected were all shear-compression tests on stone masonry walls that were sufficiently documented in the literature. The database contains both laboratory and in-situ tests. Tests other than shear-compression tests, such as for example diagonal compression tests, were not included. All typologies of stone masonry were considered. However, test units that featured unrepresentatively few stones along the wall length were excluded. Furthermore, panels strengthened with intrusive interventions that change consistently their structural behaviour (for example, application of fibre reinforced polymers or jacketing) were not included in the database. For this reason, only tests on walls that were strengthened or retrofitted by injections with lime grouts or by improving the local connections between the wall leaves were considered.

The database can be downloaded from the web repository [10.5281/zenodo.812146](https://zenodo.org/record/812146) . It comprises:

- A table with
 - characteristic data of the test units (test campaign, type of test, geometry and masonry

1.2. Database of tests on stone masonry walls

typology of test units, material properties, Masonry Quality Index as defined in Section 1.2.2, failure mode).

- the bilinear approximations of the force-displacement response. The procedure for determining the bilinear approximation is outlined in Section 1.2.1.
- o drift capacities for six different limit states. The limit states were defined in Section 1.1.
- Cyclic force-displacement curves and envelopes are provided as CSV files; these were available for 110 tests. The data was digitised from the test reports using vector graphics software. For one test campaign (Magenes et al., 2010), experimental data were directly provided by the authors.

The masonry typologies of the test units in the database were classified according to the Italian code (MIT 2009), which distinguishes between five types of stone masonry:

- Class A: irregular stone masonry, with pebbles, erratic and irregular stone units;
- Class B: uncut stone masonry, with external leaves of limited thickness and infill core (three-leaf stone masonry)
- Class C: cut stone masonry with good bond
- Class D: soft stone regular masonry (built with tuff or sandstone blocks)

Table 1.1 – Database with shear-compression tests on stone masonry walls: List of test campaigns.

Series	References	No. of units	Masonry typology	Test type	Lab./In situ
S1	Vasconcelos (2005); Vasconcelos and Lourenço (2009)	28	E1, C	Cyclic, Monotonic	Laboratory
S2	Silva et al. (2014)	16	B	Cyclic	Laboratory
S3	Mazzon (2010)	6	B	Cyclic	Laboratory
S4	Magenes et al. (2010)	5	C	Cyclic	Laboratory
S5	Almeida et al. (2012)	2	E	Cyclic	Laboratory
S6	Borri et al. (2001)	3	A	Monotonic	In-situ
S7	Borri et al. (2012)	10	A	Monotonic	In-situ
S8	Corradi et al. (2014)	2	A	Monotonic	In-situ
S9	Marcari et al. (2007)	4	D	Monotonic	Laboratory
S10	Costa et al. (2011)	1	A	Cyclic	In-situ
S11	Pinho et al. (2012)	6	A	Cyclic, Monotonic	Laboratory
S12	Lourenço et al. (2005)	7	E1	Monotonic	Laboratory
S13	Almeida et al. (2014)	12	E1, C	Cyclic	Laboratory
S14	Kržan et al. (2014)	14	C	Cyclic	Laboratory
S15	Silva et al. (2012)	1	C	Cyclic	Laboratory
S16	Faella et al. (1992)	6	D	Cyclic	Laboratory
	Total	123			

Chapter 1. Stiffness, strength and drift capacity of stone masonry walls

- Class E: Ashlar masonry, built with sufficiently resistant blocks (i.e. blocks with higher resistance than those of class D). This class was further subdivided into regular squared block masonry with mortar joints (E) and dry-joint ashlar masonry (E1).

Typical cross-sections of these masonry typologies are shown in Figure 1.2. This database will be part of the European Masonry Database, which the authors are currently establishing in collaboration with Matija Gams (University of Ljubljana).

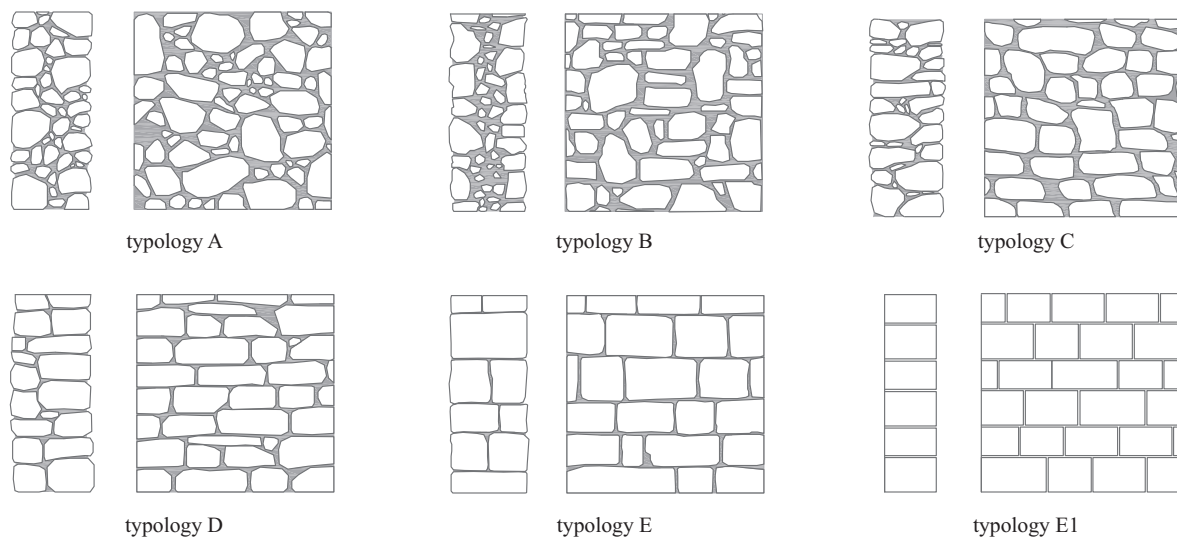


Figure 1.2 – Stone masonry typologies: sketches of typical textures and cross sections.

1.2.1 Bilinear approximation of the force-displacement curve

In shear-compression tests, the axial force is kept constant while the applied horizontal displacement is varied. The loading protocols for the horizontal displacement differed between the various campaigns and included monotonic tests and reversed cyclic tests. For the monotonic tests (35 tests, for 22 of which the load-displacement curve is available) no processing was required to obtain the envelope curve. For the reversed cyclic tests with one or three repeated cycles (24 and 57 tests, respectively), the envelope curves were derived from the digitised force-displacement hysteretic curves by connecting the points at displacement peaks. When more than one cycle was imposed per displacement amplitude, the first cycle was considered for constructing the envelope, in order to make results from different loading protocols as comparable as possible. This approach also accounts for the finding that masonry piers that are part of a building, which is subjected to a real earthquake, are not likely to be subjected to more than one or two cycles at the highest drift demand (Mergos and Beyer, 2014).

The bilinear approximation of the envelope curves was computed as described in Figure 1.3. First, the maximum recorded strength V_{max} was identified. The effective stiffness was then defined as the secant stiffness at 70% V_{max} . The ultimate drift δ_u was determined as the drift at which the strength

had dropped to 80% V_{max} . If such a large drop was not attained, the largest drift that was reached during the test was taken as δ_u . The ultimate strength V_u was defined as the strength that yields for the bilinear approximation the same area below the curve as the actual envelope up to δ_u . For cyclic tests, bilinear approximations were computed for the envelopes in the positive and negative loading direction. The final envelope curve was derived as follows: The final effective stiffness and ultimate strength correspond to the average of the values for the two directions. For the ultimate drift, however, the minimum value of the ultimate drift in the positive and negative direction was taken. When the force drop was only attained in one direction, the corresponding ultimate drift was considered for the final envelope. This procedure is similar to the one adopted by Frumento et al. (2009); unlike by Frumento et al., the envelope of the first cycles was used and not the average of envelopes corresponding to repeated cycles.

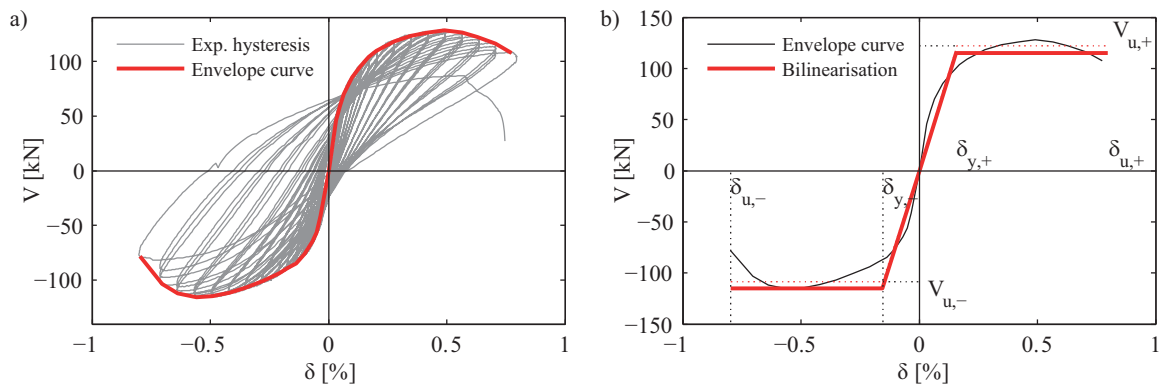


Figure 1.3 – Example of a force-displacement response curve (a) and definition of effective stiffness, strength and drift capacity based on the envelope of the response (b).

1.2.2 Distribution of properties of test units contained within the database

The collected experimental data spans a wide range of test unit configurations (Figure 1.4). Most tests were laboratory tests (111 test units, 90%); in addition, the database contains also 12 in-situ tests on walls that were isolated in an existing building. Of the laboratory tests, 87 (78%) were cyclic tests and 24 (22%) monotonic tests while 11 out of the 12 in-situ tests were monotonic tests and only one was a cyclic test. For nine in-situ tests and four laboratory tests only the peak force but not the complete force-displacement curve was reported (in total 13 tests, i.e., 11%). These tests could therefore only be used for the strength model but not when evaluating the stiffness and deformation capacity of the walls.

Figure 1.4a shows the number of tests that is available for each masonry typology. It further shows the portion of monotonic and cyclic tests. The colour code introduced in this figure with regard to the masonry typology is employed throughout the article. A large majority of the tests were carried out on relatively small test units with heights between 0.9-1.25 m and only very few tests on storey-high units (Figure 1.4b). The shear span ratio H_0/L varies between 0.5 and 2.0 (Figure 1.4c). Most of the masonry

typologies that were tested had a compressive strength less than 5 MPa while few tests of dry stone masonry (E1) had a strength larger than 50 MPa (Figure 1.4d); note that the latter value was obtained from tests on masonry prisms rather than masonry walls or wallettes. The compressive strength was in 53% of the tests determined from compression tests on walls or wallettes, in 28% of the tests from prism tests; in 7% of the tests it was assumed based on code provisions (MIT, 2009). In 12% of the tests, there was no information on the compression strength available and code guidelines could not be applied because a photo of the test unit was missing. The mortar strength was for all test units, for which this information was available, smaller than 6 MPa (Figure 1.4e). The axial stress ratio varies between 0 and 0.6 (Figure 1.4f).

To account for the individual mechanical characteristics of the stone masonry, Binda and co-workers developed a procedure for assessing the quality of the stone masonry and its compliance to the “rules of the art”, which is based on a visual inspection and the evaluation of local geometric parameters (Binda et al., 2009; Cardani and Binda, 2013). Based on these characteristics, Borri and co-workers developed a quantitative quality index (Borri and De Maria, 2009; Borri et al., 2015), named Masonry Quality Index (MQI), which has been correlated to the masonry strength. It accounts for the texture of the masonry by considering the following criteria: i) mechanical properties and conservation state of the stone units, ii) the dimensions of the stones, iii) the shape of the stones, iv) the characteristics of the wall section, including the connection of leaves, v) the horizontality of the bed-joints, vi) the staggering of the vertical joints, vii) the quality and conservation of the mortar joints. These characteristics are evaluated largely qualitatively, according to criteria specified in Borri et al. (2015). One parameter that can be determined quantitatively is the interlock of the units, both in the in-plane and out-of-plane directions, which can be described using the concept of the length of the minimum trace (LMT), as proposed by Doglioni et al. (2009). It is defined as the minimum length of a line passing only through mortar joints, between two points that are vertically aligned and at a distance h_v , generally taken equal to 100 cm:

$$\text{LMT} = \frac{\text{Min. trace through joints}}{h_v} \quad (1.3)$$

For the test units in the database, the length of the minimum trace has been determined from photos and is tabulated in the database. The MQI assigns to each criterion a value dependent on whether the criterion is satisfied, partially satisfied or not satisfied. The resulting MQI value varies between 0 and 10. The method differentiates between the behaviour under vertical loads, out-of-plane loading and in-plane loading by assigning different coefficients to the different parameters. The MQI is evaluated for all walls that are included in the database. Figure 1.4g shows the distribution of the masonry quality index for in-plane loading that are obtained for the tests in the database. Masonry walls of very good quality are somewhat overrepresented in the database due to the large number of tests on walls that belong to typology E or E1. For masonry strengths smaller than 10 MPa, the MQI correlates well with the masonry compressive strength (Figure 1.4g; note that this correlation does not improve if the vertical MQI is plotted). Figure 1.4h shows the axial load ratio against the MQI for in-plane loading. These two quantities are not directly related. The figure shows, however, that the test designs resulted in a rather strong correlation between these two variables, i.e., the higher the MQI, the smaller was in

1.2. Database of tests on stone masonry walls

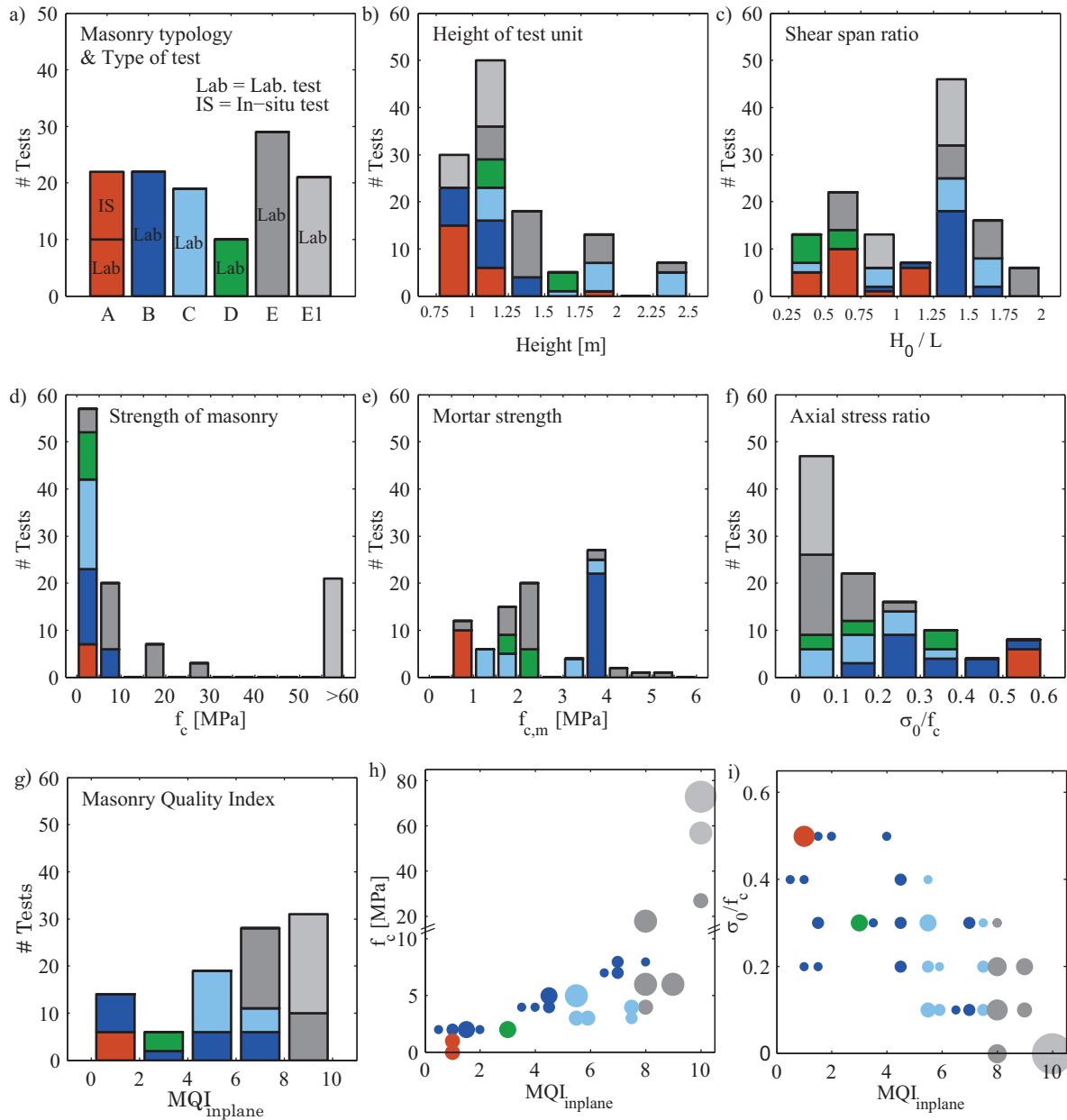


Figure 1.4 – Database of shear-compression tests on stone masonry walls: Distribution with regard to various parameters. The colours refer to the masonry typology (see plot a). For plots h) and i), the size of the marker relates to the number of test units with the corresponding parameter combination.

general the applied axial load ratio. The dataset constitutes itself out of 16 different test programs that were carried out in different laboratories. As a result, the parameters were not varied in a systematic manner, which will need to be taken into account when interpreting any trends in the data. Since all walls were subjected to relatively small axial stresses in a narrow range ($\sigma_0=0-2$ MPa), the axial stress ratio σ_0/f_c essentially depends on f_c and therefore σ_0/f_c varies strongly with MQI . It will therefore be

difficult to distinguish between the influence of MQI and the influence of axial stress ratio σ_0/f_c .

1.2.3 Quality control of measured peak strength

The 16 test series were performed by various research groups using different test setups, which might lead to slightly different boundary conditions. As a quality check of the applied boundary conditions, the peak strength obtained in the tests was compared to the theoretical rocking strength of an infinitely strong rigid body with the same dimensions of the masonry wall:

$$V_{rock} = \frac{NL}{2H_0} \quad (1.4)$$

where N is the axial force, L the wall length and H_0 the shear span. In order to compute an upper limit of the rocking strength, N is taken as the sum of the applied axial load σ_0Lt and an estimate of the self-weight of the test unit. The latter is computed assuming a specific weight of 20 kN/m³ for all test units. Figure 1.5a shows for all test units the ratio of the ultimate strength V_u , which was derived from the bilinearisation of the envelope curves, to the rocking strength. Theoretically, the peak strength V_{peak} of masonry walls let alone the ultimate strength V_u should not be larger than V_{rock} . To allow for small imperfections in the applied boundary conditions, all tests with ultimate strengths less than 1.10 times V_{rock} are considered when evaluating stiffness, strength and drifts in the following sections. Eight of the 123 tests do not pass this quality check and are in the following disregarded. Of the 115 retained tests, about half of the test units failed in flexure and half in shear or a hybrid mode. The distribution of the failure modes with regard to the masonry typologies are shown in Figure 1.5b. For masonry typologies A and D only shear failures were observed while for the other four typologies at least two out of the three failure modes were observed. Figure 1.5c shows the tests that passed the quality check and for which the force-displacement curve is available.

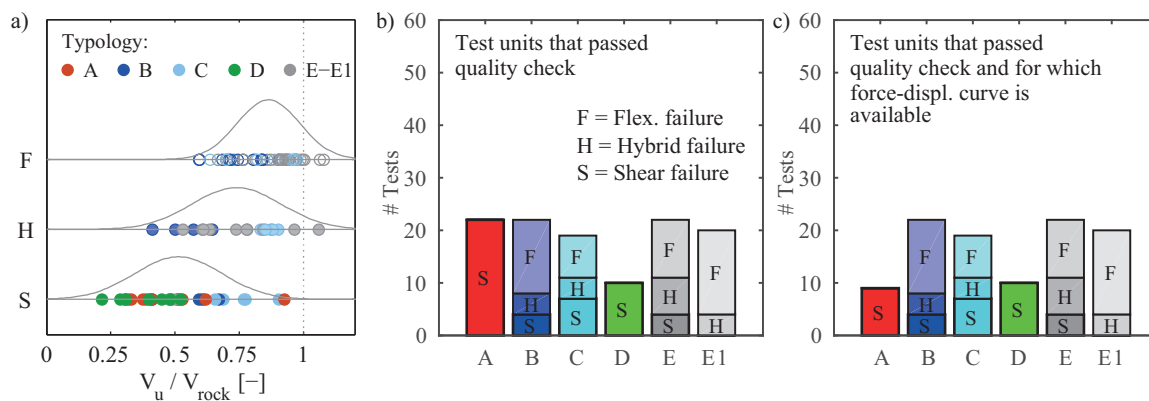


Figure 1.5 – Quality check of shear-compression tests on stone masonry walls: Ratio of maximum shear strength to rocking strength (a), distribution of all tests that passed the quality check (b), distribution of all tests that passed the quality check and for which the force-displacement curve is available.

1.3 Aleatoric variability of stiffness, strength and drift limits

Stone masonry is made of the constituents stone and—unless it is dry masonry—mortar. The properties of both constituents are subject to a certain natural variability and so is the fabric of stones and mortar that is created by the mason. The properties of stone masonry walls are therefore associated with an aleatoric uncertainty, which will be estimated in the following. The data set contains 19 groups of replicate tests, i.e., groups of tests in a test series that have been conducted with the same set of parameters. This section evaluates for each of these groups of replicate tests the variability of stiffness, strength and deformation capacity. All but one of these groups are laboratory tests; for in-situ tests only one group of replicates was available. The number of tests per group varies between 2 and 4. These group sizes are of course rather small for computing coefficients of variations. The reported values should therefore be taken as a first estimate of the scatter among replicate tests until results of replicate tests on larger groups are available.

Vasconcelos and Lourenço (2009) tested nine groups of replicates. Figure 1.6 shows the force-displacement curves of three groups of replicates from three different masonry typologies (C, E, E1). The plots show the positive and negative envelopes of each tests, which confirm that stiffness, strength and deformation capacity vary between the replicate tests. In the following, all 19 groups are analysed. For the tests shown in Figure 1.6, the strength in the negative direction tends to be slightly larger than the strength in the positive direction indicating that there might have been a slight asymmetry in the test setup. This highlights that even replicate tests might not yield an estimate of the aleatoric variability that is related to the variability of the material properties and the fabric alone but that some variability might also be related to imprecisions of the test setup.

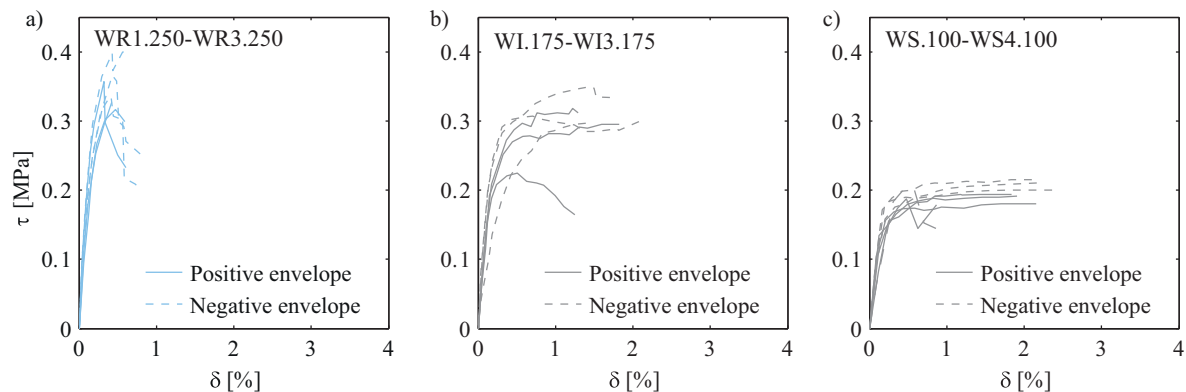


Figure 1.6 – Force-displacement envelopes of repeated tests by Vasconcelos and Lourenço (2009): Walls of masonry typology C (a), E (b) and E1 (c).

The coefficients of variation (CoVs) for all groups of replicates with regard to stiffness, strength and five deformation limits (δ_{cr} , δ_y , δ_{max} , δ_u , δ_c). Figures 1.7-1.8 visualise the distributions of these CoVs by grouping the values according to failure mode and masonry typology. Only one group of replicate tests was carried out as in-situ tests. The obtained values are larger than those obtained from most laboratory tests but not larger than the maximum values obtained from laboratory tests and therefore

laboratory and in-situ tests will be treated together. The CoVs of each group of replicates are plotted as a dot. In addition, for each bin the lognormal distribution fitted to these CoVs is plotted. The scatter of the CoVs is rather large but some trends can be identified. Figure 1.7a show the CoVs of stiffness and strength as a function of the failure mode. The CoV of the strength is slightly larger for walls that fail in shear than for walls that fail in flexure. For the stiffness, however, both failure types lead to similar CoVs.

The CoVs obtained for the drift limits δ_{max} and δ_u (Figure 1.8) tend to be larger than CoVs for stiffness and strength while δ_{cr} leads to a similar CoV. All but two of the replicate groups stem from masonry typologies that have relatively regularly shaped stones and a regular bond pattern (C, D, E, E1). For typologies A and B, the stone pattern is more irregular and therefore one might expect a larger aleatoric variability. The data shows, however, that the masonry typology does not seem to have a significant influence on the aleatoric variability of the drift values. The data base for the irregular masonry typologies A and B is very scarce (A: two groups of replicate tests, B: none) and therefore the influence of the masonry typology on the aleatoric variability cannot be conclusively answered with the available data. If estimates of the aleatoric variability of stiffness, strength and deformation limits are sought for the computation of fragility curves of a class of buildings or the probabilistic seismic assessment of a specific building, it is suggested to use the values given in Table 3. These values are based on the mean values of the CoVs and rounded to the next 0.10. Note also that no test data is available for characterising the aleatoric variability of the drift at collapse since none of the tests was continued up to a 50% drop in strength.

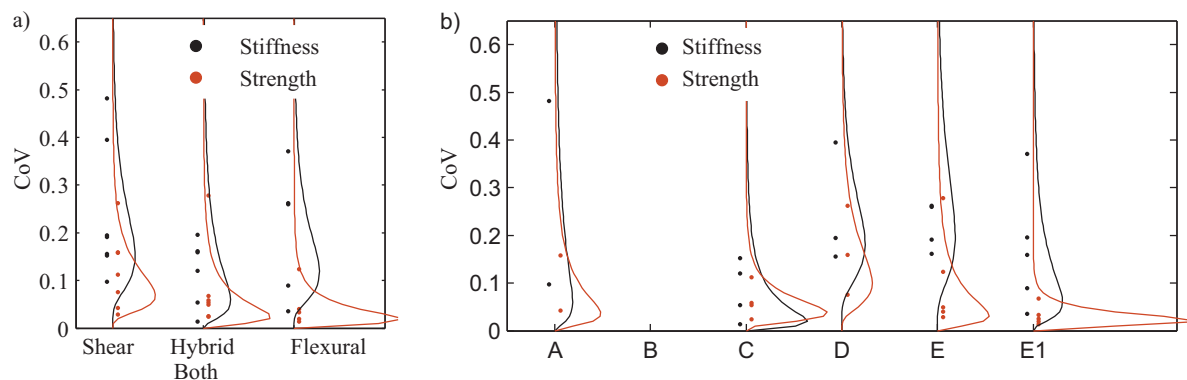


Figure 1.7 – Coefficients of variation of replicate tests for effective stiffness K_{eff} ultimate strength V_u as a function of the failure mode (a) and the masonry typology (b).

1.4 Effect of load history on stiffness, strength and drift limits

Among the 115 tests that passed the quality check there is only one pair of monotonic and cyclic tests (M13 and M17 by Pinho et al. (2012)). Figure 1.9a shows the force-displacement relationships of these two tests. It shows that test units subjected to cyclic loads tend to be stiffer and exhibit a smaller drift capacity—trends that were also confirmed by tests on clay block masonry walls, for which

1.4. Effect of load history on stiffness, strength and drift limits

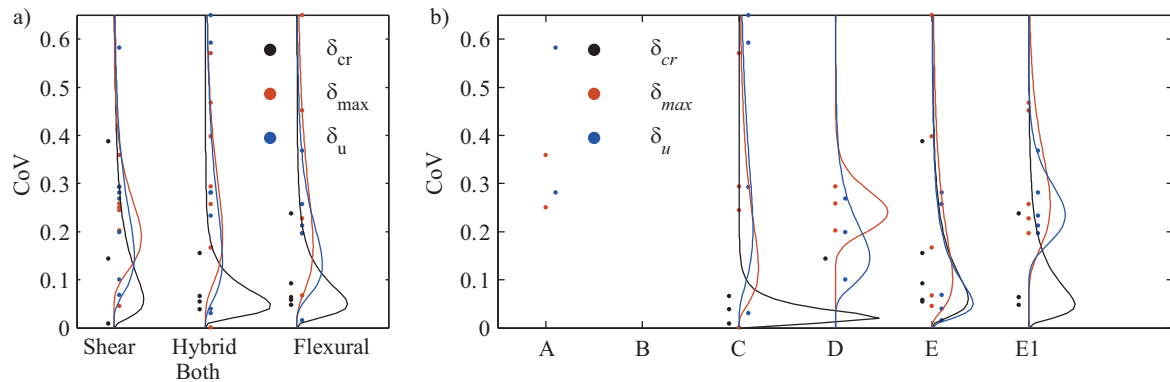


Figure 1.8 – Coefficients of variation of replicate tests for the drift at the onset of cracking δ_{cr} , the drift at maximum strength δ_{max} and the ultimate drift δ_u as a function of the failure mode (a) and the masonry typology (b).

three pairs of monotonic and cyclic tests are reported in the literature (Petry and Beyer, 2014a). For clay block masonry walls, however, the strength of walls subjected to cyclic loads was similar to that subjected to monotonic loading while for the stone masonry pair the cyclic test led to a significantly larger strength than the monotonic test. At present, a systematic study on the influence of the loading history on unreinforced masonry wall response is missing. Not only a comparison of monotonic and cyclic response would be of interest, but also the influence of the number of cycles as there is evidence that most quasi-static cyclic tests on masonry walls were carried out with more cycles than what would be representative of moderate or even high seismicity (Beyer et al., 2014; Mergos and Beyer, 2014).

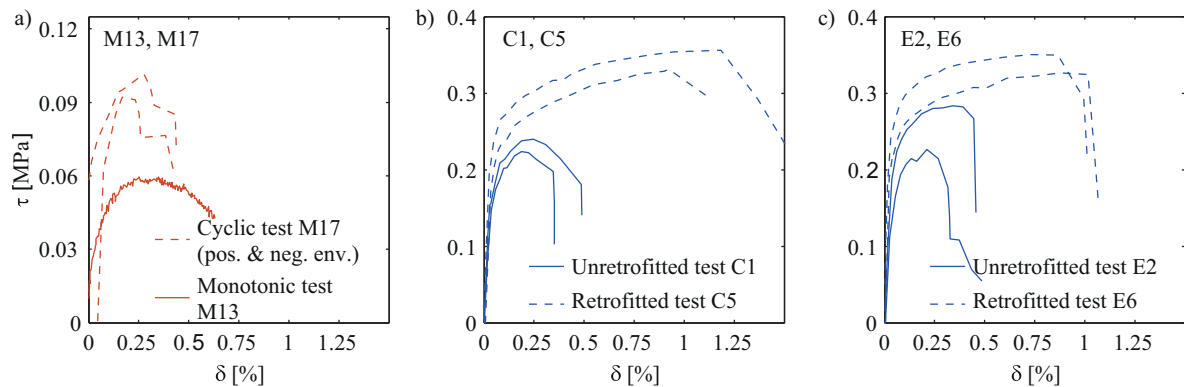


Figure 1.9 – Comparison of force-displacement relationship of monotonic and cyclic tests (a) and strengthened and unstrengthened test units (b, c).

1.5 Stiffness of stone masonry walls

Force-based and displacement-based assessment procedures require as input an estimate of the horizontal stiffness of structural walls. The stiffness is needed to compute the dynamic properties of a building as well as its force-displacement response. The initial uncracked stiffness is only of interest in engineering practice if nonlinear structural models can account explicitly for the stiffness degradation after cracking of the element. In all other cases, i.e. for simplified structural models (bilinear models for each structural element) or force-based assessment procedures, the effective stiffness is of interest. However, in the absence of better models, current codes suggest to estimate the effective stiffness as a ratio of the elastic uncracked stiffness (CEN, 2005) which, therefore, should be determined with sufficient accuracy.

This section computes from the force-displacement envelopes the ratio of effective to uncracked stiffness and compares the obtained values to code estimates (Section 1.5.1). The remainder of the section evaluates different methods of estimating the E-modulus. First, the median values and CoVs of the E-modulus are computed for the various masonry typologies (Section 1.5.2). Second, the E-modulus is computed from results of compression tests and dynamic identification tests that were carried out as part of the experimental campaigns (Section 1.5.3). The so obtained E-moduli are compared to compute the horizontal stiffness of the walls and conclusions drawn on which kind of tests are suitable for obtaining estimates of E-moduli. When assessing a masonry building, in-situ tests to determine the elastic properties, such as flat-jack tests, are often not available and their use can be questionable for multiple-leaves stone masonry. It can be necessary, hence, to estimate the E-modulus from the compressive strength of the masonry, which is often the first material parameter that is determined from tests or assumed based on code values. Section 1.5.4 proposes such an expression, which also accounts for the effect of the axial load ratio on the effective stiffness.

1.5.1 Ratio of effective to uncracked stiffness

Current codes estimate the effective stiffness postulating a constant ratio between initial uncracked stiffness and effective stiffness; EC8-3 recommends a ratio of 0.5 (CEN, 2005) and the Swiss guidelines SIA D0237 a ratio of 0.3 (Pfyl-Lang et al., 2011b). To check the applicability of these assumptions, the experimental initial uncracked stiffness was calculated from the envelopes as the secant stiffness at 15% of the maximum force; for cyclic tests, the average of the stiffness derived from the positive and negative envelopes is considered. Similarly, the effective stiffness was defined as the secant stiffness at 70% of the maximum force. Figure 1.10a shows the ratios of effective to elastic stiffness that were obtained from the wall tests. The variation is rather large for all failure modes and slightly larger for walls failing in shear or a hybrid mode than for walls failing in flexure. Clear differences between masonry typologies could not be identified. Table 1.2 summarises the experimentally determined ratios; despite the large uncertainty, a value of 0.5, as suggested by EC8, is close to a mean estimate for all failure modes.

Table 1.2 – Experimental determination of effective to elastic stiffness ratio.

Experimental ratio of effective to elastic stiffness	Experimental failure mode		
	Shear	Hybrid	Flexure
Average $K_{eff}^{exp}/K_{el}^{exp}$	0.59	0.50	0.53
CoV	0.51	0.45	0.41

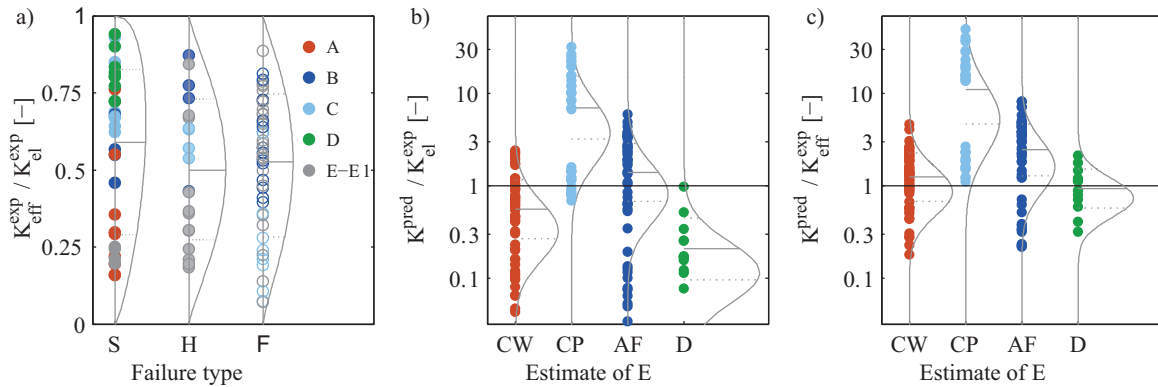


Figure 1.10 – Stiffness of walls subjected to horizontal loads: Effective to elastic wall stiffness ratios for different failure types and masonry typologies (a); estimate of the experimental elastic wall stiffness (b) and effective wall stiffness (c) from different types of tests (CW- compression tests on walls; CP – compression tests on prisms; AF – stiffness measured when applying the axial force at the beginning of the shear-compression test; D – dynamic identification tests).

1.5.2 E-modulus as a function of the masonry typology

For all tests, for which the force-displacement curve was reported, the E-modulus of the masonry can be back-calculated from the horizontal stiffness of the wall. Generally, the stiffness of masonry walls is computed by means of Timoshenko beam models, which account for both flexural and shear deformability with the latter being particularly relevant for the typical slenderness ratios of masonry piers. Applying the Timoshenko beam theory, the elastic stiffness K_{el} of a wall with a rectangular cross section with a height H and shear span H_0 that is subjected to a horizontal force at its top is:

$$K_{el} = \frac{1}{\frac{H^3}{2EI} \left(\frac{H_0}{H} - \frac{1}{3} \right) + \frac{6H}{5GLI}} \quad (1.5)$$

where E and G are the Young modulus and the shear modulus of the masonry, which is idealised as a homogeneous continuum. For back-calculating the E-modulus from the measured stiffness, it was necessary to assume a ratio of the G- to E-modulus. Eurocode 6 recommends a ratio G/E of 0.4 for all types of masonry if a better estimate is not available. Much lower G/E -ratios, in the range 0.06-0.25, are reported in the literature (Tomažević, 2007). According to the elasticity theory of homogenous isotropic materials the maximum Poisson ratio is 0.5 and therefore the minimum G/E -ratio 0.33. Considering

Chapter 1. Stiffness, strength and drift capacity of stone masonry walls

the composite anisotropic nature of the masonry material, smaller G/E -ratios are, however, possible. The Italian code (MIT, 2009) assumes for most stone masonry typologies a ratio of G/E equal to 0.33 and this ratio was also adopted here. Based on this assumption, the E-modulus can be computed from the experimental stiffness of the wall:

$$E_{exp} = K_{exp} \frac{\frac{6}{5} \left[1 + 5 \left(\frac{H_0}{H} - \frac{1}{3} \right) \frac{G}{E} \left(\frac{H}{L} \right)^2 \right]}{\frac{G}{E} L t} \quad (1.6)$$

Average values of the elastic and the effective stiffness and standard deviation derived for each masonry typology are reported in Table 1.3. The effective stiffness values are compared to the ranges indicated by the Italian code in Figure 1.12a. For typologies A, C and D the reference values proposed in the Italian code provide a reasonable estimate in terms of mean values, while the error of the predicted stiffness is considerable for the other typologies. In order to make the code ranges representative of 16th-84th fractiles of a probability distribution, as suggested in CNR (2013), the variance of the stiffness should be significantly increased for all stone masonry typologies. However, if one considers the modification factors proposed in the code for considering various mortar qualities, the code ranges for stiffness and strength would be enlarged and the variance of the distribution, therefore, increased. Nonetheless, given that a large part of the tests considered for this study are laboratory tests on panels built with good quality mortar, the variability of the stiffness and strength properties seems to be related to an aleatoric variability rather than to the quality of the materials.

Table 1.3 – Elastic and effective stiffness ranges for the various masonry typologies.

	Masonry typology					
	A	B	C	D	E	E1
Italian code ¹ , E_{el} [MPa]	870	1230	1740	1080	2800	2800
CoV	0.21	0.17	0.14	0.17	0.14	0.14
Italian code ¹ , G_{el} [MPa]	290	410	580	360	860	860
CoV	0.21	0.17	0.14	0.17	0.09	0.09
Number of tests	10	7	18	10	20	22
Elastic stiffness, E_{el} [MPa]						
median [MPa]	1110	(3650) ²	1900	510	1460	1000
CoV	0.63	(0.39) ²	0.69	0.48	0.61	0.43
Effective stiffness, E_{el} [MPa]						
median [MPa]	320	(2240) ²	900	430	550	630
CoV	0.49	(0.22) ²	0.38	0.42	0.57	0.42
E_{eff}/f_c	400	(700) ²	300	250	200	250

1 - The Italian code (MIT, 2009) gives an upper and lower bound value. According to (CNR, 2013), they can be interpreted as the 16th and 84th percentile values. The mean value given here is computed as the average of the upper lower bound bound value and the CoV, assuming a lognormal distribution, as $\sqrt{e^{\beta^2} - 1}$ where β is the logarithmic standard deviation computed as $\frac{1}{2}(\log E_{84\%} - \log E_{16\%})$

2- The values of stiffness for typology B are derived from a single test campaign.

1.5.3 Determining the E-modulus from compression tests or dynamic identification tests

Most test campaigns with shear-compression tests on stone masonry walls also comprised some material tests from which the elastic properties of the masonry can be estimated. Different types of tests were carried out for this purpose. Most common are compression tests on wallets or masonry prisms. The wallets had typically dimensions of approximately 1 m by 1 m while the prisms were much smaller and comprised just a vertical stack of 3-5 stones. In addition to compression tests, some research groups determined the elastic properties from dynamic identification tests or from the deformation measured when applying the vertical load to the wall. The G-modulus is more difficult to determine than the E-modulus, and test reports do often not report estimates for the G-modulus and such values are therefore also not included in the database.

Figure 1.10b and c show the distributions of errors in predicting the elastic and effective wall stiffness when determining the E-modulus from compression tests on wallets (CW), compression tests on prisms (P), from deformations measured when applying the axial force at the beginning of the shear-compression tests (AF) and from dynamic identification tests (D) on the walls that are later used for shear-compression tests. The estimate of the effective stiffness is in general characterised by a smaller dispersion, compared to the elastic stiffness. The results show that the elastic properties should not be derived from compression tests on prisms (Lourenço, 1996; Oliveira, 2003), but that the compression tests should be carried out on wallets. Compression tests on prisms tend to overestimate the E-modulus, most likely because the texture of prisms is typically much more uniform than that of larger masonry walls.

As presented in more detail in Figure 1.11, the test that leads to the smallest bias and uncertainty is the compression test on masonry wallets and this is therefore the preferred test for estimating the E-modulus. The stiffness derived from the axial force load stage is affected by a larger uncertainty than compression tests on masonry wallets, most likely because the walls are only loaded to relatively small axial load ratios where the stress-strain relationship can be nonlinear. Dynamic identification tests were used only for few tests and therefore conclusions on the reliability of the properties obtained from such tests cannot be derived. Based on the three more reliable estimates of the elastic properties—compression tests on walls, axial force load stage, dynamic identification tests—the effective stiffness can be estimated by assuming a ratio of effective to elastic stiffness and a G/E -ratio. Figure 1.10 shows the distribution of the errors of predicted effective stiffness if one assumes for all typologies and failure modes a ratio of effective to elastic stiffness equal to 0.5 and the ratio of G/E as 0.33. Standard deviations of the errors are in general smaller than for the elastic stiffness (Table 1.3); this might be related to the fact that the effective stiffness is a more robust measure when determined from experimental envelopes than the elastic stiffness.

1.5.4 Determining the E-modulus from the compression strength

In engineering practice, compression or dynamic identification tests can often not be conducted and reference values have to be obtained from the literature or from code provisions. Many codes only tabulate the compressive strength and estimate the E-modulus as $1000f_c$, a value suggested also

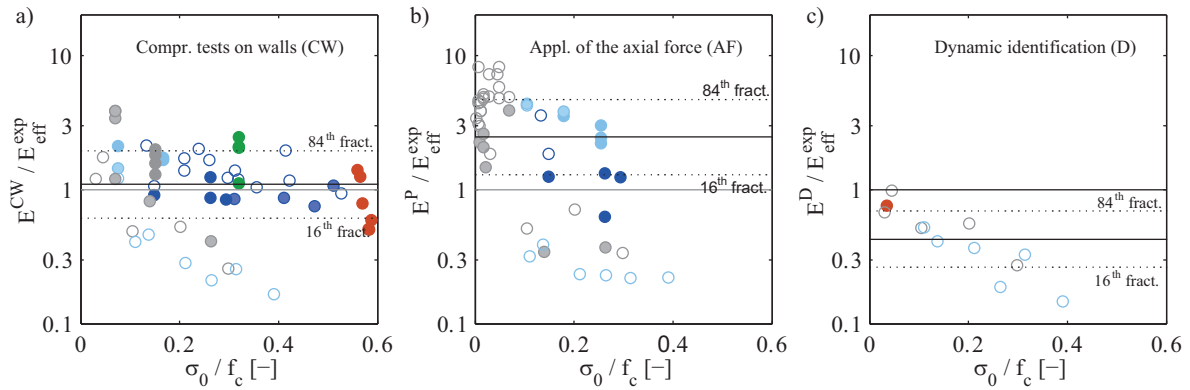


Figure 1.11 – Estimate of the effective stiffness for different experimental test: compression test on walls (a), stiffness measured during the application of the axial force before the shear-compression test (b), and dynamic identification tests (c).

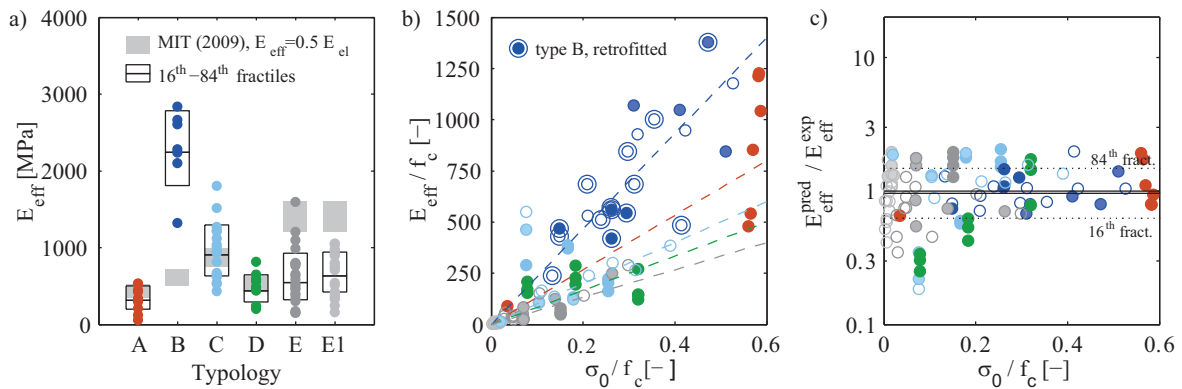


Figure 1.12 – Comparison between the experimental effective stiffness and the ranges proposed in the Italian code; b) relation between effective stiffness and axial load, normalized to the compressive strength f_c ; c) prediction of the effective stiffness through Equation 1.7.

by Eurocode 6. However, such ratio has been shown to be highly variable when determined from experimental tests, as pointed out by Tomažević (2007), who reported for this ratio values between 200 and 2000. On average, in the collected sample of tests, the ratio between the experimental effective stiffness and the compressive strength of masonry tends to increase with the axial load ratio, as shown in Figure 1.12. An increase of the effective stiffness with applied axial load had already been reported by a few authors (Vasconcelos, 2005; Bosiljkov et al., 2005). However, not all test campaigns show a clear trend in this regard (for example, Magenes et al. (2010)). Assuming that an increase of stiffness is related to the axial load ratio, the experimental effective stiffness can be estimated through an

empirical relation of the type:

$$E_{eff} = \left(\frac{E}{f_c} \right)_{ref} f_c \frac{\sigma_0}{0.30 f_c} \quad (1.7)$$

This simple linear formula has limits when applied to axial stresses close to zero. However, the available data and the significant scatter did not justify a more complex relationship between stiffness and axial load ratio (Figure 1.12b). Reference values of the expected ratio between effective stiffness and compressive strength refer to an axial load ratio of 30%. They are derived from the database and are tabulated for the various typologies in Table 6. The ratio of experimental stiffness to the stiffness predicted by Equation 1.7 is shown in Figure 1.12c.

1.6 Strength of stone masonry walls

The in-plane shear force capacity of stone masonry walls is typically evaluated from equations that model the different failure modes of the wall, namely rocking failure with crushing of the compressed toe and shear failure with diagonal cracking or sliding along the bed joints (Magenes and Calvi, 1997). Expressions to evaluate the strength capacity relative to these different failure modes are available in the literature and in the codes (CEN, 2005; MIT, 2009).

1.6.1 Strength equations in Eurocode 8, Part 3

The force capacity of a pier failing in flexure can be evaluated neglecting the tensile strength given that the tensile strength of masonry is normally very small and that horizontal cracking due to cyclic loading is expected at ultimate limit state. Eurocode 8, Part 3 computes the flexural strength as follows:

$$V_{fl} = \frac{L^2 t}{2H_0} \sigma_{0,tot} \left(1 - \frac{1}{\kappa} \frac{\sigma_{0,tot}}{f_c} \right) \quad (1.8)$$

where $\sigma_{0,tot}$ is the mean vertical stress acting at the base of the pier and f_c is the compressive strength of masonry. EC8-sets the factor $1/\kappa$ equal to 1.15, which corresponds to a rectangular stress block in which the maximum stress is equal to $\kappa f_c = 0.87 f_c$. A linear stress distribution at the wall toe would lead to a factor $1/\kappa=1.33$, while a value equal to 0 can be assumed if the compressive strength is considered infinite, for which the expression in Equation 1.8 is equivalent to the rocking capacity in Equation 1.4. For assessment purposes, EC8-3 suggests to use design values for f_c that are multiplied by a confidence factor to account for the uncertainty, which depends on the knowledge that is available on that particular structure. However, for the scope of this study, no confidence factor is applied and the compressive strength derived from compression tests are employed.

Shear failure is modelled by EC8-3 by means of a Mohr-Coulomb criterion to be applied to the portion of the wall that is subjected to compression stresses. Although EC8-3 refers only to brick or concrete block masonry, the application of the approach was checked also for stone masonry walls. This criterion is meant to describe failure due to the interaction of flexural cracking and shear at the base

of a masonry pier. The uncracked length of the wall L_c can be estimated adopting a suitable stress distribution and considering the axial force acting at the base of the wall. If the tensile strength is disregarded and a triangular stress distribution is adopted, one can write the Mohr-Coulomb criterion as follows:

$$V_{MC} = L_c t c + \mu L t \sigma_{0,tot} = L t \left(\frac{\frac{3}{2} c + \mu \sigma_{0,tot}}{1 + 3 \frac{c H_0}{\sigma_{0,tot} L}} \right) \quad (1.9)$$

where c and μ are the cohesion and the friction coefficient of masonry. The parameters c and μ should be interpreted as global strength parameters and should not be derived directly from interface tests on joint interfaces, in order to account for the non-uniform stress distribution along the compression zone. EC8-3 indicates for the friction coefficient a value equal to 0.4, while reference values for the cohesive contribution in stone masonry walls should be assumed from the literature. As an additional condition accounting indirectly for tensile cracking in the units, EC8-3 prescribes that the average shear stress in the uncracked length of the wall should be less than the 6.5% of the compressive strength of the units. However, this latter criterion is meant to be applied to brick/block masonry to account for possible shear cracking through the units. In the case of stone masonry piers, due to the typically high strength of stone units, this condition is seldom the governing criterion and alternative formulations should be used to consider the possible activation of shear failures involving sub-diagonal cracking (Turnšek and Čačovič, 1971).

1.6.2 Application of strength equations to database

The criteria proposed in EC8-3 (CEN, 2005) were applied to the tests collected in the database and the effectiveness of standard code formulations in predicting correctly the experimental failure mode and force capacity was evaluated. Mechanical properties documented in the test reports do not include the shear strength parameters c and μ . The friction coefficient value suggested in EC8-3 is applied ($\mu=0.4$). The cohesion was estimated assuming a parabolic tension cut-off as $c = 2\mu f_t$, where the tensile strength f_t can be derived from code provisions (MIT, 2009). The force capacity is defined as the ultimate shear capacity derived from the bilinear idealisation of the envelope curves. For 15 tests, the load displacement curve is not available and the maximum force capacity reported by the authors was used instead. The average ratio of maximum to ultimate force capacities is 1.04, and it exceeds the value 1.10 in less than 2% of the cases. The failure mode that was attributed to each test is based on the information provided in test reports, which assess the failure modes based on the observed damage (diagonal or horizontal cracking, sliding, crushing at the toe). However, this attribution can be somehow subjective, and mixed or hybrid failure modes are frequently observed.

EC8-3 predicts the failure mode based on the force capacities computed for flexural and shear failure: the smaller force capacity is assumed to control the failure mode. Figure 1.13a compares the experimentally observed failure mode to the failure mode predicted by EC8-3. The failure mode is well predicted for walls failing in flexure. For some walls failing in shear, EC8-3 predicts also a flexural failure. However, this does not necessarily mean that the prediction of the force capacity is wrong,

since also walls developing large shear cracks might fail due to the crushing of the compressed corner. Moreover, shear and flexural capacity equations might lead to rather similar results and while the failure mode might be incorrectly predicted the shear strength might be rather well estimated. An incorrect prediction of the failure mode can have, however, a significant influence on the estimate of the deformation capacity. Most of today's codes assign the displacement capacity based on the failure mode and assume that walls failing in flexure have roughly twice the displacement capacity of walls failing in shear. The fact that a part of the observed shear and hybrid failures are predicted to be flexural failures might therefore lead to unconservative estimates of the deformation capacity (see next section).

For flexure-dominated walls the prediction of the force capacity is fairly good (Figure 1.13b), since it depends mainly on geometrical dimensions and loading conditions, and only to a minor extent on material properties. The ratio of predicted to experimental force capacity, for flexural walls, has a median of 0.93 and a coefficient of variation (CoV) of 15%. The prediction is less accurate for higher axial load ratios, indicating that the assumption of a stress block with $\kappa = 0.87$ at the corner of the wall is probably rather conservative. The best prediction of the force capacity, with a mean of 1.00 and a CoV of 12%, is obtained for $\kappa = 1.20$, which would correspond to a local increase of the compressive strength at the base of the wall. A physical justification of this could be the presence of relatively large stones in the wall corners, which increase local strength properties. For brick masonry, also a confinement of the lowest brick row due to the foundation was observed (Petry and Beyer, 2014a). However, the refinement of the assumptions with regard to the stress block does not seem warranted, as the shift of the predicted force capacity is rather small and the coefficient of variation does not reduce consistently.

The predicted force capacity of walls showing hybrid or shear failure is affected by a larger uncertainty, related primarily to the estimation of the mechanical parameters, which play for these failure modes a significant role. The force capacity is on average overestimated, in a more evident manner for walls subjected to high axial load ratios (Figure 1.13c). This can be related to the assumptions on the friction coefficient, for which a value of 0.4 is adopted in the Eurocode, regardless of the type of masonry. Angelillo et al. (2014) indicate different reference values for stone masonry, ranging from 0.2 for rubble masonry, 0.3 for irregular masonry, to 0.4 for dry joints stone masonry.

If a Mohr-Coulomb formulation is adopted for the assessment of the shear capacity, results are strongly affected by the choice of a suitable value for the friction coefficient. In this study, the cohesive term was assumed to be dependent on the tensile strength, which was derived from code provisions. The friction coefficient, and the uncertainty related to its determination, were hence derived from a linear regression, as shown in Figure 1.14c. Only panels showing shear or hybrid failure modes were considered. Depending on the masonry typology, the so obtained friction coefficient varies between 0.2 and 0.4 (Table 1.4).

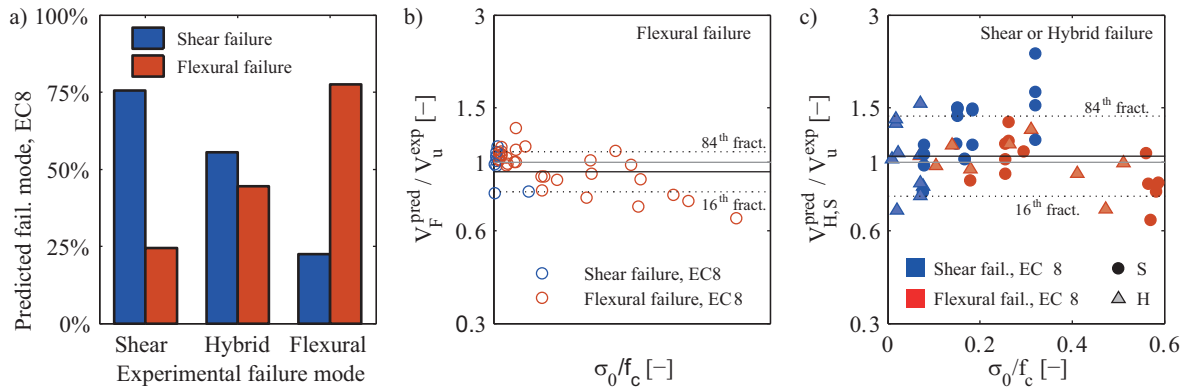


Figure 1.13 – a) Failure mode predicted by Eurocode 8 part 3; b) Estimate of the flexural capacity; c) Estimate of the shear capacity according to EC8-3 (Mohr-Coulomb criterion on the uncracked length of the section).

1.6.3 Turnšek and Čačovič criterion and calibration of the tensile strength

The Mohr-Coulomb criterion in EC8-3 is suitable for cases in which shear failure is associated with bed joint sliding and the opening of head joints. For irregular masonry typologies, however, the physical significance of such criterion can be questionable. An alternative formulation, proposed originally by Turnšek and Čačovič (1971), relates the shear force capacity to the onset of diagonal cracking. The opening of a diagonal crack can be modelled through a tensile criterion, applied to an idealised biaxial stress condition in the middle of the masonry panel, obtaining the formulation as:

$$V_{TC} = \frac{Lt}{b} f_t \sqrt{1 + \frac{\sigma_{0,mid}}{f_t}} \quad (1.10)$$

The vertical stress $\sigma_{0,mid}$ is the mean vertical stress at the mid-height of the panel, since it is assumed that diagonal cracking initiates there. The factor b models the distribution of shear stresses along a horizontal section of the wall and corresponds to 1.5 if a parabolic shear stress distribution is assumed. For squat panels, however, this idealisation can be rather crude and a value of $b = H/L$ ($1.0 \leq b \leq 1.5$) was found to be more appropriate (Benedetti and Tomažević, 1984). The parameter f_t represents the tensile strength of masonry along an inclined plane, and can be determined from diagonal compression tests. The Italian code, which suggests this equation for irregular masonry or for walls built with weak units, provides also reference values for f_t .

If the failure criterion expressed in Equation 1.10 is adopted for all tests with hybrid or shear failure modes, one experimental value of tensile strength can be derived for each test using:

$$f_t = -\frac{\sigma_0}{2} + \sqrt{\left(\frac{\sigma_0}{2}\right)^2 + \left(\frac{bV_u}{Lt}\right)^2} \quad (1.11)$$

Figure 1.14a shows the comparison of ranges proposed in the Italian code for the tensile strength of

masonry for the different typologies, with the values estimated from the collected tests. The obtained mean values are comparable—though typically slightly higher—than the values included in the Italian code. It should be noted that typology B refers to unstrengthened conditions. The values listed in Table 1.4 derive from a single test campaign and a limited number of tests, since the majority of collected tests of the same typology was strengthened through grout injections. Similarly to what was found for the effective stiffness, the code ranges do not appear currently suitable to represent 16th-84th fractiles of a probability distribution of the measure. The code ranges shown in Figure 1.14a do not include the correction factors that are proposed by the Italian code to consider that the mortar of the test units tested in laboratory conditions was most likely good quality mortar, often containing hydraulic lime. The quality of the mortar present in existing buildings can be considerably lower, since its composition and conservation state might differ significantly to the ones of mortars tested in laboratory. Therefore, depending on the state of the mortar, the adoption of conservative values for assessment purposes can be advisable. An alternative method for estimating the tensile strength of an existing stone masonry could make use of the Masonry Quality Index (MQI). In Figure 1.14b the experimental values of tensile strength are related to the MQI estimated for each panel, evaluated for in-plane actions. A regression of experimental values through a simple equation can be expressed as:

$$f_t = 0.015 + 0.006 \text{ MQI}^{1.5} \quad (1.12)$$

Equivalent expressions that link upper and lower bounds of the tensile strength to the MQI were developed by Borri et al. (2015). These expressions, although their form is slightly different, show the same trend and lead to similar estimates of the tensile strength.

Table 1.4 – Experimental and code ranges for the tensile strength of masonry f_t .

	Masonry typology				
	A	B	C	D	E-E1
Italian code ¹ , f_c [MPa]	1.40	2.50	3.20	1.90	7.00
CoV	0.30	0.20	0.19	0.27	0.14
Italian code ¹ , f_t [MPa]	0.039	0.065	0.098	0.053	0.158
CoV	0.24	0.19	0.14	0.20	0.14
Experimental, f_t					
median [MPa]	0.047	0.046	0.111	0.052	0.136
CoV	0.79	0.29	0.22	0.32	0.44
Friction coefficient, experimental					
median	0.44	0.21	0.24	0.25	0.29
CoV	0.17	0.12	0.17	0.12	0.04

¹ - Mean values and coefficients of variation calculated as in Table 1.3.

1.6.4 Comparison of different strength models

A comparison of the different capacity models for the prediction of the lateral strength of panels showing hybrid or shear failure modes are summarised in Table 1.5. In general, the application of a

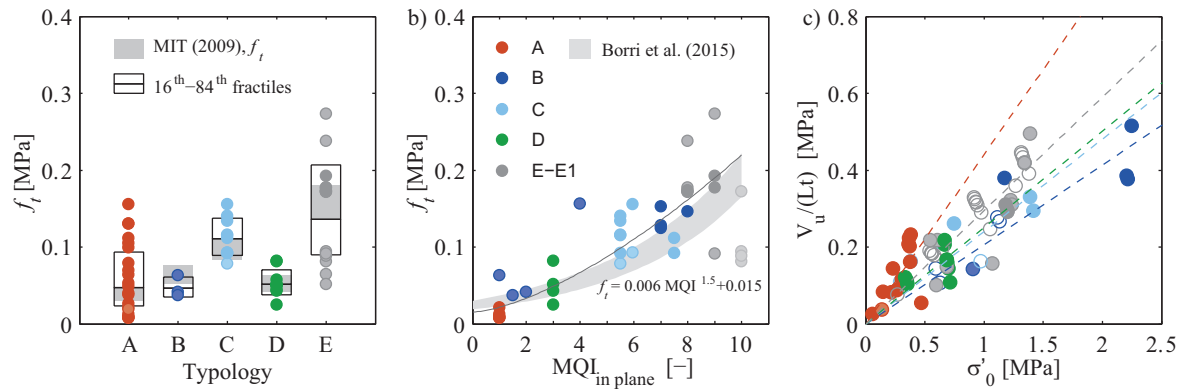


Figure 1.14 – Masonry tensile strength according to Turnšek and Čačovič (1971) criterion: comparison with ranges suggested in the Italian code (MIT, 2009); b) Estimate of the experimental tensile strength from the Masonry Quality Index; c) Regression analysis for the estimation of the friction coefficient; the cohesive contribution is subtracted, assuming $c = 2\mu f_t$. The x -axis is derived from Equation 1.9: $\sigma'_0 = \sigma_0 + 3f_t - 6\left(\frac{V_u H_0 f_t}{\sigma_0 L^2 t}\right)$ where $V_u = \mu \sigma'_0 L t$.

Turnšek and Čačovič failure criterion improves the prediction of the force capacity when compared to the standard approach prescribed in EC8-3. This applies to both approaches of estimating f_t , i.e., estimating f_t from MQI (Equation 1.12) and using reference values for f_t by the Italian code, which depend on the masonry typology. For walls that fail in shear, the Turnšek and Čačovič criterion leads also to a more accurate prediction of the failure mode than the Mohr-Coulomb criterion with $\mu = 0.4$. However, a similar accuracy can be achieved through the optimisation of the parameters of a Mohr-Coulomb criterion, such as the one in Equation 1.9, among which the friction coefficient is the more relevant.

Table 1.5 – Experimental and code ranges for the tensile strength of masonry f_t .

	EC8-3 $\mu = 0.4, c$ from MIT (2009) ¹	EC8-3 μ from Ta- ble 1.4, c from MIT (2009) ¹	Eq. 1.10 f_t from MIT (2009) ¹	Eq. 1.10 typology median f_t	Eq. 1.10 f_t from Eq. 1.12
V^{pred} / V^{exp} , median	1.04	0.88	1.04	0.95	0.94
CoV	0.31	0.26	0.22	0.18	0.24
Predicted to fail in shear	72%	85%	77%	80%	76%

1 - Table C8A.2.1. Correction coefficients in table C8A.2.2 to account for grout injections and quality of mortar.

2 - Ratio of walls predicted to fail in shear to walls that experimentally showed shear failure.

1.7 Drift capacity of stone masonry walls

The deformation capacity of walls is a key input parameter when applying displacement-based assessment methods to masonry buildings. Current code provisions do not differentiate between brick

1.7. Drift capacity of stone masonry walls

and stone masonry when specifying the drift capacity of walls (Petry and Beyer, 2014a). EC8-3 limits its application to concrete and brick masonry, but in engineering practice the values given in EC8-3 are often also applied to stone masonry. The objective of this section is to derive drift capacities for stone masonry walls, to identify parameters that influence the drift capacities at different limit states and to provide the input data that is required for a probabilistic seismic assessment of stone masonry structures. In addition, two simple drift capacity models for stone masonry are put forward, which are suitable for implementation in engineering practice.

It was shown in Section 1.4 that monotonic tests lead to significantly larger drift capacities than cyclic tests. Since drift capacity values are typically used in conjunction with seismic assessments, only cyclic tests are considered in the following. Disregarded are also tests on walls that were injected or repaired as well as all tests that did not pass the quality check. In total, 67 test were considered of which 2 belonged to masonry typology A, 8 to B, 19 to C, 6 to D, 20 to E and 12 to E1 (Figure 1.15a). The drift capacities are evaluated for the six element limit states introduced in the introduction: (i) the drift at the onset of cracking δ_{cr} , (ii) the drift at yield δ_y , (iii) the drift at maximum force δ_{max} , (iv) the drift at the limit state “Significant damage” $\delta_{SD} = \min(3\delta_{cr}, \delta_{max})$, (v) the drift at ultimate limit state (20% strength drop) δ_u , (vi) the drift at collapse (50% strength drop) δ_c . With the exception of the drift at the onset of cracking, the drift capacities are determined from the force-displacement envelope and its bilinear approximation. The drift at the onset of cracking is based on observations reported in the reference document but is not available for all tests. Note that the definition of onset of cracking differed between test campaigns. Some researchers distinguish between the appearance of flexural and shear cracks (Kržan and Bosiljkov, 2012; Silva et al., 2014), others consider any type of crack Vasconcelos, 2005. Also, the minimum crack width that was detected probably differed between test series. The drift at the onset of cracking is therefore afflicted with an additional uncertainty. A detailed definition of the individual drift limits based on the envelopes in the positive and negative loading direction is included in the accompanying database.

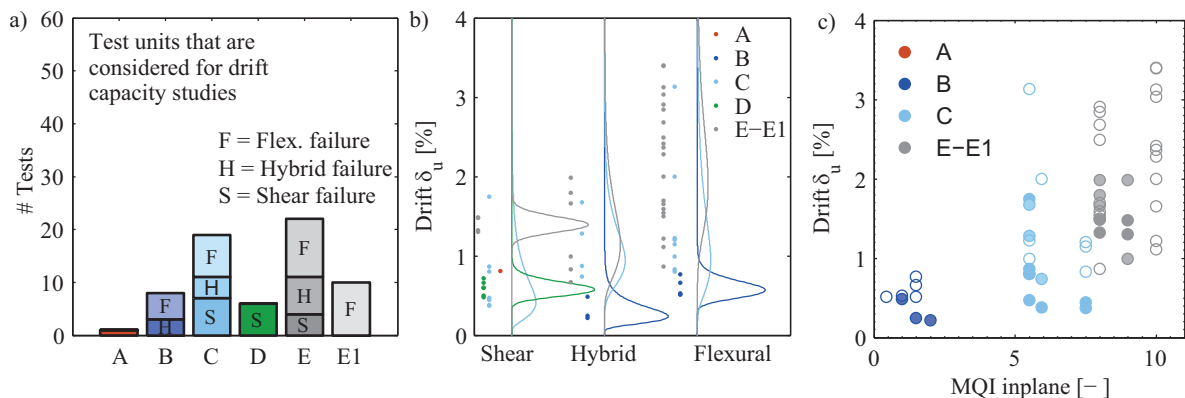


Figure 1.15 – Distribution of test units considered for drift capacity studies (a). Ultimate drift capacity δ_u as a function of the failure mode (b), and the Masonry Quality Index for in-plane loading (c). Solid markers represent walls failing in shear or a hybrid mode; empty markers walls failing in flexure.

1.7.1 Sensitivity of drift capacities at different limit states

The minimum and the maximum ultimate drift values of the 67 tests differ by more than a factor of 15 ($\delta_{u,min} = 0.22\%$ and $\delta_{u,max} = 3.4\%$). This is a rather significant ratio and the objective of this section is to identify factors that influence the drift capacity of stone masonry walls at different limit states. EC8-3 assumes that the ultimate drift capacity depends on the failure mode. Figure 1.15b shows the distribution of the drift values for shear, hybrid and flexural failure. In general, shear and hybrid failures lead to a smaller drift capacity than flexural failures. Different trends are only observed when the sample size is very small (shear failure of Type E; hybrid failures Type C). To increase the size of the groups, the masonry typologies are regrouped as follows: the first group comprises types A-D and the second group types E and E1. Table 1.6 summarises for these two groups the median drift capacities and coefficients of variations for all considered limit states. Shear and hybrid failure modes lead to similar drift capacities and coefficients of variations. This finding suggests that it is not necessary to distinguish between shear and hybrid failure modes and in the remainder of this section drift capacities obtained from hybrid failure modes are counted towards shear failures.

One might expect that the drift capacity is positively correlated with the Masonry Quality Index and this is indeed confirmed by Figure 1.15c. However, as shown by Figure 1.14i, the axial load ratio also correlates strongly with the Masonry Quality Index (the larger the Masonry Quality Index, the smaller the axial load ratio that was applied in the test). Based on the current database it is therefore not possible to identify whether the drift capacity depends on the Masonry Quality Index or the axial load ratio or both. For other masonry typologies, it was already shown that the drift capacity decreases with increasing axial load ratio (Petry and Beyer, 2014a). For this reason, we investigate in the following the influence of the axial load ratio on the drift capacity of stone masonry walls at different limit states. Note that photos of the test units of typology D (Faella et al., 1992) were not available and therefore the Masonry Quality Index could not be determined.

Figure 1.16 shows the influence of the axial load ratio on the drift capacities for the different limit states. The drift δ_{cr} at the onset of cracking is relatively independent of the axial load ratio and of the masonry typology; for most walls the drift at the onset of cracking is between 0.1 and 0.3%. Only for some walls of typology E and E1, the drift at the onset of cracking is significantly larger. Drift capacities of all limit states tend to reduce with the axial load ratio but this trend is particularly evident for δ_y , δ_{max} and δ_u .

Figure 1.17a and b show the trends of the ultimate drift capacity with axial load ratio, if δ_u is normalised by H_0/L (CEN, 2005) and by H_0/H (Pfyl-Lang et al., 2011b), respectively. The clearest trend with axial load ratio is obtained for $\delta_u L/H_0$. For brick masonry, it was further shown that the drift capacity decreases with the wall size (Petry and Beyer, 2014a). For stone masonry walls, as for brick masonry, no test series investigated the effect of size on the drift capacity systematically. Figure 1.17c show the drift capacity of the walls contained in this database as a function of the wall height. Although the drift values tend to decrease with wall height, the trend for a single masonry typology is not clear. One reason why the size effect might be less important for stone masonry walls than for brick masonry walls is the fact that the size of the stones can be relatively easily reduced while small-scale brick wall tests are typically conducted with full-size bricks.

1.7. Drift capacity of stone masonry walls

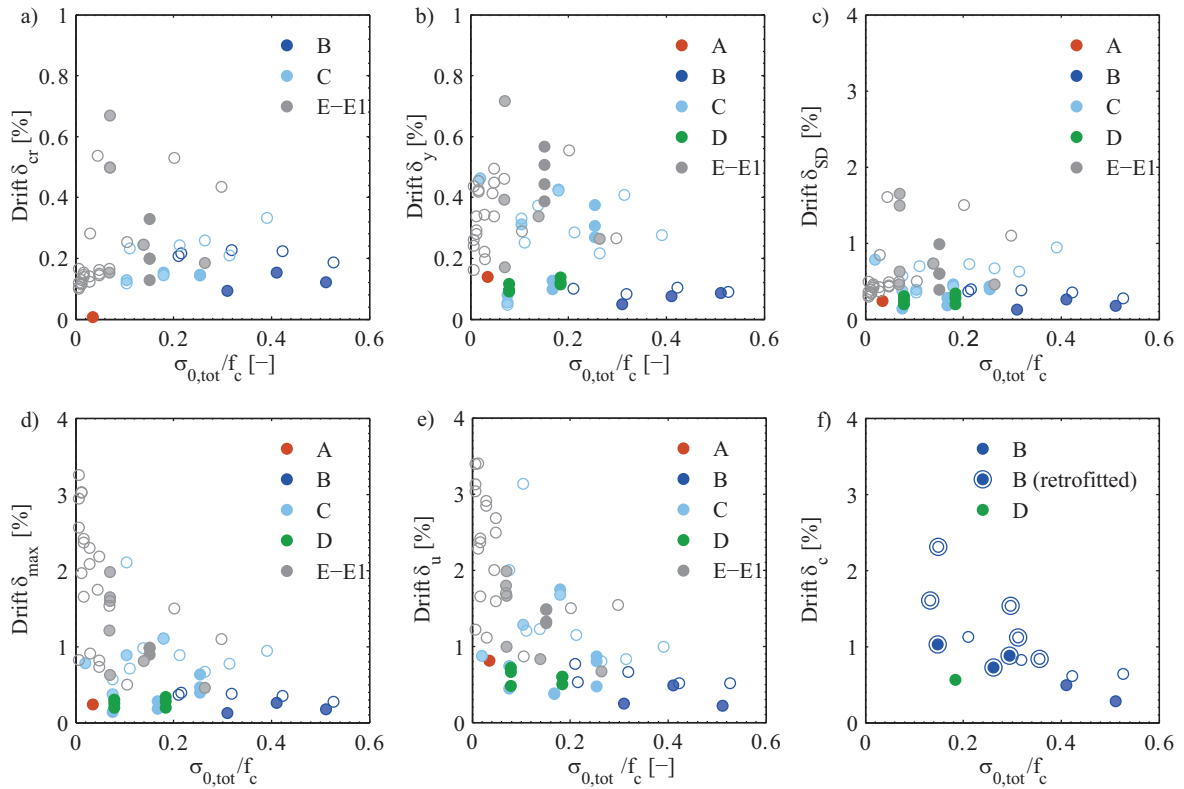


Figure 1.16 – Influence of the axial load ratio on the drift capacity at different limit states: a) Drift at the onset of cracking δ_{cr} ; b) Drift at yield δ_y ; c) Drift at maximum force δ_{max} ; d) Drift limit “Significant damage” $\delta_{SD} = \min(3\delta_{cr}, \delta_{max})$; e) Drift at ultimate LS δ_u ; f) Drift at collapse δ_c . Solid markers represent walls failing in shear of a hybrid mode; empty markers walls failing in flexure. Note: The scale of the y-axis of plot a and b is different from those in plots c-f.

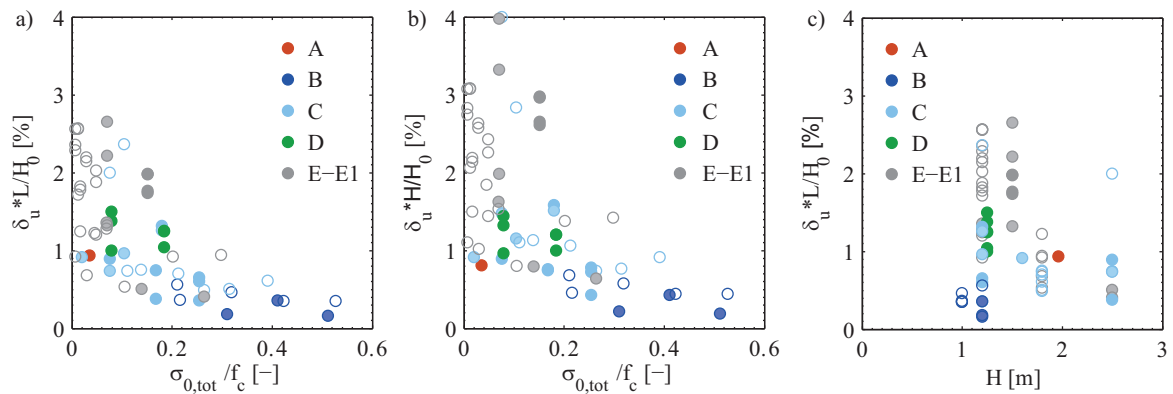


Figure 1.17 – Ultimate drift capacity δ_u : Normalising the drift capacity by L/H_0 (a) and H/H_0 (b). Influence of the wall size on the drift capacity (c).

Figure 1.18a shows the displacement ductility $\mu = \delta_u / \delta_y$ as a function of the axial load ratio. The displacement ductilities vary between $\mu = 1.5 - 13.4$ for shear and hybrid failures and between $\mu = 2.0 - 41.5$ for flexural failures. The median displacement ductilities are $\mu = 4$ for shear and hybrid failures and $\mu = 6.5$ for flexural failures. The wide ranges highlight that displacement ductility is not a suitable parameter for characterising the deformation capacity of masonry walls. The ratio of the drift at the LS “Significant Damage” to the ultimate varies for shear/hybrid and flexural failure modes between $\delta_{SD} / \delta_u = 0.5 - 1.0$ (Figure 1.18b). The median value is 0.5 and therefore smaller than what is assumed in EC8-3 ($\delta_{SD} / \delta_u = 3/4$). The ratio of 3/4 corresponds, however, rather well to the median ratios obtained for δ_{max} / δ_u (Figure 1.18c), for which a median value of 0.70 was obtained.

The limit state for which the least amount of data is available is the collapse limit state (Figure 1.16f, Figure 1.18d). Only seven tests were continued up to collapse; six walls originate from a single test series conducted by Silva et al. (2014). Out of these six tests, two failed in shear and four in flexure. The average collapse drift of these six tests is considerably smaller than the average ultimate drift of all 67 tests (Table 1.6). In order to increase the data base, the walls that were strengthened were also considered for the collapse limit state. Of the strengthened walls, eight walls were tested up to collapse; these tests were conducted by Silva et al. (2014) and Mazzon (2010). The drift at collapse decreases significantly with increasing axial load ratio (Figure 1.16f). For walls failing in flexure the drift capacities at collapse are slightly larger than for walls failing in shear but the difference for the tests reported here is not as large as one might have expected. Figure 1.18d shows the collapse drift to ultimate drift ratio for the 15 strengthened and unstrengthened walls that were tested up to collapse. This ratio seems to be rather independent of the axial load ratio and failure mode and its median value is $\delta_c / \delta_u = 1.15$.

1.7.2 Simple drift capacity models for engineering practice

The median drift values and CoVs given in Table 1.6 can be directly used in probabilistic assessments of stone masonry buildings. However, simpler models that can be summarised in fewer equations might often be more practical. The objective of this section is to propose two of such models. The first relates drift capacities to failure modes and masonry typology and the second relates drift capacity to axial load ratio, slenderness ratio and masonry typology. These models are inevitably less exact than the values of Table 1.6 and their derivation required some judgment in order to find a good balance between accuracy and simplicity.

The drift capacities are determined for the ultimate limit state (δ_u). Based on the results presented in Figure 1.18, drifts at all other limit states are expressed as a fraction of the drift at the ultimate limit state. Equations 1.13-1.17 summarise these relationships. The equations on the left represent median values and the equations on the right values that correspond to plus/minus one standard deviation assuming a lognormal distribution. One exception is the drift at the onset of cracking, for which a universal value of 0.20% is recommended, independent of the failure mode and masonry typology. The relationships between δ_u and the other drift limits apply independently of the chosen model for δ_u . For the yield drift, two approaches are investigated. In the first approach, the yield drift is computed

1.7. Drift capacity of stone masonry walls

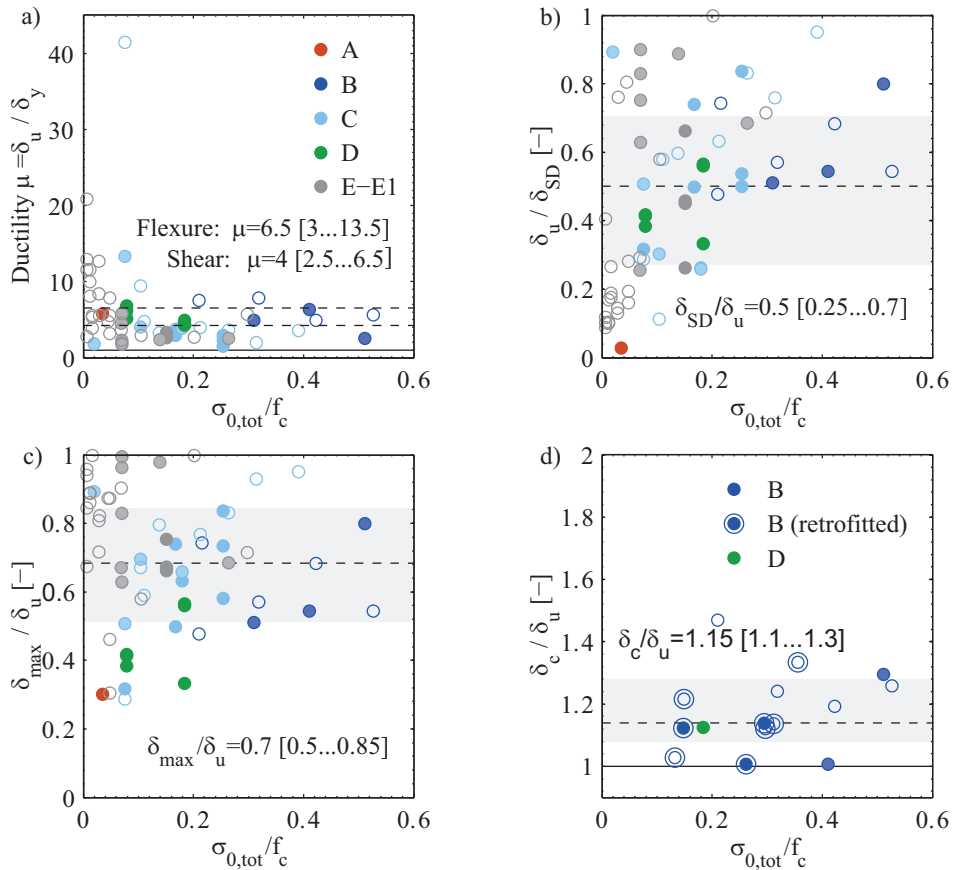


Figure 1.18 – Ratios of drifts at different limit states: a) Displacement ductility $\mu = \delta_u / \delta_y$; b) Ratio of ultimate drift δ_u to drift at the limit state “Significant Damage”; c) Ratio of collapse drift δ_c to ultimate drift δ_u . Solid markers represent walls failing in shear or a hybrid mode, empty markers walls failing in flexure. The dashed line represents the median value and the shaded area and the range corresponding to plus/minus one standard deviation.

assuming a constant displacement ductility values, which is assumed as dependent on the failure mode or independent of the failure mode. In the second approach, the yield drift is computed from the predicted shear resistance and the predicted effective stiffness (Sections 1.5 and 1.5).

$$\delta_{cr} = 0.20\%, \quad \delta_{cr} = [0.1\% \dots 0.35\%] \quad (1.13)$$

Chapter 1. Stiffness, strength and drift capacity of stone masonry walls

Table 1.6 – Median drift capacities and coefficients of variations for different limit states and masonry typologies. Drift capacities and CoVs are rounded to the nearest 0.05; shear failure comprises shear and hybrid failures.

	No of test unit per group		Drift capacity [%]		CoV	
	Shear failure	Flexural failure	Shear failure	Flexural failure	Shear failure	Flexural failure
Drift at the onset of cracking δ_{cr}						
A-D	10	12	0.15	0.25	0.35	0.20
E, E1	11	21	0.25	0.15	0.55	0.65
All	21	33	0.15	0.15	0.75	0.55
Drift at yield δ_y						
A-D	21	12	0.10	0.25	0.75	0.60
E, E1	11	21	0.45	0.35	0.55	0.30
All	32	33	0.25	0.30	0.85	0.45
Drift at "Significant Damage" LS δ_{SD}						
A-D	21	13	0.30	0.55	0.50	0.35
E, E1	11	21	0.65	0.45	0.55	0.65
All	32	34	0.40	0.45	0.80	0.55
Drift at maximum force δ_{max}						
A-D	21	13	0.30	0.65	0.75	0.65
E, E1	11	21	1.00	1.95	0.40	0.45
All	32	34	0.45	1.05	0.75	0.65
Drift at ultimate LS (20% drop in force) δ_u						
A-D	21	13	0.60	0.85	0.55	0.65
E, E1	11	21	1.50	2.35	0.30	0.35
All	32	34	0.80	1.65	0.55	0.55
Drift at collapse (50% drop in force) δ_c						
A-D	3	4	0.50	0.75	0.35	0.30
E, E1	0	0	-	-	-	-
All	3	4	0.50	0.75	0.35	0.30

Approach 1: Flexural failure: $\delta_y = 1/6.5 \delta_u$ $\delta_y = 1/[3.0...13.5] \delta_u$ (1.14)

Shear failure: $\delta_y = 1/4 \delta_u$ $\delta_y = 1/[2.5...6.5] \delta_u$ (1.15)

All failure modes: $\delta_y = 1/5 \delta_u$ $\delta_y = 1/[2.5...10.5] \delta_u$ (1.16)

$$\text{Approach 2: } \delta_y = V_R / K_{eff} \quad (1.17)$$

$$\delta_{SD} = 0.5\delta_u \quad \delta_{SD} = [0.25...0.70] \delta_u \quad (1.18)$$

$$\delta_{max} = 0.7\delta_u \quad \delta_{SD} = [0.50...0.85] \delta_u \quad (1.19)$$

$$\delta_c = 1.15\delta_u \quad \delta_c = [1.10...1.30] \delta_u \quad (1.20)$$

Model 1: Drift capacity at ultimate limit state as a function of failure mode and masonry typology

In the absence of further test data, the masonry typologies are divided into two groups only (Group 1: A-D, Group 2: E-E1). The values of Table 1.7 are simplified so that the drift capacity of walls failing in flexure corresponds to 1.5 times the drift capacity of walls failing in shear:

$$\delta_{u,flexure} = 1.5 \delta_{u,shear} \quad (1.21)$$

The drift capacity of the more regular masonry typologies (E-E1) is set to 2.5 times the drift capacity of masonry typologies A-D. The drift capacities at ultimate limit state for this first model and the corresponding CoVs are summarised in Table 1.7. The recommended CoVs for probabilistic assessments are 0.6 for masonry typologies A-D and 0.4 for masonry typologies E-E1. These recommended CoVs are approximate values of the CoVs reported in Table 1.9.

The drift capacity of the more regular masonry typologies (E-E1) is set to 2.5 times the drift capacity of masonry typologies A-D. The drift capacities at ultimate limit state for this first model and the corresponding CoVs are summarised in Table 1.7. The recommended CoVs for probabilistic assessments are 0.6 for masonry typologies A-D and 0.4 for masonry typologies E-E1. These recommended CoVs are approximate values of the CoVs reported in Table 1.7. The drift capacities at the other limit states are computed using Equations 1.13-1.17. For a deterministic assessment, one typically uses a capacity that corresponds to a lower fractile value. Strength evaluations are typically based on the 5%-fractile value, which is referred to as the characteristic value. Current code estimates for drift capacities do not specify to which fractile value the drift capacity corresponds. If one assumes a lognormal distribution and the CoVs in Table 1.7, one obtains the ratios between fractile values and the median drift capacities as given in Table 1.8. For failure modes and masonry typologies for which the drift capacity can be predicted with a CoV of 0.6, the median drift capacity needs to be multiplied by 0.40 in order to obtain a drift capacity that corresponds to the 5%-fractile value. For a CoV of 0.4, 0.55 times the median drift capacity corresponds to the 5%-fractile value.

Figure 1.19 shows the distribution of the error between predicted and experimentally determined drift values for all six limit states. Table 1.9 summarises for the same values the median ratios of the predicted to experimental drifts and the CoV for the two groups of masonry typology (Group 1: A-D, Group 2: E-E1) and failure modes (shear/hybrid and flexure). The comparison assumes that the failure mode can be predicted correctly. One point was excluded from these plots and tables; this concerns the drift at the onset of cracking for Test ID 73 (cyclic in-situ test by Costa et al. (2011)), which was

Chapter 1. Stiffness, strength and drift capacity of stone masonry walls

Table 1.7 – Drift capacity model 1: Recommended median drift capacities and coefficients of variations for δ_u .

Masonry typology	Drift capacity		CoV	
	Flexural failure	Shear failure	Flexural failure	Shear failure
A-D	0.60	0.90	0.60	0.60
E, E1	1.	50 2.25	0.40	0.40

Table 1.8 – Ratios between fractile drift values and median drift values assuming that the drift capacities follow a lognormal distribution (ratios are rounded to the closest 0.05).

Fractile value	CoV=0.10	CoV=0.20	CoV=0.30	CoV=0.40	CoV=0.50	CoV=0.60	CoV=0.70	CoV=0.80	CoV=0.90
	$\frac{\delta_{x\%}}{\delta_{median}}$	$\frac{\delta_{x\%}}{\delta_{median}}$	$\frac{\delta_{x\%}}{\delta_{median}}$	$\frac{\delta_{x\%}}{\delta_{median}}$	$\frac{\delta_{x\%}}{\delta_{median}}$	$\frac{\delta_{x\%}}{\delta_{median}}$	$\frac{\delta_{x\%}}{\delta_{median}}$	$\frac{\delta_{x\%}}{\delta_{median}}$	$\frac{\delta_{x\%}}{\delta_{median}}$
5%	0.85	0.70	0.60	0.55	0.45	0.40	0.35	0.30	0.30
10%	0.90	0.80	0.70	0.60	0.55	0.50	0.45	0.40	0.35
16%	0.90	0.80	0.75	0.70	0.65	0.60	0.55	0.50	0.45
50%	1	1	1	1	1	1	1	1	1

reported as 0.008% and which is about 25 times smaller than drifts at the onset of cracking that were reported for other walls (Fig. 19a). As outlined at the beginning of Section 1.7, the drift values at the onset of cracking are not determined from the envelope curve but are taken from the test reports and are therefore not evaluated according to uniform criteria.

The displacement ductility values $\mu = \delta_u / \delta_y$ of the walls varied greatly (Section 1.7.1). This is reflected in the relatively large uncertainties (Table 1.9) when estimating the yield drift δ_y assuming constant ductility capacities for shear and flexural failures. However, due to the large uncertainty associated with the effective stiffness (Section 1.5.1), even larger CoVs are obtained when computing the yield drift from estimates of the shear strength and the effective stiffness. The distributions plotted in Figure 1.19b show yield drift estimates that are computed assuming a fixed displacement ductility.

With the exception of the CoVs for δ_{cr} of masonry typology A-D, for which only a few data points are available, the CoVs of all limit states are rather similar and it is therefore recommended to use the CoVs that are given in Table 11 for the drift at the ultimate limit state as well for all other limit states. In some cases, the simple relationships of Equations 1.13-1.17 introduce a significant bias for a certain combination of failure mode and masonry typologies. Such a bias could of course be removed by assigning the coefficients of Equations 1.13-1.17 on a case-to-case basis. However, for the sake of simplicity and considering the imperfect data base, a drift capacity model of such complexity does not seem justified.

1.7. Drift capacity of stone masonry walls

Table 1.9 – Drift capacity model 1: Median ratios and CoV for predicted to experimentally observed drift ratios ($\delta_{pred}/\delta_{exp}$). Mean ratios capacities and CoVs are rounded to the nearest 0.05; shear failure comprises shear and hybrid failures.

Drift limit	A-D				E-E1			
	Flexure		Shear		Flexure		Shear	
	Median	CoV	Median	CoV	Median	CoV	Median	CoV
δ_{cr}	1.40	0.20	0.90	0.30	0.80	0.50	1.35	0.35
δ_y – const. duct.	1.25	0.60	0.60	0.75	0.85	0.55	1.00	0.35
$\delta = V_R/K_{eff}$	0.75	1.15	0.65	1.45	0.80	0.90	1.55	0.40
δ_{SD}	1.05	0.45	0.80	0.40	1.20	0.45	2.55	0.35
δ_{max}	1.50	0.55	0.95	0.50	1.05	0.45	0.80	0.65
δ_u	1.00	0.55	1.10	0.45	1.00	0.40	0.95	0.45
δ_c	1.40	0.40	1.40	0.25	-	-	-	-

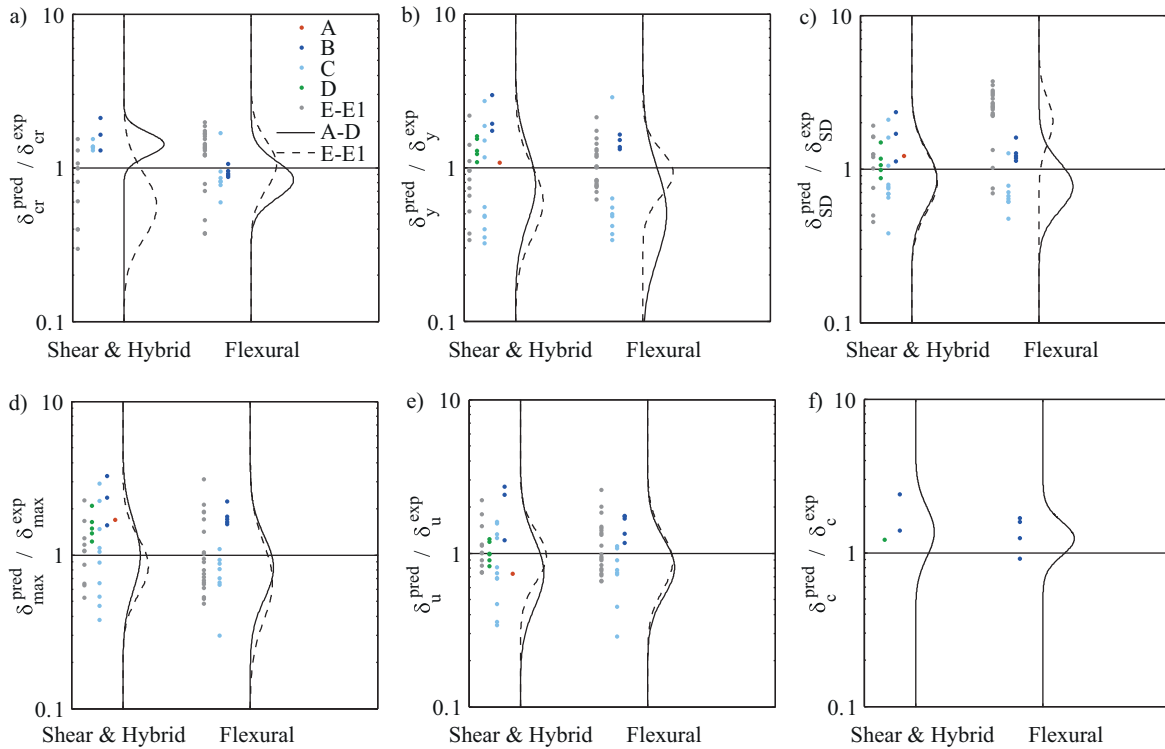


Figure 1.19 – Drift capacity model 1: Ratios of predicted to experimental drift capacities for the six different limit states.

Model 2: Drift capacity at ultimate limit state as a function of axial load ratio, shear span and masonry typology

The second drift capacity model links the ultimate drift capacity to the axial load ratio and the shear span, which is normalised by the height. It follows therefore the drift form introduced by Pfyl-Lang

Chapter 1. Stiffness, strength and drift capacity of stone masonry walls

et al. (2011b) and applied in Petry and Beyer (2014a). Figure 1.20 plots the ultimate drift capacity that was normalised by $\min(H, L)/H_0$ against the axial load ratio. The trendlines included in the figures represent median values of drifts that were obtained for bins of axial load ratio (bin width: 0.1). Equations 1.22-1.23 aim at approximating these trend lines. This method was used in order to account for the fact that the number of tests per bin varies significantly and tends to decrease with increasing axial load ratio. Therefore, the higher axial load ratios would be underrepresented if a simple linear fit was performed. For masonry typologies A-D, the following equation for the ultimate drift is proposed:

$$\delta_u = \max(1.5\% - 4\%\sigma_{0,tot}/f_c, 0.30\%) H_0/\min(H, L) \quad (1.22)$$

The equations are applicable for $\sigma_{0,tot}/f_c \leq 0.6$ (Figure 1.20b). For masonry typologies E and E1, the drift capacity is assumed to be 50% larger:

$$\delta_u = \max(2.25\% - 6\%\sigma_{0,tot}/f_c, 0.45\%) H_0/\min(H, L) \quad (1.23)$$

Note that for masonry typologies E and E1, only the first branch of the equation could be validated since walls of such typologies were not tested for large axial load ratios. For both groups and failure modes, the CoVs for the ultimate drifts lie for this second model between 0.40 and 0.60 (Table 1.10). The CoV are with this model even somewhat smaller for masonry typologies A-D than for masonry typologies E-E1. For the sake of simplicity and because clear trends are not recognisable, it is recommended to use a CoV for all masonry typologies and failure modes, if this second drift capacity model is applied. It is suggested to use $\text{CoV}=0.4$ for δ_u and $\text{CoV}=0.6$ for all other limit states. The distribution of the error between the predicted and experimentally determined drift values for the second model is shown in Figure 1.21.

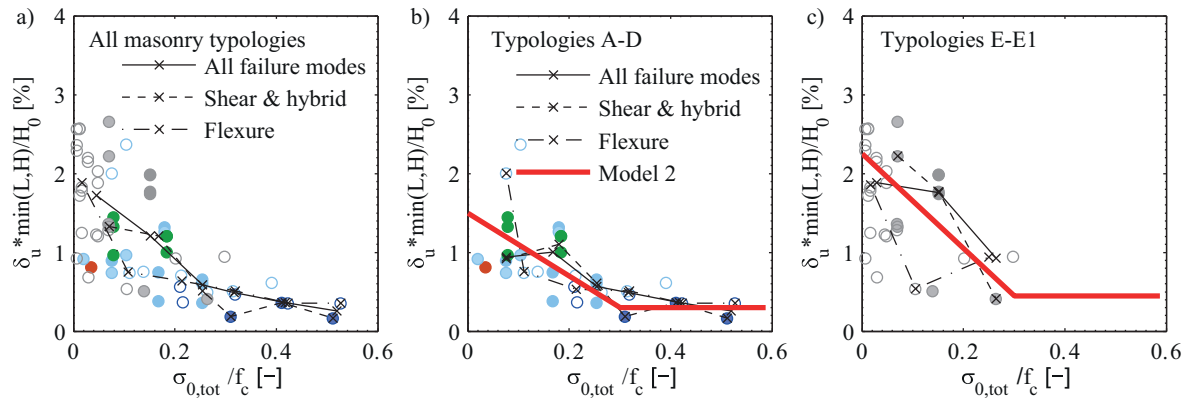


Figure 1.20 – Drift capacity model 2: Comparison of predicted and observed ultimate drift capacities for (a) all masonry typologies, (b) only masonry typology A-C, (c) only masonry typologies D-E1.

Comparison of different drift capacity models

The two models yield rather similar CoVs for the ultimate drift capacity (Model 1: 0.40-0.55; Model 2: 0.40-0.60). The error of Model 1 is expected to increase, if the predicted rather than the observed

1.7. Drift capacity of stone masonry walls

Table 1.10 – Drift capacity model 2: Median ratio and CoV for predicted to experimentally observed drift ratios ($\delta_{pred}/\delta_{exp}$). Median ratios capacities and CoVs are rounded to the nearest 0.05; shear failure comprises shear and hybrid failures

Drift limit	A-D				E-E1			
	Flexure		Shear		Flexure		Shear	
	Median	CoV	Median	CoV	Median	CoV	Median	CoV
δ_{cr}^1	1.40	0.20	0.90	0.30	0.80	0.50	1.35	0.35
δ_y – const. duct.	0.90	0.80	0.85	1.05	0.45	0.70	1.55	0.45
$\delta = V_R/K_{eff}$	0.75	1.15	0.65	1.45	0.80	0.90	1.55	0.40
δ_{SD}	1.10	0.45	0.75	0.55	0.85	0.65	3.1	0.40
δ_{max}	1.35	0.55	0.85	0.45	0.70	0.50	0.85	0.65
δ_u	1.10	0.40	0.85	0.40	0.75	0.60	1.1	0.50
δ_c^1	1.40	0.40	1.40	0.25	-	-	-	-

1) Same values as for Model 1.

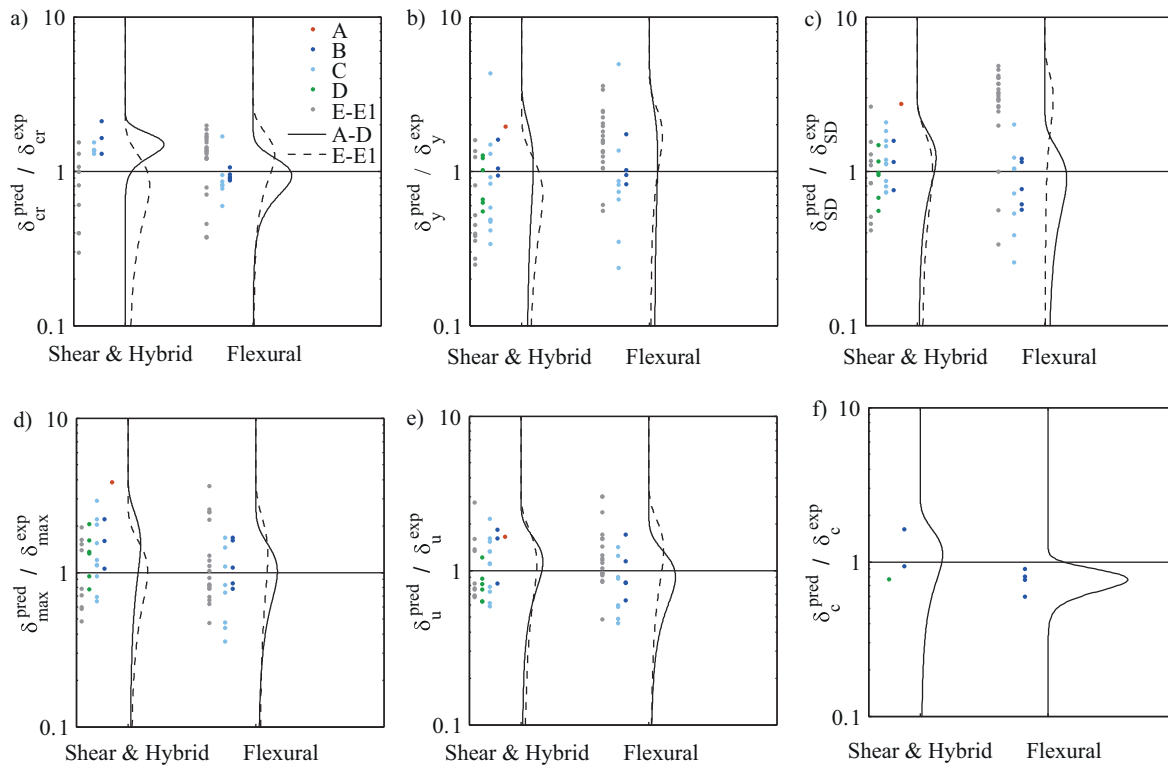


Figure 1.21 – Drift capacity model 2: Ratios of predicted to experimental drift capacities for the six different limit states.

failure is used. The CoVs related to the ultimate deformation capacities of 0.40-0.60 might seem rather large. However, these CoVs are in fact similar to CoVs obtained for deformation capacities of reinforced concrete elements. Grammatikou et al. (2015) reported for reinforced concrete walls CoVs of 0.30 for the yield drift and between 0.30 and 0.50 for the ultimate drift, depending on the model used and the cross section of the wall. For reinforced concrete walls, the smallest CoVs were obtained with empirical models fitted to the data set and the largest CoVs with plastic hinge models (Grammatikou et al., 2015). More advanced analytical models for shear-critical reinforced concrete walls predict the ultimate drift capacity, however, with CoVs of less than 0.20 (Mihaylov et al., 2016). Similar CoVs for ultimate drift capacities are, however, also reached for clay brick masonry walls failing in shear or flexure if the drift capacity is predicted by an advanced analytical model (Petry and Beyer, 2015; Wilding and Beyer, 2017). Analytical models have therefore the potential to reduce the uncertainty related to the prediction of drift capacities and it is recommended to pursue in the future the development of such models for stone masonry walls. The reduction of the uncertainty is of course limited by the aleatoric variability, which—based on the limited data available—can be estimated to result in a CoV of 0.30 for the ultimate drift capacity.

1.8 Summary and conclusions

The application of displacement-based assessment procedures requires robust estimates of the deformation capacity of every structural element. Eurocode 8, Part 3 as well as many other codes worldwide do not provide drift capacities specific to stone masonry walls. The objective of this project was to fill this gap and investigate specifically the drift capacity of stone masonry walls. In addition, the work aimed at providing input not only for the assessment of the ultimate limit state but for a large range of limit states ranging from the onset of cracking to the collapse of the wall. In view of probabilistic assessments, it was further the objective to provide next to median estimates also a measure of the confidence with which this quantity can be predicted. For this purpose, coefficients of variation (CoVs) were determined.

The work is based on a database of 123 shear-compression tests on stone masonry walls, which have been collected from 16 test campaigns documented in the literature; the database is made publically available. Based on these tests, stiffness, strength and deformation capacity were evaluated. The experimentally obtained values were compared to existing estimates and new or improved expressions proposed when this was indicated. More specifically, expressions for the following quantities as well as the corresponding CoVs were put forward:

- Stiffness: New expression for the effective E -modulus for the use in conjunction with a Timoshenko beam element model. Two types of expressions are proposed: 1) Median values and CoVs for the effective E -modulus for each masonry typology. 2) A more refined expression that accounts for the masonry typology, the compressive strength and the axial load ratio.
- Strength: New values for the friction coefficient (Mohr-Coulomb criterion) and the tensile strength (Turnšek and Čačovič criterion). The values account for differences in stone masonry

typologies.

- Drift capacity values for six limit states: Two simple drift capacity models for the ultimate limit state and relationships between other limit state and δ_u . The drift capacity models distinguish between two groups of stone masonry typologies (Group 1: A-D, Group 2: E-E1).
- Aleatoric variability: Aleatoric variabilities of stiffness, strength and drift limits for stone masonry.
- Effect of load history and light retrofit interventions: Factors accounting for the effect of load history (monotonic *vs* cyclic) and light retrofit interventions (mortar injections) on stiffness, strength and drift limits.

The following paragraphs discuss the main findings of this work and identify future research needs.

Typology:

- Following the classification in the Italian code, five typologies of stone masonry were distinguished, which account for the shape of the stones, the number of leaves and their connectivity as well as the stone properties. For regular dressed stone masonry (typology E), a sub-class E1 was introduced that comprises stone masonry walls of typology E with regular shape (ashlar) and dry joints. It was found that ashlar masonry with dry joints shows an increase in stiffness but have little influence on strength and deformation capacity.
- The current database is rather scarce with regard to tests on walls of masonry typology A and D. Due to its wide distribution in existing masonry buildings, further tests would be desirable, in particular, on walls of typology A.

Shear strength of stone masonry walls:

- From the three quantities needed to describe the bi-linear response curve of stone masonry walls (effective stiffness, strength and drift capacity), the strength of the masonry walls can be predicted with the largest confidence. However, the strength equations of the form given in EC8-3 do not predict the failure mode well. For about a quarter of the walls failing in shear, a flexural failure is predicted. To err with regard to the failure mode does not often result in a very large error with regard to the force estimate since shear and flexural capacity can be rather similar. However, it might lead to a considerable error in the drift capacity, if models are used that link the drift capacity to the failure mode (such as the one in EC8-3).
- EC8-3, which application is limited to concrete and brick masonry but in engineering practice often also applied to other masonry typologies, predicts the shear strength of masonry walls by a Mohr-Coulomb criterion assuming a friction coefficient of $\mu = 0.4$. The latter appears to be too large when applied to stone masonry and the shear strength is therefore often overestimated. Using regression analysis on the experimentally determined wall strengths, best estimates of

friction coefficients are calculated for each masonry typologies. Slightly smaller coefficients of variations are obtained if not a Mohr-Coulomb but a Turnšek and Čačovič criterion is used for predicting the shear strength. This criterion needs as input a tensile strength of the masonry. The Italian code MIT (2009); CNR (2013) provides reference values, which predicted the shear strength of the walls in the database very well. However, the CoV which could be desumed from the Italian code, assuming that the given range limits correspond to 16th and 84th percentiles, seems to be too low by a factor of approximately 2. Borri et al. (2015) proposed an expression for the tensile strength which includes the Masonry Quality Index. Regression analysis on the shear strength and Masonry Quality Index of the walls included in the database confirm the expression proposed by Borri et al. (2015).

Effective stiffness of stone masonry walls:

- Estimating the effective stiffness of stone masonry walls is considerably more challenging than estimating their strength and the CoVs of predicted to experimentally determined stiffness is for all masonry typologies approximately 2-3 times larger than the CoVs for the strength. The effective stiffness can, however, be predicted with a slightly better confidence than the elastic wall stiffness. The ratio of effective to elastic stiffness varies greatly but the median ratio is close to 0.5, which corresponds to the value recommended in EC8-3
- Available experimental results suggest that shear deformations contribute significantly to the flexibility of the walls but direct evaluations of the effective shear stiffness from experimental results are scarce. If one assumes a ratio of the shear to the elastic modulus and applies a Timoshenko beam element model, one can back-calculate the effective E -modulus from the wall stiffness. It was found that this effective stiffness depends on the masonry typology, the compression strength and the axial load ratio, i.e., the larger the axial load ratio, the larger the stiffness. The effect of the axial load ratio on the stiffness is not accounted for by modelling recommendations in current codes such as EC8-3, which connect the E -modulus solely to the compression strength, but it has already been identified by other research groups (Vasconcelos, 2005; Bosiljkov et al., 2005). A new analytical expression for the effective E -modulus, which accounts for masonry typology, compression strength and axial load ratio, is proposed.
- It was further investigated if results from material tests lead to an improved estimate of the wall stiffness. The considered material tests were compression tests and dynamic identification tests. Surprisingly none of these results led to an improved estimate of the horizontal wall stiffness. One reason could be that the material tests addressed the E -modulus (i.e. flexural deformations) while shear deformations might contribute significantly to the wall flexibility. Another reason could be that the applied Timoshenko beam model is not appropriate to describe the wall kinematics and therefore the E -moduli that yields the best prediction is not related to a mechanical property of the material.

Drift capacity of stone masonry walls

- For the analysis of the drift capacities, only the cyclic tests were considered. Comparing the results of a monotonic and a cyclic test that were carried out within one test series suggests that the deformation capacity of cyclic tests is approximately only half of the deformation capacity under monotonic loading; this ratio was also observed for brick masonry walls. The available data set did not allow more advanced analyses of the effect of the load history on the drift capacity as the parameters describing the cyclic loading protocol (number of cycles, drift intervals, mean value, ...) were not varied in any of the test campaigns.
- Six different drift limit states were considered; these are (i) the drift at the onset of cracking δ_{cr} , (ii) the drift at yield δ_y , (iii) the drift at maximum force δ_{max} , (iv) the drift at the limit state “Significant damage” $\delta_{SD} = \min(3\delta_{cr}, \delta_{max})$, (v) the drift at ultimate limit state (20% strength drop) δ_u , (vi) the drift at collapse (50% strength drop) δ_c . With the exception of the drift at the onset of cracking, all drift limits were determined from the envelope of the force-drift relationship or its bilinear approximation. The drift at the onset of cracking was, if available, taken from test reports. The drift for which the least information was available is the drift at collapse. Only a very few tests were continued up to collapse and any estimates derived for this limit state need to be considered with great caution. To research this drift limit state further, additional experimental data is needed.
- For analysing the drift capacities, the tests were divided into two groups; the first group comprised walls of typologies A-D and the second walls of typologies E-E1. Given the rather large variability of the drift capacities and the limited number of tests available, a finer analysis did not seem warranted. Next to median values and CoVs for each group and failure mode, also two simple models for the ultimate drift capacity were proposed. The first connects the drift capacity to failure mode and masonry typology and follows therefore the approach of EC8-3 and many other current codes. The second one links the drift capacity to masonry typology, axial load ratio and the factor $H_0/\min(H, L)$ where H_0 is the shear span and H and L the wall height and length, respectively. The two models lead to very similar CoVs. With the exception of the limit state at the onset of cracking, the drift capacities at the other limit states were expressed as a function of δ_u . The drift at the onset of cracking was assigned a constant value $\delta_{cr}=0.20\%$.
- The current drift capacity model as well as the models proposed in this paper are empirical drift capacity models. In future tests, it would be desirable to also develop mechanical drift capacity models, which for brick masonry walls have already led to a considerable improvement in the drift capacity prediction. For this purpose, wall tests with detailed measurements of the displacement fields are necessary. This would also allow to identify better the contributions of shear and flexural deformations to the total deformations and therefore pave the way for improved stiffness estimates. Furthermore, the effect of the stone pattern on the wall response should be investigated and first studies in this regard are currently underway.

Aleatoric variability

- The database contains 18 groups of replicate tests, which were used to estimate the aleatoric variability of stiffness, strength and drift capacities at different limit states. The strength varies in

general the least (CoV=0.1). Stiffness and drift capacities vary more (CoV=0.2-0.3). Only the drift at the onset of cracking seems to lead to a smaller CoV (CoV=0.1). None of the replicate tests was continued up to collapse and therefore the aleatoric variability could not be determined for δ_c . From the available data, it was not possible to identify the effect of the masonry typology on the aleatoric variability. Also, all but one group of replicate tests were laboratory tests, which might not necessarily reproduce the aleatoric variability in real buildings. From the available data no significant difference between laboratory and in-situ tests could be identified. In future studies it would therefore be interesting to investigate the variation of aleatoric variability with masonry typology and to conduct further replicate in-situ tests.

Effect of retrofit interventions on drift capacity

- Also included in the database are tests with minor retrofit intervention (mortar injections or reinforcement through the wall thickness to improve the connection between the leaves). By comparing walls with mortar injections to their unstrengthened counterparts, the effect of the retrofit interventions could be identified. For stiffness and strength, such factors are already available in the Italian code (MIT, 2009) and these were confirmed by the results obtained here. As a novelty, factors for the drift capacity were derived. The results showed that the ultimate drift capacity can increase by a factor of 3-6; the increase is particularly significant if the failure mode changes from shear to flexure. The experimental data on the effect of retrofit interventions is, however, still rather scarce and more data necessary. Mechanical drift capacity models, once they are available, might allow to predict the effect of retrofit interventions without testing all possible configurations.

2 Treatment of epistemic uncertainty through a Point-Estimate Method

This chapter represents the submitted version of the article:

Vanin, F., Beyer, K. (2019). "Incorporating epistemic uncertainty in the assessment of an existing masonry building through a Point Estimate Method". Submitted to *Earthquake Engineering and Structural Dynamics*.

The formatting and numbering of equations, tables and figures have been updated to this document. The contributions of the first author are: performing the analyses and writing the article. Contributions of the second and third authors: supervision of the first author, co-writing the article.

Abstract

The seismic assessment of existing buildings is affected by several sources of uncertainty, primarily related to the material properties and the displacement capacity of elements. Accounting explicitly for such uncertainties when modeling the structure introduces, however, an increase of complexity and numerical cost, often conflicting with the requirements of the engineering practice. To investigate the effectiveness of practice-oriented methods for the consideration of model uncertainty, this work proposes the use of a logic tree, and, for a further reduction of the numerical cost, of a Point Estimate method. To optimize the performance of both, a moment-matching approach is adopted for the determination of the sampling points of the numerical random variables and of the weight to be attributed to each analysis. Using a historical stone masonry building as case-study, modeled through an equivalent-frame, the proposed methods are compared to other simplified approaches (first-order second-moment, response surface method) and benchmarked against more demanding Monte Carlo simulations. The Point Estimate Method, in this case, optimally balanced an accuracy and a complexity compatible with practical applications, requiring a moderate number of pushover analyses. Furthermore, the effect of spatial correlation of material and element properties is investigated, and an approach is proposed for its incorporation in simplified methods. The uncertainty in the displacement capacity, derived from a recent database of stone masonry wall tests, proved to be the major contribution to the total epistemic uncertainty, whose magnitude was comparable, for

near-collapse limit state, to typical record-to-record variability.

2.1 Introduction

The seismic assessment of existing buildings is a fundamental step for evaluating the seismic risk and planning of retrofit interventions. Among existing structures, masonry buildings, and more specifically historical masonry buildings, are often responsible for a large part of earthquake casualties, and damage to this type of buildings heavily affects the functionality of entire city centers, as seen in recent earthquakes (central Italy, 2016 (Sorrentino et al., 2018)). The seismic assessment of such buildings, however, is a complex task affected by several sources of uncertainty that should be properly accounted for. Because the application of probabilistic assessment procedures in engineering practice is mainly limited by cost, simplified approaches that incorporate these uncertainties and require only a limited number of analyses are desirable.

Uncertainties that affect the seismic assessment of existing buildings are generally categorized as aleatory randomness, mainly attributed to ground motion variability, and epistemic uncertainty, stemming from incomplete knowledge of the structure and from the use of approximated or incorrect models. Sorting the different sources of uncertainty into one specific category can be subjective; however, in the following, all uncertainty related to modelling choices is referred as epistemic and the one related to the ground motion as aleatory. The role of both sources of uncertainty in seismic assessment has been investigated in the literature, mainly using incremental dynamic analysis (IDA) or similar nonlinear time-history analyses, in both reinforced concrete (Lee and Mosalam, 2005; Liel et al., 2009; Dolšek, 2009; Vamvatsikos and Fragiadakis, 2010) and masonry buildings (Rota et al., 2010). Aleatory uncertainty has been observed as a major cause of response variability (Lee and Mosalam, 2005), though other sources of uncertainty are relevant for limit states closer to collapse. Studies on reinforced concrete (RC) and steel structures (Liel et al., 2009; Dolšek, 2009; Vamvatsikos and Fragiadakis, 2010) identified the uncertainty related to the displacement capacity of the structural elements to be a key source of response variability. The epistemic uncertainty in masonry buildings is particularly relevant, compared to other building types, as it includes the choice itself of adequate modeling strategies (Bracchi et al., 2015) and the quantification of material properties and displacement capacities, based on a scarcer amount of experimental results, which comprise a wide range of different masonry typologies. For the determination of the displacement capacity, this study will use a recently collected database on shear-compression tests (Vanin et al., 2017b), from which experimentally observed distributions were derived.

The epistemic uncertainty in masonry buildings stemming from modeling assumptions was considered by Tondelli et al. (Tondelli et al., 2012), who evaluated the confidence factors proposed in the Italian code using a logic tree approach to simulate the sequence of decisions that an engineer should take, similarly to what proposed by Franchin et al. (Franchin et al., 2010) for RC buildings. With regard to masonry buildings, Rota et al. (Rota et al., 2014a) used a similar approach to calibrate a global safety coefficient. Cattari et al. (Cattari et al., 2015) proposed a logic tree method to account for epistemic uncertainties not treated as numerical aleatoric variables, while the uncertainty related to

the numerical variables was accounted for through a confidence factor calibrated based on a sensitivity analysis. The use of an intuitive logic tree strategy (Bracchi et al., 2015; Tondelli et al., 2012; Franchin et al., 2010; Rota et al., 2014a; Cattari et al., 2015) poses the problem, however, of determining the number of branches to consider and the weights to assign to them. To solve this problem, we present herein a derivation of optimal branches and weights that can be used when the uncertainty is related to numerical parameters.

For the treatment of parameter uncertainty, more refined methods than a logic tree approach are also available. A recently issued document by the Italian National Research Council (CNR) (CNR, 2013; Pinto and Franchin, 2014) provides guidelines for the application of probabilistic assessment procedures, which could enter future code revisions. The most general method is a Monte Carlo simulation, although expensive from a numerical point of view and therefore mainly used for research. Monte Carlo simulations coupled with pushover analyses were used by several authors both for masonry (Tondelli et al., 2012; Rota et al., 2010; Parisi and Augenti, 2012) and RC buildings (Dolšek, 2012; Fragiadakis and Vamvatsikos, 2010). Techniques that partly reduce the considerable numerical cost of Monte Carlo simulations are available, including sampling techniques like Latin hypercube sampling (LHS), as used by Dolšek (Dolšek, 2009) for the assessment of a four-story RC building, in combination to the IDA to account for ground motion variability. Using the same method, a simplified approach was proposed by the same author (Dolšek, 2012), in which the IDAs on the complete structure were substituted by non-linear dynamic analyses of an equivalent single degree of freedom (SDOF) system.

To further reduce the number of simulations required for a probabilistic assessment, several simplified methods were developed. Some of these, based on few simulations, derive surrogate models—typically first- or second-order response surfaces—to approximate the response of a computationally demanding structural model. Such approaches can provide a direct estimate of the distribution of the response (Franchin et al., 2003), provided that the response surface to be approximated is sufficiently regular. The CNR document (CNR, 2013) suggests the use of these methods in combination with a pushover analysis when less computationally expensive methods are sought. Liel et al. (Liel et al., 2009) used a limited number of IDAs to build a quadratic response surface, from which the the median collapse capacity of a structure can be estimated. Using such surrogate model, the collapse fragility could be derived inexpensively through a Monte Carlo analysis. Another approach was proposed by Giovanis et al. (Giovanis et al., 2015), who used neural networks as surrogate models.

A simpler method with a significantly lower computational cost is the first-order second-moment (FOSM) method, based on a Taylor series expansion around the mean of the response function. Several authors used this approach and benchmarked the results against Monte Carlo simulations (Liel et al., 2009; Dolšek, 2009; Vamvatsikos and Fragiadakis, 2010). Celarec and Dolšek (Celarec and Dolšek, 2013) used pushover analysis combined with FOSM and LHS to simplify the incorporation of epistemic uncertainty. They had similar observations to Liel et al. (Liel et al., 2009), however, in that the FOSM method fails to capture the shift of the mean response from that of the deterministic model based on the median values of all random variables. An even simpler method was developed by Fajfar and Dolšek (Fajfar and Dolšek, 2012) for use in engineering practice that estimates the annual probability of failure through one pushover analysis and reference dispersion measures of the variability introduced

by ground-motion and epistemic uncertainty, derived from the literature. With the same objective, Kosič et al. (Kosič et al., 2014) proposed a standard pushover analysis on a deterministic model, introducing uncertainty only at the level of the parameters defining the idealized bilinear curve (effective stiffness, strength, and displacement capacity), which are treated as random variables. Both approaches, however, require variation coefficients that must be calibrated for each building typology, and share with the FOSM the drawback of assuming that the median response corresponds to the response of the median model, which is not always true.

Alternatively, among methods requiring a limited number of model evaluations, point estimate methods (PEM) based on statistical moment matching techniques can be used. The principal idea of moment-matching is to replace a set of continuous random variables with a discrete set of point evaluations and weights, replicating as many statistical moments of the original distribution as possible. A common PEM proposed by Rosenblueth (Rosenblueth, 1975) was applied in the field of seismic assessment by Vamvatsikos and Fragiadakis (Vamvatsikos and Fragiadakis, 2010; Fragiadakis and Vamvatsikos, 2010). A more refined PEM was investigated by Ching et al. (Ching et al., 2009), who found that PEM is more accurate at the same numerical cost than the more commonly adopted FOSM method. The accuracy and the intuitiveness of PEMs render their application to seismic assessment promising. Particularly, if a PEM is combined with nonlinear static analyses, the numerical cost remains limited and within the possibilities of the professional practice, where nonlinear time history analysis methods are often too complex and demanding. When compared to a deterministic analysis, PEMs require more than one analysis but provide a better view of possible failure modes, therefore allowing a deeper insight on the seismic response of a building.

In this paper, a PEM proposed by Franceschini et al. (Franceschini et al., 2012) that solves some of the drawbacks of previously proposed PEMs, including the possibility of estimating a negative variance, is tested in a first application to structural engineering. Such method is presented in Section 2.2 together with other approaches with a similar computational cost (FOSM, response surface method, LHS on a very limited sample). In Section 2.4 such methods are benchmarked against Monte Carlo simulations of a case-study building, introduced in Section 2.3. The displacement capacity of the structural elements is found to be the major source of epistemic uncertainty when the near-collapse limit state is assessed, showing a variability of a comparable order of magnitude to the ground motion randomness. Furthermore, it is shown that the spatial distribution between material properties among the elements of the structure also has a significant influence on the results, and a simplified approach for its consideration is proposed.

2.2 Treatment of epistemic uncertainty

The most general way of treating epistemic uncertainty, in the context of seismic assessment of buildings, is a Monte Carlo simulation, which is, however, heavily costly from the numerical point of view, as it requires a large number of simulations to be performed. Several methods have been proposed in the literature with the objective of reducing such numerical cost. This section briefly presents the essential features of the ones that are used and compared in the following, i.e. the Latin

hypercube sampling, the response surface method, the first-order-second-moment method, and the point estimate method.

2.2.1 Latin Hypercube Sampling (LHS)

A method that can improve the sampling of a set of random variables is the Latin hypercube sampling. It is based on a Latin square scheme, which is a method for sampling one and only one element per row and column (Figure 2.1b) of a two-dimensional grid representing all possible combinations of a set of discrete values of two independent random variables x_1 and x_2 . The Latin hypercube extends this same concept to a higher number of dimensions, and is a well-known method for reducing the number of required analyses in simulations (Vořechovský and Novák, 2003). Each random variable X_i is sampled N_{Sim} times, where N_{Sim} is the number of simulations to be performed. The values at which the variables are sampled are defined by their probability distribution, dividing their domain into equiprobable intervals. The j -th value of X_i can be defined by Equation 2.1 if a median value of the interval is selected, or by Equation 2.2 if mean values are sampled; F_i^{-1} is the inverse cumulative distribution function (CDF) of the random variable, and f_i is its probability density function (PDF). The latter approach would be recommendable in the tails of the distribution (Vořechovský and Novák, 2003), while the difference between median and mean is typically negligible for the body of the distribution (Figure 2.1a).

$$x_{i,j} = F_i^{-1} \left(\frac{j - \frac{1}{2}}{N_{Sim}} \right) \quad (2.1)$$

$$x_{i,j} = N_{Sim} \int_a^b x \cdot f_i(x) dx, \quad a = F_i^{-1} \left(\frac{j-1}{N_{Sim}} \right), \quad b = F_i^{-1} \left(\frac{j}{N_{Sim}} \right) \quad (2.2)$$

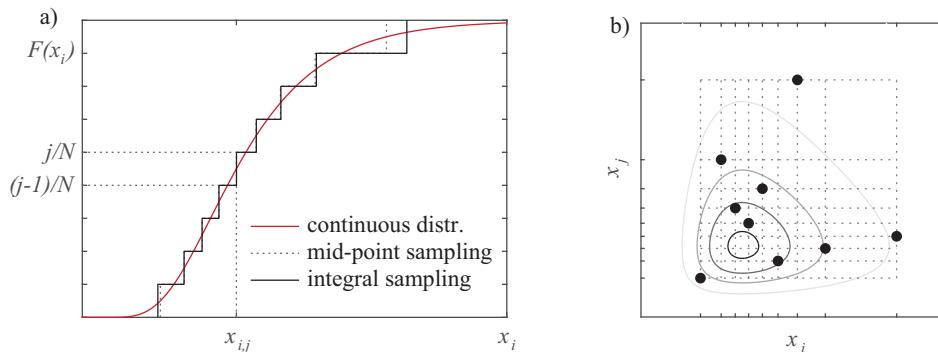


Figure 2.1 – Latin hypercube sampling (LHS): (a) Sampling one random variable, (b) and distribution of two random variables after optimizing the sample matrix.

Once the samples of the random variables are generated, they are combined by random perturbations to avoid an undesired correlation that can be generated if the initial order is maintained. This requires maintaining the structure of the sample as a Latin hypercube and proceeding until the correlation between the variables corresponds to the desired value. If the variables are independent, the combination minimizing the correlation between the variables is searched. The process can be performed through an optimization method called simulated annealing (Vořechovský and Novák, 2003), which minimizes the difference between the correlation matrix \mathbf{S} of the sample and the prescribed correlation matrix \mathbf{K} containing the correlation coefficients between the variables. A measure of the difference between the two matrices can be defined by the norm E defined in Equation 2.3, where N_V is the number of random variables of the problem.

$$E = \sqrt{\sum_{i=1}^{N_V-1} \sum_{j=i+1}^{N_V} (S_{ij} - K_{ij})^2} \quad (2.3)$$

The optimization algorithm proceeds by applying a perturbation of row and column indexes at each step in one randomly selected variable and calculating the norm E for the new arrangement. If the norm decreases, the new sample is accepted. However, for the algorithm to find a global minimum that ignores local minima, there must exist a possibility of also accepting some configurations for which the norm E increases. The possibility of accepting a configuration that does not improve the previous solution is determined by the sign of the random variable Z defined in Equation 2.4, where R is a uniformly distributed variable in the interval $(0,1)$, T is a so-called temperature parameter, and ΔE is the difference of the norm E between the current and the previous configuration.

$$Z = e^{-\Delta E/T} - R \quad (2.4)$$

This probability of accepting "worse" solutions to exit local minima is higher in the beginning of the algorithm and is progressively reduced once the solution space has been widely explored through a decrease of the parameter T . The process is stopped when the temperature parameter reaches a limit value, which has to be set depending on the number of solutions explored. Reference parameters that define the decrease of T are provided in Dolšek (Dolšek, 2009).

Applying LHS to modeling epistemic uncertainty through a Monte Carlo analysis is straightforward. Once the set of random variables modeling the uncertainties as well as the correlations between them are defined, LHS is used to generate an optimal sample of realizations, each corresponding to a structural model to be analyzed that has a specific set of values assigned to the variables. The rest of the analysis is a Monte Carlo simulation, from which the mean response and its variability due to uncertainties can be directly extracted. This type of sampling, compared to a completely randomized sampling, can reduce the required analyses from some hundreds to a few tens.

2.2.2 Response Surface Method (RSM)

A class of approximated probabilistic methods included in the recently issued CNR recommendations (CNR, 2013) are response surface methods (RSM). These methods evaluate the response function at a limited number of points, generally set according to criteria derived from experimental designs, and fit a linear or quadratic model surface that is used to evaluate the response variance. Full factorial schemes require the evaluation of m^N points if N random variables are sampled at m levels.

The number of levels chosen for each variable and their dispersion with respect to the average can be based on different optimality criteria. Two-level designs are the most common, as the number of simulations increases rapidly for a high number of random variables N . The two levels correspond to $\mu_i \pm \sigma_i$, where μ_i is the mean and σ_i is the standard deviation of the random variable i . Equivalently, the 16th and 84th fractiles of the distribution are sampled in a general formulation for non-normally distributed variables, as is also suggested in the CNR document. However, for $N > 5-6$, the application of full factorial designs becomes demanding, if not unfeasible. Partial schemes reduce the required simulations though lose some information on the coupled effects of the random variables. Star designs, designs in which one variable is varied on two levels at a time while all remaining variables are kept to their mean value, can reduce the required number of simulations to $2N + 1$.

In linear response surface methods, like the one proposed by the CNR, the function $g(x_1, \dots, x_N)$ defines the performance of the building as a function of N random variables and is approximated by the linear model $\hat{g}(x_1, \dots, x_N)$, defined as:

$$g(x_1, \dots, x_N) \approx \hat{g}(x_1, \dots, x_N) = \alpha_0 + \sum_{k=1}^N \alpha_k x_k \quad (2.5)$$

The coefficients α_i can be determined through a regression analysis. The matrix \mathbf{Z} contains the values of the input variables for all the points in the adopted experimental design scheme; the i -th row is $Z_i = [1, x_{1,i}, \dots, x_{N,i}]$. The column vector \mathbf{Y} contains the corresponding results of the nonlinear analysis, meaning $Y_i = g(x_{1,i}, \dots, x_{N,i})$. The coefficients of the regression analysis can be obtained from:

$$\boldsymbol{\alpha} = [\alpha_0, \alpha_1, \dots, \alpha_N]^T = (\mathbf{Z}^T \mathbf{Z})^{-1} \mathbf{Z}^T \mathbf{Y} \quad (2.6)$$

From this approximation, the expected value μ_g and variance σ_g^2 of the function $g(x_1, \dots, x_N)$ can be derived from the expressions in Equations 2.7-2.8, where the operator $E[\cdot]$ is the expected value. The correlation coefficient between the i -th and j -th random variables is ρ_{ij} , while the term σ_ε^2 , accounting for the model error, is the variance of the residuals, indicating the difference between the true response function and its linear approximation, evaluated at the points where the simulation was performed.

$$\mu_g = E[g(x_1, \dots, x_N)] \approx E[\hat{g}(x_1, \dots, x_N)] = \alpha_0 + \sum_{k=1}^N \alpha_k E[x_k] \quad (2.7)$$

$$\sigma_g^2 = E[(g(x_1, \dots, x_N) - \mu_g)^2] \approx \sum_{i=1}^N \sum_{j=1}^N \rho_{ij} \alpha_i \alpha_j \cdot \sigma_{x_i}^2 \sigma_{x_j}^2 \quad (2.8)$$

The evaluation of the expected value and the variance of the output is exact only if the true response function $g(x_1, \dots, x_N)$ is linear or quadratic response functions, depending on the order of the adopted response surface. If the quality of the approximation of the response function decreases, for a highly nonlinear response, the model error can become relevant. The application of RSM to existing concrete structures has been proposed by Franchin et al. (Franchin et al., 2003); specific provisions for masonry buildings and the application to one case study are included in the CNR document.

2.2.3 First-Order Second-Moment method (FOSM)

The FOSM method is another simple method often used in reliability analyses of buildings to estimate the parameters of the response distribution. FOSM uses a Taylor series expansion, centered on the mean of all model random variables, to approximate the response function $g(x)$ and derive an expression for its expected value and variance. The expansion is given in Equation 2.9, where \mathbf{X} is the vector of the random variables and $\bar{\mathbf{X}}$ is the vector of the mean values of all variables.

$$g(\mathbf{X}) \approx g(\bar{\mathbf{X}}) + \sum_{k=1}^N (x_k - \mu_{x_k}) \left. \frac{\partial g}{\partial x_k} \right|_{\bar{\mathbf{X}}} + \frac{1}{2} \sum_{k=1}^N (x_k - \mu_{x_k})^2 \left. \frac{\partial^2 g}{\partial x_k^2} \right|_{\bar{\mathbf{X}}} \quad (2.9)$$

If a first order expansion is considered (Lee and Mosalam, 2005), the expected value of the response $E[g(\mathbf{X})]$ is calculated as $g(E[\mathbf{X}])$, while the gradient of $g(\mathbf{X})$ is used to compute the variance of the response associated with the modeling uncertainties. In the frequent case in which a closed form expression of the response function is not available, the gradients (and curvatures, when needed) are obtained through a set of perturbations of single parameters, applying a finite difference approximation. In Equation 2.10, g^{k+} and g^{k-} indicate the response evaluation for a positive and negative perturbation of the parameter x_k , and g^0 is the central evaluation, where all variables are set to their mean value.

$$\frac{\partial g}{\partial x_k} \approx \frac{g^{k+} - g^{k-}}{x_k^+ - x_k^-}, \quad \frac{\partial^2 g}{\partial x_k^2} \approx \frac{g^{k+} - 2g^0 + g^{k-}}{(x_k^+ - x_k^-)/2} \quad (2.10)$$

One issue associated with FOSM lays in the truncation of the Taylor series at the first order, which can limit the accuracy and leads to the assumption that the mean response is associated with the average of all random parameters. For nonlinear response functions, the shift of the expected value calculated with this approach can be relevant, as was shown by Liel et al. (Liel et al., 2009). A more refined estimate

of the mean and variance, however, can be obtained through the same method if second-order terms are included in the Taylor expansion, ignoring mixed second-order derivatives (Vamvatsikos and Fragiadakis, 2010), as shown in Equation 2.9. In this case, a correction term, depending on the curvature of the response function, can be applied to the estimate of the mean response.

$$\mu_g \approx g^0 + \frac{1}{2} \sum_{k=1}^N \left. \frac{\partial^2 g}{\partial x_k^2} \right|_{\bar{\mathbf{x}}} \sigma_k^2 \quad (2.11)$$

$$\sigma_g^2 \approx \sum_{k=1}^N \left(\left. \frac{\partial g}{\partial x_k} \right|_{\bar{\mathbf{x}}} \right)^2 \sigma_k^2 \quad (2.12)$$

In the same framework, more advanced approaches are first- and second-order reliability methods (respectively, FORM and SORM). They differ from the simpler FOSM method in that the linearization of the response function is centered on a generic point on the failure surface (named the "design point") and not forced to the mean values of the random variables. However, finding the unknown design point, i.e. the point associated with the highest probability of failure, requires a more complex procedure for which iterative methods can be adopted. Despite the loss of the original simplicity, these approaches provide a more refined reliability evaluation. The FORM corresponds to the exact solution for linear response functions and normal independent random variables, while a better approximation of highly nonlinear functions, although at the cost of a higher computation time, is provided by second-order approximations. However, due to the much lower numerical cost, the FOSM method has been more often applied to the seismic assessment of buildings (Lee and Mosalam, 2005; Zareian and Krawinkler, 2007; Haselton, 2006).

2.2.4 Point Estimate Methods (PEM)

Alternatively, integration schemes can be applied to evaluate the integrals defining the expected values and central moments of a function of several random variables. Quadrature schemes are suitable for this because they limit the required number of evaluations of the implicit function. In this context, PEMs, which use a limited number of evaluations of the model function at a set of points replicating the probability distribution of the random variables, are efficient approximation methods. The basic concept underlying all PEMs is the approximation of a continuous random variable through a discrete set of m evaluation points and related integration weights such that the statistical moments of the discrete distribution match the ones of the original continuous distribution. For this reason, they are sometimes indicated as moment-matching methods. To calculate this, if a function of one random variable is written as a Taylor series, it is possible to write its expected value as:

$$E[g(X)] = g(\mu_X) + \sum_{k=1}^{\infty} \frac{1}{k!} \left. \frac{\partial^k g}{\partial x^k} \right|_{\mu_X} E[(X - \mu_X)^k] = g(\mu_X) + \sum_{k=1}^{\infty} \frac{1}{k!} \left. \frac{\partial^k g}{\partial x^k} \right|_{\mu_X} \mu_X^{(k)} \quad (2.13)$$

The central moments of order n of the random variable are named $\mu_X^{(n)}$. If the original random variable X is substituted by a different distribution consisting of a set of discrete points and weights (Figure 2.2) matching the first k central moments of X , then the expected value of the two Taylor series expansions of a function of the old and the new distributions truncated to the k -th term would be equal. In other words, if a Taylor series expansion of order k exactly approximates a function of one random variable, the substitution of the random variable with a discrete PDF, defined by a set of points and relative weights having the same first k central moments as X , would yield an exact estimation of the expected value of the function. Similar considerations can be made for the variance of the function, which would, however, require the correct estimation of $2k$ central moments. The same conclusions can be derived for functions of multiple random variables through a multivariate Taylor series expansion (Ching et al., 2009).

This approach was applied by Miller and Rice (Miller and Rice, 1983), who identified it as a Gaussian quadrature scheme (as discussed in more detail by Christian and Baecher (C. and B., 1999)) and proposed a numerical procedure to solve it. The position x_i of the sampling points a function of a parameter ξ_i and the mean μ_X and standard deviation σ_X of the random variable, can be defined as:

$$x_i = \mu_X + \xi_i \sigma_X \quad (2.14)$$

If a set of m points and the relative weights p_i of the substitute PDF have to be determined, it is possible to write $2m$ conditions:

$$\left\{ \begin{array}{l} p_1 + p_2 + \dots + p_k = 1 \\ p_1 \xi_1 + p_2 \xi_2 + \dots + p_k \xi_k = 0 \\ p_1 \xi_1^2 + p_2 \xi_2^2 + \dots + p_k \xi_k^2 = \frac{\mu_X^{(2)}}{\sigma_X^2} = 1 \\ \vdots \\ p_1 \xi_1^{2m-1} + p_2 \xi_2^{2m-1} + \dots + p_k \xi_k^{2m-1} = \frac{\mu_X^{(2m-1)}}{\sigma_X^{2m-1}} \end{array} \right. \quad (2.15)$$

The first equation in Equation 2.15 forces the sum of all weights to 1; successive equations force the equivalence of central moments up to the order $2m - 1$ starting from the first central moment equal to zero, i.e. the equivalence of the expected value of the continuous and discrete distributions. The optimal sample points can be found as the roots of the m -th order polynomial defined as:

$$\pi(\xi) = C_0 + C_1 \xi + C_2 \xi^2 + \dots + C_{m-1} \xi^{m-1} + \xi^m = 0 \quad (2.16)$$

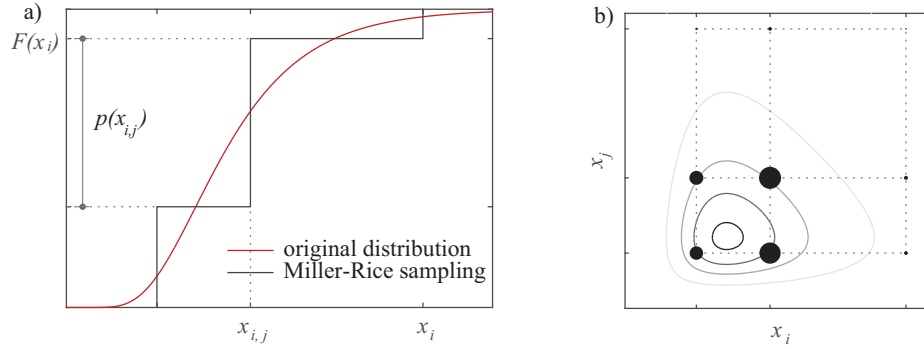


Figure 2.2 – Point estimate method (PEM) with sampling according to Miller and Rice (Miller and Rice, 1983). (a) A sampling of one random variable on three levels, (b) and a full factorial integration scheme with different weights assigned to each combination.

where the coefficients C_i are determined by the solution of the linear system:

$$\begin{bmatrix} 1 & 0 & \frac{\mu_X^{(2)}}{\sigma_X^2} & \dots & \frac{\mu_X^{(m-1)}}{\sigma_X^{m-1}} \\ 0 & \frac{\mu_X^{(2)}}{\sigma_X^2} & \frac{\mu_X^{(3)}}{\sigma_X^3} & \dots & \frac{\mu_X^{(m)}}{\sigma_X^m} \\ \vdots & \vdots & \vdots & \ddots & \vdots \\ \frac{\mu_X^{(m-1)}}{\sigma_X^{m-1}} & \frac{\mu_X^{(m)}}{\sigma_X^m} & \dots & \dots & \frac{\mu_X^{(2m-2)}}{\sigma_X^{2m-2}} \end{bmatrix} \begin{bmatrix} C_0 \\ C_1 \\ \vdots \\ C_{m-1} \end{bmatrix} = - \begin{bmatrix} \frac{\mu_X^{(m)}}{\sigma_X^m} \\ \frac{\mu_X^{(m+1)}}{\sigma_X^{m+1}} \\ \vdots \\ \frac{\mu_X^{(2m-1)}}{\sigma_X^{2m-1}} \end{bmatrix} \quad (2.17)$$

The derivation of such equations is presented in detail in Miller and Rice (Miller and Rice, 1983). Once the sample points are determined, the weights corresponding to each point can be determined in a third step by solving:

$$\begin{bmatrix} 1 & 1 & \dots & 1 \\ \xi_1 & \xi_2 & \dots & \xi_m \\ \vdots & \vdots & \ddots & \vdots \\ \xi_1^{m-1} & \xi_2^{m-1} & \dots & \xi_m^{m-1} \end{bmatrix} \begin{bmatrix} p_0 \\ p_1 \\ \vdots \\ p_m \end{bmatrix} = \begin{bmatrix} 1 \\ 0 \\ \vdots \\ \frac{\mu_X^{(m-1)}}{\sigma_X^{m-1}} \end{bmatrix} \quad (2.18)$$

Since the procedure is conceptually a quadrature integration method, the weights assigned to some points can in the general case be negative and hence should not be interpreted as probabilities (Ching et al., 2009). However, for rather regular distributions, like the variables involved in the assessment of an existing building, it is advisable to adopt point locations that belong to a physically significant range and positive weights, even at the cost of a lower order of approximation. The user also needs to check if all basic assumptions are verified. For example, global models relating failure only to the exceedance of limit element drifts can fail at correctly predicting the behavior of a building when extremely large drift limits are imposed, since other failure modes could become relevant (e.g. the

collapse of floor beams) that are not accounted for. Such problem can be solved by imposing the positions of some points and solving a reduced system of equations by the same method, considering that for every applied condition, the distribution moments can be matched to one less order. The method in Equations 2.15-2.18 represent the generic case; however, for practical applications, a two- or three-point discretization is usually applied. These equations, in the case of a two-point discretization, provide the solution:

$$\left\{ \begin{array}{l} \xi_1 = \frac{\lambda}{2} - \sqrt{\left(\frac{\lambda}{2}\right)^2 + 1} \\ \xi_2 = \frac{\lambda}{2} + \sqrt{\left(\frac{\lambda}{2}\right)^2 + 1} \end{array} \right. \quad \left\{ \begin{array}{l} p_1 = \frac{\xi_2}{\xi_2 - \xi_1} \\ p_2 = 1 - p_1 \end{array} \right. \quad (2.19)$$

where $\lambda = \frac{\mu_x^{(3)}}{\sigma_x^3}$ is the skewness. In the case of a normal distribution, as well as for all symmetric distributions for which $\lambda = 0$, the optimal sampling corresponds to points at $\pm 1\sigma$, with both weights equal to 1/2. For a three-point discretization, the solution of the system is not available in closed form. However, an expression for the points and weights can be derived by fixing it such that one point is always sampled at the mean value of the variable, which is also useful for applying schemes that reduce the combinations to be analyzed. This allows the correct estimation of the first four moments of the distribution (where $\kappa = \frac{\mu_x^{(4)}}{\sigma_x^4}$ represents the kurtosis) using:

$$\left\{ \begin{array}{l} \xi_1 = \frac{\lambda}{2} - \sqrt{\kappa - \frac{3}{4}\lambda^2} \\ \xi_2 = 0 \\ \xi_3 = \frac{\lambda}{2} + \sqrt{\kappa - \frac{3}{4}\lambda^2} \end{array} \right. \quad \left\{ \begin{array}{l} p_1 = \frac{1 + \xi_2\xi_3}{(\xi_1 - \xi_2)(\xi_1 - \xi_3)} \\ p_2 = 1 - p_1 - p_3 \\ p_3 = \frac{1 + \xi_1\xi_2}{(\xi_3 - \xi_2)(\xi_3 - \xi_1)} \end{array} \right. \quad (2.20)$$

The term in the radical is always positive since the kurtosis and skewness respect the condition $\kappa \geq \lambda^2 + 1$. For a normal distribution, the sampled points would be at $\pm\sqrt{3}\sigma$, and the weights of the extreme points would be equal to 1/6. The mathematical optimal position of the evaluation points given by Equations 2.19-2.20, however, may result in very small weights and/or evaluation points located outside the defined region of the variable (or outside a region considered of practical interest). If the position of all evaluation points is fixed *a priori* by choice of the analyst, higher errors in the approximation of the original distribution are introduced, leading to an exact estimation of $m - 1$ moments instead of $2m - 1$ moments. The weights to be assigned to each fixed evaluation point can be determined by Equations 2.19-2.20 for cases of a two- or three-point sampling scheme that fix the values of $\xi_1 \dots \xi_m$. If, on the other hand, the analyst chooses to impose the same weight to each analysis

as a simplifying assumption, the set of evaluation points can be obtained as:

$$\begin{cases} \xi_1 = -1 \\ \xi_2 = +1 \end{cases}, \quad p_1 = p_2 = \frac{1}{2} \qquad \begin{cases} \xi_1 = -\sqrt{3/2} \\ \xi_2 = 0 \\ \xi_3 = +\sqrt{3/2} \end{cases}, \quad p_1 = p_2 = p_3 = \frac{1}{3} \quad (2.21)$$

Several PEMs (Zhao and Ono, 2000; Hong, 1998; Li, 1992) were proposed, starting from the work of Rosenblueth (Rosenblueth, 1975, 1981), that were distinguished from each other by the number of points used to approximate the distribution of the input variables, the number combinations used in the multivariate case, and the way in which moments were computed if reduced schemes were applied. Indeed, if the problem was defined by N random variables, the exact Gaussian quadrature scheme would require evaluating the function for all the combinations of values of the sampled distributions, i.e. for a full factorial scheme involving m^N evaluations if all variables were sampled on m levels (Figure 2.2b). Clearly, the numerical cost becomes overly demanding for a high number of random variables, as also underlined for RSM. To overcome this drawback that would notably limit the application of PEMs, alternative reduced schemes were proposed by Hong (Hong, 1998), Li (Li, 1992), and Zhao and Ono (Zhao and Ono, 2000) to reduce the number of evaluations of the function up to $2N + 1$. In the same framework, Franceschini et al. (Franceschini et al., 2012) proposed an improved method based on a Taylor series expansion of the variance function to overcome some of the problems of other PEMs, such as the possibility of estimating a negative variance in the case of highly nonlinear problems or the oversimplification stemming from a two-point discretization. This method, developed for independent random variables with potentially asymmetric distributions, requires the evaluation of the response at a central point corresponding to the mean values of all variables plus $2N$ points, which are obtained by setting one variable at a time to its upper and lower level, i.e. $x_{i,1}$ and $x_{i,3}$ as defined by Equation 2.20.

With a notation equivalent to the one used in Equation 2.10, when the variable x_i is perturbed to its upper and lower levels $x_{i,1}$ and $x_{i,3}$ and the other variables are kept to their mean value, the evaluations of the response g are g^{i-} and g^{i+} , respectively. The estimated moments can be calculated as:

$$\mu_g = \left[1 - \sum_{i=1}^N (p_{i-} + p_{i+}) \right] g^0 + \sum_{i=1}^N (p_{i-} g^{i-} + p_{i+} g^{i+}) \quad (2.22)$$

$$e_i = p_{i-} g^{i-} + p_{i+} g^{i+} - (p_{i-} + p_{i+}) g^0 \quad (2.23)$$

$$\sigma_g^2 = \sum_{i=1}^N \left[p_{i-} (g^{i-} - g^0)^2 + p_{i+} (g^{i+} - g^0)^2 - e_i^2 (p_{i-} + p_{i+}) \right] \quad (2.24)$$

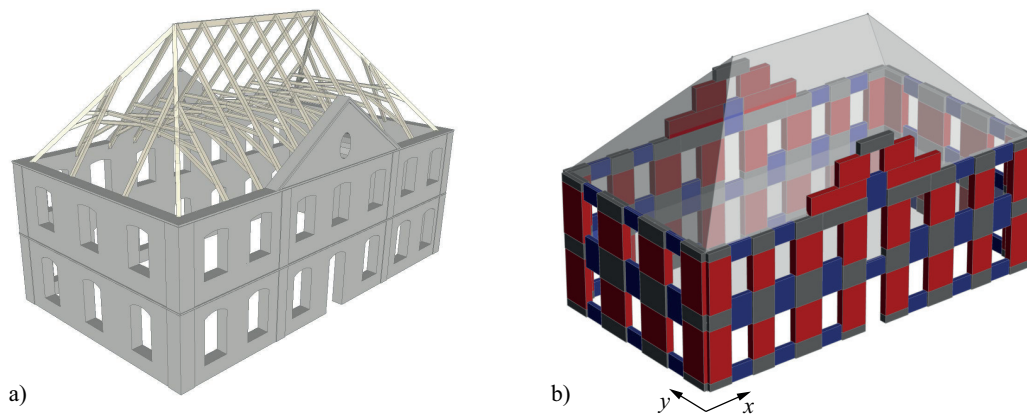


Figure 2.3 – (a) Scheme of the Holsteiner Hof building with (b) adopted macroelement structural model. Piers are represented in red, spandrels in blue, and rigid nodes in grey.

2.3 Modeling uncertainties in a historical stone masonry building

The performance of the presented PEM in estimating the distribution of the seismic response of an existing structure was investigated by applying it to the assessment of a historical stone masonry building as a case study. Different alternative methods for modeling the propagation of epistemic uncertainty, including a logic tree approach, the FOSM method, a linear RSM, and a LHS Monte Carlo analysis, were compared. The numerical cost of the analyzed methods was limited and comparable, as all procedures require a similar number of simulations (between 7 and 27). A wider Monte Carlo simulation, based on 600 analyses, was used as a benchmark, representing the best estimate of the true distribution of the response.

A historical stone masonry building located in the city center of Basel, the Holsteiner Hof, was adopted as a case study, being structurally simple, regular, and symmetric. These characteristics encouraged the application of a global pushover analysis and made the automatic processing of a very large sample of simulations easier, which was required for the Monte Carlo simulation. The building, which dates to the end of the 17th century, is a two-story, regular construction with a tall timber roof and has plan dimensions of 26x14 m. It can be considered a typical example of the construction period between the 17th and 19th century in Basel. The elevation of the façade has a regular layout, with windows laid on an ordered grid (Figure 2.3). The inter-story height, constant for both floors, is 4.50 m. The ground-floor piers have a thickness of 80 cm, and the first-floor piers have a thickness of 60 cm. The triangular wall of the gable and the spandrels have a thickness of 45 cm. The horizontal diaphragms are timber floors, spanning in the direction of the shorter side of the building.

As the purpose of the analysis is not the assessment of this specific building but the comparison of different methods for the explicit inclusion of epistemic uncertainties, the geometry of the true building was simplified and the interaction with an adjacent building ignored. Moreover, for the same

2.3. Modeling uncertainties in a historical stone masonry building

reason, only a global analysis was performed, which omitted the assessment of local out-of-plane mechanisms that would be relevant in a real-world assessment. Although in principle the proposed methods are applicable to any structural model, including local mechanisms for out-of-plane behavior, the epistemic uncertainty in the assessment of these failure modes is related more to the assumption of a suitable mechanism or model rather than to parameter uncertainty, which can be modeled by numerical random variables. For the treatment of the uncertainty related to numerical random variables, a logic tree approach seems the most practical solution.

Global pushover analyses of the building were performed on an equivalent frame model (Figure 2.3b) using the Tremuri software (Lagomarsino et al., 2013) as a compromise between the accuracy of the analysis and its applicability in the professional field. Piers and spandrels are described by the macroelement model presented in Penna et al. (Penna et al., 2014), which is able to reproduce flexural-rocking and shear damage modes of masonry elements. The nonlinear behavior of the macroelement model is determined by its geometry and material properties, as well as by limit drift capacities for shear and flexural failure modes that are imposed on each element. The loss of lateral strength of the masonry elements in near-collapse conditions, defined by the attainment of these drift thresholds, is modeled by transforming the element into a truss that maintains only its axial force capacity.

The stiffness contribution given by horizontal diaphragms is modeled by elastic orthotropic membrane elements, providing only in-plane stiffness. Perfect floor-to-wall connections, with no possible degradation, are assumed. As the elastic properties of the membrane element are particularly challenging to estimate and must also account for the quality of the connection to the external walls, they are treated here as a random parameter. The stiffness contribution of the roof structure, composed by a complex system of timber trusses, was modeled in a simplified manner consisting of elastic inclined membranes of the same type used for horizontal diaphragms.

2.3.1 Sources of uncertainty modeled through random variables

The parameter uncertainty was modeled through a set of random variables (Table 2.1) that describe the elastic properties of masonry, the strength in compression and shear, the friction coefficient, the displacement capacity of the elements in flexure and in shear, and the stiffness ratio of the timber floors in their two directions. The floor stiffness in the direction of the floor beams was assumed to be known ($E_1 = 0.68 \text{ kN/mm}$). The mechanical parameters of stone masonry are derived from provisions given in the Italian code (MIT, 2009), which are also in line with the reference values in Kržan et al. (Kržan et al., 2014). The tables provided in both sources define ranges to be adopted for each mechanical parameter, differentiating between several typologies of stone masonry from irregular rubble masonry to ashlar masonry. The ranges were interpreted as the 16th-84th fractiles of the distribution of a random variable, as also suggested in the document issued by CNR (CNR, 2013).

Lognormal distributions were assumed for all mechanical parameters to avoid the possible sampling of negative values or the truncation of the distribution. Attributing the proper typology to the real masonry was considered as an additional source of uncertainty, because of both the subjectivity in the evaluation and from an incorrect or incomplete knowledge of the masonry texture. As a rather

Chapter 2. Treatment of epistemic uncertainty through a Point-Estimate Method

conservative hypothesis, the distributions assumed in this case consider an equal probability that the masonry belongs to any of the three typologies defined in the Italian code for irregular masonry, i.e. irregular rubble masonry (type A), uncut three-leaf stone masonry with infill core (type B), or cut stone masonry with good bonding (type C). The choice to include a wider range of possible typologies was related to the heterogeneity of masonries that can be present inside a historical building, especially one that underwent several modifications. The distributions of mechanical properties defined by the code and the ones assumed in this study are plotted in Figure 2.4.

The shear capacity of the macroelements is defined by a Mohr-Coulomb model, featuring a cohesive and a purely frictional contribution. The cohesion is assumed equal to the shear strength indicated in the Italian code (MIT, 2009), although such values are more properly representing a diagonal tensile strength. For the friction coefficient, indications in Angelillo et al. (Angelillo et al., 2014), consistently with the experimental shear envelopes derived by Vasconcelos and Lourenço (Vasconcelos and Lourenço, 2009), suggest a value of 0.30 for irregular stone masonry and 0.20 for rubble stone masonry. In Vanin et al. (Vanin et al., 2017b), comparable values are derived from linear regression of the lateral force capacity of experimental shear compression tests on stone masonry walls. In other

Table 2.1 – Assumed distributions of the random variables.

Parameter		Mean	C.O.V.	Distribution	Reference
Elastic modulus	E	1280 MPa	0.35	Lognormal ($\mu = 7.10, \sigma = 0.34$)	CNR 2013; MIT 2009; Kržan et al. 2014
Shear modulus	G	430 MPa	0.35	Lognormal ($\mu = 6.10, \sigma = 0.34$)	CNR 2013; MIT 2009; Kržan et al. 2014
Compressive strength	f_c	2.39 MPa	0.45	Lognormal ($\mu = 0.78, \sigma = 0.43$)	CNR 2013; MIT 2009; Kržan et al. 2014
Cohesion	τ_0	0.045 MPa	0.45	Lognormal ($\mu = -3.19, \sigma = 0.43$)	CNR 2013; MIT 2009; Kržan et al. 2014
Friction coefficient	μ	0.25	0.12	Uniform ($a = 0.20, b = 0.30$)	Vanin et al. 2017b; An- gelillo et al. 2014; Vascon- celos and Lourenço 2009
Failure drift, flexure	δ_{fl}	1.40%	0.57	Lognormal ($\mu = 0.24, \sigma = 0.53$)	Vanin et al. 2017b
Failure drift, shear	δ_{sh}	1.10%	0.69	Lognormal ($\mu = 0.08, \sigma = 0.62$)	Vanin et al. 2017b
Floor stiffness ratio	E_2/E_1	0.51	0.55	Uniform ($a = 0.025, b = 1$)	

2.3. Modeling uncertainties in a historical stone masonry building

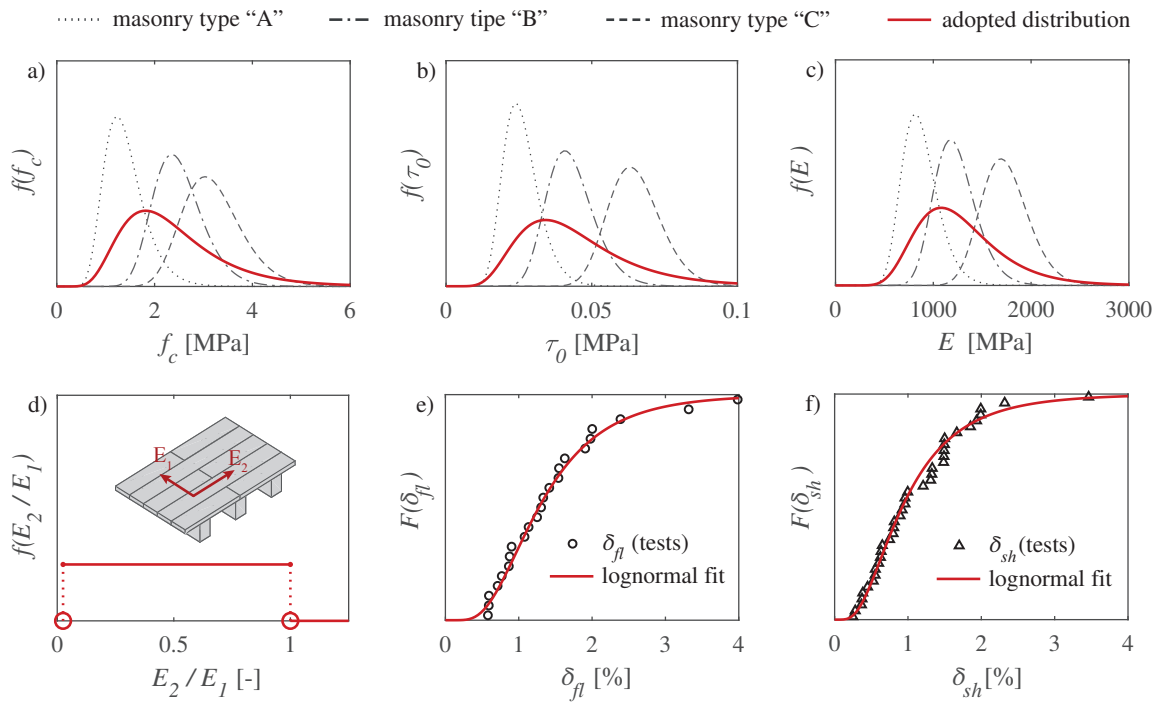


Figure 2.4 – Distribution of the random input variables: (a) compressive strength f_c , (b) cohesion τ_0 , (c) elastic modulus E , (d) floor stiffness ratio E_1/E_2 , drift at loss of lateral force capacity for (e) flexural failure δ_{fl} and (f) shear failure δ_{sh}

studies, when the friction angle was determined by calibrating the macroelement cyclic response against laboratory tests, lower values ranging from 0.05-0.08 (Rota et al., 2010) to 0.14 (Penna et al., 2016) are reported. In the shear model implemented in the applied macroelement, the friction coefficient controls both the maximum force capacity and the dissipative behavior in hysteretic cycles. Since the latter feature does not affect the monotonic pushover analyses performed in this study, the indications of studies concentrating only on the force capacity of experimental tests (Vanin et al., 2017b; Angelillo et al., 2014; Vasconcelos and Lourenço, 2009) are considered here for determining the variation range for the friction coefficient. A uniform distribution ranging between 0.20-0.30 is assumed.

The displacement capacity of the elements fundamentally impacts the seismic assessment of near-collapse limit states because the global displacement capacity of the entire building is a function of the displacement capacities of the individual structural elements. A considerable variability in displacement capacities of stone masonry walls is reported in the literature (Vanin et al., 2017b; Kržan et al., 2014) for both flexural and shear failure modes, making their determination in a model one of the most relevant sources of uncertainty. Code provisions specifically developed for stone masonry walls are currently not available, and the ones provided for masonry consist of single reference values with no indication of a probability distribution. The distributions assumed in this case were derived from a database of shear compression tests (Vanin et al., 2017b), from which only walls of the typologies considered in this study were extracted. The mean values and standard deviations of drifts that

correspond to the attainment of a near-collapse limit state were derived for flexural and shear failure from 23 and 38 tests, respectively. The coefficients of variation, although rather large, were in line with the marked uncertainty related to the displacement capacity of other structural members, as reported, for example, by Dolšek (Dolšek, 2009) and Grammatikou et al. (Grammatikou et al., 2015) for the chord-rotation capacity of RC elements. Since the literature on the displacement capacity of masonry spandrels is currently scarce, their drift-related failure is not accounted for; this is justifiable as their displacement capacity is considerably larger than that of the piers (Beyer and Dazio, 2012).

The stiffness of the timber floors is a further source of uncertainty. Because the pushover analysis will only be performed in the direction perpendicular to the main beams, the stiffness in the weak direction of the timber floors is the most relevant parameter to determine. Mechanical models developed for timber floors, as the one proposed in Brignola et al. (Brignola et al., 2008), combine the stiffness contributions from the planks and the nailed connections, though this stiffness is affected by a certain uncertainty. Moreover, because the numerical model assumes a perfect connection between the floors and the walls, the elastic parameters must also indirectly represent the real effectiveness of the connection, which adds further uncertainty to the parameter. In this case, the stiffness in the direction of the beams was calculated according to the model in Brignola et al. (Brignola et al., 2008), while the ratio between the stiffness in the perpendicular direction and the stiffness in the direction of the beams was determined by a uniformly distributed variable in the range (0.025-1.00). The lower bound was not set to zero to avoid modeling a local overturning mechanism of the shorter façade, which would not be correctly captured by the adopted equivalent frame model.

Two types of Monte Carlo simulations were run. In the first, the elements were always assigned the same properties. In the second, an element-to-element variability of the quantities defined by random variables was accounted for, assuming a coefficient of variation (COV) of 20% between the single elements for both mechanical parameters and drift thresholds. The order of magnitude of the spatial variability of material properties was derived from observations on the limited sample of repeated tests available in the literature (Vanin et al., 2017b).

2.4 Comparison of methods for evaluation of the epistemic uncertainty

The methods for evaluating the epistemic uncertainty introduced in Section 2.2 were benchmarked with respect to a reference Monte Carlo simulation, adopted as the best estimation of distribution of the seismic response of the building. Such response was described by the peak ground acceleration (PGA) corresponding to the attainment of the ultimate limit state (ULS), evaluated according to the N2 method (Fajfar, 2000). The global limit state was defined by the attainment of the near-collapse limit state in one pier.

Three major sources of uncertainty were considered, which were (i) the mechanical properties (stiffness and strength parameters), (ii) the drift capacity, and (iii) the floor stiffness. A perfect correlation between random variables of the same category was then postulated for all analyses, which assumed that a softer masonry would have a lower shear compressive strength and that a limited drift capacity in flexure would correspond to a limited shear drift capacity. Although the most realistic assumption

2.4. Comparison of methods for evaluation of the epistemic uncertainty

appears to be a partial correlation between the variables belonging to the same category, the choice to adopt a perfect correlation was made to eliminate the further uncertainty related to the determination of the correlation coefficients. Simplifying to only three sources of uncertainty, named random macro-variables, allows their distributions to be sampled in a finite set of points and for the consideration of all possible combinations, obtaining therefore m^N evaluations of the numerical model if N is the number of macro-variables and m is the number of sampled points. This approach, corresponding to a complete quadrature scheme for the integration of the response function, can also be visualized in a logic tree as in Figure 2.5.

A three-point sampling of the material properties and drift capacities was performed according to Equation 2.20, which gives the optimal set of three sampling points and relative weights. As the building performance is sensitive to the variable representing the floor stiffness mainly in the lower range of its distribution, the position of the one sampling point was imposed to 5%, and the second sampling point and the two weights were solved to match the first two statistical moments of the original distribution. A total of 18 analyses are required for a complete combination scheme, and these results are shown

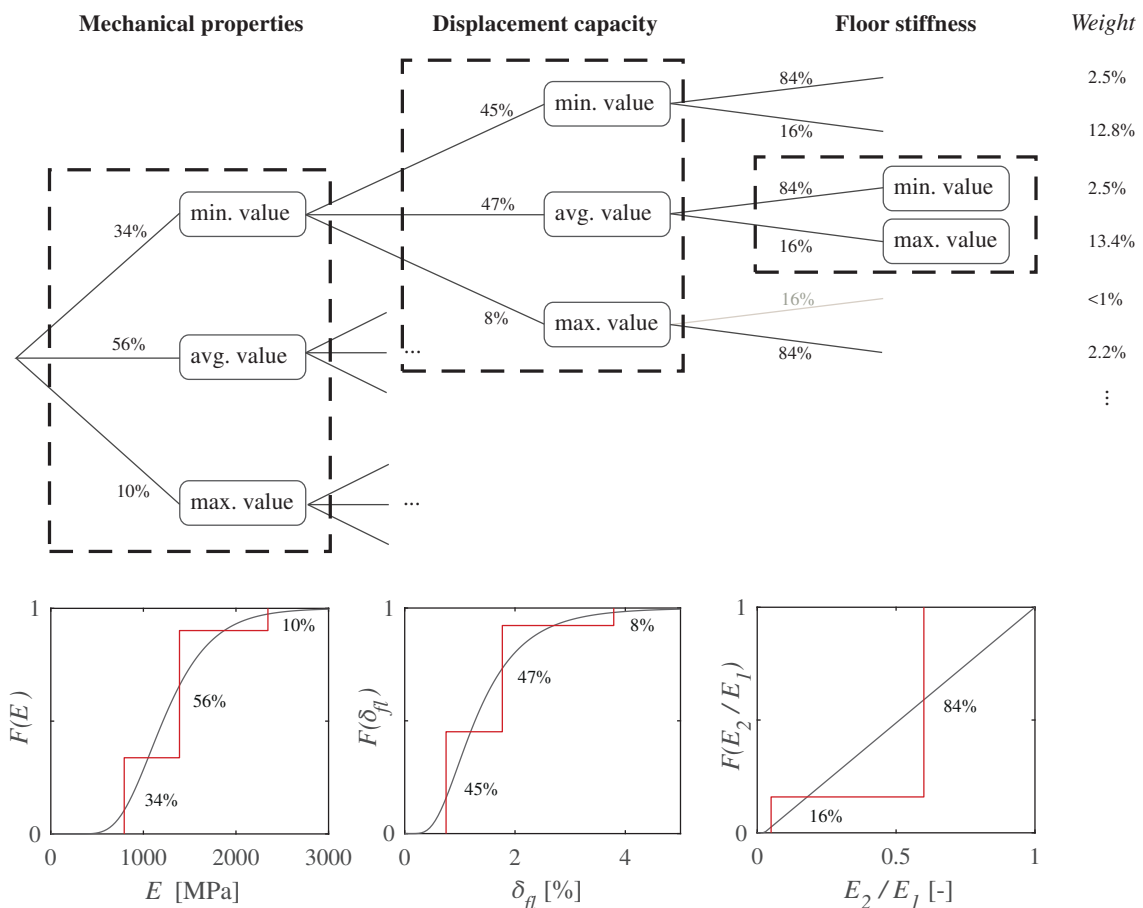


Figure 2.5 – Logic tree approach. Sampled values for the random variable distributions and weights.

in Figure 2.6 together with the ones obtained from the 18-model LHS. The overall weight relative to each analysis derives from the combination of the weights assigned to the single branches. Since the weights corresponding to some analyses were particularly small, the application of a threshold weight of 1% was introduced to reduce the number of required simulations, and all branches with weights below this threshold were eliminated, reducing the number of required evaluations to 12. Results relative to both combination schemes are compared to the distribution obtained from the Monte Carlo simulation with perfect spatial correlation in Table 2.2.

Other simplifying scenarios for the construction of a logic tree were compared, such as imposing a all evaluation points and calculating optimal weights (18 analyses) as well as the opposite approach of imposing equal weights to each analysis and calculating the resulting optimal evaluation points. When the position of evaluation points is imposed, the corresponding weights can be obtained from Equation 2.18; evaluation points of three-point discretisations were imposed at the mean value and at 5-95% fractiles. When on the other hand the weights is imposed, Equation 2.21 applies. The simplifications slightly affected the accuracy of the calculated response distribution, particularly in the model that assumes equal weights for all analyses, which tends to investigate combinations of parameters further from the distribution tails. Since the simplification introduced in these logic trees solely regarded the sampling procedure, as only the determination of mean values and the variance of the random variable were required, their use seems suitable only if higher order moments of the distribution are not available. However, if the hypothesis of log-normality of the distribution is accepted and higher order moments are hence derived directly as a function of the mean and variance of the distribution, the use of more refined sampling schemes does not introduce further complexity to the analysis, ensuring a yet higher accuracy of the integration scheme.

Together with a logic tree approach, the PEM presented in Section 2.2.4 was also considered and compared to the other simplified methods (linear RSM and FOSM). The PEM and the FOSM were implemented using $2N + 1$ evaluations of the numerical model, resulting in a star scheme with a central point corresponding to the mean of all random variables. The RSM was implemented with a two-level factorial scheme following the recommendations in the CNR document (CNR, 2013), also adding the evaluation of the central point. For the PEM, the optimal sampling points and weights were determined by Equation 2.20 with no further assumptions. For the RSM and the FOSM, the lower and upper values of each random variable corresponded to the 16th and 84th fractiles of their distributions, as suggested in the CNR document. Moreover, the results of a full factorial combination, requiring 27 analyses, which corresponds to an optimal complete Gaussian quadrature scheme, are presented.

The analysis that provided the best estimate of the mean and variance of the output response was the full factorial scheme, which required, however, 27 evaluations of the numerical model. A similar performance was achieved by the PEM, though a higher error was obtained for the mean response estimate compared to the logic tree with imposed sampling points and the LHS. The PEM, however, considerably reduced the numerical cost (7 analyses) and performed better than the other methods requiring the same number of analyses, particularly in evaluating second-order moments. The logic tree approach led to better estimations than the LHS for the same number of analyses. The reduction in numerical cost with the logic tree method obtained by imposing a threshold to the weight of the

2.4. Comparison of methods for evaluation of the epistemic uncertainty

analyses, however, corresponded to an increase in the variance estimation error and does not seem to be an optimal approach. More consistent methods, such as the PEM, performed better at a smaller numerical cost.

2.4.1 Simplified method for accounting for spatial variability of properties

Almost all presented analyses, despite the variability of the input parameters, showed the same global failure mode corresponding to the flexural failure of the first-story piers. For this failure mode the global force capacity and the coupling effect of the spandrels depended largely on geometrical parameters, meaning the uncertainty in the response depended on the uncertainty in the displacement capacity of the single elements. This resulted in a consistent shift of the median response for the Monte Carlo simulations that featured a spatial variability of random variables, since a drift-based failure criterion,

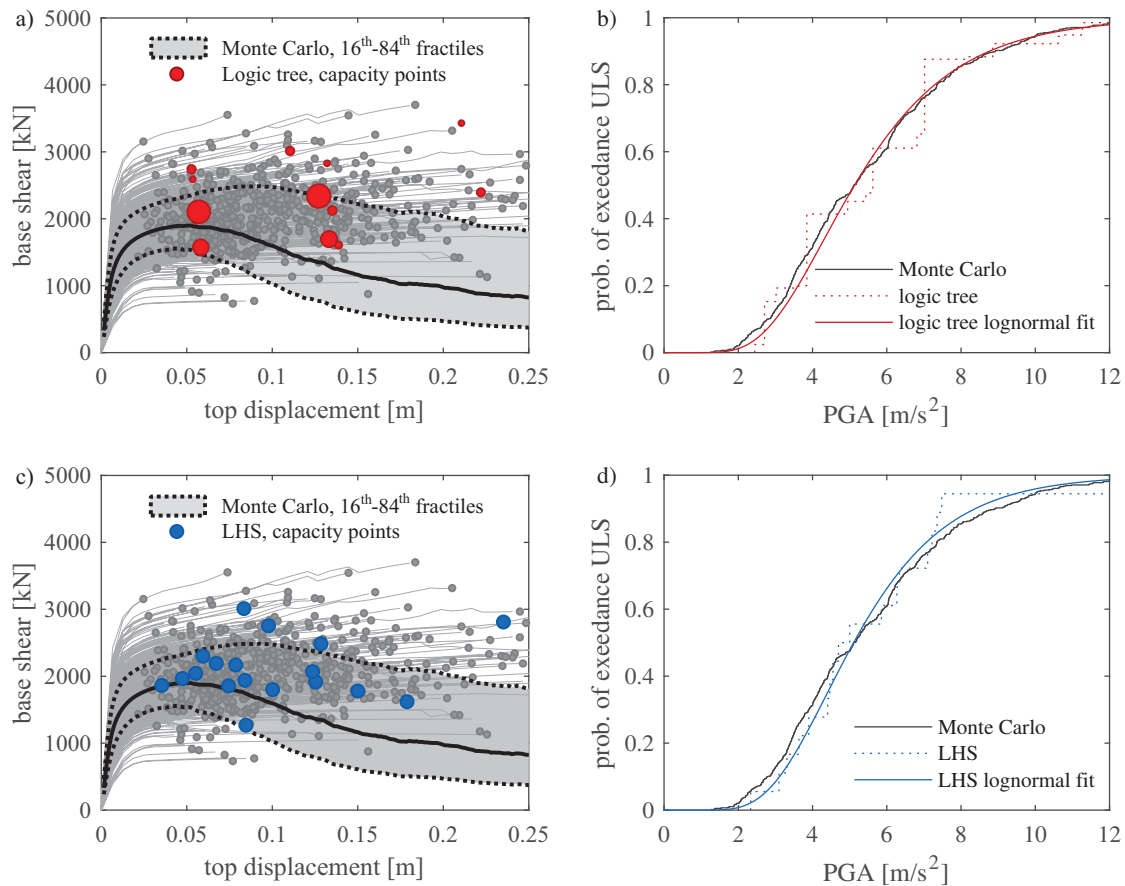


Figure 2.6 – Pushover curves obtained from the Monte Carlo simulation and (a) the logic tree approach or (c) Latin Hypercube Sampling (LHS). Distribution of estimated seismic capacity at the ultimate limit state (ULS) obtained from the Monte Carlo simulation and (b) the logic tree or (d) via LHS. Perfect spatial correlation of mechanical parameters and drift capacity is assumed.

Chapter 2. Treatment of epistemic uncertainty through a Point-Estimate Method

Table 2.2 – Performance of the tested methods in estimating the mean and standard deviation of the PGA corresponding to ULS.

	Analyses	Mean [m/s ²]		Standard. dev. [m/s ²]	
Reference Monte Carlo	550	5.47		2.42	
Logic tree, opt. sampling points and weights	18	5.60	+2.3%	2.44	+1.0%
Logic tree, imposed sampling points	18	5.42	-1.0%	2.39	-0.9%
Logic tree, imposed weights	18	5.24	-4.3%	1.98	-17.9%
Reduced logic tree	12	5.46	-0.3%	2.25	-6.7%
Latin hypercube sampling	18	5.50	+0.6%	2.27	-5.9%
Full factorial combination	27	5.46	-0.1%	2.39	-1.1%
Point Estimate Method	7	5.41	-1.1%	2.39	-1.1%
Response Surface Method	7	5.82	+6.4%	2.81	+16.2%
First-order second-moment method	7	5.39	-1.4%	2.98	+23.6%

as the one assumed, coupled to a story mechanism, led to an earlier attainment of the limit state.

Figure 2.7 shows this effect both when the displacement capacity was the only parameter varying from element to element (dashed line) and when the spatial variability accounted for all random variables (continuous line). This effect was only partially related to the adopted failure criterion (global failure defined as first-pier failure). When the global failure was defined as a 20% drop in the lateral force capacity, the failure was also consistently reached for smaller displacements if the spatial variability in the drift capacities was accounted for and a story mechanism developed, as shown in Figure 2.8. The force capacity drop and the attainment of the failure drift in the piers do not correspond to the same top displacement, since the latter is computed with a different definition of drift, compared to the drift calculated by the software Tremuri. The first accounts only for the rotation at the base node of a pier, the second for rotations at both end nodes.

For a regular building layout, if failure is related to a story mechanism and the failure mode does not change, the model can be effectively approximated by a series system whose response is governed by the element with the lowest displacement capacity. Therefore, if N_s is the number of critical elements and \mathbf{d} is the vector of N_s displacement capacities assigned to each, the response can be approximated by an equivalent system in which all elements are assigned the same displacement capacity equal to the minimum of \mathbf{d} . The vector \mathbf{d} can be considered a set of N_s realizations of a random variable X . The cumulative distribution function $F_{min(\mathbf{d})}$ of the lowest element of \mathbf{d} can be expressed as:

$$F_{min(\mathbf{d})}(x) = 1 - [1 - F_X(x)]^{N_s} \quad (2.25)$$

where F_X is the cumulative distribution of the random variable X . Inverting Equation 2.25, it is possible to express the median value $\tilde{\delta}_{min}$ of the lowest element of \mathbf{d} as a function of the inverse cumulative

2.4. Comparison of methods for evaluation of the epistemic uncertainty

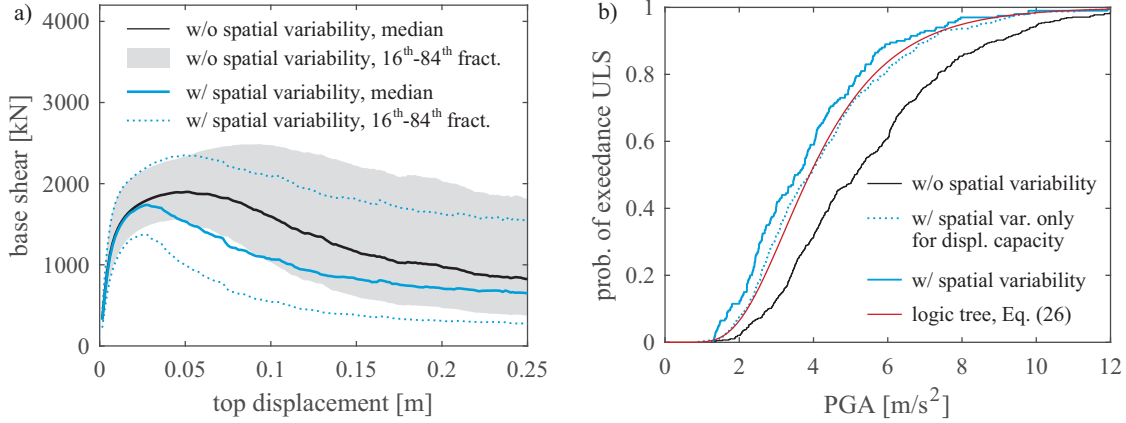


Figure 2.7 – Effect of spatial variability of drift capacity and mechanical properties throughout the structure: (a) median capacity curves and (b) fragility curves at ULS compared to a logic tree approach modified through Equation 2.26.

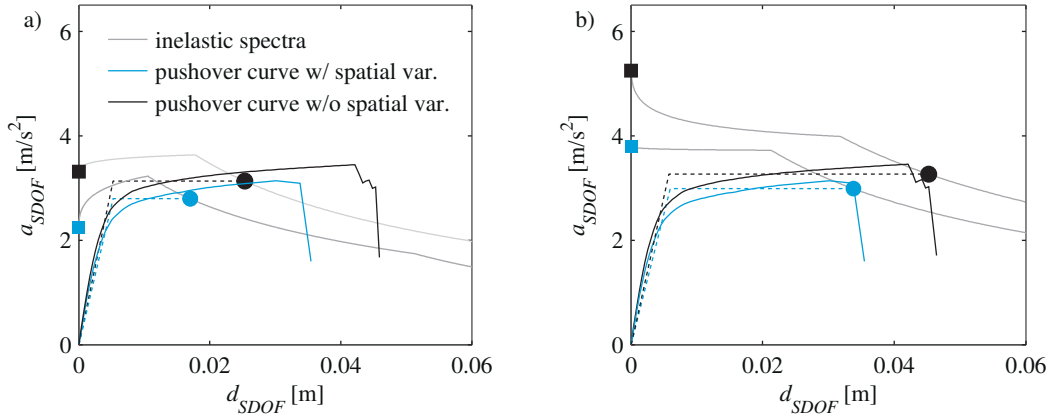


Figure 2.8 – Scheme of the analysis performed using the N2 method for different ULS definitions. (a) The first element reaching a drift threshold and (b) a 20% force capacity drop.

distribution of the random variable X , as:

$$\tilde{\delta}_{min} = \text{min}(\mathbf{d}) = F_X^{-1} \left(1 - 2^{-\frac{1}{N_s}} \right) \quad (2.26)$$

The response obtained by accounting for spatial variability can therefore be approximated for a series system by a model with perfect spatial correlation if all elements are assigned a reduced displacement capacity that corresponds to the minimum displacement capacities of the N_s elements of the floor where failure is expected to happen. The median value of this reduced displacement capacity can be derived from Equation 2.26. The the distribution of the response estimated through a logic tree approach, adopting this simplification, are shown in Figure 2.7b. The method approximates the

Chapter 2. Treatment of epistemic uncertainty through a Point-Estimate Method

Table 2.3 – Estimates of the mean and standard deviation of the PGA corresponding to ULS, for shear failure of the building.

	Analyses	Mean [m/s ²]		Standard. dev. [m/s ²]	
Reference Monte Carlo	850	3.32		1.69	
Logic tree approach	18	3.21	-3.4%	1.43	-15.4%
Full factorial combination	27	3.30	-0.6%	1.53	-9.7%
Point estimate method	7	3.38	+1.6%	1.44	-14.9%

distribution of the response of a model featuring a partial spatial correlation of the displacement capacity assigned to each pier. Similar results are obtained when the PEM is used.

2.4.2 Influence of modeling uncertainties for flexural and shear global failure modes

As shown in the previous section, when flexural failure dominates the global response of the building, the uncertainty of the response is largely related to the uncertainty in the displacement capacity of the piers. To investigate whether the influence of the drift capacity was similarly strong when the piers fail in shear, a Monte Carlo simulation, the PEM, and the logic tree analysis were performed on the building after intentionally induce a first-story shear failure by positioning post-tensioned tie-rods at the floor levels. The high compression force induced into the spandrels, averaging 0.8 MPa in this case, was sufficient to guarantee their coupling action until shear failure was reached in the piers for all analyses. It should be noted that such highly tensioned tie-rods were inserted only to change the failure mode through an increase in the force capacity of the spandrels, and are not meant to represent a realistic retrofit intervention. The simplified methods captured the mean response predicted by the Monte Carlo simulation run under the same set of hypotheses (Table 2.3). All the methods tended to slightly underestimate the standard deviation, though remained in the acceptable range of error for approximated approaches. For a shear failure mechanism of the building, a smaller mean capacity was derived due to the reduced displacement capacity of piers failing in shear. The sensitivity to each source of uncertainty is shown by plotting the PGA at ULS, calculated by varying each random variable between its 16th and 84th fractiles and keeping the average values for the other random variables (Figure 2.9a).

The influence of the different sources of uncertainty in determining the total epistemic uncertainty is evaluated in Figure 2.9b by means of their contribution to the dispersion β_U of the response (i.e., the standard deviation of the natural logarithm of the response, considering only epistemic uncertainties). The single contributions are calculated using a linear approximation of the response surface obtained using all evaluations of the Monte Carlo simulations. The use of the FOSM to calculate the single contributions to the total uncertainty gave very similar results. For both global failure mechanisms, the displacement capacity was the largest contribution. The role of mechanical parameters becomes, as expected, more relevant for shear failure modes since the force capacity is more directly related to the material properties than for flexural failure modes, which depend largely on the static and kinematic boundary conditions and the geometry of the element. It should be outlined, moreover, that

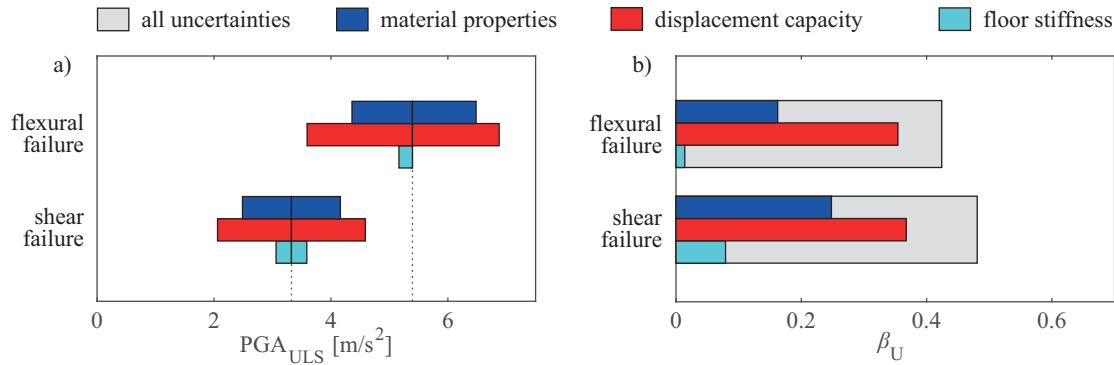


Figure 2.9 – (a) Sensitivity of the seismic response to the different sources of uncertainty, and (b) contribution of each modeled source of uncertainty in determining the dispersion β_U of the response.

considering the determination of the masonry typology itself as a source of uncertainty may constitute an overestimation of the material parameters uncertainty.

The total epistemic uncertainty, mainly due to the large uncertainty affecting the determination of the displacement capacity, is on the order of 0.40-0.45 for both failure modes. This value should be combined with the dispersion β_R related to aleatory randomness, which depends on the record-to-record variability of the response and which can be assumed as log-normally distributed and as uncorrelated to the epistemic uncertainty. This means that the total dispersion β of the response can be derived from a square-root-sum-of-squares combination of β_U and β_R . Both sources of uncertainty appear to be relevant in determining the total dispersion, if we assume the dispersion β_R related to record-to-record-variability for a masonry building to be in the range found for other building typologies (Vamvatsikos and Fragiadakis (Vamvatsikos and Fragiadakis, 2010) obtained a dispersion β_R in the order of 0.30-0.40 for a steel frame, Dolšek obtained a value closer to 0.50 for a RC structure (Dolšek, 2009, 2012)).

2.5 Conclusions

We herein demonstrated the modeling of epistemic uncertainty on the seismic performance of a stone masonry regular building through simplified methods aimed at professional applications. The sources of uncertainty considered in the study are essentially parameter uncertainties in the definition of the material elastic and strength properties, the element displacement capacity, and the role of the deformable diaphragms, though the uncertainty related to the choice of structural model was disregarded. The distribution assigned to the random variables was derived, when possible, from code provisions or the literature, with that of the element displacement capacity, whose contribution to the uncertainty in global seismic performance is of major importance, derived from a recently collected database of shear compression tests.

Different methods for the assessment of epistemic uncertainty were applied to a case study, and their

performances were compared. A novel application of a PEM is proposed, as well as the use of a logic tree approach to account for all considered sources of uncertainty. Combined with a consistent derivation of mathematically optimal sampling schemes, both methods better estimated the parameters (mean response and dispersion) defining the seismic performance when compared to other simplified methods (FOSM, RSM) of similar numerical cost. Regardless, all methods led to reasonably accurate predictions of the response distribution. The use of simplified analysis strategies, resorting only to pushover analyses on simple structural models, together with approximated methods for uncertainty estimation, results in a limited numerical demand that can be compatible also with the requirements of the professional practice.

The uncertainty related to the determination of the displacement capacity is the main source of parameter uncertainty affecting the seismic response of the analyzed building, both when failure is determined by a local drift criterion and when it is related to a global force capacity drop. This dependency is stronger when the global failure mode is a floor mechanism with flexural damage of the piers because the flexural strength of a pier is largely determined by its static and kinematic boundary conditions, its geometry, and to a lesser extent, by material properties. If the piers fail in shear, the role of material properties becomes more relevant, although the total uncertainty remains primarily related to the displacement capacity of the elements. The role of the uncertainty in the displacement capacity becomes particularly evident when the spatial variability of the parameters is accounted for. The spatial variability leads to a reduction in the median response, since the model is essentially a series system for which the first element attaining its limit capacity determines the global response when the failure mode is a floor mechanism.

Mainly because of high uncertainty in the displacement capacity, the dispersion of the response deriving from the considered parameters can be compared to the expectable range of dispersion of the displacement demand related to the aleatory record-to-record variability. Given the order of magnitude of the epistemic uncertainty, a correct assessment of a near-collapse global limit state of one stone masonry building should therefore consider both sources of uncertainty.

All conclusions were derived for a near-collapse limit state; further investigation should be devoted to estimating the relevance of different sources of uncertainty for other limit states, which could be of comparable interest for heritage buildings of higher cultural value, for example. It can be noted, however, that the uncertainty in the drift capacities for less severe limit states (such as a significant damage or the loss of artistic value) is not necessarily smaller (Vanin et al., 2017b).

2.6 Repository

All results presented in the paper can be reproduced through the materials shared to the Zenodo repository [10.5281/zenodo.2669183](https://zenodo.org/record/2669183). Template input files, model results and the Matlab files used to plot the figures are provided, as well as Matlab functions performing the sampling of random variables according to the methods in Section 2.2.1-2.2.4.

2.7 Acknowledgements

This work was funded by the Prevention of Major Accidents and Earthquake Mitigation Section of the Swiss Federal Office of the Environment as part of the project "Logic Tree Verfahren zur Beurteilung der Unsicherheiten bei der Berechnung der Erdbebensicherheit von bestehenden Bauwerken am Beispiel des kulturhistorisch bedeutenden Holsteiner Hofes in Basel". The authors would also like to thank Dario Zaganelli, who worked on a part of this work for his master thesis at the École Polytechnique Fédérale de Lausanne.

3 Three-dimensional macro-element for modelling masonry walls

This chapter represents the submitted version of the article:

Vanin, F., Penna, A., Beyer, K. (2019). "A three-dimensional macro-element for modelling of the in-plane and out-of-plane response of masonry walls". Submitted to *Earthquake Engineering and Structural Dynamics*

The formatting and numbering of equations, tables and figures have been updated to this document. The contributions of the first author are: deriving the formulation of the macro-element and the material models presented in the chapter, implementing the code in OpenSees, performing the analyses and writing the article. Contributions of the second and third authors: supervision of the first author, co-writing the article.

Abstract

Equivalent frame modelling is a common modelling approach when assessing the seismic performance of unreinforced masonry buildings. Its computational efficiency allows conducting a large number of analysis, which are often required to account for epistemic and aleatoric uncertainties. In order to obtain a full description of the building response, in-plane and out-of-plane failure modes need to be considered. Previous elements for equivalent frame models of unreinforced masonry buildings only accounted for the in-plane response. This paper presents the formulation of a three dimensional macro-element for modelling the dynamic in-plane and out-of-plane behaviour of masonry panels, extending the approach of a previously developed macro-element for the simulation of the in-plane response. The proposed three-node, three-dimensional macro-element, implemented in the software OpenSees, describes the main features of the in-plane and out-of-plane behaviour of a masonry wall, including second-order geometrical effects, a coupled shear/flexural response, and allowing for the use of complex material models. The proposed element is used to simulate experimental results for in-plane shear-compression tests and out-of-plane free vibrations tests of masonry panels. The implemented element, as well as the example models, are openly shared through the repository <https://github.com/eesd-epfl/OpenSees/wiki>.

3.1 Introduction

Unreinforced masonry buildings are among the most vulnerable buildings under earthquake loading, often contributing to a large extent to the economic and social impact of a seismic event. For this reason, it is common to conduct nonlinear seismic analyses when assessing or even designing unreinforced masonry buildings. Several approaches with different levels of detail have been proposed in the literature for the modelling of structural masonry. In detailed micro-modelling approaches (Zhang et al., 2017) the heterogeneity of the material is treated explicitly, while in simplified micro-models joints are modelled by interface elements (Lourenço and Rots, 1997; Wilding et al., 2017). Less computationally expensive models are homogenised micro-models (Milani et al., 2007; Zucchini and Lourenço, 2009; Milani, 2011), or models in which damage is smeared into a continuum (Lotfi and Shing, 1991; Berto et al., 2002; Pelà et al., 2013). As an alternative to finite element modelling, discrete elements have been used for blocky structures (Psycharis et al., 2003; DeJong and Dimitrakopoulos, 2014) accounting for the complex dynamics of interacting blocks. Although such modelling approaches comprise different levels of complexity, and are, as a result, applicable at different scales, dynamic analysis of entire masonry buildings by these approaches is still limited, especially in the professional field, mainly due to their considerable computational cost. In particular, the need of numerous sets of analyses for investigating the variability of the dynamic behaviour of a building for epistemic and aleatoric uncertainties (Bracchi et al., 2015; Rota et al., 2014b) call for computationally very efficient building models. As a compromise between a sufficient level of accuracy and a limited computational cost, equivalent frame modelling of masonry buildings (Lagomarsino et al., 2013; Roca et al., 2005; Belmouden and Lestuzzi, 2009; Addessi et al., 2014; Parisi and Augenti, 2013b) is a widely adopted modelling choice (see Quagliarini et al. (2017) for a comprehensive review). Such modelling technique assumes that a masonry façade can be simplified into a frame of pier and spandrel elements, connected by portions of masonry subjected to lower deformations, and less prone to damage, generally considered as rigid nodes. Such approach can be applied if the façade layout is relatively regular; in this case, comparisons with experimental tests (Mandirola et al., 2016; Penna et al., 2016; Cattari et al., 2014) and more detailed numerical analyses (Kappos et al., 2002; Siano et al., 2018) have shown that equivalent frame models is a robust modelling approach for unreinforced masonry buildings.

Existing tools for equivalent frame modelling of masonry buildings consider an assemblage of two-dimensional frames that represent the in-plane response of the masonry elements and neglect their out-of-plane behaviour (Lagomarsino et al., 2013; Penna et al., 2014). The out-of-plane response is typically not critical if the walls are tied together at all storey levels. However, in particular for historical buildings, out-of-plane failure is often the failure mode that leads to collapse and casualties (D'Ayala and Paganoni, 2011). When equivalent frame models that do not capture the out-of-plane behaviour are used, other types of analyses (for instance, rigid body limit analysis of collapse mechanisms (Lagomarsino, 2015), or discrete element modelling (DeJong and Vibert, 2012; Malomo et al., 2018; Tondelli et al., 2016b)) have to be additionally performed. This method necessarily assumes, however, that the in-plane and out-of-plane response are not coupled. A more complex plane rectangular macro-element, applicable also to shell structures and accounting for the out-of-plane behaviour, was proposed by Calì et al. (2012). In such approach the building is modelled as an assemblage of panels,

that can describe any geometry layout, including vaults or complex geometries, such as churches (Pantò et al., 2016), partially losing, however, the inherent simplicity of equivalent frame modelling. On the other hand, equivalent frame models with force-based beam elements (Siano et al., 2018; Raka et al., 2015) could theoretically be used to model also the out-of-plane response though this has not yet been attempted. Furthermore, they imply a certain increase of numerical complexity and, in their current implementation, cannot yet describe the coupling between the shear response and the applied axial loads on each element (Siano et al., 2018; Raka et al., 2015).

As a contribution towards the development of equivalent frame models that allow an integrated in-plane and out-of-plane assessment of a masonry building, this paper proposes a novel three-dimensional macro-element formulation. It accounts for material and geometrical nonlinearity and is able to capture the main features of the in-plane and out-of-plane dynamic response of a masonry wall. The formulation is based on the macro-element developed by Penna et al. (2014) for modelling the in-plane behaviour of masonry panels. The new element is implemented in the open-source software OpenSees (McKenna et al., 2000) and is therefore freely and openly available to the research community. Extensive documentation and example models of masonry sub-assemblages and buildings are shared through the repository "<https://github.com/eesd-epfl/OpenSees/wiki>". By integrating it in OpenSees, future research can make use of the existing library of material models and element types, increasing the complexity of the equivalent frame models of unreinforced masonry buildings or mixed building types that can be developed. To maximise the versatility of the element and investigate various modelling assumptions on the overall seismic response of a masonry building, this macro-element allows the choice between various section models, including fibre sections in combination with any uniaxial material laws, as well as between various shear models, mass discretisations and damping models. Moreover, the macro-element comprises a versatile drift capacity model with which the drift capacity at the loss of the horizontal load bearing capacity can be expressed as a function of the failure mode, axial load ratio and shear span to element height ratio. In addition, it also allows modelling the loss of the vertical load bearing capacity at a drift, which is a multiple of the drift at horizontal load failure. These modelling options are implemented in order to facilitate sensitivity studies on modelling assumptions.

3.2 Macroelement formulation

The macro-element is formulated as a one-dimensional element defined by three nodes, two at the element ends and one at midspan. All three nodes are defined in the three-dimensional space. It consists of an assemblage of two panels subjected to the same average shear deformation, separated by three nonlinear sections accounting for deformations due to axial strains. The kinematic of this element is, therefore, the one presented in Figure 3.1. The shear response is controlled by a non-linear interface located at mid-height of the element, in which all shear deformations of the two panels are lumped (Figure 3.1b). The shear strength of the section is coupled to the axial load that acts on the mid-section. In order to decouple shear deformations from the axial deformations and therefore avoid an iterative element state determination procedure to enforce equilibrium, a non-dilatant behaviour of the shear interface is postulated.

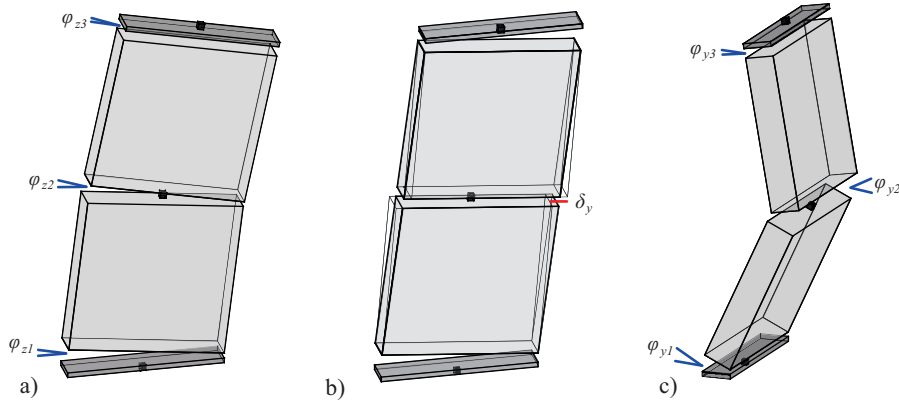


Figure 3.1 – Deformation modes of the macro-element: in-plane flexure only (a), in-plane flexure and shear (b), out-of-plane response (c).

The flexural response is described by three sections, that can model coupled in-plane and out-of-plane rocking. The section at midspan of the element allows modelling in a simplified way the one-way out-of-plane bending of the element. The uplift related to the in-plane and out-of-plane flexural response can be properly described by suitable sectional models. This feature is, for example, particularly relevant if the macro-element is used to model piers coupled by RC slabs or spandrels in buildings with highly deformable floors, in which the axial deformations related to the flexural response can largely increase the axial load in the spandrels, and consequently the shear force that such spandrels can transfer. Moreover, for the out-of-plane response, the uplift in rocking constitutes an important source of resistance when the vertical displacements of the pier are partially restrained by, for example, a rigid floor with considerable out-of-plane stiffness. The macro-element can therefore represent the out-of-plane failure of piers with transient static boundary conditions (e.g. change in axial load related to the rocking response of the pier) and transient kinematic boundary conditions (e.g. sliding or uplift of the floor).

The element nodes are located at the extremities and at midspan of the element; the implementation allows for rigid offsets of the end nodes. The end nodes (named i and j in Figure 3.1) are standard three-dimensional nodes whose degrees of freedom describe three displacements and three rotations in space. The internal node e defines the displacements in the three directions of the extremities of block A and B (points A' and B' in Figure 3.1), from which the finite rotations of the two blocks can be derived. The degrees of freedom of the three nodes are arranged in the vector \mathbf{u}_{local} (Figure 3.2a) as:

$$\begin{aligned} \mathbf{u}_{local} &= [u_i, v_i, w_i, \varphi_{xi}, \varphi_{yi}, \varphi_{zi}, \quad u_j, v_j, w_j, \varphi_{xj}, \varphi_{yj}, \varphi_{zj}, \quad u_A, v_A, w_A, u_B, v_B, w_B]^T \\ \mathbf{q}_{local} &= [N_i, V_{yi}, V_{zi}, T_{xi}, M_{yi}, M_{zi}, \quad N_j, V_{yj}, V_{zj}, T_{xj}, M_{yj}, M_{zj}, \quad N_{eA}, V_{yA}, V_{zA}, N_{eB}, V_{yB}, V_{zB}]^T \end{aligned} \quad (3.1)$$

From the vector of local displacements, the 11 displacements (Figure 3.2b) defining the displacements at the flexural sections, the shear deformations of the panels and a constant torsional deformation

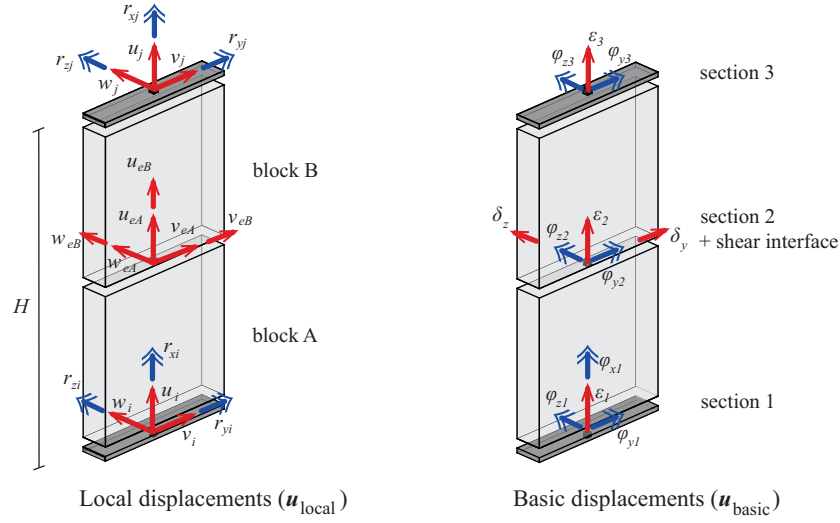


Figure 3.2 – Definition of local and basic degrees of freedom of the macro-element.

along the element ($\mathbf{u}_{\text{basic}}$) can be obtained as:

$$\mathbf{u}_{\text{basic}}^{(P-\Delta)} = \begin{bmatrix} d_1 \\ \varphi_{z1} \\ \varphi_{y1} \\ d_2 \\ \varphi_{z2} \\ \varphi_{y2} \\ d_3 \\ \varphi_{z3} \\ \varphi_{y3} \\ s_y \\ s_z \\ \varphi_{tors} \end{bmatrix} = \begin{bmatrix} u_{eA} - u_i + \frac{(v_{eA} - v_i)^2 + (w_{eA} - w_i)^2}{H} \\ -\varphi_{zi} - (v_{eA} - v_i) \frac{2}{H} \\ -\varphi_{yi} - (w_{eA} - w_i) \frac{2}{H} \\ -u_{uA} + u_{eB} \\ (-v_{eA} - v_{eB} + v_i + v_j) \frac{2}{H} \\ (w_{eA} + w_{eB} - w_i - w_j) \frac{2}{H} \\ -u_{eB} + u_j + \frac{(v_{eB} - v_j)^2 + (w_{eB} - w_j)^2}{H} \\ \varphi_{zj} + (v_{eB} - v_j) \frac{2}{H} \\ \varphi_{yj} + (w_{eB} - w_j) \frac{2}{H} \\ v_{eB} - v_{eA} \\ w_{eB} - w_{eA} \\ \varphi_{xj} - \varphi_{xi} \end{bmatrix} \quad (3.2)$$

The exact formulation of the compatibility relations, accounting for finite rotations in space, is reported in the supplemental materials (see Section 3.8). To avoid the complexity of the co-rotational formulation while still accounting for second-order effects for moderate displacements, the element was implemented using only a $P - \Delta$ formulation, expressed by Equation 3.2, derived as a second-order Taylor-series expansion of the exact equations. Second-order effects are typically less relevant for the in-plane behaviour of a masonry element, but must be considered when modelling its out-of-plane behaviour.

The section models adopted for the three flexural sections and the shear interface shown in Figure 3.2 provide the local response, in terms of sectional forces and the stiffness matrices of these sections. The

Chapter 3. Three-dimensional macro-element for modelling masonry walls

vector of basic forces \mathbf{q}_{basic} is assembled as:

$$\mathbf{q}_{basic} = [N_1, M_{z1}, M_{y1}, N_2, M_{z2}, M_{y2}, N_3, M_{z3}, M_{y3}, V_y, V_z, M_{tors}] \quad (3.3)$$

The axial and flexural behaviour of each section is described by three section models, relating a set of deformations $\boldsymbol{\varepsilon}_i$ (one axial deformation ε_{0i} and two curvatures χ_{zi} and χ_{yi}) to the corresponding sectional forces $\mathbf{q}_{basic}^{(i)}$:

$$\mathbf{q}_{basic}^{(i)} = \begin{bmatrix} N_i \\ M_{zi} \\ M_{yi} \end{bmatrix} = \mathbf{q}_{sect}^{(i)}(\boldsymbol{\varepsilon}_i) \quad (3.4)$$

In addition to the sectional models, two shear interfaces describe the nonlinear in-plane and out-of-plane shear response, through a biaxial material law coupled to the axial load applied to the middle section. The torsional behaviour, accounted for by the first section model, is modelled as linear elastic and decoupled from all other behaviour modes.

The basic displacements $\mathbf{u}_{basic}^{(i)}$ corresponding to the flexural response can be interpreted as the result of constant flexural deformations $\boldsymbol{\varepsilon}_i$ integrated along a certain length of the macro-element $w_i H$, if H is the total height of the element:

$$\boldsymbol{\varepsilon}_i = \begin{bmatrix} \varepsilon_{0i} \\ \chi_{zi} \\ \chi_{yi} \end{bmatrix} = \frac{1}{w_i H} \begin{bmatrix} d_i \\ \varphi_{zi} \\ \varphi_{yi} \end{bmatrix} = \frac{1}{w_i H} \mathbf{u}_{basic}^{(i)} \quad (3.5)$$

As a consequence, the stiffness matrix $\mathbf{K}^{(i)}$ relative to the interface i needs therefore to be derived from the stiffness of the sectional model $\mathbf{K}_{sect}^{(i)}$ as:

$$\mathbf{K}^{(i)} = \frac{\partial \mathbf{q}_{basic}^{(i)}}{\partial \mathbf{u}_{basic}^{(i)}} = \frac{1}{w_i H} \frac{\partial \mathbf{q}_{sect}^{(i)}}{\partial \boldsymbol{\varepsilon}_i} = \frac{1}{w_i H} \mathbf{K}_{sect}^{(i)} \quad (3.6)$$

The portion of the macro-element attributed to each section can be assigned by the user, similarly to assigning weights to different integration points along the axis of a beam element. The weights can be chosen such that the flexural response of the macro-element reproduces exactly the one of a force-based beam element with three integration points, since the equilibrium condition is strictly imposed at every section, avoiding the potential force unbalance at section level that displacement-based elements show. However, the solution procedure of the here proposed macro-element is simpler than the solution procedure of a classical force-based beam element and avoids a nested internal iteration scheme, because the equilibrium condition at the section level is imposed directly by the global iterative scheme. The optimum choice, in terms of correspondence between the behaviour of the macro-element and the solution of a beam subjected to a generic nonlinear curvature profile, is given by the set of weights \mathbf{w} of a Gauss-Lobatto integration scheme with three integration points, i.e. the set of weights $[1/6, 2/3, 1/6]$. Such scheme leads to the exact integration of a polynomial of order three. The top displacements of the macro-element correspond therefore to the exact solution of a beam subjected to a parabolic curvature profile, including clearly the elastic solution when no

element loads are applied. However, other choices of integration weights are possible; they can be related, for example, to the adoption of a user-defined plastic hinge length, improving the modelling of the nonlinear range, at the cost of a lower accuracy of the linear elastic solution. The in-plane response of the macroelement by Penna et al. (Penna et al., 2014) and implemented in Tremuri is obtained assuming that only the two end sections can deform, which leads, for some loading conditions, to an elastic element stiffness that is lower than the one of an elastic beam. In order to reproduce the behaviour of the macroelement by Penna et al. (Penna et al., 2014) by the macro-element implemented in OpenSees, the following set of weights is used, if the Tremuri-flag is activated: $[0.495, 0.01, 0.495]$. Note that all assigned weights must be positive and therefore the central interface should be assigned a positive negligible integration weight. In order to reproduce the behaviour best, the central interface should be modelled as linear elastic.

The shear interface, for simplicity, is split into two components, namely the in-plane component along the local axis y , and the out-of-plane component along the local axis z . The two components, in the general formulation, can be assigned two different shear models. Both shear models must be biaxial material models, describing the shear response as a function of a shear displacement s_y , s_z , and an axial displacement s_n :

$$V_y = V_y(s_n, s_y), \quad V_z = V_z(s_n, s_z) \quad (3.7)$$

For the modelling of masonry elements, a nonlinear shear model, such as the one presented in Section 3.4, can be applied in the in-plane direction and an elastic model in the out-of-plane direction, since the out-of-plane force capacity is controlled by the flexural behaviour. If, however, the user imposes two nonlinear models for the two directions, a rectangular strength domain is obtained for combined in-plane/out-of-plane loading. The coupling with the axial load is accounted for by the axial deformation s_n assigned to the shear interface. The macro-element formulation assumes a non-dilatant behaviour of the shear models. In such way, equilibrium between the axial force acting on the interface and the axial force N_2 transferred by the midheight section can be simply enforced through Equation 3.8, without the need of an internal iterative scheme. The axial stiffness k_n of the shear interface is a parameter that can be chosen as an arbitrary positive number.

$$s_n = N_2/k_n \quad (3.8)$$

The dependency of the shear response on the axial force N_2 needs to be considered also when assembling the basic stiffness matrix of the macro-element. Considering Equation 3.8, for the chain rule the derivative that is needed for the shear model in the in-plane direction reads:

$$\frac{\partial V_y}{\partial \mathbf{u}_{basic}^{(2)}} = \frac{dV_y}{ds_n} \frac{ds_n}{dN_2} \frac{\partial N_2}{\partial \mathbf{u}_{basic}^{(2)}} \quad (3.9)$$

The vectors $\overline{\mathbf{k}}_y$ and $\overline{\mathbf{k}}_z$ containing the can be defined therefore as a function of the stiffness matrix \mathbf{K}_{int}

of the shear interface as:

$$\bar{\mathbf{k}}_y = \left(\frac{\partial V_y}{\partial \mathbf{u}_{basic}^{(2)}} \right)^T = \frac{K_{int2,1}^{(y)}}{k_n} \cdot [1, 0, 0] \mathbf{K}^{(2)} \quad (3.10)$$

The basic stiffness matrix is then assembled as:

$$\mathbf{K}_{basic} = \frac{\partial \mathbf{q}_{basic}}{\partial \mathbf{u}_{basic}} = \begin{bmatrix} [\mathbf{K}^{(1)}]_{3 \times 3} & \mathbf{0} & \mathbf{0} & \mathbf{0} & \mathbf{0} & \mathbf{0} \\ \mathbf{0} & [\mathbf{K}^{(2)}]_{3 \times 3} & \mathbf{0} & \mathbf{0} & \mathbf{0} & \mathbf{0} \\ \mathbf{0} & \mathbf{0} & [\mathbf{K}^{(3)}]_{3 \times 3} & \mathbf{0} & \mathbf{0} & \mathbf{0} \\ \mathbf{0} & [\bar{\mathbf{k}}_y]_{1 \times 3} & \mathbf{0} & K_{int2,2}^{(y)} & 0 & 0 \\ \mathbf{0} & [\bar{\mathbf{k}}_z]_{1 \times 3} & \mathbf{0} & 0 & K_{int2,2}^{(z)} & 0 \\ \mathbf{0} & \mathbf{0} & \mathbf{0} & 0 & 0 & K_{tors}^{(1)} \end{bmatrix} \quad (3.11)$$

The transformation of forces and stiffness matrix from the basic to the local system is defined by the incremental compatibility and equilibrium matrices, which can include geometrical effects, if the user chooses this option. The incremental compatibility matrix Γ_C is obtained by derivation of the expressions defining the basic displacements in Equation 3.2, with respect to the set of nodal displacements \mathbf{u}_{local} . It needs to be computed at every update of trial nodal displacements, if the quadratic terms in Equation 3.2, defining the geometric nonlinearity, are considered. If such terms are omitted, the formulation becomes linear with respect to the geometry and the compatibility relations remain constant. The inverse path, from basic forces to nodal forces, is defined by the equilibrium matrix Γ_E . Applying the principle of contragradiency, such equilibrium matrix, which expresses the equilibrium conditions in the deformed configuration, can be obtained as in Equation 3.12. The complete expression defining the equilibrium matrix is reported in a supplemental document (see Section 3.8) and is valid for the $P - \Delta$ formulation.

$$\Gamma_C = \frac{\partial \mathbf{u}_{basic}}{\partial \mathbf{u}_{local}} = (\Gamma_E)^T \quad (3.12)$$

The equilibrium matrix can be derived, equivalently, formulating equilibrium conditions in the deformed configuration of the nodal forces. Since distributed loads acting in the direction of the element axis can induce second-order effects, their effect is included in the vector \mathbf{q}_0 and must be added to the sectional forces in the basic system. Once such forces are expressed in the local system through the incremental equilibrium matrix Γ_E , a second vector \mathbf{p}_0 , containing the reactions in the local system to the applied element loads, needs to be subtracted to ensure equilibrium at the nodes:

$$\mathbf{q}_{local} = \Gamma_E (\mathbf{q}_{basic} + \mathbf{q}_0) - \mathbf{p}_0 \quad (3.13)$$

The macro-element can account for element forces distributed with a rectangular or triangular profile acting along its axis; the derivation of the expressions for \mathbf{q}_0 and \mathbf{p}_0 , for both cases, can be found in the supplemental materials. The transformation of the stiffness matrix from the basic to the local system is slightly more involved, and requires the derivation of the geometrical stiffness matrix as in Equation

3.14. For linear geometry, the term \mathbf{K}_{geom} vanishes.

$$\mathbf{K}_{local} = \frac{\partial \mathbf{q}_{local}}{\partial \mathbf{u}_{local}} = \frac{\partial}{\partial \mathbf{u}_{local}} (\Gamma_E)(\mathbf{q}_{basic} + \mathbf{q}_0) + \Gamma_E \mathbf{K}_{basic} \Gamma_C \quad (3.14)$$

$$\mathbf{K}_{local} = \mathbf{K}_{geom} + \Gamma_E \mathbf{K}_{basic} \Gamma_E^T \quad (3.15)$$

3.3 Three-dimensional flexural response

Any sectional model available in OpenSees can be used for describing the section response of the macro-element, including a fibre section of generic shape in combination with any uniaxial material model at the local scale. The macro-element formulation proposed in Penna et al. (Penna et al., 2014) does not use fibre sections but uses an analytically integrated section modelling the flexural response. This approach is computationally efficient; it is therefore extended to bi-axial bending and also implemented in OpenSees. Such section model provides a direct relation between sectional deformations $\boldsymbol{\varepsilon}_{sect}$ ($\varepsilon_0, \chi_z, \chi_y$ as defined in Figure 3.3) and the associated forces \mathbf{q}_{sect} (N, M_z, M_y) of a rectangular section, without a numerical integration of a fibre response. This direct relation is derived for a material with zero tensile strength and limited compressive strength. The coupled response for in-plane and out-of-plane flexure-rocking is exact if no compressive damage occurs, resulting in a nonlinear elastic model.

The section response is obtained by analytical integration of the stresses in the compressed part of the section. In the reference system indicated in Figure 3.3, the field of axial deformations $\varepsilon(y, z)$ can be expressed as:

$$\varepsilon(y, z) = \varepsilon_0 - \chi_z y + \chi_y z = \begin{bmatrix} 1 & -y & z \end{bmatrix} \boldsymbol{\varepsilon}_{sect} = \mathbf{b}(y, z)^T \boldsymbol{\varepsilon}_{sect} \quad (3.16)$$

Equation 3.17 gives the y coordinates l_1 and l_2 of the intersection of the neutral axis with the section edge, for $z = t/2$ and $z = -t/2$. The position of the neutral axis defines the cracking condition of the section.

$$l_1 = \frac{2\varepsilon_0 + \chi_y t}{2\chi_z}, \quad l_2 = \frac{2\varepsilon_0 - \chi_y t}{2\chi_z}, \quad (3.17)$$

The section is fully compressed when both l_1 and l_2 are bigger than $L/2$ and the curvature χ_z is positive or, conversely, when they are both smaller than $-L/2$ and χ_z is negative. In this case, the elastic solution given in Equation 3.18 applies. In the opposite case, the section is completely in tension and, according to the hypothesis of zero tensile strength, cannot transfer any force.

$$\mathbf{q}_{sect,el}^{(i)} = \begin{bmatrix} N_{el} \\ M_{z,el} \\ M_{y,el} \end{bmatrix} = \begin{bmatrix} E L t \varepsilon_0 \\ E \frac{tL^3}{12} \chi_z \\ E \frac{L t^3}{12} \chi_y \end{bmatrix} \quad (\text{elastic case}) \quad (3.18)$$

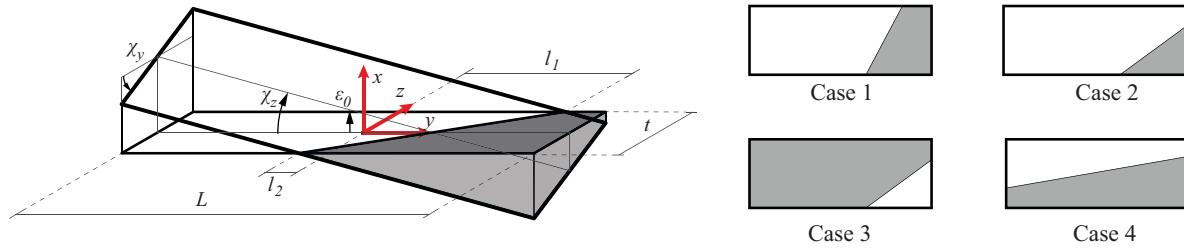


Figure 3.3 – Definition of sectional reference system, variables, and various cases of neutral axis orientation to be solved.

Else, when the section is only partially compressed, four main cases can be defined as shown in Figure 3.3. The analytical solution of these cases yields a nonlinear elastic model, provided in the supplemental materials (Section 3.8)., which represents the bi-axial flexural response of the section without resorting to a numerical integration of a fibre section with a uniaxial constitutive model.

Such nonlinear elastic model can describe the flexural response of a rectangular section for a no-tension material in the absence of compressive damage. However, although typical axial load ratios of masonry piers are rather low, toe-crushing is often observed as a phenomenon causing the lateral failure of the element and defining its displacement capacity. Modelling the element failure in flexure as a consequence of crushing, though, requires the definition of the softening response of the material, which for field applications is often not available or reliable. Alternatively, the displacement capacity of masonry elements is more practically defined in codes and in the literature in terms of drift limits. If, following this approach, the displacement capacity of a flexure-controlled element is defined through a drift limit, the phenomena related to toe-crushing that the section model needs to describe are mainly the reduction of lateral strength and some energy dissipation in loading/unloading cycles. To define the hysteretic response of a section model that does not include a numerical integration of a fibre section, the approach by Penna et al. (Penna et al., 2014) is followed. They assume a bilinear constitutive model for masonry in compression, with a damage stiffness degradation, and derive correction terms to be applied to the section forces for in-plane bending. As an approximated solution of the problem for bi-axial bending, the section can be divided into n slices (Figure 3.4) of width t_j , where the index j indicates the j -th slice. Their position is defined by the coordinate z_j (Equation 3.19). It is recommended to choose for n a value in the order of 5-20, depending on the level of detail that is required for modelling the crushing under out-of-plane bending, as the discretisation of the section implies an approximated solution in out-of-plane bending.

$$z_j = \left(j - \frac{1}{2}\right) \frac{t}{n} - \frac{t}{2}, \quad t_i = t_n \quad (3.19)$$

$$\boldsymbol{\varepsilon}^{(j)} = \begin{bmatrix} \varepsilon_0^{(j)} \\ \chi^{(j)} \end{bmatrix} = \begin{bmatrix} \varepsilon_0 + z_j \chi_y \\ \chi_z \end{bmatrix} = \begin{bmatrix} 1 & 0 & z_j \\ 0 & 1 & 0 \end{bmatrix} \boldsymbol{\varepsilon}_{sect} \quad (3.20)$$

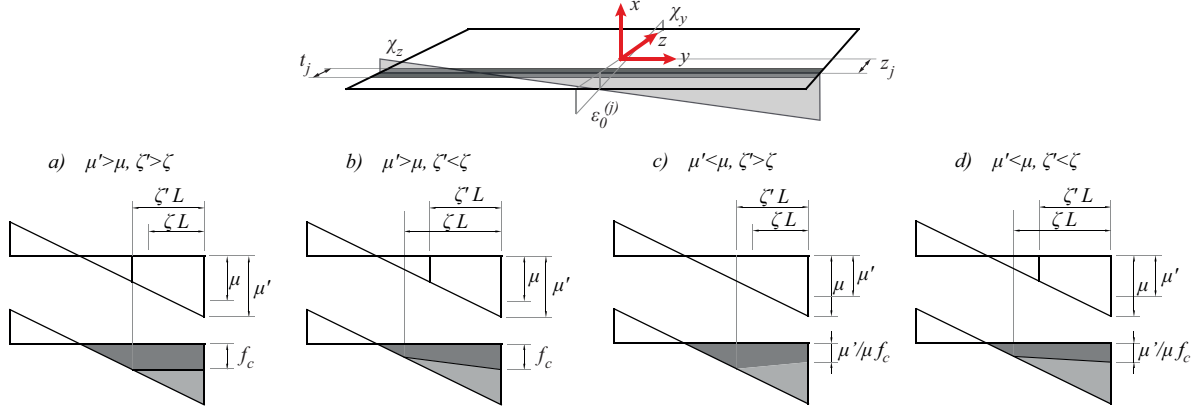


Figure 3.4 – Stress distributions for different evolution cases of crushing damage variables.

The correction term $N_{c,j}$ to be applied to each slice follows the formulation already derived in Penna et al. (Penna et al., 2014). It is based on two damage variables per edge, describing the maximum ductility demand experienced by the slice edge (μ_j) and the portion of section involved in the compressive nonlinearity (ζ_j). When a new displacement step is imposed, trial values of the damage variables (μ'_j and ζ'_j , with respect of the positive edge of the section) can be calculated from Equations 3.22-3.23. The compact notation making use of the vectors defined in Equation 3.21 is introduced only in order to ease the derivation of the stiffness matrix.

$$\mathbf{b}_j = \mathbf{b}\left(\frac{L}{2}, z_j\right) = \begin{bmatrix} 1 & -\frac{L}{2} & z_j \end{bmatrix}^T, \quad \mathbf{c} = \begin{bmatrix} 0 & \frac{L}{3} & 0 \end{bmatrix}^T \quad (3.21)$$

$$\mu'_j = \frac{-E(\varepsilon_0^{(j)} - \frac{L}{2}\chi^{(j)})}{f_c} = -\frac{E}{f_c} \mathbf{b}_j^T \boldsymbol{\varepsilon}_{sect} \quad (3.22)$$

$$\zeta'_j = \frac{(\mu'_j - 1)\frac{f_c}{E}}{\chi_z L} = -\frac{\mathbf{b}_j^T \boldsymbol{\varepsilon}_{sect} + \frac{f_c}{E}}{3\mathbf{c}^T \boldsymbol{\varepsilon}_{sect}} \quad (3.23)$$

Depending on the previous load history, for each slice j , four cases can occur, as shown in Figure 3.4. Each case is defined by the relative values of the trial damage variables (μ' , ζ'), and the committed value of the damage variables reached in the previous load history (μ , ζ). If any of the current values μ' , ζ' is bigger than the corresponding values μ , ζ , the damage parameter needs to be updated. Based on this update of the damage variables, the stress distributions shown in Figure 3.4 can be described. Cases b, c and d, are approximate stress distributions, which feature a nonlinear distribution of stresses

in the portion of the section where crushing occurs, as shown in Figure 3.5. The correction term $N_{c,j}$ accounting for crushing is:

$$N_{c,j} = -E \frac{\mu_j - 1}{2\mu_j} t_j (\zeta_j L) \mathbf{b}_j^T \boldsymbol{\varepsilon}^{(j)} \quad (3.24)$$

From Equation 3.24 the sectional forces can be derived as:

$$\mathbf{q} = \mathbf{q}_{el} + \sum_{j=1}^n \begin{bmatrix} 1 \\ -\left(\frac{L}{2} - \frac{\zeta_j L}{3}\right) \\ z_j \end{bmatrix} N_{c,j} = \mathbf{q}_{el} + \sum_{j=1}^n (\mathbf{b}_j + \zeta_j \mathbf{c}) N_{c,j} \quad (3.25)$$

The correction corresponding to crushing at the negative edge can be derived in the same manner. The complete expression of the correction terms including both edges of the section is not reported here for brevity. The tangent matrix of the sectional model can be derived from Equation 3.25, as:

$$\mathbf{K}_{sect} = \frac{\partial \mathbf{q}_{el}}{\partial \boldsymbol{\varepsilon}} + \sum_{j=1}^n \left[(\mathbf{b}_j + \zeta_j \mathbf{c}) \left(\frac{\partial N_{c,j}}{\partial \boldsymbol{\varepsilon}^{(j)}} + \frac{\partial N_{c,j}}{\partial \mu_j} \frac{\partial \mu_j}{\partial \boldsymbol{\varepsilon}^{(j)}} + \frac{\partial N_{c,j}}{\partial \zeta_j} \frac{\partial \zeta_j}{\partial \boldsymbol{\varepsilon}^{(j)}} \right)^T + \mathbf{c} \left(\frac{\partial \zeta_j}{\partial \boldsymbol{\varepsilon}^{(j)}} \right)^T N_{c,j} \right] \quad (3.26)$$

The first term includes the derivatives of the expressions provided in the supplemental document (Section 3.8). The derivatives of the damage variables are obtained from Equations 3.22-3.23 in case of evolution of the corresponding damage variable in the current step, being equal to zero otherwise.

Based on this formulation, the flexural behaviour of the section under combined in-plane and out-of-plane cyclic loading can be modelled. Figure 3.5 shows the moment-curvature hysteresis for different orientations θ of the applied moment, ranging from pure in-plane loading ($\theta=0^\circ$) to pure out-of-plane loading ($\theta=90^\circ$). The figure is plotted for a constant axial load and a geometrical ratio $L/t = 5$. It shows that toe-crushing leads to a reduction of the moment capacity and a reduced uplift related to rocking. The consideration of toe-crushing has also an effect on the dissipative behaviour of the section, that would be otherwise null. However, the energy dissipation related to in-plane flexural failure of masonry elements is typically much smaller than the one observed for shear failure. A final remark regards the maximum curvature capacity of the section, that is not limited by this toe-crushing model. The loss of lateral and/or axial force capacity must be related, in this case, to a drift criterion, as discussed in Section 3.5.

3.4 Shear response

The in-plane shear failure of a masonry panel under lateral loading can be characterised by different failure mechanisms, which can be summarised in (i) the cracking along its diagonal in the direction of the compression strut, following only the head and bed joints or involving also the tensile cracking of units and (ii) sliding along the bed joints (Magenes and Calvi, 1997). Different failure criteria can be applied to model the two main failure mechanisms, namely a tensile criterion, such as the one proposed by Turnšek and Čačovič (1971), and a frictional criterion. However, if the diagonal

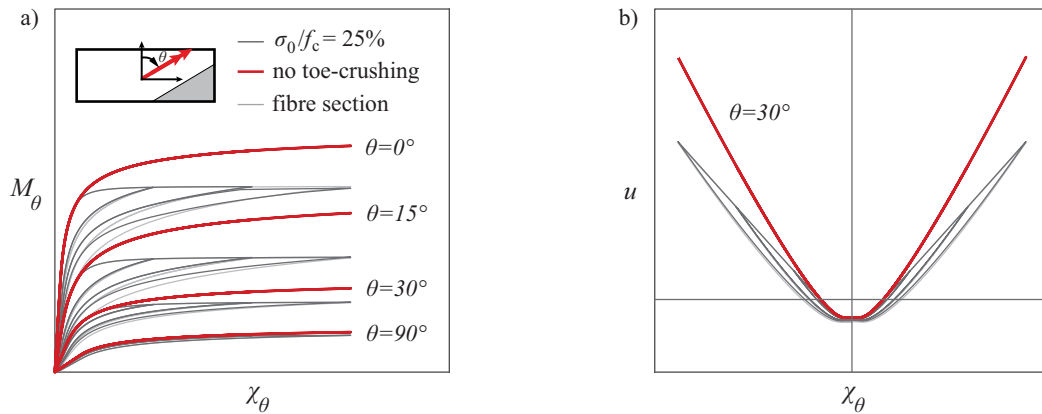


Figure 3.5 – Cyclic flexural behaviour of a section for combined in-plane/out-of-plane loading using the analytical solution ($L/t = 5$, constant axial load ratio 25%); the fibre section solution obtained for the same material model is shown as reference. a) Moment-curvature response for different moment orientations, with and without toe-crushing; b) uplift of the section for an orientation of the moment vector of $\theta = 30^\circ$.

cracking is approximated by a combination of sliding surfaces along the bed joints (disregarding the possible cracking of units), a frictional criterion can be applied to model both failure modes. It can be considered, moreover, that a linear failure surface in the $N - V$ plane, which describes a frictional criterion, can be obtained as a Taylor-series approximation of the parabolic failure surface that corresponds to a tensile cracking criterion (Penna et al., 2014).

As Penna et al. (2014), the macro-element models shear deformations as a constant shear deformation along the entire element (see Figure 3.1). This constant strain can be lumped into a finite displacement s of a shear spring, located at the centre of the element, related to the shear and compression forces by a nonlinear shear model. Such model needs to describe adequately the in-plane shear response of a panel in the cyclic range, including a maximum force capacity depending on the current axial load, the stiffness reduction due to cracking before the peak force is attained, a post-peak softening response, and an energy dissipation in hysteresis cycles compatible with the one observed experimentally. For this purpose, an interface model representing the macroscopic integration of a local shear criterion is needed. In this study, the Gambarotta and Lagomarsino (1997) shear model adopted in the macroelement by Penna et al. (2014), as well as a different shear model corresponding to an adaptation of the cohesive/frictional interface model proposed by Alfano and Sacco (2006) were implemented.

The latter model postulates that the whole surface A subjected to shear transfer can be divided into two parts, one undamaged part A_u , completely elastic, and a damaged part A_d , where frictional sliding occurs, governed by a damage evolution law. Both parts are subjected to the same displacement, as in Equation 3.28.

$$A = Lt = A_u + A_d = (1 - D)A + DA \quad (3.27)$$

$$\mathbf{s} = \begin{bmatrix} s_n \\ s \end{bmatrix} = \begin{bmatrix} s_{n,u} \\ s_u \end{bmatrix} = \begin{bmatrix} s_{n,d} \\ s_d \end{bmatrix} \quad (3.28)$$

The total forces transferred by the shear spring can be calculated as the sum of the contributions of the two parts:

$$\mathbf{q} = \begin{bmatrix} N \\ V \end{bmatrix} = (1-D) \begin{bmatrix} N_u \\ V_u \end{bmatrix} + D \begin{bmatrix} N_d \\ V_d \end{bmatrix} = (1-D) \mathbf{q}_u + D \mathbf{q}_d \quad (3.29)$$

The elastic properties of the shear spring are described by Equation 3.30, which imposes on the macro-element the shear stiffness of an elastic beam with rectangular section, where G is the shear modulus of masonry. The frictional sliding is represented by the inelastic displacements s^{in} . Assuming zero-dilatancy, the expression in Equation 3.31 can be derived.

$$\mathbf{q}_u = \mathbf{K}_{el} \mathbf{s} = \begin{bmatrix} k_n & 0 \\ 0 & k_s \end{bmatrix} \cdot \begin{bmatrix} s_n \\ s \end{bmatrix} = \begin{bmatrix} k_n & 0 \\ 0 & \frac{5GA}{6H} \end{bmatrix} \cdot \begin{bmatrix} s_n \\ s \end{bmatrix} \quad (3.30)$$

$$\mathbf{q}_d = \mathbf{K}_{el} (\mathbf{s} - \mathbf{s}^{in}) = \begin{bmatrix} k_n & 0 \\ 0 & k_s \end{bmatrix} \cdot \begin{bmatrix} s_n \\ s - s^{in} \end{bmatrix} \quad (3.31)$$

If the axial force transferred by the mid-section is non-positive and the section therefore in compression (which is always verified by the section model in Section 3.3), the axial strain to be applied to the shear spring can be derived as in Equation 3.8. If on the contrary the axial force N_2 is positive, because of the use of sectional model accounting also for some tensile strength of the material, it is assumed that the shear spring does not transfer any load. The plastic frictional model that is used is a simple Mohr-Coulomb law, defined by the yield function f in Equation 3.32, which is a function of the friction coefficient μ_R , and the non-associated plastic potential g .

$$f(\mathbf{q}_d) = \mu_R N + |V|, \quad g(\mathbf{q}_d) = |V| \quad (3.32)$$

Such potential enforces the zero-dilatancy hypothesis, since:

$$\mathbf{s}^{in} = \lambda \frac{\partial g}{\partial \mathbf{q}_d} = \lambda \begin{bmatrix} 0 \\ \text{sign}(V) \end{bmatrix} \quad (3.33)$$

Loading-unloading conditions are defined by the usual Kuhn-Tucker conditions, i.e.:

$$\dot{\lambda} \geq 0, \quad f(\mathbf{q}_d) \leq 0, \quad \dot{\lambda} f(\mathbf{q}_d) = 0 \quad (3.34)$$

The solution of a finite displacement increment does not require any iterations if the friction angle is constant. A trial state corresponding to a purely elastic increment can be defined as:

$$\mathbf{q}_d^{trial} = \mathbf{K}_{el} (\mathbf{s} - \mathbf{s}_n^{in}) \quad (3.35)$$

If the trial value of the yield function is positive in the trial state defined by Equation 3.35, the increment of the plastic multiplier $\Delta\lambda$ is calculated as:

$$\Delta\lambda = \frac{\mu_R N^{trial} + |V^{trial}|}{k_s} \quad (3.36)$$

The damage evolution law, which controls the evolution of the damaged portion of the surface subjected to shear, has to account for all the phenomena that cause a reduction of the force capacity and stiffness of a masonry element failing in shear. If the local response is modelled, a common hypothesis is to assume that only the cohesive contribution undergoes damage (Alfano and Sacco, 2006; Gambarotta and Lagomarsino, 1997). However, when modelling the element response of a masonry wall, the values of cohesion and friction angle are typically derived by fitting a linear trend to the force capacity measured in experimental tests (Vanin et al., 2017b). Assuming that damage is only associated to cohesion can in this case result in an insufficient reduction of the force capacity in the post-peak range and an excessive energy dissipation in hysteresis cycles. To overcome this short-coming, the damage law originally used by Alfano and Sacco (2006) is modified and it is assumed that also part of the frictional contribution can be lost in the damage process. In such model, the maximum force capacity is controlled by a friction coefficient μ_0 , which can be derived directly from experimental test series or code values. In addition, a residual friction coefficient μ_R is defined, which can be tuned to match better the post-peak response and energy dissipation. The residual force capacity is $\mu_R N$ and the total loss in force corresponds therefore to the cohesive contribution and part of the frictional contribution equal to $(\mu_0 - \mu_R)N$.

The progressive force capacity loss is controlled by the damage law, which is defined as a function of the total interface displacements s in order to obtain a phenomenological model that reproduces the main features of the cyclic response of a masonry wall. The pre-peak response is defined by a maximum force capacity V_{max} reached for a certain displacement s_{max} . As in Penna et al. (2014), s_{max} is written as a function of a parameter G_c , which controls the stiffness reduction after damage initiation (Figure 3.6a). The force capacity can, in principle, be defined by any criterion depending on the axial force N , provided that it is bigger than the residual shear strength for any possible value of N . For this study, the Mohr-Coulomb criterion in Equation 3.37 is applied, which satisfies this condition for all $\mu_0 \leq \mu_R$.

$$V_{max} = cLt - \mu_0 N \quad (3.37)$$

This linear criterion can be interpreted also as a linearisation of different failure criteria (Penna et al., 2014), such as the criterion proposed by Mann and Muller (Mann and Muller, 1982) or Turnšek and Čačovič (1971), around the expected level of axial load. The displacement s_{max} can be defined as a function of the displacement s_0 , corresponding to the attainment of the maximum frictional contribution, after which damage evolves, and the displacement s_{el} , equal to cLt/k_s , associated to the

cohesive contribution:

$$s_{max} = \frac{-\mu_R N}{k_s} + (1 + G_c) \frac{V_{max} + \mu_R}{k_s} = s_0 + (1 + G_c) s_{el} \quad (3.38)$$

An adimensional parameter x can then be defined as:

$$x = \frac{k_s |s| + \mu_R N}{k_s s_{max} + \mu_R N} \quad (3.39)$$

When x is smaller than one, the element is in the pre-peak part of its response and the damage evolution law is expressed by Equation 3.40, which ensures that the peak force is attained for a displacement s_{max} , with a zero tangent stiffness.

$$D = \left(1 - \frac{1}{1 + G_c}\right) x^{\frac{1}{G_c}}, \quad \text{for } x \leq 1 \quad (3.40)$$

The post-peak response is characterised by a progressive reduction of the force capacity, which is imposed as linear by the present model. The post-peak stiffness k_{pp} (assumed positive for softening response) can be expressed as a function of the displacement s_ξ , for which a force drop of ξV_{max} is attained:

$$k_{pp} = \frac{\xi V_{max}}{s_\xi - s_{max}} \quad (3.41)$$

Setting $\xi = 0.2$ allows defining the post-peak response as a function of the displacement corresponding to a 20% force drop. This displacement, expressed in terms of drift, is often considered when defining the ultimate limit state of a masonry wall, and can be derived either from experimental results or from code provisions. Imposing a linear decrease of the force capacity in the post-peak range, the second branch of the damage law can then be defines as:

$$D = \frac{1}{k_s |s| + \mu_R N} \left[(k_s + k_{pp}) |s| - \frac{k_{pp}}{k_s} G_c \mu_R N - \frac{k_{pp}}{k_s} (1 + G_c) V_{max} - V_{max} \right] \leq 1, \quad \text{for } x > 1 \quad (3.42)$$

The algorithmic tangent operator can be obtained as in Alfano and Sacco (2006), by computing the derivatives of the damage evolution law with respect to the interface displacements. Such derivatives, omitted here for brevity, can be obtained, when damage evolution occurs, directly from Equations 3.40-3.42, applying the condition in Equation 3.8 for axial equilibrium and the chain rule. If there is sliding and therefore $\Delta\lambda > 0$, the matrix \mathbf{H}_t can be obtained from Equation 3.44; in all other cases $\mathbf{H}_t = \mathbf{K}_{el}$.

$$\mathbf{K}_{int} = (1 - D)\mathbf{K}_{el} + D\mathbf{H}_t - \mathbf{K}_{el}\mathbf{s}\left(\frac{\partial D}{\partial \mathbf{s}}\right)^T + \mathbf{q}_d^{trial}\left(\frac{\partial D}{\partial \mathbf{s}}\right)^T \quad (3.43)$$

$$\mathbf{H}_t = \begin{bmatrix} k_n & 0 \\ -\text{sign}(V)\mu_R k_n & 0 \end{bmatrix}, \quad \Delta\lambda > 0 \quad (3.44)$$

The influence of the model parameters on the envelope of the shear response is shown in Figure 3.6a. The nonlinear behaviour enters the nonlinear range when the shear force exceeds the residual frictional contribution $\mu_0 N$. The maximum force is reached for a displacement determined by the parameter G_c , which controls the softening of the response after nonlinearity occurs; for a value $G_c = 1$ the response is linear up to the maximum capacity. The linear postpeak branch is determined by specifying the drift at which a 20% force drop is reached. When damage is completed, the residual force capacity $\mu_R N$ is retained. The cyclic response is governed mainly by the choice of μ_R , which controls both the residual force capacity and the shape of hysteresis cycles. Since the influence of μ_R in determining the force envelope is rather small, and complete damage is usually attained for high drifts, this parameter can be used mainly for controlling the dissipation related to the cyclic response. The introduction of the residual friction coefficient μ_R allows therefore imposing different hysteretic responses without altering the peak force capacity. (Figure 3.6b).

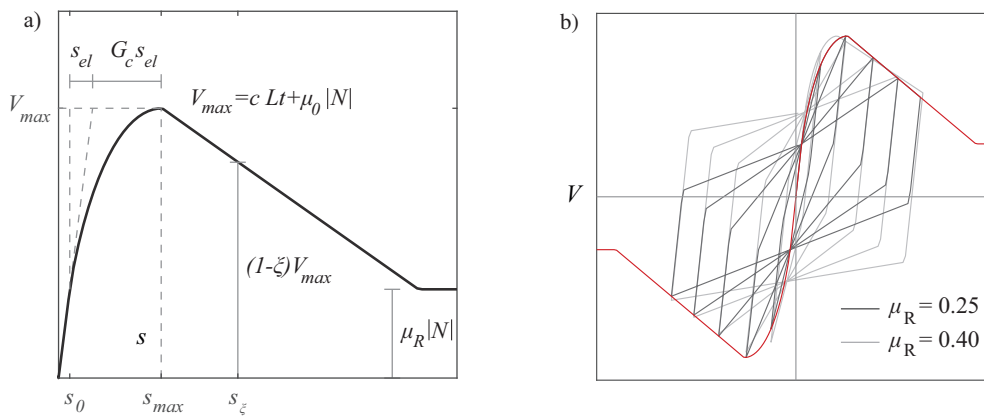


Figure 3.6 – Parameters defining the envelope of the shear response ($G_c=3$, $\mu_0=0.40$, $\mu_R=0.25$, $\xi=0.20$).
 b) influence of the residual friction coefficient μ_R on the cyclic shear response.

As an alternative to the model presented in Equations 3.27-3.44, the shear model proposed by Gambartotta and Lagomarsino and implemented in the research version of the software Tremuri (Penna et al., 2014), was implemented in OpenSees and can be used in combination with the proposed macro-element. Such model describes the cyclic shear response also as a combination of a frictional contribution and a cohesive contribution. Only the cohesive contribution undergoes damage, as one obtains with the model in Equations 3.27-3.44 if $\mu_R = \mu_0$. Details on the implementation are given in Penna et al. (2014), to which only the derivation of the tangent operator was added, in order to allow for quadratic convergence in global iterations. If the user wishes to decouple the shear response from the axial load, any uniaxial material law implemented in OpenSees can be used to describe the shear response.

The application of the model in Equations 3.27-3.44 to three shear and compression cyclic experimental tests on stone masonry walls is shown in Figure 3.7. The experimental curves were derived in a test campaign (Godio et al., 2019) on six single-leaf stone masonry walls. The walls, of dimensions

0.90x0.90x0.20 m, were built with a regular masonry texture made of squared limestone blocks and hydraulic lime mortar (for a comprehensive description of the test campaign refer to Godio et al. (Godio et al., 2019)). All walls were tested under fixed-fixed boundary conditions, imposing a constant shear span equal to half of the wall height. Different loading histories were applied, ranging from monotonic to cyclic with 2 or 100 repeated cycles per drift level. Only cyclic tests with two repeated cycles per drift level are extracted, as they are in general the most representative of the seismic demand imposed on masonry walls in regions of low to moderate seismicity. Figure 3.7 shows the comparison between experimental results and numerical simulations for walls SC1, SC5 and SC4, which were tested under an axial load ratio of 7.5%, 11.25% and 15%, respectively, and all failed in shear. The macro-element parameters applied to all three tests are given in Table 3.1. The elastic modulus E and the compressive strength f_c are derived from two compression tests on masonry wallettes. The shear modulus G is assumed to be equal to $E/3$. The cohesion c and the friction coefficient μ_0 are derived from linear regression of the maximum shear capacities of all six tested walls (Godio et al., 2019). The drift at 20% capacity drop δ_u is derived as the average of the drift capacities of walls SC5 and SC4, considering both the positive and negative envelopes. The residual friction coefficient μ_R is assumed to be equal to $\mu_0/3$. Imposing the same displacement histories as applied in the physical tests, the macro-element captures the envelope and some of the features of the cyclic response of the tested walls. In particular, the possibility of defining an initial friction coefficient, controlling the maximum force capacity, and a residual friction coefficient, controlling mainly the dissipative hysteretic behaviour, uncouples the fitting of the envelope curve, under different axial loads, from the fitting of a proper hysteretic energy dissipation. The asymmetry of the numerical response of the walls depends only on the asymmetry of the imposed displacement history, since the applied shear model would not define any asymmetric behaviour under a symmetric displacement history.

Table 3.1 – Material properties used in the numerical simulations of the three tests SC1, SC5 and SC4 (Godio et al., 2019).

E [MPa]	G [MPa]	f_c [MPa]	c [MPa]	μ_0	μ_R	G_c	δ_u [%]
4200	1400	10.0	0.05	0.47	0.16 ^(*)	6.0 ^(*)	0.87

(*) Calibrated parameter; all remaining values provided in Godio et al. (2019)

3.5 In-plane displacement capacity

A masonry pier subjected to in-plane loading loses first its horizontal and ultimately its axial load bearing capacity. Masonry buildings are often highly redundant structures and assuming that such buildings fail when the first element fails would be very conservative. For this reason, a modelling approach that captures the progressive strength loss and force redistribution to other members is often necessary. For this reason, the macro-element is formulated such that both the horizontal and axial load bearing loss can be simulated.

As a consequence of their formulations, the sectional models used for the flexural and the shear

3.5. In-plane displacement capacity

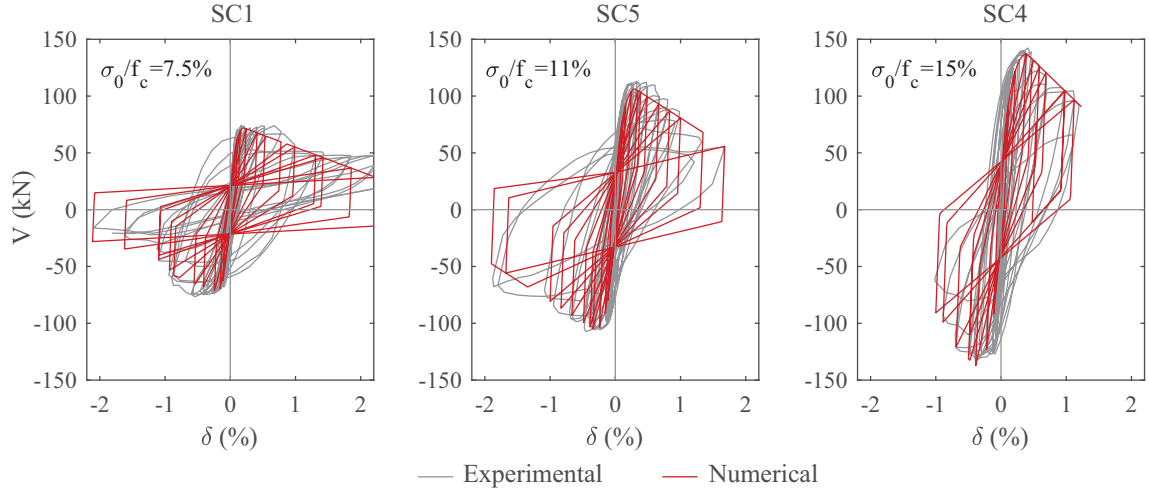


Figure 3.7 – Comparison between numerical and experimental (Godio et al., 2019) cyclic shear responses under three different axial load ratios.

response of the macro-element may not properly simulate the loss of lateral strength of existing masonry walls. The shear model presented in Section 3.4 describes a strength decrease in the post-peak range and a residual strength contribution but once the residual strength $\mu_R N$ is reached the strength does not degrade further. The sectional model proposed for the flexural response in Section 3.3 does not describe explicitly a maximum displacement capacity nor a loss of axial load bearing capacity. Although more complex sectional models could capture explicitly both features, for example through the use of a fibre section and a material law modelling a softening response after crushing, the new macro-element offers the possibility to specify on the element level drift limits at which first the horizontal and then the axial load bearing capacity are lost.

The in-plane shear and flexural drift components of the element in a deformed configuration are extracted from the basic displacements defined in Equation 3.2, removing rigid-body rotations, as:

$$\delta_{SH} = \frac{|s_y|}{H} \quad (3.45)$$

$$\delta_{FL} = \max\left[\left|\varphi_{z1} + \frac{\varphi_{z2}}{2}\right|, \left|\varphi_{z3} + \frac{\varphi_{z2}}{2}\right|\right] \quad (3.46)$$

Drift models derived from collections of experimental shear and compression tests on masonry walls show, together with a high uncertainty related to the estimation of this parameter, some trend relating a decrease of lateral drift capacity with increasing axial load ratio, both for modern unreinforced brick masonry (Pfyl-Lang et al., 2011a; Petry and Beyer, 2014a; Wilding and Beyer, 2018) and for stone masonry walls (Vanin et al., 2017b). In order to account for this, two generic drift models, one for shear and one for flexural failure, which can be expressed as a function of the applied axial load ratio $\frac{\sigma_0}{f_c}$ and the shear span H_0 , calculated at the current analysis step. Such models can be expressed in a generic

form as:

$$\delta_{SH,HC} = f_1 \left(\frac{\sigma_0}{f_c} \right) \cdot \left(\frac{H_0}{H} \right)^\beta, \quad \delta_{FL,HC} = f_2 \left(\frac{\sigma_0}{f_c} \right) \cdot \left(\frac{H_0}{H} \right)^\beta, \quad (3.47)$$

in which the user can define f_1 and f_2 as functions of the axial load ratio and the coefficient β . They can represent the a piecewise linear drift model (Petry and Beyer, 2014a; Vanin et al., 2017b), or, more simply, a constant drift capacity disregarding any effect of the axial load ratio, as indicated by the current version of Eurocode 8 (CEN, 2005). When exceeding the drift capacity specified by Equation 3.47, the lateral force capacity of the macro-element is either set to zero or reduced by a user-specified factor. At this point, the axial load bearing capacity is still maintained. The axial load bearing capacity is cancelled when the drifts specified by Equation 3.47 are exceeded by a factor $\alpha_{\frac{AC}{HC}}$.

$$\delta_{AC} = \alpha_{\frac{AC}{HC}} \cdot \delta_{HC} \quad (3.48)$$

After attainment of the drift limit corresponding to axial load collapse δ_{AC} defined Equation 3.48, the element capacity in axial and lateral directions is cancelled or reduced by a user-defined factor.

3.6 Out-of-plane behaviour

The out-of-plane response of unreinforced masonry walls includes a first phase in which the wall deforms and cracks, and a second phase in which a rocking mechanism develops until the stability point of the wall is reached, where the wall cannot resist any out-of-plane action. The problem can be analysed considering the masonry elements as an assembly of rigid blocks (Giuffr , 1994; Lagomarsino, 2015) or deformable blocks (Doherty et al., 2002; Griffith et al., 2003; Godio and Beyer, 2017).

When performing dynamic analyses of out-of-plane loaded masonry walls, it is essential to capture the force-displacement behaviour over the entire range of displacements, because the lateral accelerations that an element subjected to out-of-plane rocking can resist before overturning are significantly larger than the ones that lead to the initiation of the rocking mechanism (Doherty et al., 2002). The first part of the out-of-plane response of the new macro-element is governed by the chosen sectional model, while the second part of the response is controlled by the stability mechanisms, which depends on the $P - \Delta$ formulation. In the following, the behaviour of the macro-element under static out-of-plane loading is compared to limit analysis results (Section 3.6.1). Then, the dynamic behaviour, which depends next to the static force-displacement curve also on the chosen mass discretisation and damping model, is compared to analytical solutions and experimental results (Section 3.6.2).

3.6.1 Static Out-Of-Plane Response

The force-displacement behaviour of a single macro-element under uniform out-of-plane loading is compared in Figure 3.8 to the limit response of rigid block models. The analyses are performed for three different boundary conditions. The rigid block response (red line in Figure 3.8) is defined by a limit load multiplier λ_0 and a stability point at which the horizontal force drops to zero. For the

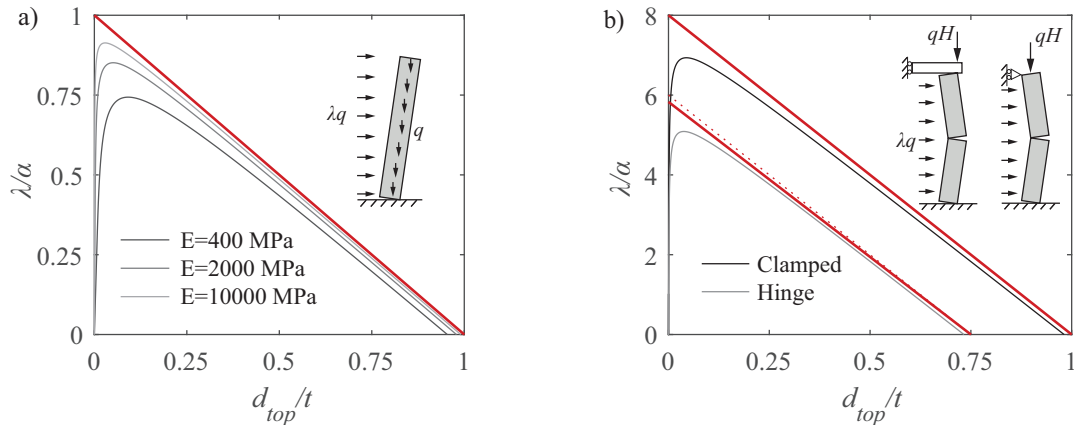


Figure 3.8 – Comparison of the out-of-plane response of one macro-element with rigid body solutions ($H=1.1$ m, $t=0.22$ m, $\alpha=H/t=5$): cantilever element under distributed loads (a); simply supported wall spanning between floors for different boundary conditions, subjected to overweight and distributed lateral load (b).

comparison a sectional model was chosen that reflects the hypotheses of limit analysis of rocking blocks (zero tensile strength, infinite compressive strength, very high axial stiffness) and therefore the two analyses provide close results. The reduction of the force capacity with reducing stiffness of the macro-element is in line with the results of analytical models (Godio and Beyer, 2017).

The macro-element solution provides the same results as the rigid block analysis for a cantilever wall (Figure 3.8a) and a wall with clamped-clamped boundary conditions (Figure 3.8b, case "Clamped"). When the wall is clamped at the bottom but the rotations at the top are unrestrained (Figure 3.8b, case "Hinge"), the minimum load multiplier obtained through limit analysis corresponds to a mechanism with the middle hinge slightly above mid-span. The formulation of the macro-element assumes that the third hinge is always at midheight, which introduces a small error. However, the rigid block solution, which corresponds to a hinge location at mid-span (dotted line in Figure 3.8b), is rather close to the exact solution with the hinge above midheight. This agrees with the findings by Derakhshan et al. (Derakhshan et al., 2013), who stated that the hypothesis of locating the hinge at mid-span is typically acceptable, since the theoretical position of the hinge is not too different for most overburden to self-weight ratios. Rotations may be restrained, for example, by slabs with considerable out-of-plane bending stiffness or ring beams. In the case of very flexible floors, which is common for historical buildings, the rotation at the wall top is often not significantly restrained.

3.6.2 Dynamic Out-Of-Plane Response

The dynamic out-of-plane response of the macro-element is governed not only by the quasi-static capacity curve, but also by the chosen mass distribution along the element and by the applied damping model. A consistent derivation of the mass matrix, accounting for all deformation modes and a

uniformly distributed mass along the element axis was derived, as well as the approximated diagonal lumped mass matrix. The consistent mass matrix leads to an improved modelling of inertial properties when compared to a diagonal lumped mass matrix but implies a slight increase in numerical cost. For implicit analyses such increase is often marginal, for some explicit analyses however the use of a diagonal mass matrix can provide a significant cost reduction. The derivation of both consistent and lumped mass matrices, and the error related to the use of the latter, are reported the supplemental materials (Section 3.8). Both mass matrices have been implemented for the macro-element in OpenSees and the user can chose between the two; all results presented in the following are obtained with a consistent mass matrix formulation.

A further aspect that governs the out-of-plane dynamic response of the macro-element is the damping model accounting for energy dissipation in rocking oscillations. The macro-element can model dissipative phenomena both at the level of the sectional response and through viscous damping and/or numerical damping. However, since for moderate axial loads significant crushing at the section edge does not take place, the dissipative behaviour under rocking oscillations is related mainly to damping. Since the first analytical studies on rigid blocks (Housner, 1963), dissipative phenomena of a rocking block are assumed to take place primarily at each impact. This energy dissipation is described by a coefficient of restitution relating the angular velocities after and before the impact. Using this approach, the free oscillation motion of a rigid rocking block is described by the following equation (Makris and Konstantinidis, 2003):

$$I_O \ddot{\theta} - mgR \sin(\alpha \operatorname{sign} \theta - \theta) = 0 \quad (3.49)$$

where α is equal to $\operatorname{atan}(H/t)$, m is the mass of the block and $R^2 = H^2 + t^2$ (see Figure 3.9). One criterion that can be applied to define the coefficient of restitution is the conservation of the angular momentum at the instant of an impact. As derived by Housner (Housner, 1963), the ratio e between the angular velocity before the impact $\dot{\theta}_1$ and the one after the impact $\dot{\theta}_2$ can be expressed, in this case, as:

$$e = \frac{\dot{\theta}_2}{\dot{\theta}_1} = 1 - \frac{3}{2} \sin^2 \alpha \quad (3.50)$$

Energy dissipation in finite element tools used in structural engineering is commonly treated, however, through viscous models. Although a rocking block and an elastic oscillator are fundamentally different (Makris and Konstantinidis, 2003), for a numerical simulation with common finite element solvers there is the need of approximating the instantaneous energy dissipation at impacts of a rigid body with an equivalent damping model. A possible approach is to rely uniquely on numerical damping, if a dissipative integration scheme is applied, as proposed by Vassiliou et al. (Vassiliou et al., 2017). If, however, the element is used in a larger structural model, including at the same time elements that are mainly loaded in-plane and elements with a principal out-of-plane response, the use of a classical Rayleigh damping can be desirable. In this case, the modelling of the energy dissipation must be achieved through an appropriate viscous damping model. Inserting a velocity-proportional term in

the inverted pendulum equation gives:

$$I_O \ddot{\theta} + c \dot{\theta} - mgR \sin(\alpha \operatorname{sign} \theta - \theta) = 0 \quad (3.51)$$

A calibration of the viscous damping c , which produces an energy dissipation comparable to the one of Housner's model in Equation 3.49 for fairly large rotation angles θ , was proposed by Vassiliou et al. (Vassiliou et al., 2014) as:

$$c(\alpha, m, R) = c_0 = 0.02 \left(\frac{\alpha}{0.1} \right)^2 mg^{0.5} R^{1.5} \quad (3.52)$$

If a stiffness proportional Rayleigh damping model is applied to the macro-element, where the damping matrix \mathbf{C} is set equal to $\beta_K \mathbf{K}$, an equivalent expression for β_K is needed. Considering an initial stiffness proportional model, for an idealised element rotation θ as a rigid block, one can assume that only the base section of the macro-element deforms, and that the rotation takes place exactly around the edge of the section. In this case, Rayleigh damping forces can be written as:

$$\mathbf{C}^{(1)} \dot{\mathbf{u}}^{(1)} = \beta_K \mathbf{K}_{in}^{(1)} \dot{\mathbf{u}}^{(1)} = \beta_K \frac{1}{w_1 H} \begin{bmatrix} EA & 0 & 0 \\ 0 & EI_z & 0 \\ 0 & 0 & EI_y \end{bmatrix} \begin{bmatrix} t/2 \\ 0 \\ 1 \end{bmatrix} \dot{\theta} \quad (3.53)$$

It can then be imposed that the moment around point O resulting from the stiffness proportional damping forces is equal to the viscous damping moment, which yields Equation 3.54. For a rectangular section, Equation 3.55 gives an explicit expression for the Rayleigh coefficient β_K .

$$M_O = \frac{\beta_K}{w_+ H} \left(EA \frac{t^2}{4} + EI_z \right) \dot{\theta} = c_0 \dot{\theta} \quad (3.54)$$

$$\beta_K = c_0 \frac{w_1 H}{4I_y} \quad (3.55)$$

It is known that the use of initial stiffness proportional Rayleigh damping can be problematic for strongly nonlinear systems (Petrini et al., 2008; Hall, 2006). Initial stiffness proportional damping is, however, preferred here over tangent stiffness proportional damping in order to avoid negative damping, due to the negative terms in the stiffness matrix related to nonlinear geometry effects, and to avoid abrupt changes of damping forces at each impact, which would introduce numerical damping and an excessive time-step dependency of the solution. Moreover, the calibration of the damping coefficient according to Equations 3.52-3.55 mitigates the problem of unrealistically high damping forces (Hall, 2006) that often occurs when initial stiffness proportional damping is used. The possibility of using the same damping model, for both in-plane loaded and out-of-plane loaded elements, remains, however, an open theme.

Numerical solutions of the differential equations in Equations 3.49 and 3.51, and the response of a sin-

Chapter 3. Three-dimensional macro-element for modelling masonry walls

gle macro-element subjected to free vibrations are compared in Figure 3.9a. The equivalent damping ratio of the macro-element is calculated from the free-vibration response with the logarithmic decrement method, assuming a damping ratio $\xi \ll 1$ and comparing maximum rotation amplitudes at the beginning and at the end of each complete rocking cycle, i.e., after two impacts at the base. Figure 3.9b plots the equivalent viscous damping ratios. The energy dissipation of the macro-element model, evaluated in terms of equivalent damping ratio, agrees in particular for larger rotations rather well with Housner's solution. The results are obtained for a stiff block ($E=50$ GPa) of dimensions 1.10×0.22 m, using a consistent mass matrix formulation and neglecting the inertia contributions in the axial direction, in order to avoid the modelling of vertical vibrations at impacts. Results can be compared also to the simplified expression given in Makris and Konstantinidis (Makris and Konstantinidis, 2003) (Equation 3.56) which, yields for the considered case a constant equivalent viscous damping equal to 4% for any θ to α ratio.

$$\xi = -0.34 \ln e^2 \quad (3.56)$$

The coefficient of restitution derived by Housner under the hypothesis of conservation of angular momentum is a reference solution that provides a theoretical framework defining a reasonable range for the energy dissipation related to the rocking motion, and highlights the main parameter governing the phenomenon, i.e. the slenderness of the rocking block. This dependency is generally confirmed by experimental results, which show a higher energy dissipation for stockier blocks (Peña and Lourenço, 2006). However, an exact experimental confirmation of Housner's hypothesis is lacking, particularly for materials, such as masonry, which do not respect perfectly the hypotheses of the theoretical model. Tests on two-way rocking of masonry parapets (Sorrentino et al., 2011; Degli Abbati and Lagomarsino, 2017) tend to show a higher energy dissipation. Sorrentino et al. (Sorrentino et al., 2011) found that

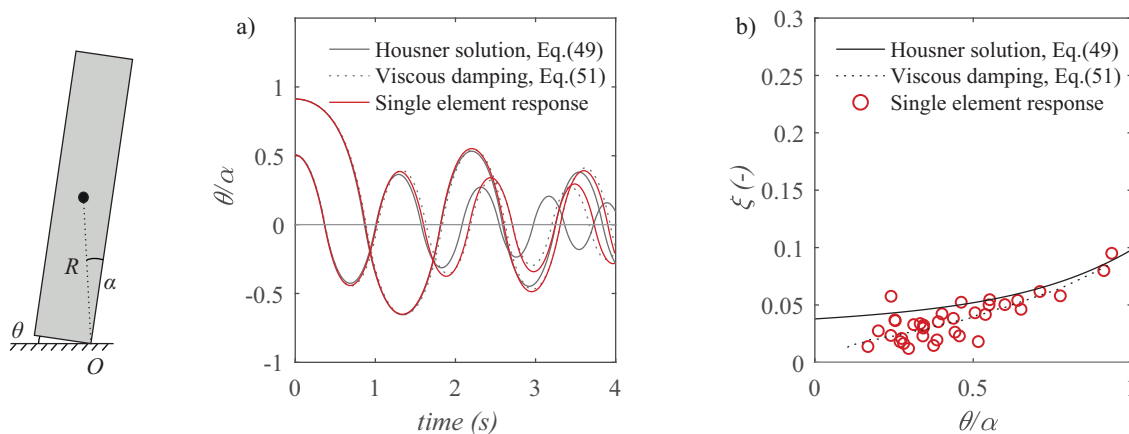


Figure 3.9 – Rigid block theoretical solution and numerical response of free vibrations of a single block: displacement history (a) and equivalent viscous damping ratio (b).

coefficients of restitution derived from experiments are approximately 5-8% lower than the theoretical coefficients. Although the difference appears to be small, the effect on the experimental displacement histories and therefore on the equivalent damping ratio is considerable. The effect of the block stiffness and the interface conditions is studied in detail in ElGawady et al. (ElGawady et al., 2011), who found also a non-negligible increase in energy dissipation for blocks rocking under imperfect conditions. On the other hand, when the stiffness of the material and the characteristics of the rocking surface approach the ideal conditions of the model, such as the granite tested by Peña and Lourenço (Peña and Lourenço, 2006), the experimental results are closer to the theoretical solution.

When modelling the out-of-plane response of a masonry wall through a single macro-element, an experimental energy dissipation larger than the one corresponding to Housner's model can be either captured by calibration of the viscous damping, or by modelling explicitly the finite stiffness of the block and the possible crushing at the interface. As reference experimental results, a free-vibration out-of-plane test on an irregular stone masonry cantilever wall, carried out by Degli Abbatì and Lagomarsino (Degli Abbatì and Lagomarsino, 2017), is used here. In this campaign, three-leaf stone masonry walls built with lime mortar were tested by imposing an initial out-of-plane displacement, which was subsequently released in order to perform a free-vibration test. Each wall was subjected to several free vibration tests. From the test series, which comprises three walls, "panel 1" (dimensions 1.10x0.90x0.22 m) is the most regular in terms of physical hinge location and slenderness ratio, and modelled through a single macro-element. Experimental results are compared to the numerical displacement time-histories and equivalent damping ratio (Figure 3.10).

The dissipative behaviour of the experimental specimen is markedly higher than the ideal one shown in Figure 3.9 for a rigid block of the same dimensions. The increased damping can be related, as commented in Degli Abbatì and Lagomarsino (Degli Abbatì and Lagomarsino, 2017), to the sum of three phenomena, i.e., the progressive detachment from the base when, at impacts, the centre of rotation switches from one edge to the other, the elastic deformability of the panel, and the inelastic deformations at the toe. Although such features are accounted for by the macro-element model, in order to capture the correct energy dissipation an increased viscous damping must be specified. A factor 6 is found between the damping coefficient derived in Equation 3.55 and the damping coefficient matching these experimental results best over all θ to α ratio. The viscous damping model, compared to Housner's model, tends to underestimate the energy dissipation for smaller rocking amplitudes (see Figure 3.9b). However, experimental results follow a similar trend, showing a smaller energy dissipation than the one postulated by Housner's model for low amplitude oscillations (Figure 3.10b).

3.7 Conclusions

A novel macro-element formulation for modelling masonry structures by means of equivalent frame models was developed and implemented in the open-source software OpenSees. The in-plane response of the macro-element builds on the macro-element by Penna et al. (Penna et al., 2014). As a novelty the element captures also the out-of-plane response of the masonry element. The macro-element can be used to model with a single element the nonlinear behaviour of a pier or spandrel or a

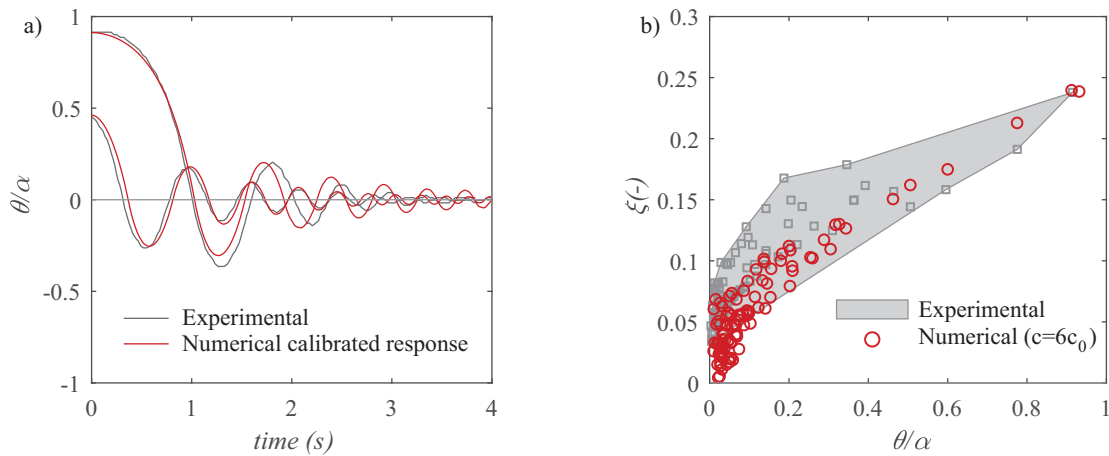


Figure 3.10 – Comparison of experimental (digitised from Degli Abbati et al. (Degli Abbati et al., 2014)) and numerical response of a single element: displacement history (a) and equivalent damping ratio (b).

gable wall (for the latter a mass matrix accounting for the triangular shape has been derived).

The presented macro-element is defined by the degrees of freedom of three nodes defined in the three-dimensional space. These three nodes are the two end nodes and a node at midspan. The degrees of freedom are used to describe the kinematics of two blocks, which are deformable in shear and bounded by three interfaces capturing axial and flexural deformations. The macro-element can account for second-order geometrical effects through a $P - \Delta$ formulation. The macro-element can reproduce exactly, in the elastic regime, the displacements at the extremities of a three-dimensional Timoshenko beam subjected to forces concentrated at the end nodes and linearly distributed loads. In the nonlinear range, it ensures the exact application of equilibrium conditions at three flexural interfaces. It couples therefore the flexural behaviour as well as the shear behaviour with the axial load, without the need of nested internal iterations.

If the element is used to simulate the in-plane and out-of-plane response of a masonry wall, adequate sectional models need to be applied. Any sectional model available in OpenSees can be used for the macro-element. For the flexural response, fibre sections with suitable constitutive laws for the fibres can be used. As an alternative, in this study, an analytical sectional model describing three-dimensional rocking, accounting for zero tensile strength and toe-crushing, is proposed. Developed with the objective of reducing the computational cost of the analysis, which is a key feature for applications in dynamic analyses of equivalent frame models, it can capture the main features of the in-plane and out-of-plane flexural response. For shear, a model based on the damage model and friction interface model by Alfano and Sacco (Alfano and Sacco, 2006) is developed, which couples the shear behaviour to the axial load. The results of the macro-element compare fairly well with experimental results in terms of the force-displacement envelope and hysteretic energy dissipation. The in-plane behaviour of the macro-element, when coupled with the proposed sectional models,

agrees with well-established formulations for the force capacity of masonry walls, and with numerical simulations obtained through the software Tremuri (Lagomarsino et al., 2013; Penna et al., 2014), whose shear model is as well implemented, as an alternative given to the user.

The possibility of including both the in-plane and out-of-plane response of a masonry wall in the macro-element response opens up the potential of using one equivalent frame model to assess, through dynamic time-history analyses, both types of failure. The macro-element is shown to replicate the rigid block limit analyses of one-way bending out-of-plane mechanisms. In dynamic analyses, the macro-element response depends strongly on the applied damping model, for which a possible approach using initial stiffness proportional damping is proposed, which approximates theoretical solutions and experimental results well. The application of such damping model in a more complex structure, including both elements loaded in-plane and out-of-plane, remains, however, topic for future research.

Equivalent frame models, applied in conjunction with dynamic simulations, despite their simplicity, can provide useful insights with regard to the seismic behaviour of masonry buildings at a moderate numerical cost. As a result, they are well suited to investigate the effect of aleatoric and epistemic uncertainties on the building response. In this spirit, the macro-element implemented in OpenSees allows the user the choice between several options with regard to (i) the mass matrix (consistent vs lumped mass matrix), (ii) shear models (two models were implemented for the macro-element; in addition any user-defined biaxial constitutive model, or, if the user wishes to decouple the shear response from the axial load, uniaxial constitutive model can be used), (iii) damping models (initial-stiffness proportional vs tangent-stiffness proportional models), (iv) drift capacity models for the in-plane response, which can be dependent of the failure mode and/or the axial load ratio. Furthermore, the macro-element offers the choice to reduce not only the horizontal stiffness and strength when a certain drift limit is reached, but also the axial load bearing capacity. The drift at which the axial load bearing capacity is cancelled or reduced is given by a user-defined factor times the drift at horizontal load failure.

In addition to the modelling choices linked to the macro-element, when modelling a masonry building using in OpenSees, the user can profit from all the possibilities of a complex finite element software, in terms of nonlinear material models, elements types and sectional models. The new macro-element can therefore also be used to investigate the performance of mixed structures or retrofitted structures. For the latter, fibre sections, coupled with adequate material models, might be applied for describing the behaviour of spandrels or elements retrofitted through, for instance, jacketing or FRP application.

3.8 Repository

The code of the element can be downloaded from <https://github.com/eesd-epfl/OpenSees/wiki>. The repository contains, next to the element implementation, an OpenSees library including the element. Furthermore, the repository shares examples used to produce the figures in this manuscript, and a supplemental document including the derivations omitted here for brevity (<https://github.com/eesd-epfl/OpenSees/wiki/Supplemental-materials>).

3.9 Acknowledgements

This work was prepared as part of the Basel-Project, which is supported by the Swiss Federal Office of the Environment and the Construction Department of the Canton Basel-Stadt.

4 Simulation of shaking table tests including out-of-plane response

Abstract

Equivalent frame models are an effective tool for the seismic assessment of existing masonry structures, which, due to its simplicity, allows performing multiple nonlinear dynamic analyses, accounting explicitly for different sources of modelling uncertainty. It is well-established in the literature that equivalent frame models can effectively estimate the global response of buildings whose behaviour is dominated by in-plane failure modes. Such analyses can be conducted with two-dimensional elements simulating only the in-plane response of masonry walls. The recent development of a three-dimensional macro-element formulation for the modelling of both the in-plane and the out-of-plane response allows extending the use of equivalent frame models to the study of also local out-of-plane mechanisms of a building. This study applies the newly developed formulation, implemented in OpenSees, to the modelling of two shaking table tests on a stone masonry building and on a mixed concrete-unreinforced masonry structure. Since the modelling approach allows explicitly accounting for the quality of connections in the building (i.e. wall-to-wall, and floor-to-wall connections), specific elements and material models were developed for modelling such connections in an equivalent frame idealisation. Through the comparison with the experimental results, the performance of the modelling approach is discussed, and the sensitivity of the response to the major sources of modelling uncertainty (quality of connections, damping model) is assessed.

4.1 Introduction

The assessment of the seismic behaviour of buildings through and equivalent-frame idealisation is a widely used approach, both in research and in the professional field. It allows for the nonlinear analysis of building, also the dynamic range, with limited computational cost, when compared to more detailed methods, such as macro-modelling of masonry structures through continuum material models (Lotfi and Shing, 1991; Berto et al., 2002), often based on homogenisation (Milani et al., 2007; Zucchini and Lourenço, 2009; Milani, 2011) or, in increasing order of both complexity and computational demand, micro-modelling approaches (Lourenço and Rots, 1997; Wilding et al., 2017; Zhang et al., 2017), in

Chapter 4. Simulation of shaking table tests including out-of-plane response

which units and interfaces are modelled explicitly. Compared to these models, the equivalent frame approach offers the advantage of a reduced cost and a simpler calibration, based directly on structural element tests, since phenomenological laws are generally applied to describe the nonlinear behaviour of the entire element and define its displacement capacity.

The use of an equivalent frame idealisation of a building, however, implies the compliance with the rather strong assumptions connected with the modelling approach, the first, and more obvious, of which is the possibility of defining a frame structure of pier elements, spandrels and nodes that replicates reliably the layout of a façade (Berti et al., 2017). A second hypothesis is that the connections between the walls of a building, provided by floor diaphragms and the link between orthogonal elements, are sufficient to ensure that out-of-plane failure modes cannot develop before the building can attain its entire in-plane capacity, or, more generally, that the analysis performed through an equivalent frame model is reliable as long as local out-of-plane mechanisms do not appear. When this assumption holds, the method can be used in conjunction with element numerical formulations which tackle only the in-plane response of masonry walls. This approach has been, in the literature, predominant when elements to be used in equivalent frame models are defined (Penna et al., 2014; Lagomarsino et al., 2013; Addessi et al., 2014; Belmouden and Lestuzzi, 2009; Roca et al., 2005). The application of such models in nonlinear dynamic simulations proved that they can provide good estimates of the global response of a building in terms of displacement and drift demands and acceleration profiles (Mandirola et al., 2016; Penna et al., 2016).

However, restricting the field of applicability of equivalent frame models to buildings which have a good system of connections providing a sufficient restraint to out-of-plane mechanisms can be limiting when dealing with existing historical buildings, which typically have very weak connections. Moreover, even in modern buildings, the boundary conditions that are applied to an out-of-plane loaded element can vary with the increase of lateral deformations, to the point that the element could lose the restraint and activate a mechanism (Tondelli et al., 2016a). If the model does not account for any out-of-plane response, a different assessment strategy needs to be adopted for the out-of-plane mechanism, typically a rigid-body analysis of the kinematic chain that can potentially activate. Such analysis, however, remains uncoupled from the in-plane assessment.

Integrating the out-of-plane response in equivalent frame model can, on the contrary, account directly for the interaction of the in-plane response in determining the loads that are applied to an element loaded out-of-plane, for example by horizontal diaphragms, as well as the transient variation of boundary conditions, and the magnitude, and when relevant, the phase of the accelerations that are imposed to it. Additionally, it is possible to relax the hypothesis that the out-of-plane loaded mass is rigidly lumped to the in-plane walls, improving also the modelling of the in-plane response, and the estimate of the periods and modes.

In order to develop such a model, however, the element formulation used for masonry members needs to account properly for their out-of-plane response. Models developed with the use of force-based elements (Raka et al., 2015; Siano et al., 2018), although not used yet in this context, can be a potential tool able to capture the out-of-plane response. One macro-element formulation explicitly developed

4.2. Tools developed for 3D equivalent frame modelling in OpenSees

for this scope is presented in Chapter 3, and will be used in the following. The use of these models, moreover, implies the explicit definition of modelling details that are neglected in standard in-plane equivalent-frame analyses, such as the possibly nonlinear behaviour of all connections, including wall-to-wall connections at corners and floor-to-wall connections, or more generally the nonlinear response of weak floors.

This chapter presents in Section 4.2 the tools implemented in OpenSees for developing a full three-dimensional equivalent frame model with the use of the macro-element presented in Chapter 3, and discusses the most relevant modelling choices and their effect on the numerical simulations. The analysis concentrates on the effect of out-of-plane mass, not rigidly lumped to the orthogonal walls, on the modelling of roofs and gable elements, and on the sensitivity of the response to the assumptions on the behaviour of connections (wall-wall and wall-slab connections) and the damping model. To address these topics, the results of two shake table tests will be used as a comparison for the numerical models: a stone masonry building aggregate of two buildings, presented in Section 4.3 and a modern mixed reinforced concrete/masonry structure, shown in Section 4.4, in which out-of-plane loaded walls were subjected to variable boundary conditions depending on the in-plane behaviour. Numerical simulations are discussed through the comparison with experimental results in terms of global quantities (floor displacements and accelerations), local deformations (displacements of out-of-plane loaded elements, slip between wall and floors), and distribution of damage and drift demands in the walls of the building.

4.2 Tools developed for 3D equivalent frame modelling in OpenSees

4.2.1 Macro-element formulation

All masonry elements, both piers and spandrels, in the following analyses are modelled through the macro-element formulated in Chapter 3. They can therefore model the in-plane and out-of-plane flexural response through three sectional models applied at the element ends and at the central section, being able to reproduce the deformations modes shown in Figure 4.1. Those sections are equipped with the section model presented in 3.3, accounting for possible crushing at the section edges. The shear model applied in all analyses is the one presented in 3.4, to which the reader is referred for further details. Since the stone masonry building presents three rather tall gables, triangular gable elements, based on the same formulation, are used. These elements are equipped with a section which decreases in size along the height of the elements and with a consistent mass matrix derived specifically for triangular elements. In order to capture the out-of-plane behaviour of the element, a $P - \Delta$ formulation is always applied.

4.2.2 Orthotropic membrane elements

The modelling of the floor stiffness is a key aspect in equivalent frame models of existing buildings, which often feature deformable timber floors providing a weak coupling between different walls, which cannot be idealised as rigid diaphragms. Such elements present some stiffness in the main direction of

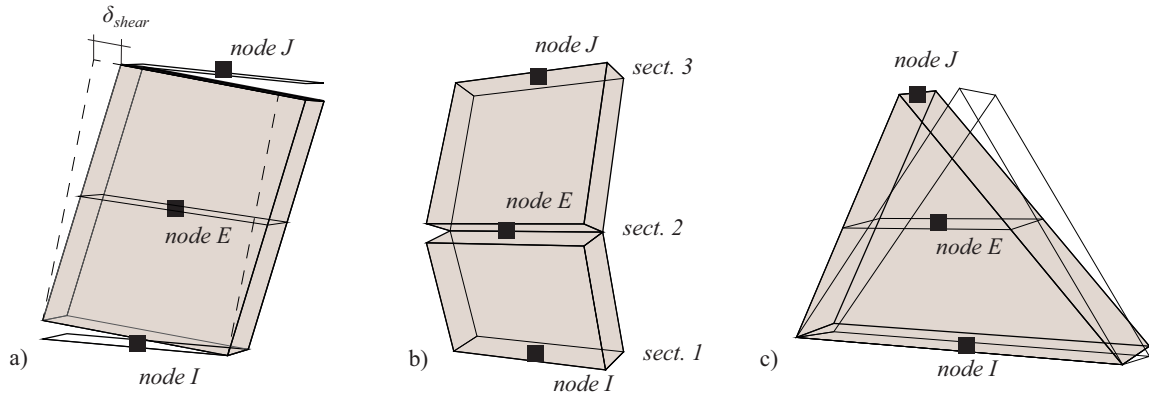


Figure 4.1 – (a) In-plane and (b) out-of-plane deformation of the applied macro-element formulation, including flexural and shear components; (c) gable elements used in the simulations.

the floor, parallel to the principal beams, and a lower stiffness in the orthogonal direction and in shear deformations. To account properly for their deformability, and allow for comparisons between results of different models, the same orthotropic elastic model assumed in the software Tremuri (Lagomarsino et al., 2013) was implemented in OpenSees as a section model to be applied to quadrangular shell elements. The model accounts only for membrane stresses (σ_x , σ_y and τ_{xy} , referred to a local system of two axes x and y) and provides no stiffness to bending deformations. Such stresses are related to local deformations through:

$$\begin{bmatrix} \sigma_x \\ \sigma_y \\ \tau_{xy} \end{bmatrix} = \mathbf{K}_{basic} \begin{bmatrix} \epsilon_x \\ \epsilon_y \\ \gamma_{xy} \end{bmatrix} = \begin{bmatrix} \frac{E_x}{1-\nu^2} & \frac{\nu E_x}{1-\nu^2} & 0 \\ \frac{\nu E_x}{1-\nu^2} & \frac{E_y}{1-\nu^2} & 0 \\ 0 & 0 & G_{xy} \end{bmatrix} \begin{bmatrix} \epsilon_x \\ \epsilon_y \\ \gamma_{xy} \end{bmatrix} \quad (4.1)$$

where e is the ratio between the two stiffness moduli in the two orthogonal directions x and y , i.e. $e = \frac{E_y}{E_x}$. The stiffness of the orthotropic membrane is further defined by the Poisson's ratio ν and the shear modulus G_{xy} , which is independent from the other parameters. Section forces are hence simply obtained by integration of constant membrane stresses along the element thickness. The parameters E_x and E_y are referred to the local orientation system, defined by the orientation in space of the shell element. If the element is defined between four nodes I, J, K and L , the direction x is given by the average direction of sides IJ and LK .

4.2.3 Nonlinear floor connections

If we assume that deformable floors remain linearly elastic throughout the shaking, the connection must account properly for their nonlinear behaviour and possible failure of the connection at the support of beams. If the only nonlinearity is represented by a slip of the beams with respect to the wall, a friction model accounting for the compression acting on the connection can be applied. In order to model such beam slip, a simple friction model as the one schematically drawn in Figure 4.2 was implemented in OpenSees. The nodes of the floor must be modelled independently from the nodes

4.2. Tools developed for 3D equivalent frame modelling in OpenSees

of the walls, to capture possible relative displacements. The connection can be modelled through zero-length elements accounting for coupled material models along the different directions.

The implemented model features zero strength in all directions when traction deformations are applied. When subjected to compression, the connection can transfer transversal forces proportional to a friction coefficient μ in the plane of the floor. In the following, a two-dimensional formulation will be used. In this formulation, the sliding can take place only in the direction perpendicular to the wall. At every increment of the deformations $(\Delta u, \Delta v)$, in the vertical load direction and in the direction of sliding, respectively, a trial state can be estimated as:

$$N^{trial} = N_n + k_N \Delta u, \quad V^{trial} = V_n + K_V \Delta v, \quad (4.2)$$

where k_N and k_V are the penalty stiffness applied in the vertical and in the transversal directions. The sliding condition to check is given by the yield function f :

$$f(N, V) = \mu N + |V| \geq 0 \quad (4.3)$$

when the condition $f \geq 0$ is not met, sliding can occur. Assuming zero dilatancy, the correction to be applied to V is easily calculated as:

$$v_{n+1}^{sliding} = v_{n+1}^{sliding} + \frac{f}{k_V} \frac{|V^{trial}|}{V^{trial}}, \quad V_{n+1} = k_V (v - v_{n+1}^{sliding}) \quad (4.4)$$

In the following analyses it is further assumed that when no slip is possible towards the wall, i.e. the interface can close and apply some pounding forces to the walls. This condition is simply applied enforcing the value of $v_{n+1}^{sliding}$ to be non negative after every update, defined in Equation 4.4. For corner nodes, when out-of-plane failure of one of the two walls is modelled, the floor node needs to be connected to the nodes belonging to the wall perpendicular to the main direction of the floor, in order to apply loads and restraints against an out-of-plane mechanism to the correct elements.

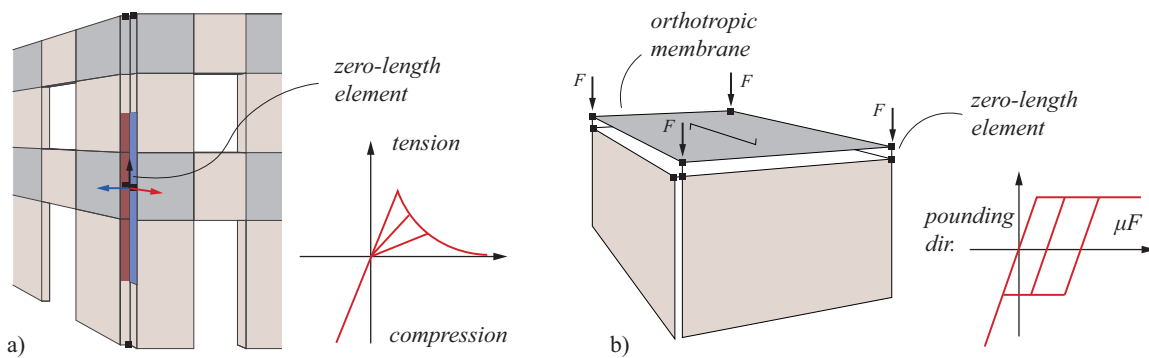


Figure 4.2 – Definition of zero-length elements for modelling (a) the interaction between orthogonal walls and (b) the floor-to-wall connection allowing for frictional slip of beams and pounding.

4.2.4 Wall-to-wall connections

The connection between orthogonal walls is also modelled through zero-length elements. The connection can potentially exhibit a nonlinear behaviour, for the development, for example, of a vertical crack and the initiation of an out-of-plane overturning of one façade. This can be modelled in a simplified approach through point connections at the corner nodes, to which appropriate tensile properties are assigned. The maximum tension force that the interface can transfer can be defined by the integration of a tensile strength assigned to the masonry along a tributary section, as shown in Figure 4.2a. Alternatively, a more precise modelling can be obtained by the use of fibre zero-length sections, which, however, were not used in this study. In order to apply a simple material model, the interfaces used in the following make use of a material specifically implemented for this scope in OpenSees, featuring a linear elastic response in compression and a damage tension law with exponential softening. The material is defined only by its elastic properties, the tensile strength and its fracture energy in mode I opening, representing the area under the stress-displacement relation that it models.

4.3 Stone masonry building

The first case study to which the proposed equivalent frame model approach accounting for out-of-plane behaviour and complex nonlinear connections is a stone masonry recently tested in a shaking table test in EUCENTRE, Pavia (Italy). The building, built in half scale due to the space limitations imposed by the testing equipment, is composed of two adjacent units of different height, weakly connected (Figure 4.3). Its characteristics, in terms of openings layout, dimensions, height, structure and inclination of roofs, are intended to reproduce the typological characteristics of the historical building stock of the city of Basel, Switzerland. The building is made of two-leaf stone masonry walls of reducing thickness along the height (starting from 35 cm to 25 cm). Because the test unit represents the prototype at half-scale, adequate scaling laws for time, mass and stiffness/strength properties must be applied. The scaling of material properties was approximated by the use of expanded polystyrene spheres added in 40% proportion to the mortar (Guerrini et al., 2018). The connection between the two units was realised limiting the interlocking between stones, in order to reproduce the condition of a building built adjacent to a pre-existing construction.

The horizontal diaphragms are timber floors with a single layer of planks and therefore very deformable in-plane. The orientation of the floor beams varies between storeys, i.e. the first two floors span parallel to the orientation of the shaking, while the third floor spans perpendicular to the shaking direction. As a result, the third floor provides a much weaker constraint to the out-of-plane loaded elements. A stiffer system of trusses constitutes the roof structure, as shown in Figure 4.4.

The structure was subjected to ground motions of increasing intensities. First some low intensity records were applied, which will not be simulated here. The main shaking was obtained by scaling the Montenegro earthquake (1979). The available data include acceleration measures, relative displacements between the structure and a stiff steel frame placed inside the structure and moving with the shaking table, and the displacements measured through an optical system of a grid of markers in the South, East and North façades. The prototype was subjected to eight main runs, up to a ground

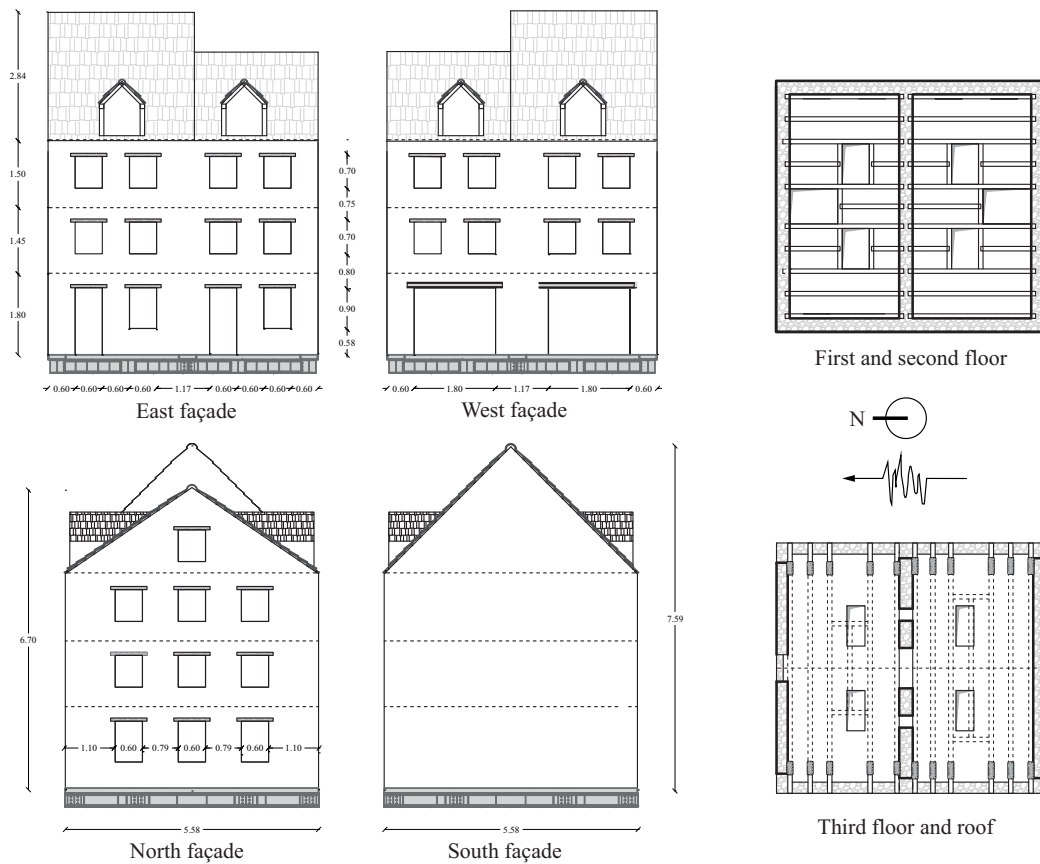


Figure 4.3 – Front views and floor layout of the stone masonry building tested on the shaking table.

motion with a Peak Ground Acceleration (PGA) of around 0.35g (175% of the original record). After this level, since the initiation of an out-of-plane deformation of the South gable was observed, the connection between floors and walls was improved by closing some connectors previously installed in order to continue the testing to higher intensities. For the scope of study, we analyse only the first eight runs, performed on a building with weak connections. A more detailed description of the building prototype, the construction details and the testing procedure, are given in Senaldi et al. (2019), to which the reader is referred.

4.3.1 Model calibration

An equivalent frame model of the building has been defined as in Figure 4.4a. The gables were modelled through single triangular elements, to which an exact mass distribution is applied. The element can overturn around the edge of the base section. Despite the low interlocking of the interface, the connection between the two units showed little damage and no significant pounding between the two buildings was observed. For this reason, the central pier is modelled through a single element.

Chapter 4. Simulation of shaking table tests including out-of-plane response

The beam over the ground floor openings is considered simply supported by the adjacent piers, in order to avoid that the element acts as a reinforcement to the first story spandrels. Since the thickness reduction of the walls takes place at the floor levels, spandrels are assigned an averaged thickness.

Floors are modelled through orthotropic membrane elements. The shear stiffness of the single-plank diaphragms was assumed equal to 10 MPa, consistently with the approach proposed in Brignola et al. (2008). The roof stiffness, due to the presence of a system of trusses, is considerably higher. From linear elastic analysis of the static system shown in Figure 4.4, the stiffness of the two trusses is assumed equal to 3.70 and 6.60 kN/mm, respectively, for the North and the South roof elements.

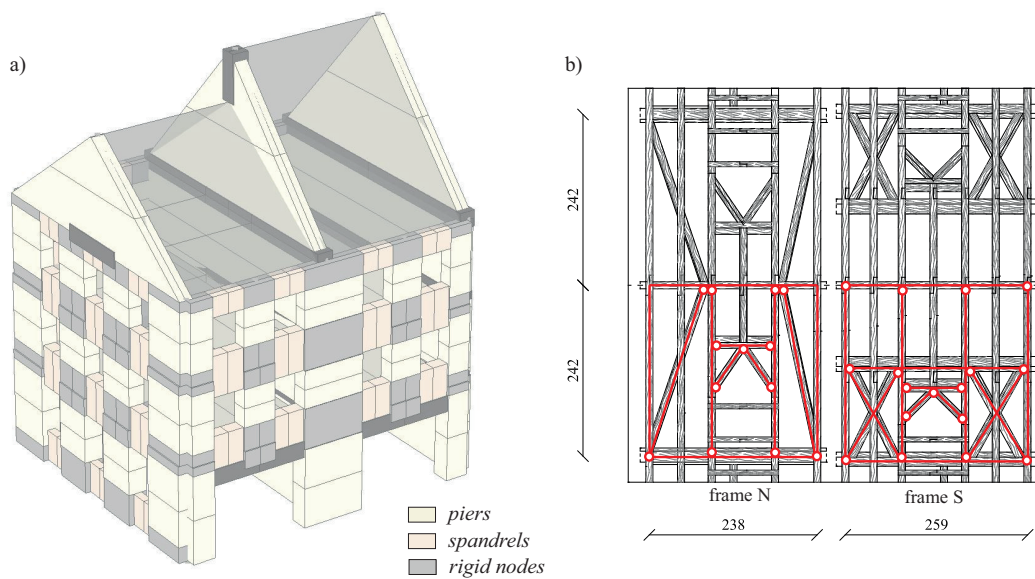


Figure 4.4 – Stone masonry building: (a) Equivalent frame model of the complete building; (b) Timber frames providing shear stiffness to the roof diaphragms

The properties of masonry could be derived from different sources, including uniaxial compression tests, diagonal compression tests (Senaldi et al., 2019) and four shear compression tests on two squat ($H=1.45$ m, $L=1.17$ m, $t=0.30$ m) panels and two slender panels ($H=1.80$ m, $L=0.60$ m, $t=0.30$ m), representing the dimensions of the ground story piers of the East façade. The source that was considered more reliable for the estimate of the lateral stiffness and strength of the masonry elements was considered the shear compression test series, based also on the results presented in Vanin et al. (2017b). A Young's modulus E equal to 2170 MPa was derived from the average of the initial lateral stiffness measured in the tests, assuming a G/E ratio of 0.30 (with G therefore equal to 650 MPa). Since the model accounts explicitly for stiffness loss in the peak phase, the effective stiffness was not considered for this estimation.

The nonlinear properties are calibrated based on the shear compression tests as well. Assuming a friction coefficient $\mu_0 = 0.40$, a value of cohesion $c = 0.09$ MPa could be derived. The residual friction coefficient μ_R , controlling the shape of hysteresis cycles, is assumed equal to 0.10. The 20% post-peak

force drop is calibrated to a drift of 0.8%. The compressive strength derived from compression tests (equal to 1.30 MPa) was calibrated considering the response of panels failing in flexure, and a value of 2.20 MPa was assumed in order to reproduce correctly the force capacity of slender piers. The same set of properties was applied to pier and to spandrel elements.

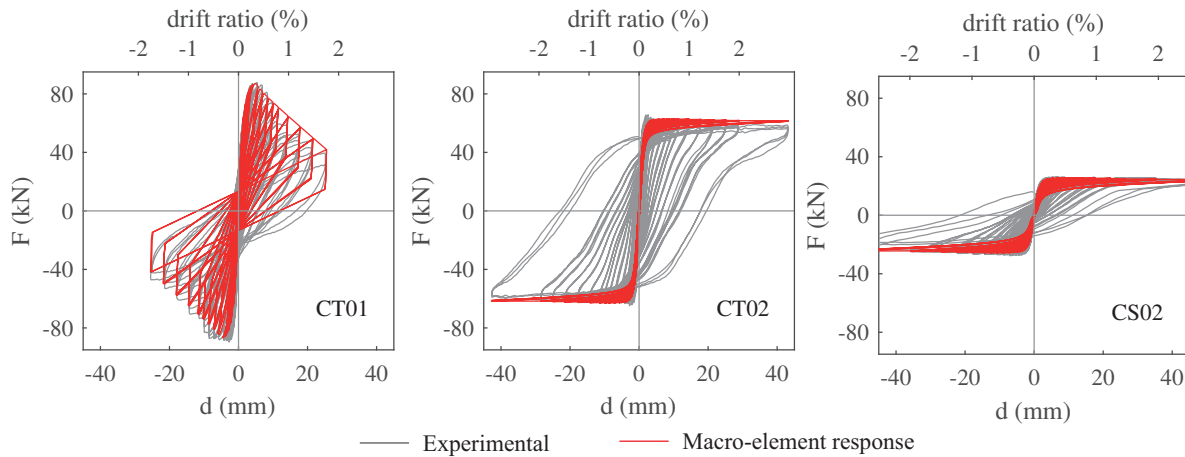


Figure 4.5 – Stone masonry building: Calibration of the mechanical properties of the macro-elements against three shear compression tests on the same masonry typology of the prototype.

The mass of masonry elements is considered distributed along their axes; the floor masses, including some additional masses that were placed at the floor levels, is lumped to the corner nodes. The total mass of the model, consistently with the tested prototype, is equal to 82.1 t. Modal analysis performed on the numerical model shows that the approach captures the first three modal shapes and periods reasonably well, when compared to the modal shapes and the periods extracted from dynamic identification. Further calibration of the elastic properties of floors and masonry elements could improve the match; values obtained directly from tests, however, are applied in all following analyses. It is worth noticing that the modelling of the roof structure provides a significant shift of the modal properties, compared to the model with rigidly lumped gable and roof masses. This is also due to the particularly high aspect ratio of the gable.

4.3.2 Sensitivity analysis

A set of nonlinear dynamic analyses of the building was performed with the objective of identifying the effect on the seismic response of two major sources of uncertainty for the modelling of this building, i.e. the damping model and the modelling of connections. Since cracking at the corners was not observed during the physical test, a rather high value of tensile strength equal to 0.05 MPa was assumed for wall-to-wall connections, ensuring a linear behaviour, at least until an irreversible out-of-plane displacement of a façade takes place. For the other two parameters, the friction coefficient to assign to the floor-to-wall connections and the damping ratio, a factorial combination on three levels was assumed. The damping ratio was varied between 1, 2 and 3%. A Rayleigh damping model, proportional to the mass and the initial stiffness matrix is assumed. The damping ratio is applied exactly at the

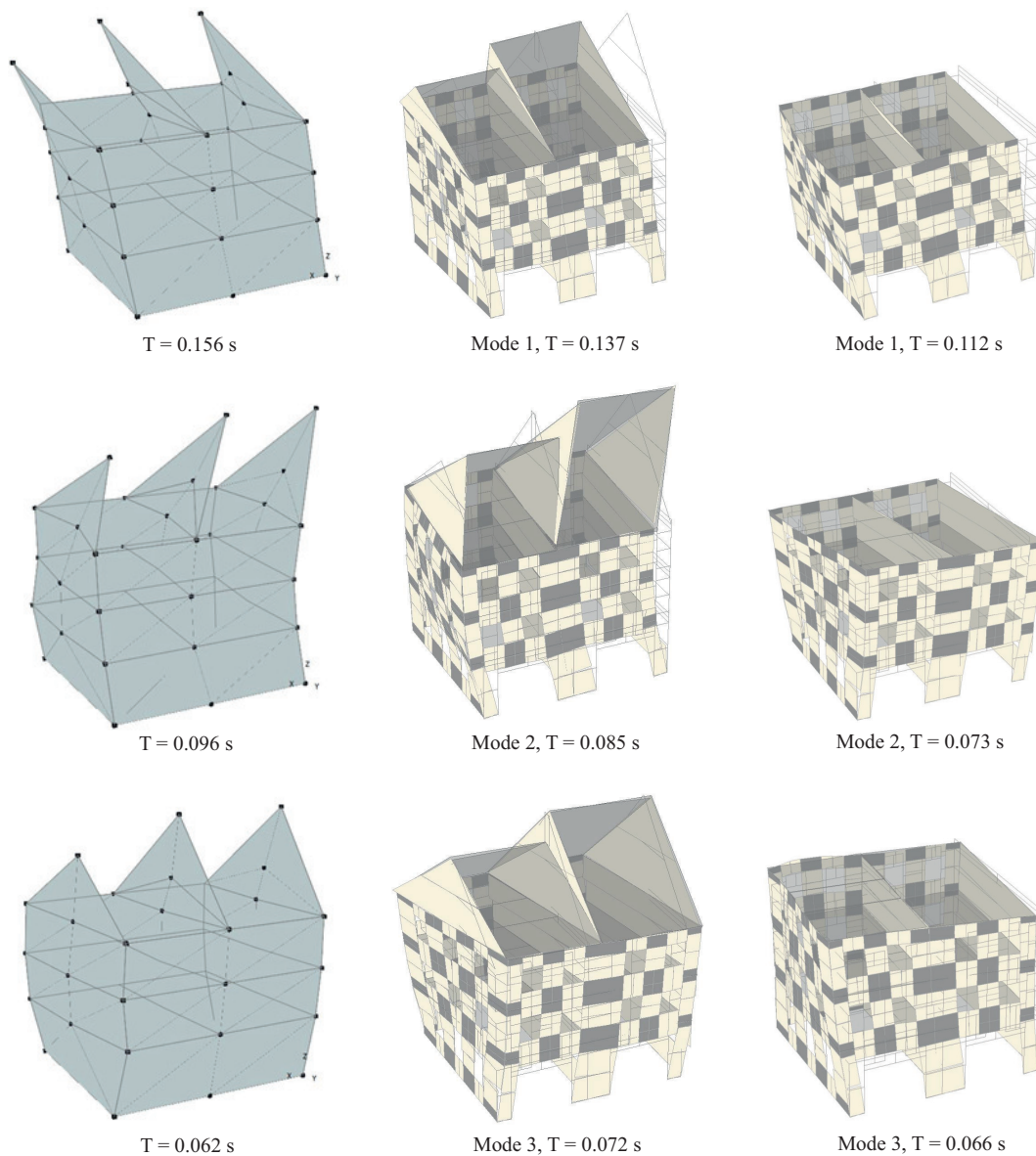


Figure 4.6 – Stone masonry building: Modal analysis of the complete model and the simplified model without explicit modelling the gable. Modal shapes and periods are compared to the results of the dynamic identification.

period of the second mode and at three times the first period, to obtain a rather large period interval in which the damping ratio is approximately constant, considering that damage accumulation produces a period shift also in the model. The friction coefficient was varied in the range 0.80-1.00-1.20 in order to obtain a variation of the interface behaviour.

Each model was subjected to the entire sequence of eight ground motions, modelling the accumulation

4.3. Stone masonry building

of damage, as in the shake table test. The analysis of failure modes and maximum drift demands on the elements, presented in Figure 4.7, shows a high sensitivity of the model to the damping ratio that is assumed, which influences both the drift demand on the masonry elements and the failure mode itself for models with weaker connections.

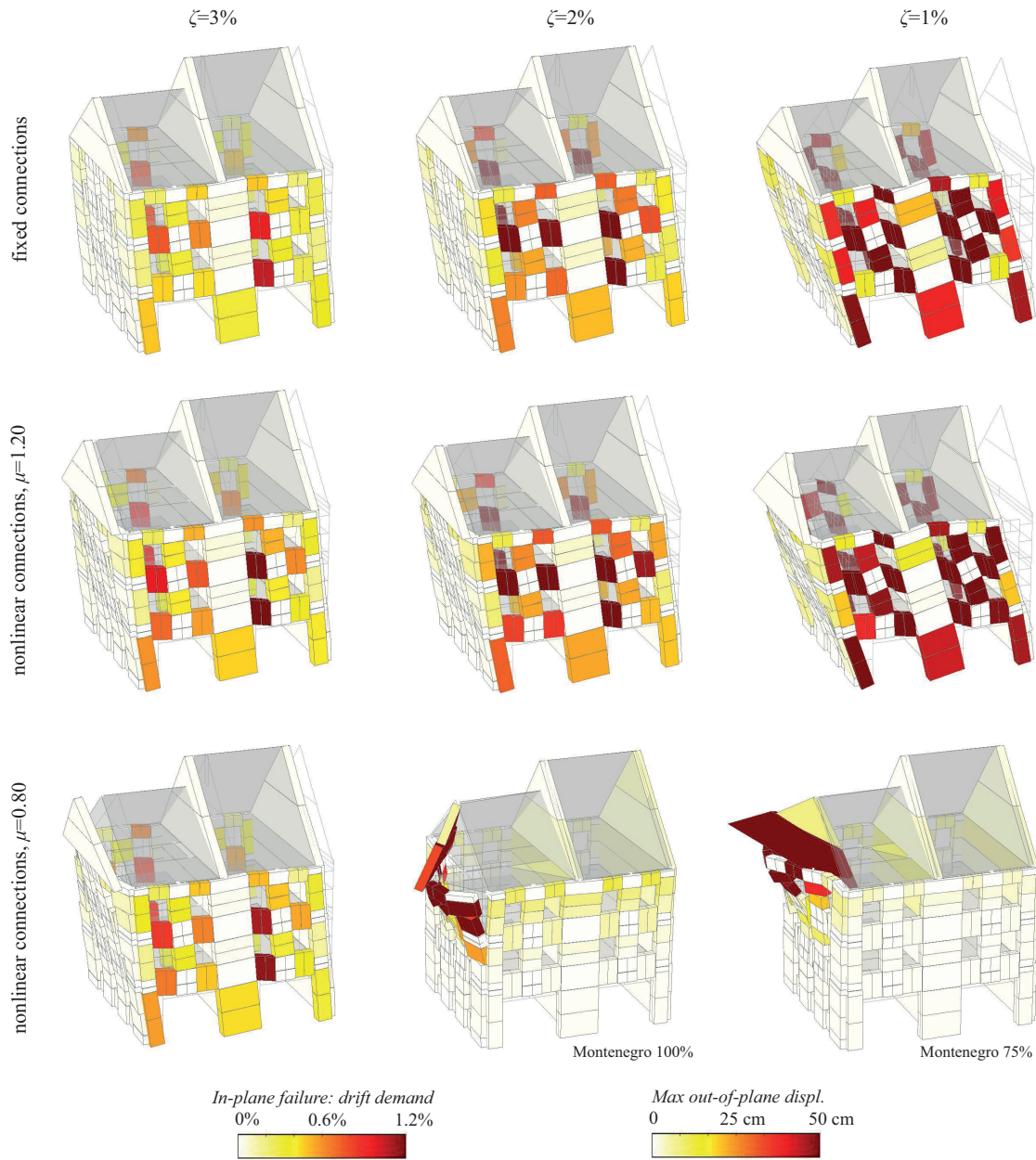


Figure 4.7 – Stone masonry building: Sensitivity of failure modes to the effectiveness of floor-to-wall connections and to the damping ratio ζ . Deformation scale: 25 (in-plane failure modes), 1 (out-of-plane mechanisms).

Chapter 4. Simulation of shaking table tests including out-of-plane response

A similar trend is observed for the friction coefficient of the sliding floor interfaces. The maximum transversal load transferred from the floors to the walls is given by the friction coefficient and by the compression force that is attributed to each interface. For all floors, 80% of the load was given to the walls between which the floor spans, and the remaining 20% to the walls parallel to the span. Since the attribution of the compressive loads is rather arbitrary, physically high values of friction coefficient could be linked to an underestimation of the compression on the walls parallel to the floor span, and should be interpreted simply as an increase of the effectiveness of the connection between floors and walls. Results however clearly show that an increase of force transfer between floor to wall connections produces a dramatic change in the failure mode, that passes from an out-of-plane failure mode to an in-plane behaviour. The higher vulnerability of the last floor, due to the different floor orientation, is correctly predicted by the model.

The comparison between numerical and experimental displacement demands at the upper storey and at the gable level (Figure 4.8) shows that the set of analyses that predict the closest demands to the experimental values is the one performed with 1% damping ratio. With higher damping ratios, the damping forces reduce excessively the displacement demands on the building, which does not reach the deformation level attained experimentally. The different assumptions on the effectiveness of connections, as long as the force transfer is sufficient to prevent out-of-plane failure, do not lead to a considerable change in global demand parameters. When looking at local deformation quantities, such as the sliding of floors with respect to the walls (Figure 4.9), the model that predicts a correct order of magnitude of local sliding is the one corresponding to the highest level of connection strength ($\mu = 1.20$).

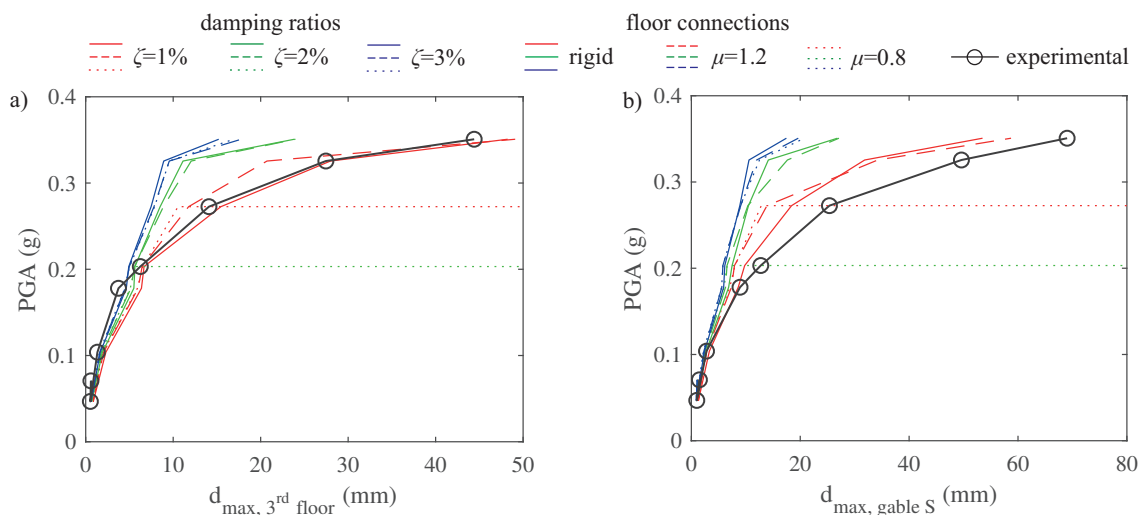


Figure 4.8 – Stone masonry building: Estimates of global response quantities with models featuring rigid floor-to-wall connections or nonlinear connections: (a) third floor maximum displacement, (b) gable maximum displacement.

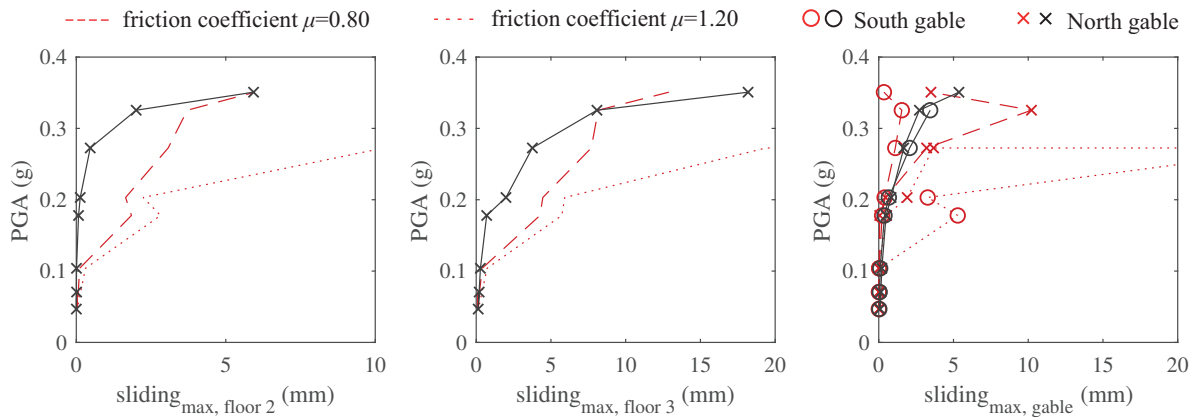


Figure 4.9 – Stone masonry building: Sliding between diaphragms and walls: comparison of experimental measures with the numerical displacements in floor-to-wall connections, for different values of the friction coefficient applied to the zero-length interface.

4.3.3 Time-history response

Selecting from the results of this sensitivity analysis the one that predicts best the displacement demand and the local sliding of connections, i.e. the analysis run with a damping ratio of 1% and a friction coefficient equal to 1.20, the force-displacement response (Figure 4.10) and the time history response (Figure 4.11) of the model compares well with experimental results. Experimental displacement measures are obtained from hard-wire measures of the relative displacements between the floors and the fixed reference steel frame. The base shear is obtained from the acceleration measured by all available accelerometers, to each of which a share of the total mass of the building is attributed. The drift demand on every element of the East façade is obtained discretising the wall into pier, spandrels and nodes and computing deformations from the marker displacements. For the pier elements of the upper storeys the rigid body rotation was removed. It was estimated from the average rotation of the two horizontal sides of the node below the element. The approach, however, introduces a certain degree of approximation, since some deformations which experimentally are attributed to the nodes, as a function of the true position of the cracks with respect to the markers, are actually captured by the pier elements in the numerical simulation.

Since the base piers of the East façade are subjected to mainly flexural/rocking deformations, however, the total drift demand is not representative of the damage level to expect on every element. The comparison with the crack pattern surveyed experimentally shows, in Figure 4.12, that a much more reliable estimate of damage in the elements is obtained considering only the shear drift demands, i.e. the drift computed from shear deformations only. A concentration of damage is predicted on spandrels and little damage on piers. The magnitude of shear drift demands corresponding to cracking of the spandrels is in the order of 0.2%, while shear drift demands when severe and extensive damage on spandrels is observed exceeds often 0.6%.

Given an appropriate set of model parameters, such equivalent frame model predicts with sufficient

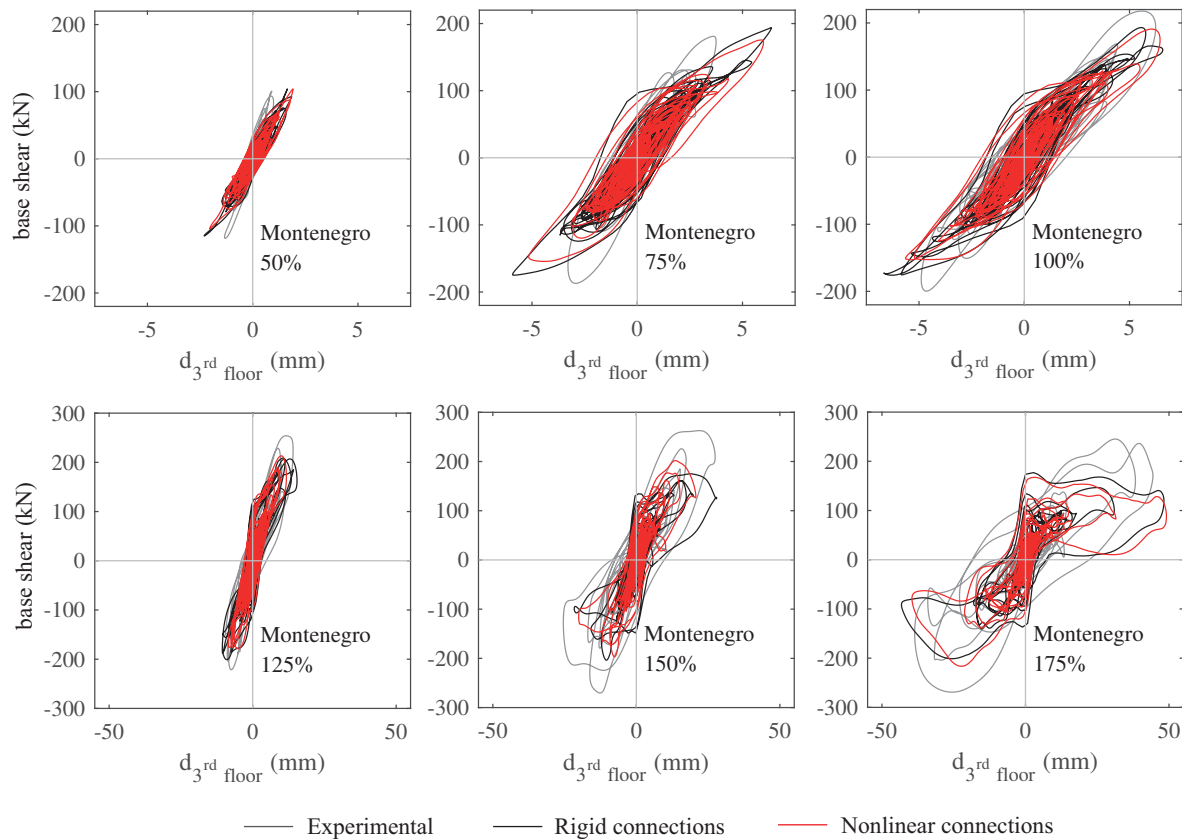


Figure 4.10 – Stone masonry building: Comparison between experimental and numerical force-displacement global response.

precision the magnitude of the displacement demand, and also the failure mode and the distribution of the drift demand on elements, both at lower ground motions intensities and at the most severe shaking. While the drift and displacement demands for low seismic intensity are well estimated by all analysed models, the response at higher seismic intensities is rather sensitive to the model parameters, mainly the damping ratio and the connection strength. Since their calibration requires a strong experimental basis, a probabilistic approach considering different scenarios seems necessary and can improve the insight on the possible structural behaviour of the building when such information is not available.

4.4 Mixed reinforced concrete/unreinforced masonry structure

The effectiveness of the modelling approach in capturing complex interactions between in-plane and out-of-plane response of buildings was tested modelling a modern mixed reinforced concrete (RC)/unreinforced masonry (URM) structure, tested as well in a shaking table at EUCENTRE, Pavia, which showed an out-of-plane failure of thin URM walls (Beyer et al., 2015). The building prototype, as a part of the CoMa project, was indeed designed to address, among other topics, the different response of RC/URM buildings in the positive and negative directions, deriving from the grouping

4.4. Mixed reinforced concrete/unreinforced masonry structure

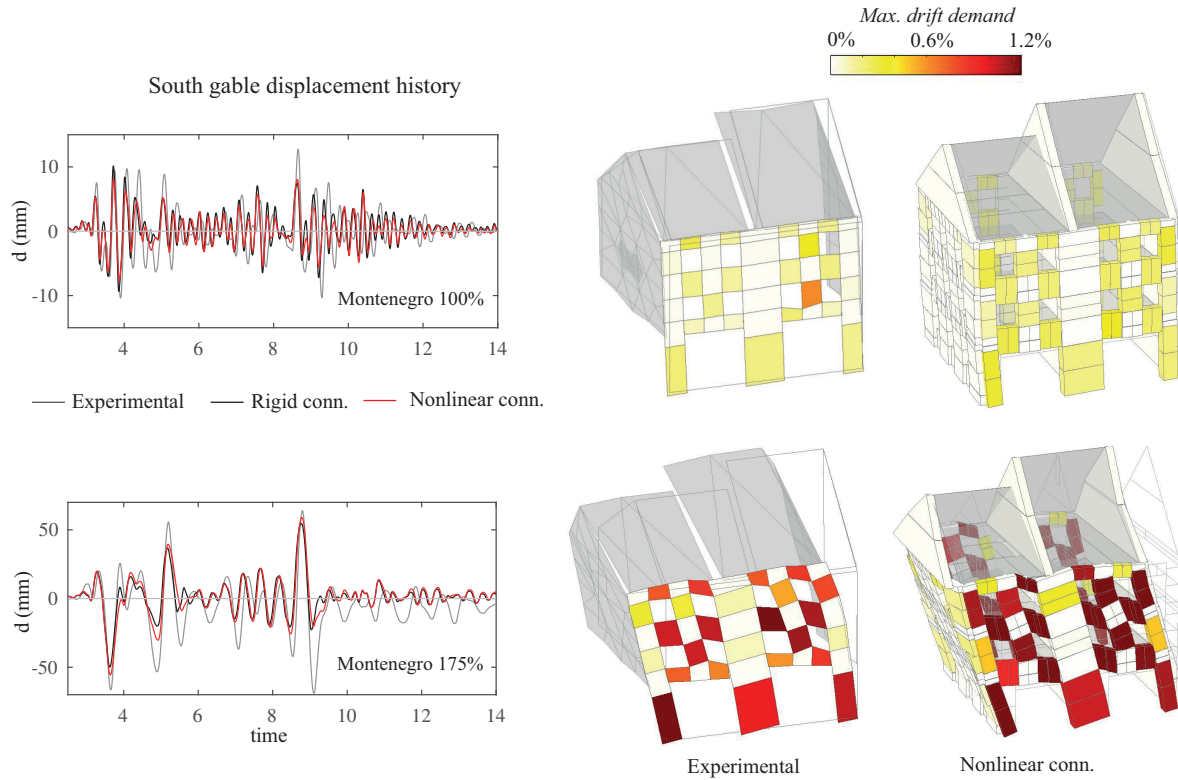


Figure 4.11 – Stone masonry building: Time-history displacement response of the north gable.

of RC members at one end of the building, and related to this, the issue of the vulnerability of out-of-plane loaded elements, subjected to variable boundary conditions and possible loss of contact with the concrete slabs. The test specimen, symmetric in plan, was a 4-storey half-scale building, featuring two URM piers and one RC wall per side in the direction of shaking (Figure 4.13). In the out-of-plane direction, one URM wall at each side was present, confined at the top and the bottom by the concrete slabs of the building. The building was subjected to nine main ground motions of increasing intensity, obtained by scaling the Montenegro (1979) ground motion, i.e., the same ground motion that was used for the test of the stone masonry building. It was instrumented with accelerometers and potentiometers measuring local deformations, including the out-of-plane deformation of the walls at all storeys, which will be compared in the following to the deformations of the numerical model. Storey displacements are derived from an optical measurement system, equivalent to the one used for the building in Section 4.3. The base shear was calculated from the recorded accelerations, to which a tributary mass is assigned. In the last two runs, the accelerometers at the two upper storeys saturated, hence accelerations were calculated from the displacement histories recorded by the optical measurement system. The processing of the data is presented in more detail in Beyer et al. (2015).

The collapse of the out-of-plane loaded walls of the North side during the last run was already studied in Tondelli et al. (2016a) with the use of a discrete element modelling approach. Tondelli et al. (2016a) modelled a storey-high wall and subjected it to the experimentally recorded horizontal and vertical

Chapter 4. Simulation of shaking table tests including out-of-plane response

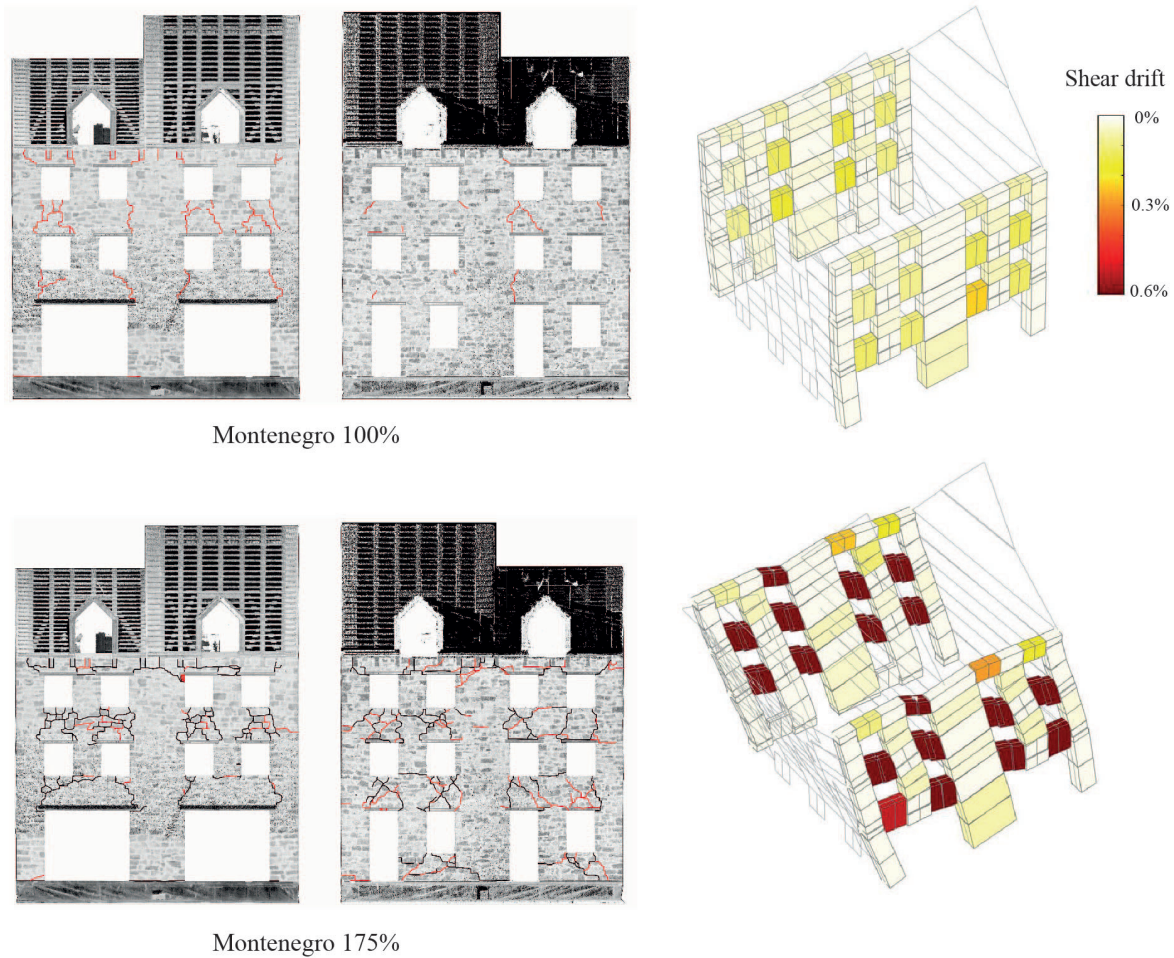


Figure 4.12 – Stone masonry building: Comparison between experimental crack patterns and shear drifts in the elements after run Montenegro 100% and Montenegro 175%.

velocity histories of the third and fourth storey at the North end of the building. These velocity histories also described the change of boundary conditions due to the slab uplift as a result of the rocking of the in-plane loaded URM walls of the fourth storey of the building. The walls at the North end rock when the building moves in the South direction. When the out-of-plane URM loses the contact with the top slab, its axial load is reduced and it loses the constraint against axial elongation, which triggers an out-of-plane mechanisms towards the interior of the building. It can be assumed that while the vertical constraint is lost, the horizontal constraint remains effective (Tondelli et al., 2016a) . In the test setup, for safety reasons, a support against out-of-plane collapse was placed at 60 mm distance from the out-of-plane walls, which was touched during the last run.

4.4. Mixed reinforced concrete/unreinforced masonry structure

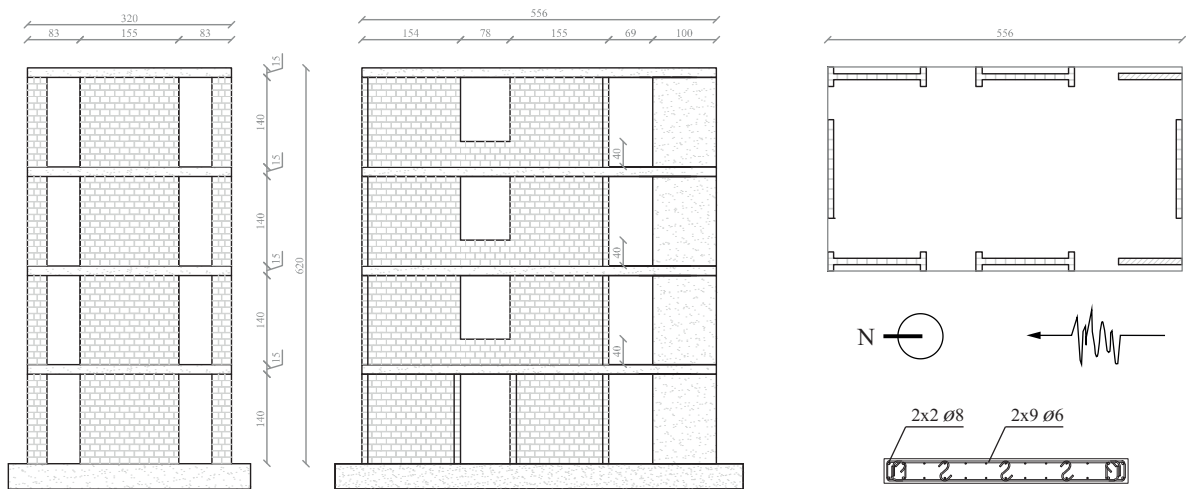


Figure 4.13 – Mixed RC-URM building: Plan, side views and RC wall section of the RC/URM building prototype

4.4.1 Model calibration

The discrete element model of the isolated fourth storey wall, subjected to the recorded accelerations and boundary conditions, captures the failure mechanism correctly. In this study the same problem is assessed through an equivalent frame model (Figure 4.14), modelling both storey accelerations and the slab uplift as a function of the in-plane behaviour. Concrete walls are modelled through a single force-based beam element per storey, with five integration points. A fibre section approach is used to model the sectional behaviour. Since local deformations in the concrete elements are not of interest, the force-based element approach is considered sufficiently accurate for the scope of the study. Unreinforced masonry elements, both piers and spandrel elements, are modelled with a single macroelement. For pier elements loaded in their out-of-plane direction, since the location of the hinge of the out-of-plane mechanism, in the test, was close to the midheight, further discretisation was not considered necessary (Tondelli et al., 2016a). The slabs are modelled with elastic shell elements. Unlike in the model of the stone masonry building where orthotropic membrane elements were used to represent the slabs, the RC slabs of the mixed building had a considerable bending stiffness and were therefore modelled with shell elements.

The material properties of concrete and steel were derived from material tests as described in Beyer et al. (2015). The compressive strength of concrete is set to 39 MPa for the whole section; the yield strength of the steel is set to 530 MPa. As for the building in Section 4.3, the material properties of URM elements are extracted from the available shear compression tests (Petry and Beyer, 2014b) performed for characterising the material. The test series included five tests, with different boundary conditions (ratios between shear span and height ranging between 0.5 to 1.5) and axial loads applied. From the series, two tests that developed shear failure are plotted in Figure 4.15. The Young's modulus of

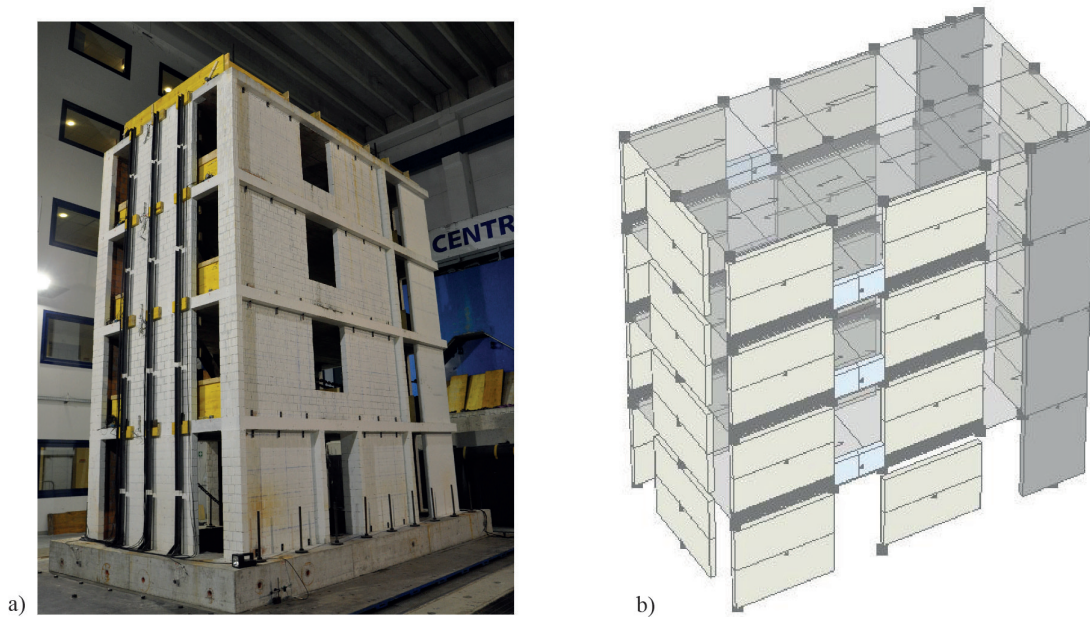


Figure 4.14 – Mixed RC-URM building: (a) Test prototype on the shaking table. (b) Equivalent frame model of the building

masonry is assumed equal to 4500 MPa, and the shear modulus to 1500 MPa. The compression strength derived from compression tests, equal to 5.66 MPa, describes sufficiently well the response of the flexural panels. A cohesion equal to 0.23 MPa and a friction coefficient $\mu_0 = 0.23$ define the maximum shear strength. The hysteretic dissipation and the post-peak force drop are defined, respectively, by a residual friction coefficient of $\mu_R = 0.15$ and a 20% force drop at a drift of 0.25%.

4.4.2 Time history response

The simulations of the nine experimental runs were performed applying the accelerogram recorded at the level of the shaking table. Two models, featuring damping ratios of 1% and 2%, were considered. The damping model was assumed as a Rayleigh damping proportional to the initial stiffness only, in order to avoid damping excessively the out-of-plane oscillations of the masonry elements, which increase considerably in period as a function of their amplitude. The global response, as shown in Figure 4.16, is predicted better by the 1% damping ratio model, remaining however reasonably good for both models, both for displacement and for acceleration demands at the top floor. The out-of-plane local displacements predicted for the walls of the North side are shown in Figure 4.17. The initiation of the phenomenon is captured at the right seismic intensity by both models, and the magnitude of out-of-plane displacement is described better by the model with the lower damping ratio.

The slab uplift and loss of vertical load on the out-of-plane elements is captured by the model, and is the phenomenon that originates the increase of out-of-plane displacements also in the simulations.

4.4. Mixed reinforced concrete/unreinforced masonry structure

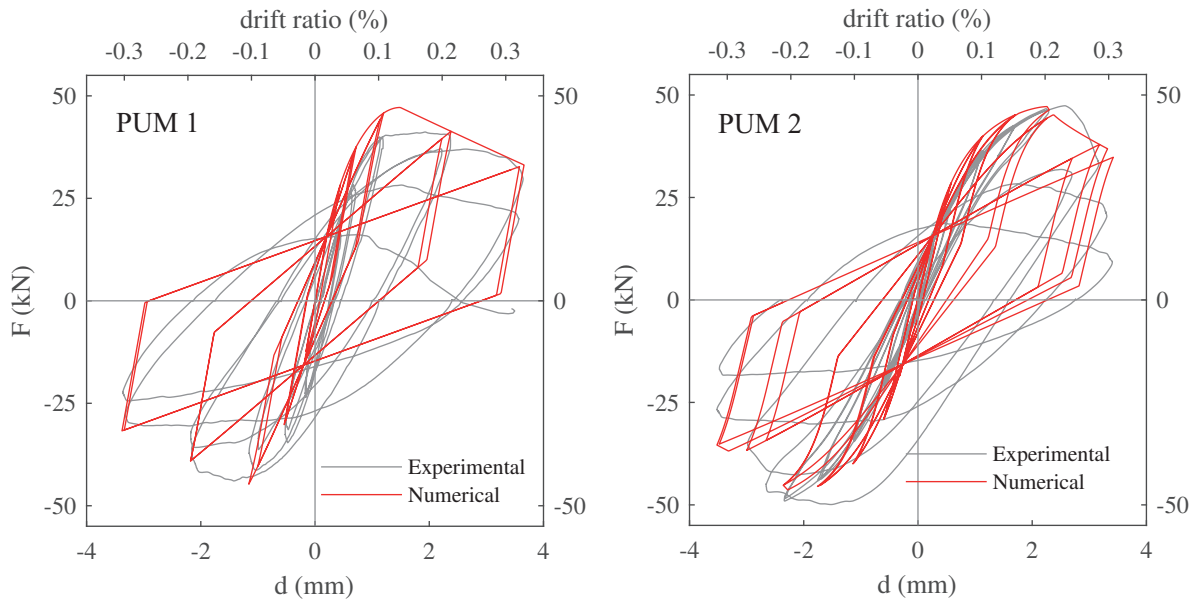


Figure 4.15 – Mixed RC-URM building: Calibration of the numerical shear model based on two shear compression tests, PUM1 (a) and PUM2 (b), on scaled masonry walls, as described in Petry and Beyer (2014b)

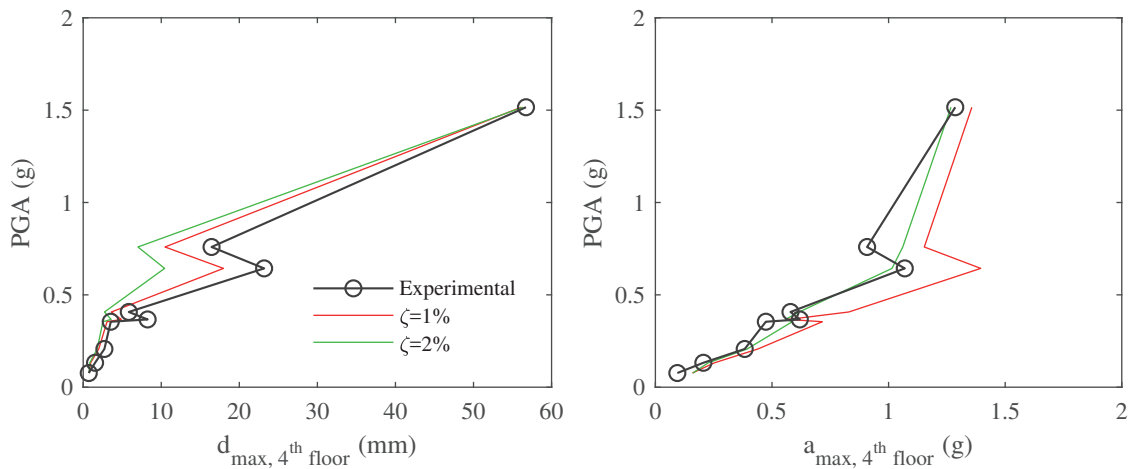


Figure 4.16 – Mixed RC-URM building: Global response parameters predicted by the models for different damping ratios: (a) displacement demand and (b) maximum acceleration at the top floor

However, the model fails in describing the complete out-of-plane collapse in the last run. Since the global demand, in terms of magnitude of maximum forces, accelerations and displacements, as shown in Figures 4.18-4.19, is correctly predicted also for the last run, the underestimation of the out-of-plane displacement can be attributed to the sensitivity of the phenomenon to the local change of boundary conditions. Although the model can capture the kinematics of the phenomenon, the development of an out-of-plane failure requires the exact prediction of the time history response in the instants of

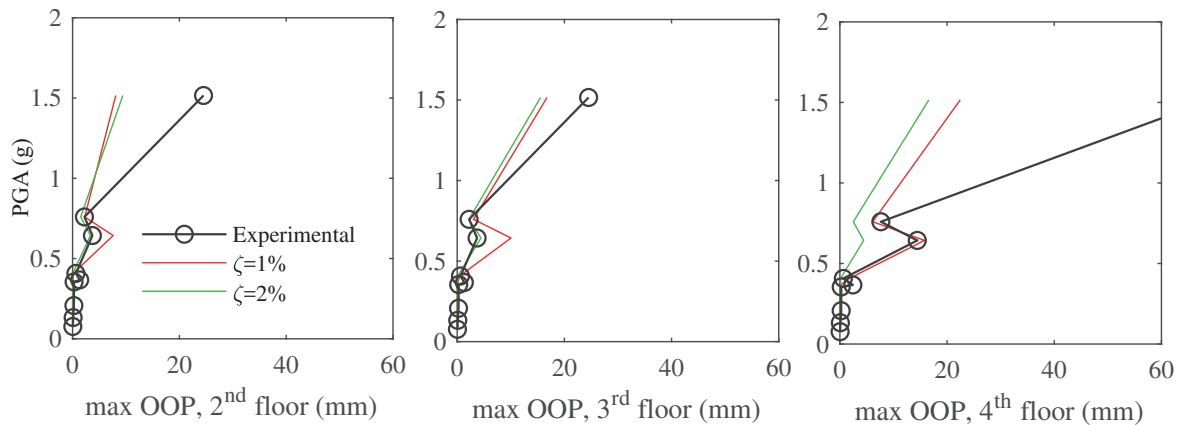


Figure 4.17 – Mixed RC-URM building: Comparison of experimental and numerical out-of-plane displacements at second, third and fourth storeys, for increasing levels of ground motion intensities

slab uplift, and is rather sensitive in particular to the duration of the predicted uplift. Such level of detail is hardly achievable in a time history analysis and therefore the modelling approach seems only suitable for predicting the onset of the out-of-plane mechanisms, when the kinematics is related to the transient variation of boundary conditions depending on the in-plane response.

4.5 Conclusions

The novel implementation of a macro-element for the simulation of the in-plane and out-of-plane behaviour of masonry panels allows the use of equivalent frame models to unreinforced masonry buildings that develop in-plane and out-of-plane failure modes. In addition, elements and materials for a refined modelling of connections have been implemented. In such way, the common hypothesis for equivalent frame models of perfect connection between orthogonal walls and between floors and walls can be relaxed and the method can be applied to buildings, such as historical masonry buildings, which do not meet the requirement of perfect connections.

The calibration of such models by means of test results is generally sufficient to predict the stiffness and the modal characteristics of the building, also when complex roof structures and tall gables are present, and the maximum force capacity. The time history response, and therefore the prediction of failure mode, drift demand and damage on single elements depends on the damping model that is applied and the modelling of connections. However, the numerical simplicity of equivalent frame models allows for multiple dynamic analyses which can explicitly model the parameter uncertainty. In such way, a scenario of possible failure modes and damage estimation at different seismic intensities can be estimated, including modelling uncertainties that cannot be calibrated without sound experimental results to be used as comparison.

The out-of-plane failure of elements confirms to be sensitive to the modelling hypothesis regarding the connection to the floors, for buildings with deformable diaphragms, and to the exact modelling

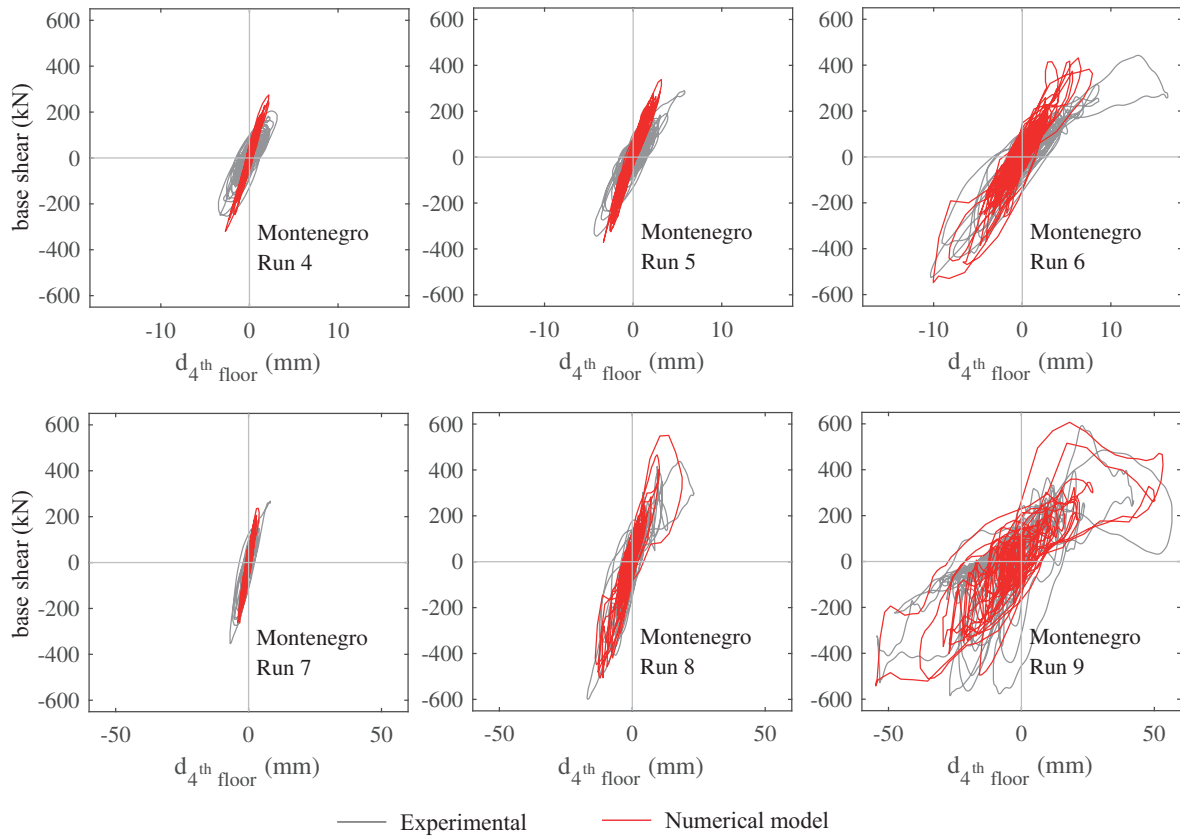


Figure 4.18 – Mixed RC-URM building: Force displacement global response of the building (damping ratio $\zeta = 1\%$)

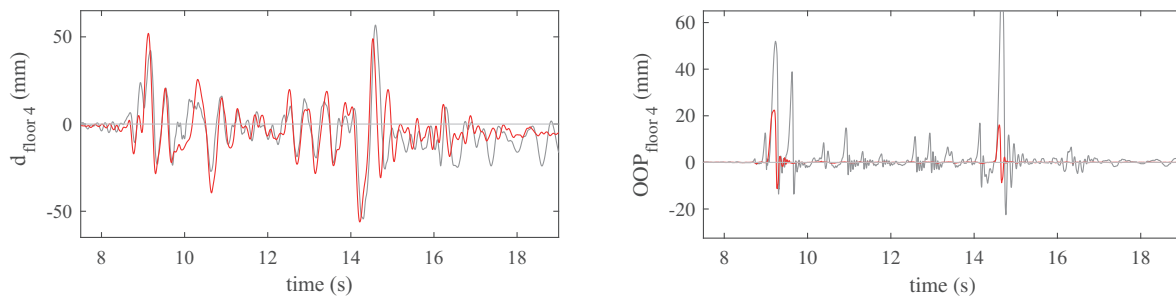


Figure 4.19 – Mixed RC-URM building: Comparison of time-history responses for Run 9: displacement of the top floor and out-of-plane deformation at the top storey.

of boundary connections, for buildings with stiff floors. For the first case, the effectiveness of the connection, i.e. the maximum force transfer which can take place between floors and walls, governs the problem and defines the failure mode. A model accounting for nonlinear connections can therefore capture the change in the seismic response, from out-of-plane failure modes to in-plane failure, that

Chapter 4. Simulation of shaking table tests including out-of-plane response

can be obtained by improving the building connections and show the vulnerability of a building to this type of failure mode.

For buildings with stiff floors, the change of boundary conditions related to the in-plane response is explicitly captured. Despite modelling correctly the kinematics of the phenomenon, the response is sensitive to the duration of the boundary condition change, and the prediction on the out-of-plane response is therefore reliable only up to the mechanism initiation.

Conclusions

The work presented in this thesis constitutes a proposition of an integrated approach for modelling both the in-plane and out-of-plane response of masonry buildings through equivalent frame models, to be used in multiple simulations, accounting explicitly for all sources of uncertainty in a probabilistic framework. The main contributions of this work regard:

- the development of a macro-element for the modelling of in-plane and out-of-plane response of masonry walls in equivalent frame buildings, implemented in OpenSees and available to the research and professional community.
- the implementation into OpenSees of additional tools for the modelling of the out-of-plane response of buildings, accounting for complex and nonlinear interactions between structural elements (floor to wall connections, wall to wall connections)
- the quantification of the main sources of uncertainty on the lateral response of stone masonry walls, deriving from a database of 128 shear compression tests the statistical distributions of material properties and displacement capacities to be used in a consistent probabilistic assessment.
- the proposition and validation in case study of a simplified probabilistic approach, requiring few nonlinear static analyses, defined to be potentially used out of the domain of academic research.

The collection and analysis of a database of shear compression tests allowed observing trends and evaluating the uncertainty on the mechanical parameter that are adopted for modelling the in-plane response of stone masonry walls. In particular, the analysis highlighted the high variability of all parameters related to displacements, i.e. the displacement capacities at different limit states (the yielding drift, evaluated on the bilinear approximation of the capacity curve of a wall, the cracking drift, the drift at maximum force, the significant damage limit state drift, the collapse drift) and the estimates of the initial and effective stiffness of walls. Resorting only to empirical models for the determination of the drift limits, the scatter of the response is reduced if drift values are normalised by the minimum between the length of the wall and the shear span. Moreover, the displacement capacity of stone masonry walls tends to reduce with increasing axial load ratios, and accounting for this effect could further reduce the scatter of experimental drift determinations. However, this would require the

Conclusions

use of numerical tools which capture this effect: for this reason, in the displacement capacity model implemented in the proposed macro-element, a possible dependency on the axial load ratio of the drift at which the element loses the lateral load bearing capacity is introduced.

The determination of stiffness properties of stone masonry wall is characterised by an equally relevant uncertainty. It was observed that measures of stiffness derived from material tests, in particular compression tests, are not adequate for estimating reliably the lateral stiffness of the walls in the database. This observation is confirmed by the simulation of the stone masonry building presented in Chapter 4, for which the stiffness estimate obtained through the available compression tests was higher than the stiffness measured in shear compression tests of a factor 1.6. The latter, however, provided a reasonably accurate estimate of the modal characteristics of the building. The effective to initial stiffness ratio is a parameter subjected to a big scatter. Its median value, anyway, is close to the one (0.5) prescribed by the EC-8. The stiffness of stone masonry walls showed a dependency trend on the axial load ratio, i.e. the panels with the highest compression level were also stiffer. This trend extends also to URM walls, and could be explained with the closure of voids and micro-cracks for higher axial load ratios.

The determination of the force capacity is affected by a smaller uncertainty. The estimate of the force capacity for shear dominated walls, however, are significantly affected by uncertainties on the tensile strength of masonry, if a tensile criterion is applied, or by the cohesion and friction to apply, if a frictional criterion is preferred. Available data do not allow concluding on which of the two criteria describes more accurately the shear capacity of stone masonry walls. If the friction coefficient is extracted from regression analysis, values closer to 0.3, compared to the 0.4 indicated by the codes, are found to fit better the available data.

When these findings are brought into the probabilistic assessment of a building, they reflect in a different impact of the modelling uncertainties on the estimated seismic capacity. Although conclusions on this regard could be influenced by the fact that only significant damage limit state was assessed, and that failure of the building and failure was assumed when the first element reached its displacement capacity, ignoring therefore possible redistribution among the remaining elements, the analysis proved that the quantities related to displacements, primarily the displacement capacity of the elements, are the major source of model uncertainty. Significantly lower impact has the estimate of the force capacity, particularly for flexural failure modes.

Given the level of indetermination of the displacement capacity, the order of magnitude of the epistemic uncertainty approximates the expected record to record variability, suggesting that both sources of uncertainty, for stone masonry buildings at least, should be considered, as none of them is largely predominant.

On the methodological point of view, the proposed Point Estimate method, and the more intuitive logic tree approach, both proved to be sufficiently accurate in the estimate of the distribution of the model response.

The proposed macro-element approach is effectively modelling the static and dynamic in plane and

out-of-plane response. The shear model that was derived for the in-plane response approximates well the force-displacement curve of experimental results obtained for different axial load ratios. The out-of-plane response approximates the rigid body analysis for big deformations; the dynamic response, and in particular the energy dissipation at impacts in rocking motion is captured through equivalent Rayleigh damping models. However, this approximation requires careful calibration of the damping model in order to produce realistic predictions.

When extended to the modelling of complete buildings, calibration of the material properties of the proposed macro-element through shear compression tests is sufficient to obtain reasonably close estimates of the dynamic response, particularly for smaller levels of nonlinearity. The modelling approach allows studying explicitly the role of the quality of connections in the seismic response of a building. Such response proved to be rather sensitive to the applied damping ratio and the modelling of connections. A sensitivity analysis showed that the model captures a transition between in-plane failure to out-of-plane failure for degrading quality of connections, and captures the main expected vulnerabilities of both analysed structures. However, when the out-of-plane response is related to the exact estimate of transient boundary conditions, depending on the in-plane behaviour, the models fail capturing collapse; it can however describe the activation of out-of-plane mechanisms consistently with experimental results.

Future work

The future developments of the presented work should tackle the following points, that may improve the accuracy of the proposed approach:

- all models including the out of plane response proved to be rather sensitive to the damping ratio that was applied. In particular, the rocking oscillator dissipates energy, in the numerical simulations, only through viscous damping and, if the algorithm allows for it, numerical damping. It would be necessary to check if the assumption of applying viscous damping models to a body that in reality dissipates energy at impacts is applicable. Moreover, it should be verified whether the same damping model can be applied to in-plane and out-of-plane mechanisms, or a more refined modelling of damping for out-of-plane mechanisms is required. Since for rocking vibrations usually dissipation is assumed to take place only at impacts and to be governed by a coefficient of restitution, a numerical detection of impact conditions and the application of suitable models for a finite energy dissipation during the impact step could be a strategy to apply. Finally, the role of vibrations of the mass in axial direction at impacts should be carefully investigated.
- the models derived in this work for the in-plane response are conceived and calibrated to reproduce the behaviour of pier elements. Since spandrels may have a consistently different response, a calibration of this approach on spandrels and a possible imple-

Conclusions

mentation of proper models (for example, a shear model, or a flexural section model) dedicated to their modelling would be necessary.

- the modelling of connections between structural elements on equivalent frame models including the out-of-plane response is a key point: models correctly accounting for the crack opening at interfaces, depending on the level of interlocking of the masonry, and proper account of the flange effect of orthogonal walls, depending on the stiffness and the dimensions of the corners, should be implemented.

A Formulation of the three dimensional macro-element: derivations

A.1 Co-rotational formulation of compatibility relations

The basic displacements can be computed from local displacements in a co-rotational formulation using Euler's formula for finite rotations in the three-dimensional space. A rotated vector \mathbf{v}' is expressed as a function of the undeformed vector \mathbf{v} and the set of three finite rotations α_1 , α_2 and α_3 as:

$$\mathbf{v}' = \mathbf{v} \cos \gamma + (\mathbf{n} \times \mathbf{v}) \sin \gamma + (1 - \cos \gamma)(\mathbf{n} \cdot \mathbf{v})\mathbf{n} \quad (\text{A.1})$$

The orientation vector of the two blocks (i.e. the direction vector from node i to node e , and from node e to node j , respectively) in the undeformed configuration can be expressed as $\mathbf{v} = [1, 0, 0]^T$. The direction vector of the first block in the deformed configuration, where H is the height if the element, can be expressed as:

$$\mathbf{v}' = \frac{1}{H'_A} \begin{bmatrix} \frac{H}{2} + u_{eA} - u_i \\ v_{eA} - v_i \\ w_{eA} - w_i \end{bmatrix}, \quad H'_A = \sqrt{\left(\frac{H}{2} + u_{eA} - u_i\right)^2 + (v_{eA} - v_i)^2 + (w_{eA} - w_i)^2} \quad (\text{A.2})$$

Furthermore, if one postulates that no torsional rotation is imposed to the block, the last term of Equation A.1 vanishes. Solving Equation A.1 for the remaining two rotations of the first block one obtains:

$$\gamma = \arccos v'_{(1)} \quad (\text{A.3})$$

$$\mathbf{n} = \frac{1}{\sqrt{1 - v'_{(1)}}} \begin{bmatrix} 0 \\ -v'_{(3)} \\ v'_{(2)} \end{bmatrix} \quad (\text{A.4})$$

Appendix A. Formulation of the three dimensional macro-element: derivations

Proceeding in the same way for the second block, the compatibility equations defining the basic displacements in co-rotational formulation take the following form:

$$d_1 = -\frac{H}{2} + H'_A \quad (\text{A.5})$$

$$\varphi_{z1} = -\varphi_{zi} + \frac{(v_{eA} - v_i) \arccos \frac{\frac{H}{2} + u_{eA} - u_i}{H'_A}}{\sqrt{H'^2_A - \left(\frac{H}{2} + u_{eA} - u_i\right)^2}} \quad (\text{A.6})$$

$$\varphi_{y1} = -\varphi_{yi} + \frac{(-w_{eA} + w_i) \arccos \frac{\frac{H}{2} + u_{eA} - u_i}{H'_A}}{\sqrt{H'^2_A - \left(\frac{H}{2} + u_{eA} - u_i\right)^2}} \quad (\text{A.7})$$

$$d_2 = \frac{-(u_{eA} - u_{eB})(H - u_i + u_j) + (v_{eA} - v_{eB})(v_i - v_j) + (w_{eA} - w_{eB})(w_i - w_j)}{\sqrt{(H + u_j - u_i)^2 + (v_j - v_i)^2 + (w_j - w_i)^2}} \quad (\text{A.8})$$

$$\varphi_{z2} = \frac{(-v_{eA} + v_i) \arccos \frac{\frac{H}{2} + u_{eA} - u_i}{H'_A}}{\sqrt{H'^2_A - \left(\frac{H}{2} + u_{eA} - u_i\right)^2}} + \frac{(-v_{eB} + v_j) \arccos \frac{\frac{H}{2} - u_{eB} + u_j}{H'_B}}{\sqrt{H'^2_B - \left(\frac{H}{2} - u_{eB} + u_j\right)^2}} \quad (\text{A.9})$$

$$\varphi_{y2} = \frac{(w_{eA} - w_i) \arccos \frac{\frac{H}{2} + u_{eA} - u_i}{H'_A}}{\sqrt{H'^2_A - \left(\frac{H}{2} + u_{eA} - u_i\right)^2}} + \frac{(w_{eB} - w_j) \arccos \frac{\frac{H}{2} - u_{eB} + u_j}{H'_B}}{\sqrt{H'^2_B - \left(\frac{H}{2} - u_{eB} + u_j\right)^2}} \quad (\text{A.10})$$

$$d_3 = -\frac{H}{2} + H'_B \quad (\text{A.11})$$

$$\varphi_{z3} = \varphi_{zj} + \frac{(v_{eB} - v_j) \arccos \frac{\frac{H}{2} - u_{eB} + u_j}{H'_B}}{\sqrt{H'^2_B - \left(\frac{H}{2} - u_{eB} + u_j\right)^2}} \quad (\text{A.12})$$

A.1. Co-rotational formulation of compatibility relations

$$\varphi_{y3} = \varphi_{yj} + \frac{(w_{eB} - w_j) \arccos \frac{\frac{H}{2} - u_{eB} + u_j}{H'_B}}{\sqrt{H'^2_B - \left(\frac{H}{2} - u_{eB} + u_j\right)^2}} \quad (\text{A.13})$$

$$s_y = \frac{-(v_{eA} - v_{eB})(H - u_i + u_j) - (u_{eA} - u_{eB})(v_i - v_j) +}{\sqrt{(H + u_j - u_i)^2 + (v_j - v_i)^2 + (w_j - w_i)^2}} \quad (\text{A.14})$$

$$s_z = \frac{-(w_{eA} - w_{eB})(H - u_i + u_j) - (u_{eA} - u_{eB})(w_i - w_j) +}{\sqrt{(H + u_j - u_i)^2 + (v_j - v_i)^2 + (w_j - w_i)^2}} \quad (\text{A.15})$$

A.2 Incremental equilibrium matrix

The incremental compatibility matrix Γ_C can be derived directly from the relations expressing the basic displacements as a function of local displacements. Enforcing the principle of contragradiency, the equilibrium matrix Γ_E , expressing the equilibrium conditions in the deformed configuration, can be obtained as the transpose of the incremental compatibility matrix. The expressions in Equation 2 can be obtained by Taylor-series expansion in Annex A.1, under the assumption that the orientation of the central interface remains defined by the undeformed configuration. This simplifies the equilibrium matrix, as defined in Equation A.16, where the displacement-dependent terms define the $P - \Delta$ effect.

$$\Gamma_E = \begin{bmatrix} -1 & 0 & 0 & 0 & 0 & 0 & 0 & 0 & 0 & 0 & 0 & 0 & 0 \\ \frac{2}{H}(v_i - v_{eA}) & -\frac{2}{H} & 0 & 0 & \frac{2}{H} & 0 & 0 & 0 & 0 & 0 & 0 & 0 & 0 \\ \frac{2}{H}(w_i - w_{eA}) & 0 & \frac{2}{H} & 0 & 0 & -\frac{2}{H} & 0 & 0 & 0 & 0 & 0 & 0 & 0 \\ 0 & 0 & 0 & 0 & 0 & 0 & 0 & 0 & 0 & 0 & 0 & 0 & -1 \\ 0 & 0 & -1 & 0 & 0 & 0 & 0 & 0 & 0 & 0 & 0 & 0 & 0 \\ 0 & -1 & 0 & 0 & 0 & 0 & 0 & 0 & 0 & 0 & 0 & 0 & 0 \\ 1 & 0 & 0 & 0 & 0 & 0 & 0 & 0 & 0 & 0 & 0 & 0 & 0 \\ 0 & 0 & 0 & 0 & \frac{2}{H} & 0 & \frac{2}{H}(v_j - v_{eB}) & -\frac{2}{H} & 0 & 0 & 0 & 0 & 0 \\ 0 & 0 & 0 & 0 & 0 & -\frac{2}{H} & \frac{2}{H}(w_j - w_{eB}) & 0 & \frac{2}{H} & 0 & 0 & 0 & 0 \\ 0 & 0 & 0 & 0 & 0 & 0 & 0 & 0 & 0 & 0 & 0 & 0 & 1 \\ 0 & 0 & 0 & 0 & 0 & 0 & 0 & 0 & 0 & 1 & 0 & 0 & 0 \\ 0 & 0 & 0 & 0 & 0 & 0 & 0 & 0 & 1 & 0 & 0 & 0 & 0 \\ 1 & 0 & 0 & -1 & 0 & 0 & 0 & 0 & 0 & 0 & 0 & 0 & 0 \\ \frac{2}{H}(v_{eA} - v_i) & \frac{2}{H} & 0 & 0 & -\frac{2}{H} & 0 & 0 & 0 & 0 & 0 & -1 & 0 & 0 \\ \frac{2}{H}(w_{eA} - w_i) & 0 & -\frac{2}{H} & 0 & 0 & \frac{2}{H} & 0 & 0 & 0 & 0 & 0 & -1 & 0 \\ 0 & 0 & 0 & 1 & 0 & 0 & -1 & 0 & 0 & 0 & 0 & 0 & 0 \\ 0 & 0 & 0 & 0 & -\frac{2}{H} & 0 & \frac{2}{H}(v_{eB} - v_j) & \frac{2}{H} & 0 & 1 & 0 & 0 & 0 \\ 0 & 0 & 0 & 0 & 0 & \frac{2}{H} & \frac{2}{H}(w_{eB} - w_j) & 0 & -\frac{2}{H} & 0 & 1 & 0 & 0 \end{bmatrix} \quad (\text{A.16})$$

A.3 Effect of distributed loads along the element

Accounting for distributed element forces along the element axis, which can induce second-order effects, requires the definition of the two vectors \mathbf{q}_0 and \mathbf{p}_0 . The former adds an

equivalent second-effect of the distributed load to the sectional forces in the basic system, while the latter ensures equilibrium conditions for the four bodies in Figure A.1, i.e. nodes i and j and the blocks A and B. Since the distributed load is defined in the undeformed local system, its direction does not rotate with the macro-element. If the load is constant along the axis of the element, the vector \mathbf{q}_0 can be defined as in Equation A.17. If the load is triangular, with its maximum value in correspondence to the first node, Equation A.18 holds. Such loading can be useful when modelling the overturning of a gable element subjected mainly to its self-weight. In both expressions only the axial component of the distributed load affects the geometrical nonlinearity, coherently with the assumed $P - \Delta$ formulation.

$$\mathbf{q}_0^{(rect)} = \left[-\frac{q_x H}{4}, 0, 0, 0, 0, 0, \frac{q_x H}{4}, 0, 0, 0, 0, 0 \right] \quad (\text{A.17})$$

$$\mathbf{q}_0^{(tr)} = \left[-\frac{5q_x H}{24}, 0, 0, 0, 0, 0, \frac{q_x H}{24}, 0, 0, 0, 0, 0 \right] \quad (\text{A.18})$$

The set of reactions \mathbf{p}_0 ensuring equilibrium is defined in Equations A.19 and A.20 for rectangular and triangular distributed loads, respectively.

$$\mathbf{p}_0^{(rect)} = \left[\frac{q_x H}{4}, \frac{q_y H}{4}, \frac{q_z H}{4}, 0, 0, 0, \frac{q_x H}{4}, \frac{q_y H}{4}, \frac{q_z H}{4}, 0, 0, 0, \frac{q_x H}{4}, \frac{q_y H}{4}, \frac{q_z H}{4}, \frac{q_x H}{4}, \frac{q_y H}{4}, \frac{q_z H}{4} \right] \quad (\text{A.19})$$

$$\mathbf{p}_0^{(tr)} = \left[\frac{5q_x H}{24}, \frac{5q_y H}{24}, \frac{5q_z H}{24}, 0, 0, 0, \frac{q_x H}{24}, \frac{q_y H}{24}, \frac{q_z H}{24}, 0, 0, 0, \frac{q_x H}{6}, \frac{q_y H}{6}, \frac{q_z H}{6}, \frac{q_x H}{12}, \frac{q_y H}{12}, \frac{q_z H}{12} \right] \quad (\text{A.20})$$

A.4 Nonlinear elastic flexural model

The flexural interface described in Section 3, if a no-tension material, linear elastic in compression, is postulated, is essentially a nonlinear elastic model. It is governed by the position of the neutral axis in the section, and the consequent variation of the integration domain of the strain field defined in Equation 16. In addition to the elastic solution solution provided in Equation 18 for a fully compressed section, and the null solution for the case in which the section is subjected to only traction, four cases need to be defined (Figure 3). Solutions of case 1, 2 and 4 are provided in Equations A.21-A.23. The solution of case 3, for a triangular integration domain, can be obtained by subtraction of the solution of case 2 (Equation A.22) from the linear elastic case (Equation 18).

Appendix A. Formulation of the three dimensional macro-element: derivations

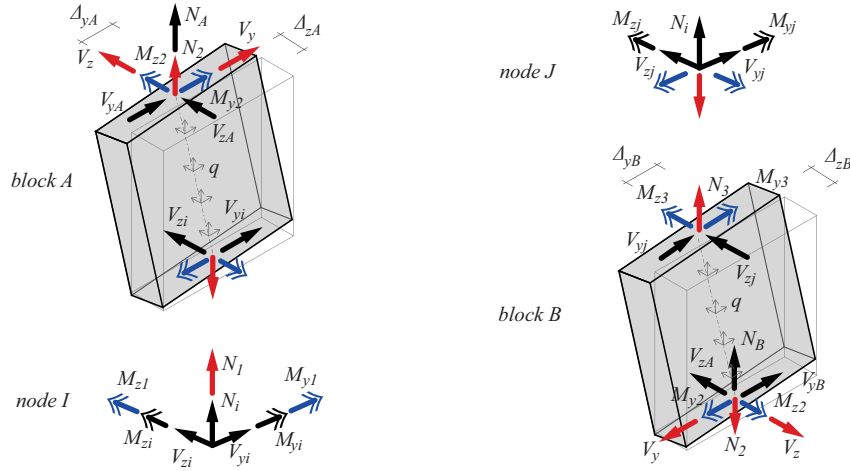


Figure A.1 – Derivation of local forces from equilibrium conditions applied in the deformed configuration.

$$\begin{cases} N_{el} &= -\frac{Et}{24|\chi_z|} \left[t^2 \chi_y^2 + 3(L|\chi_z| - 2\varepsilon_0)^2 \right] \\ M_{z,el} &= \frac{Et}{24\chi_z|\chi_z|} \left(4\varepsilon_0^3 + t^2 \varepsilon_0 \chi_y^2 - 3L^2 \varepsilon_0 \chi_z^2 + L^3 |\chi_z^3| \right) \\ M_{y,el} &= \frac{Et}{24|\chi_z|} \chi_y t^2 (L|\chi_z| - 2\varepsilon_0) \end{cases} \quad (\text{case 1}) \quad (\text{A.21})$$

$$\begin{cases} N_{el} &= -\frac{E}{48|\chi_y \chi_z|} \left(-2\varepsilon_0 + t|\chi_y| + L|\chi_z| \right)^3 \\ M_{z,el} &= \frac{E}{384|\chi_y \chi_z| \chi_z} \left(-2\varepsilon_0 + t|\chi_y| - 3L|\chi_z| \right) \left(-2\varepsilon_0 + t|\chi_y| + L|\chi_z| \right)^3 \\ M_{y,el} &= \frac{E}{384|\chi_y \chi_z| \chi_y} \left(2\varepsilon_0 + 3t|\chi_y| - L|\chi_z| \right) \left(-2\varepsilon_0 + t|\chi_y| + L|\chi_z| \right)^3 \end{cases} \quad (\text{case 2}) \quad (\text{A.22})$$

$$\begin{cases} N_{el} &= -\frac{EL}{24|\chi_y|} \left[L^2 \chi_z^2 + 3(t|\chi_y| - 2\varepsilon_0)^2 \right] \\ M_{z,el} &= \frac{EL}{24|\chi_y|} \chi_z L^2 (t|\chi_y| - 2\varepsilon_0) \\ M_{y,el} &= \frac{EL}{24\chi_y|\chi_y|} \left[(\varepsilon_0 + t|\chi_y|)(2\varepsilon_0 - t|\chi_y|)^2 + \varepsilon_0 L^2 \chi_z^2 \right] \end{cases} \quad (\text{case 4}) \quad (\text{A.23})$$

A.5 Consistent mass matrix

A consistent formulation of the mass matrix can be derived by imposing that the kinetic energy of the element with distributed mass and the element with lumped mass be equal; the kinematic energy is defined as a function of the velocity vector $\dot{\mathbf{u}}(x)$ of every point x along the element axis and the mass associated to each point as:

$$E_{kin} = \frac{1}{2} \rho A \int_0^H \dot{\mathbf{u}}(x)^T \dot{\mathbf{u}}(x) dx \quad (\text{A.24})$$

In Equation A.24 it is postulated that the mass is equally applied in all directions, and that all mass is concentrated along the element axis, since in the OpenSees implementation the element has no information on the actual geometry of the section. Such distributed mass is expressed by the quantity ρA (i.e. mass per unit length), constant along the element height. For gable elements, the latter hypothesis does not hold, and a lumped matrix as in Equation A.29 can be applied.

The velocity vector $\dot{\mathbf{u}}(x)$ can be derived as a function of the nodal displacements and a shape function $\mathbf{N}_A(x)$ defined for every point x . For simplicity of notation, the point position can be defined by a normalised coordinate ξ_A or ξ_B for block A and B (Figure A.2a). The expressions of such shape functions are rather simple, since the macro-element is composed by rigid blocks with linear displacement fields. For block A, the function $\mathbf{N}_A(\xi_A)$ can be defined as:

$$\mathbf{N}_A(\xi_A) = \begin{bmatrix} 1 - \xi_A & 0 & 0 & 0 & 0 & 0 & \xi_A & 0 & 0 & 0 & 0 & 0 \\ 0 & 1 - \xi_A & 0 & 0 & 0 & 0 & 0 & \xi_A & 0 & 0 & 0 & 0 \\ 0 & 0 & 1 - \xi_A & 0 & 0 & 0 & 0 & 0 & \xi_A & 0 & 0 & 0 \end{bmatrix} \quad (\text{A.25})$$

$$\dot{\mathbf{u}}(\xi_A) = \mathbf{N}_A(\xi_A) \dot{\mathbf{u}}_{local} \quad (\text{A.26})$$

Substituting this expression in Equation A.24, the kinetic energy of block A can be expressed as:

$$E_{kin,A} = \frac{1}{2} \dot{\mathbf{u}}_{local}^T \left[\rho A \frac{H}{2} \int_0^1 \mathbf{N}_A(\xi_A)^T \mathbf{N}_A(\xi_A) d\xi_A \right] \dot{\mathbf{u}}_{local} = \frac{1}{2} \dot{\mathbf{u}}_{local}^T \mathbf{M}_{local,A} \dot{\mathbf{u}}_{local} \quad (\text{A.27})$$

Solving the integral and summing the contributions of both rigid blocks A and B, the consistent

Appendix A. Formulation of the three dimensional macro-element: derivations

mass matrix of the macro-element can be therefore derived as:

$$M_{local}^{(cons.)} = \rho AH \begin{bmatrix} \frac{1}{6}[I]_{3 \times 3} & \mathbf{0} & \mathbf{0} & \mathbf{0} & \frac{1}{12}[I]_{3 \times 3} & \mathbf{0} \\ \mathbf{0} & [\mathbf{0}]_{3 \times 3} & \mathbf{0} & \mathbf{0} & \mathbf{0} & \mathbf{0} \\ \mathbf{0} & \mathbf{0} & \frac{1}{6}[I]_{3 \times 3} & \mathbf{0} & \mathbf{0} & \frac{1}{12}[I]_{3 \times 3} \\ \mathbf{0} & \mathbf{0} & \mathbf{0} & [\mathbf{0}]_{3 \times 3} & \mathbf{0} & \mathbf{0} \\ \frac{1}{12}[I]_{3 \times 3} & \mathbf{0} & \mathbf{0} & \mathbf{0} & \frac{1}{6}[I]_{3 \times 3} & \mathbf{0} \\ \mathbf{0} & \mathbf{0} & \frac{1}{12}[I]_{3 \times 3} & \mathbf{0} & \mathbf{0} & \frac{1}{6}[I]_{3 \times 3} \end{bmatrix} \quad (A.28)$$

Since for some explicit analyses the performance of the solver can be significantly improved by the use of a diagonal mass matrix, as an additional option available to the user, a lumped mass formulation was implemented. One criterion that may be applied for determining an optimal scheme of mass lumping is the equivalence of the inertial forces originating from a constant acceleration profile along the macro-element, between the two cases of distributed (Figure A.2b) and concentrated masses (Figure A.2c). If a limit analysis approach is used to determine the capacity of two overturning mechanisms, for both cantilever elements and walls spanning between floor/ceiling supports, such equivalence can be expressed in terms of the load multiplier corresponding to the activation of the mechanisms. This condition is satisfied for both sets of boundary conditions when half of the element mass is assigned to the central node (Equation A.29), which is the standard approach implemented in OpenSees.

$$M_{local}^{(lumped,pier)} = \frac{1}{4}\rho AH \begin{bmatrix} [I]_{3 \times 3} & \mathbf{0} & \mathbf{0} & \mathbf{0} & \mathbf{0} & \mathbf{0} \\ \mathbf{0} & [\mathbf{0}]_{3 \times 3} & \mathbf{0} & \mathbf{0} & \mathbf{0} & \mathbf{0} \\ \mathbf{0} & \mathbf{0} & [I]_{3 \times 3} & \mathbf{0} & \mathbf{0} & \mathbf{0} \\ \mathbf{0} & \mathbf{0} & \mathbf{0} & [\mathbf{0}]_{3 \times 3} & \mathbf{0} & \mathbf{0} \\ \mathbf{0} & \mathbf{0} & \mathbf{0} & \mathbf{0} & [I]_{3 \times 3} & \mathbf{0} \\ \mathbf{0} & \mathbf{0} & \mathbf{0} & \mathbf{0} & \mathbf{0} & [I]_{3 \times 3} \end{bmatrix} \quad (A.29)$$

If the element is defined as gable element, following the same approach, a lumped mass matrix can be defined as:

$$M_{local}^{(lumped,gable)} = \rho AH \begin{bmatrix} \frac{5}{12}[I]_{3 \times 3} & \mathbf{0} & \mathbf{0} & \mathbf{0} & \mathbf{0} & \mathbf{0} \\ \mathbf{0} & [\mathbf{0}]_{3 \times 3} & \mathbf{0} & \mathbf{0} & \mathbf{0} & \mathbf{0} \\ \mathbf{0} & \mathbf{0} & \frac{1}{12}[I]_{3 \times 3} & \mathbf{0} & \mathbf{0} & \mathbf{0} \\ \mathbf{0} & \mathbf{0} & \mathbf{0} & [\mathbf{0}]_{3 \times 3} & \mathbf{0} & \mathbf{0} \\ \mathbf{0} & \mathbf{0} & \mathbf{0} & \mathbf{0} & \frac{1}{3}[I]_{3 \times 3} & \mathbf{0} \\ \mathbf{0} & \mathbf{0} & \mathbf{0} & \mathbf{0} & \mathbf{0} & \frac{1}{6}[I]_{3 \times 3} \end{bmatrix} \quad (A.30)$$

However, the mass matrix in Equation A.29 does not yield the exact rotational moment of inertia for a cantilever overturning mechanism such as the one in Figure A.2d. Comparing the exact moment of inertia I_O , relative to a rotation around the point O , to the solutions of the consistent (Equation A.28) and lumped mass matrix (Equation A.29), the error can be

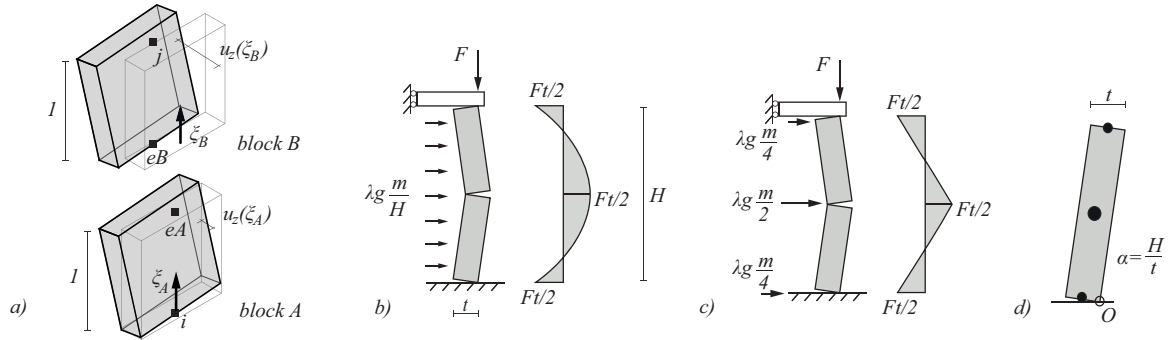


Figure A.2 – "Shape functions" for derivation of a consistent mass matrix (a). Equivalent limit analysis solutions for a wall spanning between floor levels with distributed mass (b) and lumped masses (c). Cantilever overturning mechanism with lumped masses (d).

computed as a function of the height to thickness ratio $\alpha = H/t$ of the element:

$$\frac{I_O^{(cons.)}}{I_O} = 1 - \frac{1}{2} \frac{1}{1 + \alpha^2} \quad (A.31)$$

$$\frac{I_O^{(cons.)}}{I_O} = \frac{9}{8} \left(1 - \frac{1}{2} \frac{1}{1 + \alpha^2} \right) \quad (A.32)$$

For the consistent formulation the only error introduced depends on the assumption of concentrating the mass along the element axis; it remains however reasonably small for common slenderness ratios. The lumped mass matrix introduces a further error of a factor $9/8$. Although for this particular mechanism the error would be reduced if the central node were assigned $2/3$ of the mass instead of $1/2$, the matrix in Equation A.29 is still preferred as a standard option since, as discussed, it provides exact results in terms of load multiplier under constant lateral acceleration.

Bibliography

- Addressi, D., Mastrandrea, A., and E., S. (2014). An equilibrated macro-element for nonlinear analysis of masonry structures. *Engineering Structures*, 70:82 – 93.
- Alfano, G. and Sacco, E. (2006). Combining interface damage and friction in a cohesive-zone model. *International Journal for Numerical Methods in Engineering*, 68:542–582.
- Almeida, C., Arêde, A., Guedes, J. P., and Costa, A. (2014). Shear-compressive experimental behaviour of one-leaf stone masonry in North of Portugal. In *Second European conference on earthquake Engineering and Seismology*, pages 1–13, Istanbul.
- Almeida, C., Guedes, J. P., and Arêde, A. (2012). Shear and compression experimental behaviour of one leaf stone masonry walls. In *Proceedings of the 15th World Conference on Earthquake Engineering*, pages 1–10, Lisbon.
- AlShawa, O., Sorrentino, L., and Liberatore, D. (2017). Simulation of shake table tests on out-of-plane masonry buildings. part (ii): Combined finite-discrete elements. *International Journal of Architectural Heritage*, 11(1):79–93.
- Angelillo, M., Lourenço, P. B., and Milani, G. (2014). Masonry behaviour and modelling. In Angelillo, M., editor, *Mechanics of Masonry Structures*, volume 551 of *CISM International Centre for Mechanical Sciences*, pages 1–26. Springer Vienna, Vienna.
- Belmouden, Y. and Lestuzzi, P. (2009). An equivalent frame model for seismic analysis of masonry and reinforced concrete buildings. *Construction and Building Materials*, 23(1):40–53.
- Benedetti, A. and Steli, E. (2008). Analytical models for shear-displacement curves of unreinforced and FRP reinforced masonry panels. *Construction and Building Materials*, 22(3):175–185.
- Benedetti, D. and Tomažević, M. (1984). Sulla verifica sismica di costruzioni in muratura. *Ingegneria sismica*, 1:9–16.

Bibliography

- Berti, M., Salvatori, L., Orlando, M., and Spinelli, P. (2017). Unreinforced masonry walls with irregular opening layouts: reliability of equivalent-frame modelling for seismic vulnerability assessment. *Bulletin of Earthquake Engineering*, 15(3):1213–1239.
- Berto, L., Saetta, A., Scotta, R., and Vitaliani, R. (2002). An orthotropic damage model for masonry structures. *International Journal for Numerical Methods in Engineering*, 55(2):127–157.
- Beyer, K. and Dazio, A. (2012). Quasi-static cyclic tests on masonry spandrels. *Earthquake Spectra*, 28(3):907–929.
- Beyer, K. and Mangalathu, S. (2012). Review of strength models for masonry spandrels. *Bulletin of Earthquake Engineering*, 11(2):521–542.
- Beyer, K., Petry, S., Tondelli, M., and Paparo, A. (2014). Towards displacement-based seismic design of modern Unreinforced Masonry Structures. In Ansal, A., editor, *Perspectives on European Earthquake Engineering and Seismology*, volume 34 of *Geotechnical, Geological and Earthquake Engineering*, pages 401–428. Springer International Publishing.
- Beyer, K., Tondelli, M., Petry, S., and Peloso, S. (2015). Dynamic testing of a four-storey building with reinforced concrete and unreinforced masonry walls: prediction, test results and data set. *Bulletin of Earthquake Engineering*, 13(10):3015–3064.
- Binda, L., Cardani, G., and Saisi, A. (2009). Caratterizzazione sperimentale della qualità muraria. In *Proceedings of the Conference "Anidis 2009"*, pages 1–10, Bologna.
- Borri, A., Castori, G., and Corradi, M. (2012). Evaluation of shear strength of masonry panels through different experimental analyses. In *14th Structural Faults and Repair*, pages 1–13, Edinburgh.
- Borri, A., Corradi, M., Castori, G., and De Maria, A. (2015). A method for the analysis and classification of historic masonry. *Bulletin of Earthquake Engineering*, 13(9):2647–2665.
- Borri, A., Corradi, M., and Vignoli, A. (2001). Il problema della valutazione della resistenza a taglio della muratura mediante prove sperimentali. In *Proceedings of the Conference "Anidis 2001"*, pages 1–11, Potenza-Matera.
- Borri, A. and De Maria, A. (2009). L'indice di qualità muraria (IQM): evoluzione e sue applicazioni nell'ambito delle NTC 2008. *L'Edilizia*, 160:46–57.
- Bosiljkov, V. Z., Totoev, Y. Z., and Nichols, J. M. (2005). Shear modulus and stiffness of brickwork masonry: An experimental perspective. *Structural Engineering and Mechanics*, 20(1):21–43.
- Bracchi, S., Rota, M., Penna, A., and Magenes, G. (2015). Consideration of modelling uncertainties in the seismic assessment of masonry buildings by equivalent-frame approach. *Bulletin of Earthquake Engineering*, 13(11):3423–3448.

- Brignola, A., Podestà, S., and Pampanin, S. (2008). In-plane stiffness of wooden floor. In *Proc. of the New Zealand Society for Earthquake Engineering Conference, Wairakei, New Zealand*.
- C., J. T. and B., G. B. (1999). Point-estimate method as numerical quadrature. *Journal of Geotechnical and Geoenvironmental Engineering*, 125(9):779–786.
- Caliò, I., Marletta, M., and Pantò, B. (2012). A new discrete element model for the evaluation of the seismic behaviour of unreinforced masonry buildings. *Engineering Structures*, 40:327–338.
- Cardani, G. and Binda, L. (2013). Guidelines for the masonry quality evaluation in built heritage. pages 107–115.
- Casolo, S. and Milani, G. (2010). A simplified homogenization-discrete element model for the non-linear static analysis of masonry walls out-of-plane loaded. *Engineering Structures*, 32(8):2352–2366.
- Cattari, S., Chiocciariello, A., Degée, H., and Doneux, C. (2014). Seismic assessment of masonry buildings from shaking table tests and nonlinear dynamic simulations by the Proper Orthogonal Decomposition. In *2nd European Conference on Earthquake Engineering and Seismology, Istanbul*.
- Cattari, S., Lagomarsino, S., Bosiljkov, V., and D’Ayala, D. (2015). Sensitivity analysis for setting up the investigation protocol and defining proper confidence factors for masonry buildings. *Bulletin of Earthquake Engineering*, 13:129–151.
- Celarec, D. and Dolšek, M. (2013). The impact of modelling uncertainties on the seismic performance assessment of reinforced concrete frame buildings. *Engineering Structures*, 52:340–354.
- CEN (2005). Eurocode 8: Design of structures for earthquake resistance, Part 3: Assessment and retrofitting of buildings. Technical Report EN 1998-3, Brussels.
- Ching, J., Porter, K. A., and Beck, J. L. (2009). Propagating uncertainties for loss estimation in performance-based earthquake engineering using moment matching. *Structure and Infrastructure Engineering*, 5(3):245–262.
- CNR (2013). DT 212/2013: Istruzioni per la valutazione affidabilistica della sicurezza sismica di edifici esistenti.
- Corradi, M., Borri, A., Castori, G., and Sisti, R. (2014). Shear strengthening of wall panels through jacketing with cement mortar reinforced by GFRP grids. *Composites Part B: Engineering*, 64:33–42.
- Costa, A. A., Arêde, A., Costa, A., and Oliveira, C. S. (2011). In situ cyclic tests on existing stone masonry walls and strengthening solutions. *Earthquake Engineering & Structural Dynamics*, 40(4):449–471.

Bibliography

- Costa, A. A., Penna, A., Arède, A., and Costa, A. (2015). Simulation of masonry out-of-plane failure modes by multi-body dynamics. *Earthquake Engineering & Structural Dynamics*, 44(14):2529–2549.
- D’Ayala, D. and Speranza, E. (2003). Definition of Collapse Mechanisms and Seismic Vulnerability of Historic Masonry Buildings. *Earthquake Spectra*, 19(3):479–509.
- D’Ayala, D. F. and Paganoni, S. (2011). Assessment and analysis of damage in l’aquila historic city centre after 6th april 2009. *Bulletin of Earthquake Engineering*, 9(1):81–104.
- Degli Abbati, S. and Lagomarsino, S. (2017). Out-of-plane static and dynamic response of masonry panels. *Engineering Structures*, 150:803–820.
- Degli Abbati, S., Rossi, M., and Lagomarsino, S. (2014). Out-of-plane experimental tests on masonry panels. In *2nd European Conference on Earthquake Engineering and Seismology*, Istanbul.
- DeJong, M. J. and Dimitrakopoulos, E. G. (2014). Dynamically equivalent rocking structures. *Earthquake Engineering and Structural Dynamics*, 43(10):1543–1563.
- DeJong, M. J. and Vibert, C. (2012). Seismic response of stone masonry spires: Computational and experimental modeling. *Engineering Structures*, 40:566–574.
- Derakhshan, H., Griffith, M. C., and Ingham, J. M. (2013). Out-of-Plane Behavior of One-Way Spanning Unreinforced Masonry Walls. *Journal of Engineering Mechanics*, 139(4):409–417.
- Doglioni, F., Mirabella Roberti, G., and Bondanelli, M. (2009). Definizione della Linea di Minimo Tracciato come elemento per la qualifica dell’ingranamento nel piano e fuori dal piano, Prodotto finale Linea 1, progetto Reluis. Technical report.
- Doherty, K., Griffith, M. C., Lam, N., and Wilson, J. (2002). Displacement-based seismic analysis for out-of-plane bending of unreinforced masonry walls. *Earthquake Engineering and Structural Dynamics*, 31:833–850.
- Dolšek, M. (2009). Incremental dynamic analysis with consideration of modeling uncertainties. *Earthquake Engineering and Structural Dynamics*, 38:805–825.
- Dolšek, M. (2012). Simplified method for seismic risk assessment of buildings with consideration of aleatory and epistemic uncertainty. *Structure and Infrastructure Engineering*, 8(10):939–953.
- ElGawady, M. A., Ma, Q., Butterworth, J. W., and Ingham, J. (2011). Effects of interface material on the performance of free rocking blocks. *Earthquake Engineering and Structural Dynamics*, pages 375–392.
- Faella, G., Manfredi, G., and Realfonzo, R. (1992). Cyclic behaviour of tuff masonry walls under horizontal loadings. In *6th Canadian Masonry Symposium*, Saskatoon, Canada.

- Fajfar, P. (2000). A Nonlinear Analysis Method for Performance-Based Seismic Design. *Earthquake Spectra*, 16(3):573–592.
- Fajfar, P. and Dolšek, M. (2012). A practice-oriented estimation of the failure probability of building structures. *Earthquake Engineering and Structural Dynamics*, (41):531–547.
- Fragiadakis, M. and Vamvatsikos, D. (2010). Fast performance uncertainty estimation via pushover and approximate IDA. *Earthquake Engineering and Structural Dynamics*, (39):683–703.
- Franceschini, S., Tsai, C., and Marani, M. (2012). Point estimate methods based on Taylor series expansion—the perturbation moments method—a more coherent derivation of the second order statistical moment. *Applied Mathematical Modelling*, 36(11):5445–5454.
- Franchin, P., Lupoi, A., Pinto, P. E., and Schotanus, M. I. J. (2003). Seismic Fragility of Reinforced Concrete Structures Using a Response Surface Approach. *Journal of Earthquake Engineering*, 7(Special Issue 1):45–77.
- Franchin, P., Pinto, P. E., and Rajeev, P. (2010). Confidence Factor? *Journal of Earthquake Engineering*, 14(7):989–1007.
- Frumento, S., Magenes, G., Morandi, P., and Calvi, G. M. (2009). *Interpretation of experimental shear tests on clay brick masonry walls and evaluation of q-factors for seismic design*. IUSS Press, Pavia.
- Gambarotta, L. and Lagomarsino, S. (1997). Damage models for the seismic response of brick masonry shear walls. Part I: the mortar joint model and its applications. *Earthquake Engineering and Structural Dynamics*, 26:423–439.
- Giovanis, D. G., Fragiadakis, M., and Papadopoulos, V. (2015). Epistemic uncertainty assessment using Incremental Dynamic Analysis and Neural Networks. *Bulletin of Earthquake Engineering*, 14(2):529–547.
- Giuffré, A. (1994). Seismic safety and strengthening of historical buildings and urban fabrics. In *10th World Conference of Earthquake Engineering*, Balkema, Rotterdam.
- Godio, M. and Beyer, K. (2017). Tri-linear model for the out-of-plane seismic assessment of vertically-spanning unreinforced masonry walls. *submitted to ASCE Structural Engineering Journal*.
- Godio, M., Vanin, F., Zhang, S., and Beyer, K. (2019). Quasi-static shear-compression tests on stone masonry walls with plaster: influence of load history and axial load ratio (under review). *Engineering Structures*, pages 1–26.
- Grammatikou, S., Biskinis, D., and Fardis, M. N. (2015). Strength, deformation capacity and failure modes of RC walls under cyclic loading. *Bulletin of Earthquake Engineering*, 13(11):3277–3300.

Bibliography

- Griffith, M. C., Magenes, G., Melis, G., and Picchi, L. (2003). Evaluation of out-of-plane stability of unreinforced masonry walls subjected to seismic excitation. *Journal of Earthquake Engineering*, 7:141–169.
- Grünthal, G. (1998). Macroseismic Scale 1992 (EMS-92). European Seismological Commission, sub commission on Engineering Seismology, working Group Macroseismic. *Cahiers du Centre Européen de Géodynamique et de Séismologie*.
- Guerrini, G., Senaldi, I. E., Comini, P. and Kallioras, S., Vanin, F., Godio, M., Graziotti, F., Magenes, G., Beyer, K., and Penna, A. (2018). Experimental and numerical assessment of the seismic performance of a half-scale stone masonry building aggregate. In *16th European Conference on Earthquake Engineering*.
- Hall, J. F. (2006). Problems encountered from the use (or misuse) of Rayleigh damping. *Earthquake Engineering and Structural Dynamics*, 35:525–545.
- Haselton, C. B. (2006). *Assessing Seismic Collapse Safety of Modern Reinforced Concrete Moment Frame Buildings*. Phd thesis, Stanford University.
- Hong, H. (1998). An efficient point estimate method for probabilistic analysis. *Reliability Engineering & System Safety*, 59(3):261–267.
- Housner, G. W. (1963). The behavior of inverted pendulum structures during earthquakes. *Bulletin of the Seismological Society of America*, 53(2):403–417.
- Kappos, A. J., Penelis, G. G., and Drakopoulos, C. G. (2002). Evaluation of simplified models for lateral load analysis of unreinforced masonry buildings. *Journal of Structural Engineering*, 128(7):890–897.
- Kosič, M., Fajfar, P., and Dolšek, M. (2014). Approximate seismic risk assessment of building structures with explicit consideration of uncertainties. *Earthquake Engineering and Structural Dynamics*, 43(10):1483–1502.
- Kržan, M. and Bosiljkov, V. (2012). Results of laboratory and in-situ tests on masonry properties and tables with mechanical parameters to be adopted in numerical modelling, PERPETUATE Project, Deliverable D15, www.perpetuate.eu. Technical report.
- Kržan, M., Gostič, S., Cattari, S., and Bosiljkov, V. (2014). Acquiring reference parameters of masonry for the structural performance analysis of historical buildings. *Bulletin of Earthquake Engineering*, 13(1):203–236.
- Lagomarsino, S. (2006). On the vulnerability assessment of monumental buildings. *Bulletin of Earthquake Engineering*, 4(4):445–463.
- Lagomarsino, S. (2015). Seismic assessment of rocking masonry structures. *Bulletin of Earthquake Engineering*, 13:97–128.

- Lagomarsino, S., Penna, A., Galasco, A., and Cattari, S. (2013). TREMURI program: An equivalent frame model for the nonlinear seismic analysis of masonry buildings. *Engineering Structures*, 56:1787–1799.
- Lee, T. H. and Mosalam, K. M. (2005). Seismic demand sensitivity of reinforced concrete shear-wall building using FOSM method. *Earthquake Engineering and Structural Dynamics*, 34(14):1719–1736.
- Li, K. S. (1992). Point-estimate Method for Calculating Statistical Moments. *Journal of Eng. Mechanics*, 118(7):1506–1511.
- Liel, A. B., Haselton, C. B., Deierlein, G. G., and Baker, J. W. (2009). Incorporating modeling uncertainties in the assessment of seismic collapse risk of buildings. *Structural Safety*, 31(2):197–211.
- Lotfi, H. R. and Shing, P. B. (1991). An appraisal of smeared crack models for masonry shear wall analysis. *Computers and Structures*, 41(3):413–425.
- Lourenço, P. B. (1996). *Computational strategies for masonry structures*. PhD thesis.
- Lourenço, P. B., Oliveira, D. V., Roca, P., and Orduña, A. (2005). Dry joint stone masonry walls subjected to in-plane combined loading. *Journal of Structural Engineering*, 131(11):1665–1673.
- Lourenço, P. B. and Rots, J. G. (1997). Multisurface interface model for analysis of masonry structures. *Journal of Engineering Mechanics*, 123(7).
- Magenes, G. and Calvi, G. M. (1997). In-plane seismic response of brick masonry walls. *Earthquake Engineering and Structural Dynamics*, 26(11):1091–1112.
- Magenes, G., Penna, A., Galasco, A., and Rota, M. (2010). Experimental characterisation of stone masonry mechanical properties. In *8th International Masonry Conference*, Dresden, Germany.
- Makris, N. and Konstantinidis, D. (2003). The rocking spectrum and the limitations of practical design methodologies. *Earthquake Engineering and Structural Dynamics*, 32(2):265–289.
- Malomo, D., Pinho, R., and Penna, A. (2018). Using the applied element method to simulate the dynamic response of full-scale urm houses tested to collapse or near-collapse conditions. In *16th European Conference on Earthquake Engineering*, Thessaloniki.
- Mandirola, M., Galasco, A., Penna, A., and Magenes, G. (2016). Nonlinear macroelement modelling of experimental tests on masonry buildings with rigid diaphragms. In *Proceedings of the 16th International Brick and Block Masonry Conference*, Padova.
- Mann, W. and Muller, H. (1982). Failure of shear-stressed masonry. An enlarged theory, tests and application to shear walls. In *Proceedings British Ceramic Society Society*.

Bibliography

- Marcari, G., Manfredi, G., Prota, A., and Pecce, M. (2007). In-plane shear performance of masonry panels strengthened with FRP. *Composites Part B*, 38:887–901.
- Marini, A. and Spacone, E. (2006). Analysis of reinforced concrete elements including shear effects. *ACI Structural Journal*, 103(5):645.
- Mazzon, N. (2010). *Influence of grout injection on the dynamic behaviour of stone masonry buildings*. Phd thesis, University of Padova, Italy.
- McKenna, F., Fenves, G. L., Scott, M. H., and Jeremic, B. (2000). Open System for Earthquake Engineering Simulation (OpenSees). Technical report, Berkeley.
- Mendes, N., Costa, A. A., Lourenço, P. B., Bento, R., Beyer, K., de Felice, G., Gams, M., Griffith, M. C., Ingham, J. M., Lagomarsino, S., et al. (2017). Methods and approaches for blind test predictions of out-of-plane behavior of masonry walls: A numerical comparative study. *International Journal of Architectural Heritage*, 11(1):59–71.
- Mergos, P. E. and Beyer, K. (2014). Loading protocols for European regions of low to moderate seismicity. *Bulletin of Earthquake Engineering*, 12(6):2507–2530.
- Mihaylov, B. I., Hannewald, P., and Beyer, K. (2016). Three-Parameter Kinematic Theory for Shear-Dominated Reinforced Concrete Walls. *Journal of Structural Engineering*, 142(7):04016041.
- Milani, G. (2011). Simple homogenization model for the non-linear analysis of in-plane loaded masonry walls. *Computers and Structures*, 89(17-18):1586–1601.
- Milani, G., Lourenço, P. B., and Tralli, A. (2007). 3D homogenized limit analysis of masonry buildings under horizontal loads. *Engineering Structures*, 29(11):3134–3148.
- Miller, A. C. and Rice, T. R. (1983). Discrete Approximations of Probability Distributions. *Management Science*, 29(3):352–362.
- MIT (2009). Istruzioni per l'applicazione delle "Nuove norme Tecniche per le Costruzioni" di cui al decreto ministeriale 14/1/2008. Technical report, Min. delle Infrastrutture e dei Trasporti.
- Oliveira, D. V. (2003). *Experimental and Numerical Analysis of Blocky Masonry Structures Under Cyclic Loading*. Phd thesis, University of Minho.
- Pantò, B., Cannizzaro, F., Caddemi, S., and Calì, I. (2016). 3D macro-element modelling approach for seismic assessment of historical masonry churches. *Advances in Engineering Software*, 97:40–59.
- Parisi, F. and Augenti, N. (2012). Uncertainty in Seismic Capacity of Masonry Buildings. *Buildings*, 2(3):218–230.

- Parisi, F. and Augenti, N. (2013a). Seismic capacity of irregular unreinforced masonry walls with openings. *Earthquake Engineering & Structural Dynamics*, 42(1):101–121.
- Parisi, F. and Augenti, N. (2013b). Seismic capacity of irregular unreinforced masonry walls with openings. *Earthquake Engineering and Structural Dynamics*, 42(1):101–121.
- Pelà, L., Cervera, M., and Roca, P. (2013). An orthotropic damage model for the analysis of masonry structures. *Construction and Building Materials*, 41:957–967.
- Peña, F. and Lourenço, P. B. (2006). Modeling the dynamic behaviour of masonry walls as rigid blocks. *Computational Mechanics*, (June):5–8.
- Penna, A. (2015). Seismic assessment of existing and strengthened stone-masonry buildings: critical issues and possible strategies. *Bulletin of Earthquake Engineering*, 13(4):1051–1071.
- Penna, A., Lagomarsino, S., and Galasco, A. (2014). A nonlinear macroelement model for the seismic analysis of masonry buildings. *Earthquake Engineering and Structural Dynamics*, 43:159–179.
- Penna, A., Senaldi, I. E., Galasco, A., and Magenes, G. (2016). Numerical simulation of shaking table tests on full-scale stone masonry buildings. *International Journal of Architectural Heritage*, 10(2-3):146–163.
- Peruch, M., Spacone, E., and Camata, G. (2019a). Nonlinear analysis of masonry structures using fiber-section line elements. *Earthquake Engineering & Structural Dynamics*, pages 1–20.
- Peruch, M., Spacone, E., and Shing, P. B. (2019b). Cyclic analyses of reinforced concrete masonry panels using a force-based frame element. *Journal of Structural Engineering*, 145(7).
- Petrini, L., Maggi, C., Priestley, M. J. N., and Calvi, G. M. (2008). Experimental verification of viscous damping modeling for inelastic time history analyses. *Journal of Earthquake Engineering*, 12:S1:125–145.
- Petry, S. and Beyer, K. (2014a). Influence of boundary conditions and size effect on the drift capacity of URM walls. *Engineering Structures*, 65:76–88.
- Petry, S. and Beyer, K. (2014b). Scaling unreinforced masonry for reduced-scale seismic testing. *Bulletin of Earthquake Engineering*, 12(6):2557–2581.
- Petry, S. and Beyer, K. (2015). Force-displacement response of in-plane-loaded URM walls with a dominating flexural mode. *Earthquake Engineering & Structural Dynamics*, 44(14):2551–2573.
- Pfyl-Lang, K., Braune, F., and Lestuzzi, P. (2011a). SIA D0237: Beurteilung von Mauerwerksgebäuden bezüglich Erdbeben. Technical report, Zürich.

Bibliography

- Pfyl-Lang, K., Braune, F., and Lestuzzi, P. (2011b). SIA D0237: Beurteilung von Mauerwerksgebäuden bezüglich Erdbeben (SIA D 0237: Evaluation de la sécurité parasismique des bâtiments en maçonnerie). Technical report, Zürich.
- Pinho, F. F. S., Lúcio, V. J. G., and Baião, M. F. C. (2012). Rubble stone masonry walls in Portugal strengthened with reinforced micro-concrete layers. *Bulletin of Earthquake Engineering*, 10(1):161–180.
- Pinto, P. E. and Franchin, P. (2014). Existing buildings: the new italian provisions for probabilistic seismic assessment. *Perspectives on European earthquake engineering and seismology*, 34.
- Psycharis, I. N., Lemos, J. V., Papastamatiou, D. Y., and Zambas, C. (2003). Numerical study of the seismic behaviour of a part of the Parthenon Pronaos. *Earthquake Engineering and Structural Dynamics*, 32:2063–2084.
- Quagliarini, E., Maracchini, G., and Clementi, F. (2017). Uses and limits of the Equivalent Frame Model on existing unreinforced masonry buildings for assessing their seismic risk : A review. *Journal of Building Engineering*, 10(March):166–182.
- Raka, E., Spacone, E., Sepe, V., and Camata, G. (2015). Advanced frame element for the seismic analysis of masonry structures: model formulation and validation. *Earthquake Engineering and Structural Dynamics*, 44:2489–2506.
- Roca, P., Molins, C., and Marí, A. R. (2005). Strength Capacity of Masonry Wall Structures by the Equivalent Frame Method. *Journal of Structural Engineering*, 131(10):1601–1610.
- Rosenblueth, E. (1975). Point estimates for probability moments. *Proc. of the National Academy of Sciences of the United States of America*, 72(10):3812–4.
- Rosenblueth, E. (1981). Two-point estimates in probabilities. *Applied Mathematical Modelling*, 5(5):329–335.
- Rota, M., Penna, A., and Magenes, G. (2010). A methodology for deriving analytical fragility curves for masonry buildings based on stochastic nonlinear analyses. *Engineering Structures*, 32:1312–1323.
- Rota, M., Penna, A., and Magenes, G. (2014a). A framework for the seismic assessment of existing masonry buildings accounting for different sources of uncertainty. *Earthquake Engineering and Structural Dynamics*, (43):1045–1066.
- Rota, M., Penna, A., and Magenes, G. (2014b). A framework for the seismic assessment of existing masonry buildings accounting for different sources of uncertainty. *Earthquake Engineering and Structural Dynamics*, 43(7):1045–1066.

- Senaldi, I. E., Guerrini, G., Comini, P., Graziotti, F., Penna, A., Beyer, K., and Magenes, G. (2019). Experimental seismic performance of a half-scale stone masonry building aggregate. *Bulletin of Earthquake Engineering*.
- Siano, R., Roca, P., Camata, G., Pelà, L., Sepe, V., Spacone, E., and Petracca, M. (2018). Numerical investigation of non-linear equivalent-frame models for regular masonry walls. *Engineering Structures*, 173(July):512–529.
- Silva, B., Dalla Benetta, M., Da Porto, F., and Modena, C. (2014). Experimental assessment of in-plane behaviour of three-leaf stone masonry walls. *Construction and Building Materials*, 53:149–161.
- Silva, B., Guedes, J. M., Arêde, A., and Costa, A. (2012). Calibration and application of a continuum damage model on the simulation of stone masonry structures: Gondar church as a case study. *Bulletin of Earthquake Engineering*, 10(1):211–234.
- Sorrentino, L., AlShawa, O., and Decanini, L. D. (2011). The relevance of energy damping in unreinforced masonry rocking mechanisms. Experimental and analytic investigations. *Bulletin of Earthquake Engineering*, 9:1617–1642.
- Sorrentino, L., Cattari, S., da Porto, F., Magenes, G., and Penna, A. (2018). Seismic behaviour of ordinary masonry buildings during the 2016 central italy earthquakes. *Bulletin of Earthquake Engineering*, pages 1–25.
- Tomažević, M. (2007). Damage as a measure for earthquake-resistant design of masonry structures: Slovenian experience. *Canadian Journal of Civil Engineering*, 34(11):1403–1412.
- Tondelli, M., Beyer, K., and DeJong, M. (2016a). Influence of boundary conditions on the out-of-plane response of brick masonry walls in buildings with rc slabs. *Earthquake Engineering & Structural Dynamics*, 45(8):1337–1356.
- Tondelli, M., Beyer, K., and DeJong, M. (2016b). Influence of boundary conditions on the out-of-plane response of brick masonry walls in buildings with rc slabs. *Earthquake Engineering and Structural Dynamics*, 45(8):1337–1356.
- Tondelli, M., Rota, M., Penna, A., and Magenes, G. (2012). Evaluation of Uncertainties in the Seismic Assessment of Existing Masonry Buildings. *Journal of Earthquake Engineering*, 16(sup1):36–64.
- Turnšek, V. and Čačovič, F. (1971). Some experimental results on the strength of brick masonry walls. In *Proceedings of the 2nd International Brick Masonry Conference*, pages 149–156, Stoke-on-Trent, England.
- Vamvatsikos, D. and Fragiadakis, M. (2010). Incremental dynamic analysis for estimating seismic performance sensitivity and uncertainty. *Earthquake Engineering and Structural Dynamics*, (39):141–163.

Bibliography

- Vanin, F., Saraiva Esteves Pacheco de Almeida, J., and Beyer, K. (2017a). Force-based finite element for modelling the cyclic behaviour of unreinforced masonry piers. In *Proceedings of the 16th World Conference on Earthquake Engineering*, number CONF.
- Vanin, F., Zaganelli, D. Penna, A., and Beyer, K. (2017b). Estimates for the stiffness, strength and drift capacity of stone masonry walls based on 123 quasi-static cyclic tests reported in the literature. *Bulletin of Earthquake Engineering*, 15(12):5435–5479.
- Vasconcelos, G. (2005). *Experimental investigations on the mechanics of stone masonry: Characterization of granites and behavior of ancient masonry shear walls*. Phd thesis, University of Minho, Portugal.
- Vasconcelos, G. and Lourenço, P. B. (2009). In-Plane Experimental Behavior of Stone Masonry Walls under Cyclic Loading. *Journal of Structural Engineering*, 135:1269–1277.
- Vassiliou, M. F., Mackie, K. R., and Stojadinović, B. (2014). Dynamic response analysis of solitary flexible rocking bodies: modeling and behavior under pulse-like ground excitation. *Earthquake Engineering and Structural Dynamics*, 43(10):1463–1481.
- Vassiliou, M. F., Mackie, K. R., and Stojadinović, B. (2017). A finite element model for seismic response analysis of deformable rocking frames. *Earthquake Engineering and Structural Dynamics*, 46(3):447–466.
- Vořechovský, M. and Novák, D. (2003). Statistical correlation in stratified sampling. In *Proc. of 9th Int. Conf. on Applications of Statistics and Probability in Civil Engineering–ICASP*, volume 9, pages 119–124.
- Wilding, B. V. and Beyer, K. (2017). Force–displacement response of in-plane loaded unreinforced brick masonry walls: the Critical Diagonal Crack model. *Bulletin of Earthquake Engineering*, 15(5):2201–2244.
- Wilding, B. V. and Beyer, K. (2018). Analytical and empirical models for predicting the drift capacity of modern unreinforced masonry walls. *Earthquake Engineering and Structural Dynamics*, 47(10):2012–2031.
- Wilding, B. V., Dolatshahi, K. M., and Beyer, K. (2017). Influence of load history on the force-displacement response of in-plane loaded unreinforced masonry walls. *Engineering Structures*, 152:671–682.
- Zareian, F. and Krawinkler, H. (2007). Assessment of probability of collapse and design for collapse safety. *Earthquake Engineering and Structural Dynamics*, 36(13):1901–1914.
- Zhang, S., Mousavi, S. M. T., Richart, N., Molinari, J.-F., and Beyer, K. (2017). Micro-mechanical finite element modeling of diagonal compression test for historical stone masonry structure. *International Journal of Solids and Structures*, 112:122–132.

- Zhao, Y. and Ono, T. (2000). New Point Estimates for Probability Moments. *Journal of Eng. Mechanics*, 126(4):433–436.
- Zucchini, A. and Lourenço, P. B. (2009). A micro-mechanical homogenisation model for masonry: Application to shear walls. *International Journal of Solids and Structures*, 46(3-4):871–886.

Francesco Vanin

Chemin de La Criblette 3, 1091 Grandvaux (CH)

Tel. +41 21 69 39376

Email · francesco.vanin@epfl.ch

EDUCATION

2013 – 2014

Advanced Masters in Structural Analysis of Monuments and Historical Constructions (SAHC)

University of Minho, Guimarães, Portugal

Technical University of Catalunya, Barcelona, Spain

Thesis: *“Applicability of classic calculus methods on arches with a critically low number of voussoirs”*

2010 – 2013

MSc in Civil Engineering

University of Padova, Italy

Grade: 110/110 with honours

2007 – 2010

BSc in Architectural Engineering

University of Padova, Italy

Grade: 110/110

RESEARCH EXPERIENCE

2015 – 2019

PhD candidate, Earthquake Engineering and Structural Dynamics

École Polytechnique Fédérale de Lausanne (EPFL), Switzerland

Supervisor: prof. Katrin Beyer

Project: Basel project, 2015-2018 (Seismic verification and testing of stone masonry buildings)

Discussion: July 2019 (expected)

Thesis: *“Equivalent-frame models for in-plane and out-of-plane response of unreinforced masonry buildings”*

- Developed and implemented in the software OpenSees a macro-element for simulating the three-dimensional response of a masonry wall;
- Investigated the influence of modelling assumptions and parameter uncertainty in equivalent-frame models of masonry buildings;
- Performed quasi-static shear tests on masonry walls and collaborated in the planning and execution of a shaking-table test of a half-scale stone masonry aggregate.

2013

Research fellow, Dept. of Civil, Architectural and Environmental Engineering

University of Padova, Italy

Supervisor: prof. Maria Rosa Valluzzi

Project: PROVACI

Short-term collaboration (March-September 2013): Seismic damage and vulnerability of artistic assets attached to masonry structures in historical buildings

PUBLICATIONS

- Vanin, F., Zaganelli, D., Penna, A., Beyer, K. (2017) *“Estimates for the stiffness, strength and drift capacity of stone masonry walls based on 123 quasi-static cyclic tests reported in the literature”*. Bulletin of Earthquake Engineering, 15, 12, 5435-5479
- Vanin, F., Penna, A., Beyer, K. (2019). *“A three-dimensional macro-element for modelling of the in-plane and out-of-plane response of masonry walls”*. Submitted to Earthquake Engineering and Structural Dynamics (under revision)
- Vanin, F., Beyer, K. (2019). *“Incorporating epistemic uncertainty in the assessment of an existing masonry building through a Point Estimate Method”*. Submitted to Earthquake Engineering and Structural Dynamics (under revision)
- Vanin, F., Senaldi, I.E., Beyer, K. (2019). *“Equivalent-frame modelling of shaking table tests of unreinforced masonry buildings including out-of-plane behaviour”* (in preparation)
- Godio, M., Vanin, F., Zhang, S., Beyer, K. (2019) *“Quasi-static shear-compression tests on stone masonry walls with plaster: Influence of load history and axial load ratio”*. Engineering Structures (accepted, in press)

PRESENTATIONS

- 16th World Conference on Earthquake Engineering (WCEE), Santiago de Chile (January 2017)
“Force-based finite element for modelling the cyclic behaviour of unreinforced masonry piers”.
Vanin, F., Almeida, J. P., Beyer, K.
- 13th Canadian Masonry Symposium (CMS), Halifax, Canada (June 2017)
“Modelling the shear cyclic behaviour of a masonry pier through a force-based beam element”.
Vanin, F., Almeida, J. P., Beyer, K.
- 7th International Conference on Advances in Experimental Structural Engineering (AESE), Pavia, Italy, September 2017
“Experimental mechanical characterisation of stone masonry under uniaxial and biaxial stress state”. Vanin, F., Beyer, K.
- 16th European Conference on Earthquake Engineering (ECEE), Thessaloniki, Greece, June 2018
“Application of a Point Estimate Method for incorporating epistemic uncertainty in the seismic assessment of a masonry building”. Vanin, F., Beyer, K.
- 1st Eurasian Conference on OpenSees (EOS), Hong Kong, June 2019
“Macro-element for the in-plane and out-of-plane behaviour of masonry walls”. Vanin, F., Beyer, K.

PERSONAL SKILLS

Mother tongue: Italian

Other languages:

- English (C1)
- French (B1-B2)
- Spanish (B1)

Computer skills:

- developer of some OpenSees libraries (elements, materials) for masonry
- use of common finite element commercial software (DIANA, Abaqus)
- programming languages: good knowledge of C++, Matlab, Fortran, basics of Python
- good command of Microsoft Office and CAD tools.

Teaching experience:

- teaching assistant of the course “Statique I” (2015-2019)
- supervision of 6 master theses on numerical simulation of stone masonry buildings

REFEREES

Professor Katrin Beyer,

Earthquake Engineering and Structural Dynamics laboratory, EPFL, Lausanne, Switzerland

Phone: +41 21 69 36234

e-mail: katrin.beyer@epfl.ch

Professor Andrea Penna,

EUCENTRE, Pavia, Italy

Phone: +39 0382 5169824

e-mail: andrea.penna@unipv.it

